# Sheffield Hallam University

## A Sheffield Hallam University thesis

# INITIATION & GROWTH OF CORROSION FATIGUE CRACK FOR AVPP TREATED STAINLESS STEEL

## SALAH A. GNEFID

### Ph.D.

## SHEFFIELD HALLAM UNIVERSITY

### 2011

# INITIATION & GROWTH OF CORROSION FATIGUE CRACK FOR AVPP TREATED STAINLESS STEEL

## SALAH A. GNEFID

**A Thesis Submitted in Partial Fulfilment of the Requirement of Sheffield Hallam University for the Degree of Doctor of Philosophy**

**February 2011**

**DEDICATED**

**TO**

**MY PARENTS**

**&**

**To the Soul of My Brother Hamuda who was killed By The Gaddafi Forces on the 4th July 2011**

# Acknowledgments

It is said that who does not thank people, does not thank God. Therefore I would like to thank these people without whom this thesis would not have been possible. I am grateful to my supervisor Prof. Robert Akid for his advice and support during my study.

I would like to show my gratitude to Dr. David Greenfield for teaching me different electrochemical techniques during my present study. In this regard I would like also to thank Mr. Gary Robinson for material supply and samples manufacturing. Special thanks are due to Mr. Alex Walton University of Leeds, for his continuous cooperation and advices in the XPS analysis.

I wish to express my sincere feelings to my lab and Office mates for their help at various stages of my work and for keeping a congenial atmosphere during my stay in the department.

I wish to acknowledge from the depth of my heart the persistent efforts made by my parents, brothers and sisters to achieve the highest degree in the field of education. My special thanks go to my wife Hanan and daughters, Fatema, Doha and Sarah, for their love, patience, support and encouragement.

Last, but not least, the Libyan Education General Committee and the Libyan Culture Affairs in London are acknowledged for sponsoring me to join the Sheffield Hallam University.

# ABSTRACT

The influence of material surface condition, notably passive film condition and surface residual stress and the effect of applied surface stress on the development of corrosion pits has been assessed in relation to their role on the fatigue behaviour of stainless steel materials, in particular the early stages of corrosion fatigue. Several experimental techniques have been used to quantify changes in material response during stress and corrosion interactions.

The original surface film of 316L austenitic stainless steel was modified electrochemically using an alternative voltage passiviation process (AVPP) to study the effects of this modification on the mechanical and corrosion properties. The composition, structure and thickness state of the original and modified oxide films were analysed applying X-Ray photoelectron spectroscopy (XPS) technique. Chromium enrichment in the modified passive film surface was observed, as was increase in the passive film thickness for the modified surface.

Potentiodynamic polarization and electrochemical impedance spectroscopy (EIS) tests were performed in artificial seawater on the original and the modified passive film, in order to evaluate the differences in corrosion behaviour of the material. Results show that the pitting potential $E_p$ of the modified film is higher than the original film. Also EIS results show improvement in the corrosion resistance in material surface with the modified film. Potentiostatic measurements using the Scanning Droplet Cell (SDC) system were used to investigate the effects of surface finish and the electrolyte flow rates on localised corrosion (pitting). The localised corrosion rate increased as the flow rate and surface roughness increased.

Changes in surface residual stress state of the native and modified oxide films during cyclic loading were studied using X-Ray Diffraction technique. Surface compressive residual stress was found to decreased as a result of the introduction of a new oxide film.

Nanoindentation tests using a Berkovich diamond indenter were performed to explore the differences in mechanical properties between 316L SS oxide film before and after AVPP treatment. The load–depth curves of the native oxide film surface were compared with those of the modified oxide film surface to investigate the differences in the mechanical properties. It was found that the 316L oxide-film has a higher hardness compared to the AVPP oxide-film. Tensile tests were conducted to investigate the tensile strength of the material, results show that the yield strength and the tensile strength of 316L SS samples were about 300 MPa and 600 MPa respectively.

The effect of corrosion pits on the fatigue behaviour of stainless steel materials in particular the short crack regime was investigated using the SDC in combination with a fatigue rig. The mechanism of corrosion fatigue crack growth, which consists of, pit nucleation, pit growth, transition from pitting to fatigue crack initiation, and short crack growth were studied. This system consists of a fatigue rig, and electrochemical droplet cell. Results showed improvement in the corrosion fatigue life in the AVPP modified 316L SS surface compared to the native surface due to a delay in pit initiation.

# Table of Contents

# Chapter 1- Introduction

Although stainless steel alloys are known to provide good resistance to general corrosion, they are susceptible to localised corrosion even in alloys with high percentages of chromium and nickel, such as duplex stainless steels. Resistance of stainless steel alloys to pitting corrosion is dependent on their oxide film structure, chemical compositions and thickness [1, 2, 3]. Recently, there have been attentions to produce a homogenous oxide film in order to obtain a novel surface function of metallic materials. The alternating voltage passivation process (AVPP) was reported to enhance the corrosion resistance of stainless steels as a result of increasing the oxide layer thickness and changing in its composition [4, 5]. It has been suggested as an environmentally-friendly surface treatment compared to other surface treatments because it does not use high temperature or Cr(IV) solutions. Surface treatment techniques such as laser treatment and ion implantation are also recognised to improve the corrosion resistance of some materials, however the high costs limit their application [6].

The effects of stress conditions on the AVPP passive film conductivity of 316L SS were studied by Vignal and co-workers [4]. They found that the conductivity of the passive film changes depends on the stress value and on whether the applied stress is tensile or compressive.

Chambreuil et al. [7] found an improvement in the stress corrosion cracking behaviour of 316L SS when subjected to a cyclic pre-stressing at saturation, thereby causing a delay in the initiation of cracking increasing the time to failure to about 50%.

By applying a square-wave potential pulse polarization procedure in sulphuric acid, Fujimoto et al. [8] produced a very thick and porous passive oxide film on a 304 stainless steel surface. The authors discussed the film formation mechanism and the resulting electrochemical, structural and morphological properties of the film in detail. They concluded that the method could be used to form thick and porous oxide films on alloys consisting of an (easily-dissolving) base metal and an oxide-stable alloying element (e.g. FeCr, NiCr, FeTi).

The present work is concentrated on understanding the changes in the 316L SS passive film composition, structure and thickness as a result of the application of the Alternating Voltage Passivation Process. Accordingly, the effects of the modification of the passive oxide film of austenitic 316L SS on the electrochemical and the mechanical properties were investigated. These effects were examined through comprehensive electrochemical and mechanical experimental study. The effects of the AVPP surface treatment on the electrochemical activities were assessed through several experiments such as potentiodynamic polarisation, potentiostatic polarisation, linear voltammetry and electrochemical impedance spectroscopy. Most of the electrochemical tests were performed using a Scanning Droplet Cell (SDC). The SDC is a new and versatile tool for locally resolved electrochemical investigation of metallic surfaces.

Mechanical tests include tensile strength test, nano-indenter hardness test and residual stress measurement using x-ray diffraction technique. Finally corrosion fatigue tests were conducted to assess the influence of surface modification by AVPP on the corrosion fatigue life and on the corrosion fatigue crack initiation and early crack growth.

Historically fatigue studies have been conducted based upon structures or components containing pre-existing defects and therefore address the long-crack propagation regime. However some studies [9] have been concerned with the prediction of lifetime for structures, components, nominally free from defects. These studies have shown that some 70-90% of lifetime may be taken up in growing defects of a size less than 0.5mm, i.e., the short-crack growth regime.

The majority of these studies have however, been conducted in air. This is of particular concern from the standpoint of fatigue crack study where the effects of environment are not considered as it is now recognised that the environment can have a dramatic effect on short-crack growth, i.e., elimination of stage I cracking, and a decrease in ultimate fatigue life [10].

While several studies have been conducted on corrosion fatigue crack initiation and growth [11,12, 13, 14, 15, 16], these studies are commonly performed using a conventional corrosion cell. To our knowledge no other studies have employed the SDC technique in corrosion fatigue tests. The SDC in this study was used to generate corrosion pits and monitoring the localised electrochemical response produced during corrosion fatigue tests.

Failure regimes will be identified for given environmental and loading conditions and damage mechanism will be constructed [17, 18, 19]. Failure mechanism for selected conditions outside existing literature data will be studied based upon an understanding of corrosion/fracture mechanics. Therefore, corrosion fatigue tests based upon the selected conditions were conducted.

The main aim of this study was to understand the role of AVPP treatment on corrosion fatigue lifetime. In order to achieve this aim, the initiation of pits and their transition to a fatigue crack was studied.

This study is exclusive because of the following aspects:

- Present the structure and composition of AVPP passive film in detail.

- Investigate the electrochemical behaviour of AVPP passive film using SDC.

- Investigate the AVPP passive film nano-indentation hardness.

- Investigate the change in the surface residual stress using XRD because of AVPP.

- Investigate the corrosion fatigue behaviour of AVPP using particularly designed mechanical-electrochemical system using SDC.


Taking in account all these aspects, the corrosion pits growth and its transition to small corrosion crack of stainless steels materials, in corrosive medium is complex. To our knowledge no information has been published about corrosion fatigue of stainless steel materials subjected to AVPP treatment. Accordingly it is clear that a comprehensive understanding of this matter is still lacking.

# Chapter 2- Literature Review

The literature review presented in this thesis contains general information about stainless steels including the historical development and some of their applications. Secondly, comprehensive understanding is required of the theory of fatigue in air including fatigue crack initiation and fatigue crack propagation processes. Section (2.2) of the literature review includes the general principles of fatigue cracking in air and providing a review on the crack initiation and crack propagation processes. Section (2.3) provides a review of corrosion and its theory including the mechanism of pitting and passive film breakdown.

Section (2.4) includes a review of the corrosion fatigue phenomenon, with an emphasis on the pitting process in the presence of fatigue, reporting some of the published models used to interpret the corrosion fatigue crack development.

The last sections of the literature review represent fundamental information concerning characterisation techniques e.g. X-ray Diffraction (XRD) Technique for Residual Stress Measurements and X-Ray Photoelectron Spectroscopy (XPS) which is used to determine quantitative atomic and chemical compositions of thin films.

## 2.1 Stainless Steels

### 2.1.1. Historical Overview

The 19th century is known as the industrial era, which established a strong base and notable progress, using cast and wrought iron, and carbon steel as the main metals. The developing advanced industries in the last century increase the demand in producing new metals which can be used in aggressive environments to resist corrosion. For example, improvements in power generating plants required materials with combined oxidation resistance and good mechanical

properties, expansion of chemical and petrochemical industries demanded high corrosion resistance materials, etc.

Stainless steels were developed in the beginning of the last century in the United Kingdom and Germany [20]. Different grades of stainless steels were developed, the most common being the austenitic phase alloys. Brearley [21] had introduced in 1916 a 12-13% Cr martensitic steel for cutlery in Sheffield, but it was in 1924 that the well known 18% Cr - 8%Ni with 0.10-0.15%C austenitic steel was produced as a development of a 0.25%C - 20%Cr - 7%Ni steel introduced by Strauss in Germany. Its excellent mechanical properties and high corrosion resistance established this as the prototype of stainless steels [22]. Nowadays, the term stainless steel is applied to a wide range of chromium-bearing iron alloys with not less than 11%Cr content, although other elements are commonly added to enhance certain desired, properties.

Stainless Steels are iron alloys containing at least 11% chromium. This percentage enables the alloys to resist corrosion in aggressive environments due to the development of complex Cr-Fe oxide film. The film is principally stable and self-healing in the presence of oxygen. The presence of this protective film results in a very low corrosion rate, despite the high thermodynamic tendency of the steel to react in aggressive environments. It is from this property that the known expression "stainless" is used for these kind of steels.

The earliest stainless steel types were martensitic and ferritic iron-chromium alloys but later austenitic iron-chromium-nickel steels became the largest group. This was mainly due to the ease of production and fabrication, particularly welding, of these types of steel. The minimum carbon concentration that could be reached with the production and refining processes existent at that time was 0.08%. This made the steels susceptible to grain boundary carbide precipitation during heat treatment and welding operations. This carbide precipitation and the consequent

formation of chromium depleted zones after welding, (the heat affected zone), could induce sensitisation of the alloy and susceptibility to localised attack [23]. Intergranular stress corrosion cracking (IGSCC) is the most common forms of stress-assisted localised attack of sensitised austenitic stainless steels in chloride environments.

Many different alloys can be denoted as stainless steel and each steel-manufacturer continues to produce new alloys with some compositional changes. In some stainless steels the chromium content now approaches 30%, and many other elements are added to provide specific properties. For example, nickel, nitrogen and molybdenum are added to improve corrosion resistance; carbon, titanium, aluminium, molybdenum, nitrogen and copper for strength; sulphur and selenium for machinability; and nickel for formability and toughness [24].

According to metallurgical structure stainless steels are divided into three groups: austenitic "$\gamma$" face centred cubic (fcc), ferritic "$\alpha$" body centred cubic (bcc), and martensitic (body centred tetragonal or cubic). There is another stainless alloy, duplex ($\gamma$, $\alpha$), which possesses a two-phase microstructure with approximately equal amounts of austenite and ferrite [25].

## 2.1.2 Austenitic Stainless Steels

Austenitic stainless steel is essentially an iron-chromium-nickel alloy, containing between 18 and 30 wt% chromium, 8-20 wt% nickel and 0.03-0.1 wt% carbon [26]. It retains the austenitic structure to ambient temperature. The basic austenitic stainless steel is 304 which is an iron-based alloy containing nominally 18% chromium and 8.5% nickel, minor amounts of carbon , nitrogen, manganese, and silicon [22]. From this basic composition a family of modifications on the original 304 alloy have been produced. These are known as the standard austenitic stainless steels and an example is shown in Figure 2.1. The initial solution-treated state of the 300 series

austenitic stainless steels is thermodynamically unstable and, consequently, changes in their microstructure can be induced by thermo-mechanical treatment. Rapid quenching of the leaner alloys can promote martensite formation whilst thermal ageing of all steels promotes precipitation of carbides and intermetallics which may continue for considerable periods of time.
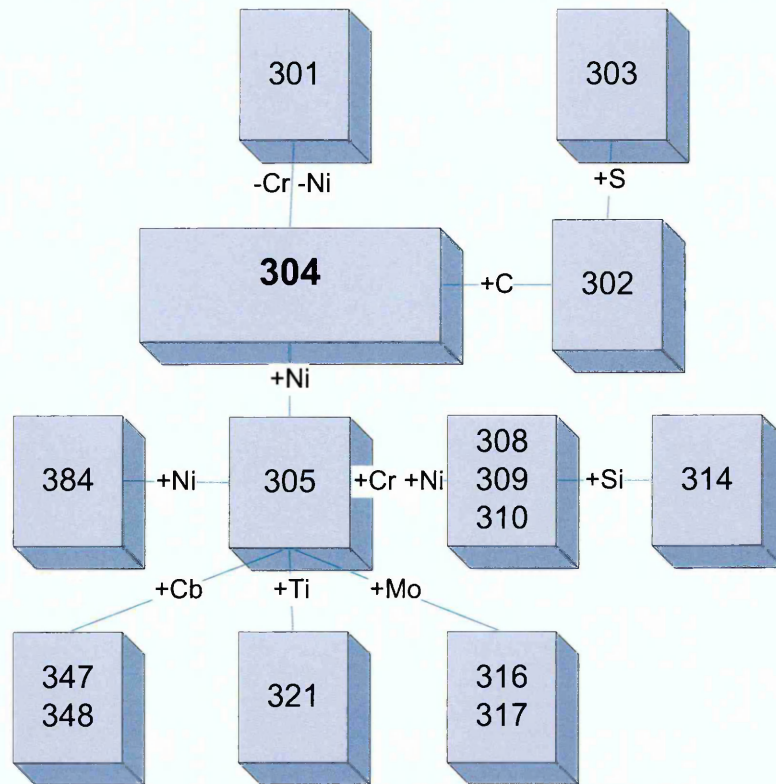


**Figure 2.1:** Standard austenitic stainless steels [27].

To a first approximation, the high temperature constitution of austenitic stainless steels is predicted from relevant isothermal sections of the ternary Fe-Cr-Ni equilibrium diagram, which uses the chromium and nickel equivalents which are calculated as follows [25].

Cr equivalent (wt %) = % Cr + 2.0% Si + 1.5% Mo + 5% Va + 5.5% Al + 1.75% Nb + 1.75% Ti + 0.75% W.

Ni equivalent (wt %) = % Ni + % Co + 0.5% Mn + 30% C + 0.3% Cu + 25% N.

The relative tendency of the elements to promote or inhibit the formation of ferrite has been quantified by numerous equations involving chromium and nickel equivalents. The actual amount of ferrite present in steel composed mainly for austenite depends not only on the overall chemical composition, but also on the solidification and cooling rates and any thermo-mechanical treatments.

Austenitic stainless steels are commonly used in different processes of the chemical industry. Their high ductility and good resistance to general corrosion make these kinds of steels one of the most used around the world. However, the most conventional austenitic stainless steel (ANSI 304) is susceptible to stress corrosion cracking failure in chloride containing environments as well as localised corrosion notably pitting and crevice corrosion in the same media even at room temperature.

It has been proposed [28] that commercial austenitic stainless steels are not safe in marine applications because of the presence of chloride ions and microbiological activity, which can lead to a bio-film formation in the surface. The bio-film activity promotes changes in the rest potential towards more noble values so pitting corrosion can occur more easily. On the other hand, when the passive film is mechanically, chemically or electrochemically ruptured in seawater localised corrosion starts and in some cases this results in the failure of the component. For marine applications, the use of higher nickel, chromium and molybdenum austenitic stainless steels, or even ferritic stainless steels is suggested. The problem is that alloying austenitic stainless steels makes them more expensive, while ferritic stainless steels are not sufficiently ductile and are difficult to weld.

For most of austenitic grades the minimum yield strength is 205 MPa. Exceptions are 304L and 316L with 170MPa minimum yield strength because of their lower carbon content. Grades have a small nitrogen addition which raises the yield strength to 250 MPa, and the high nitrogen grades have substantially higher strength. Minimum tensile strength values generally follow the yield strength values.

The physical properties of the austenitic stainless steels are different than those of iron and steel in that the elastic modulus are slightly lower and the thermal conductivity is substantially lower, while the coefficient thermal expansion and electrical resistivity are significantly higher. The austenitic stainless steels are also nonmagnetic in the annealed condition if they contain no delta ferrite. Small amounts of delta ferrite that result from welding, or martensite produced by cold work, will produce a small amount of ferromagnetism.

## 2.1.3 Duplex Stainless Steels

The duplex stainless steel alloys, contain a dual-phase structure where austenite and ferrite phases are present. The percentage of each of these phases is normally 50%. The duplex alloys result from the development of stainless steels. Different grades of stainless steels were developed before the duplex stainless steels, the most common being the austenitic phase alloys. The earliest published data which refers to the ferritic-austenitic duplex stainless steel was in 1927 by Bain and Griffith [29].

The modern grades of duplex stainless steel with 22% Cr were developed in the beginning of 1970s. Examples of these grades included 2205, which was claimed to be resistant to intergranular corrosion following welding because of a balanced chemistry, including the addition of nitrogen [30]. However, highly ferritic heat affected zones (HAZs) were created

because of an increase of the compositional range limits, which resulted in a reduction in corrosion resistance [31].

For enhanced weldability, compositional limits are required by producers and manufacturers. For example, the allowed percentage of nitrogen is kept at the highest limit for DS2205. This progress in the production and welding metallurgy establishing a new generation of duplex stainless steels. The new generation of duplex stainless steels appeared in the beginning of 1980s, being developed from cast alloys. They are reknowed for their enhanced properties, including high strength and excellent resistance to corrosion. Many grades have been developed from this time and the demand of duplex has increased significantly. Considering their features duplex stainless steels are rather new alloys, thus some important properties of these alloys are not totally covered. Specifically corrosion problems and manufacturing difficulties are not commonly included [32].

The melt for a duplex stainless steel alloy can be produced using high alloyed scrap in an electric arc furnace followed by argon-oxygen decarburisation, vacuum oxygen decarburisation or vacuum arc remelting [33]. This method produces a high quality metallurgy with low sulphur content. Reducing sulphur and phosphorus, increases the ultimate corrosion resistance [34]. Table 2.1.1 presents the chemical compositions of some of duplex stainless steels grades. Deoxidation and inoculation using a mixture of mediators such as; SiCaMn, SiCaCe, Al, Ti, Mg, Nb, Zr, leads to the precipitation of minute oxides which act as multiple nucleation sites for ferrite crystals and thus provide grain refinement.

**Table 2.1.1** Chemical compositions of some austenitic and duplex stainless steels [35].

| Avesta Polarit | EN | International No ASTM | Typical Composition, % C | N | Cr | Ni | Mo |
|---|---|---|---|---|---|---|---|
| 4301 | 1.4301 | 304 | 0.04 | 0.05 | 18.1 | 8.3 | - |
| 4404 | 1.4404 | 316L | 0.02 | 0.04 | 17.2 | 10.2 | 2.1 |
| 4436 | 1.4436 | 316 | 0.02 | 0.05 | 16.9 | 10.7 | 2.6 |
| 940L | 1.4539 | N08904 | 0.01 | 0.06 | 20 | 25 | 4.5 |
| 254 SMO | 1.4547 | S31254 | 0.01 | 0.2 | 20 | 18 | 6.1 |
| 3RE60 | 1.4417 | S31500 | 0.02 | - | 18.5 | 5 | 2.7 |
| 4460 | 1.4460 | 329 | 0.02 | 0.09 | 25.2 | 5.6 | 1.4 |
| SAF 2304 | 1.4362 | S32304 | 0.02 | 0.10 | 23 | 4.8 | 0.3 |
| 2205 | 1.4462 | S32205 | 0.02 | 0.17 | 22 | 5.7 | 3.1 |
| SAF 2507 | 1.4410 | S32750 | 0.02 | 0.27 | 25 | 7 | 4 |

The exact combinations of carbon and oxygen content play a key role in the final mechanical properties and corrosion resistance [36]. The rate of cooling also has an influence on the grain size. There are also other elemental additions that influence the structure and properties of the alloys such as: chromium, molybdenum, nickel, nitrogen, manganese, copper, tungsten, silicon and carbon. Only chromium, nickel, and nitrogen are mentioned in this section because of their important role.

The most important effect of adding chromium to a duplex alloy is the enhancement of localised corrosion resistance. This occurs when a passive chromium oxyhydroxide film is formed [37]. This is gained electrochemically if the passive limit is extended [38] and decreasing the rate of general corrosion. There is a limit to the amount of chromium, which can be added to the alloy, because increasing chromium content can result in the precipitation of inclusions [39]. These inclusions often have a negative effect on mechanical and corrosion properties. Polak [40], in an experimental study on 2205 duplex stainless steels, states that a non-metallic inclusions are the initiation sites of fatigue cracks, due to local stress and strain concentration.

Nickel also has some influence on the corrosion resistance, for example it increases the pitting potential in the noble direction and reduces general corrosion. However, the main role of nickel is to control the phase balance and elemental partitioning in the alloy [41].

The influence of nitrogen on stainless steels is that of increasing the pitting resistance, austenite content and strength. It has a similar influence on pitting as Cr, notably increasing the pitting potential in the noble direction and thus increasing the passive potential range [42]. During prolonged passivation of stainless steel in acid solutions, surface nitrogen enrichment has been observed, [43] thus indicating how nitrogen can affect repassivation. However, in order to breakdown the passive film the anodic current density must be high, of the order of several A/cm$^2$ [44].

Nitrogen has also been observed to increase the crevice corrosion resistance. It has been suggested that, this is due to nitrogen changing the crevice solution chemistry or by segregation to the surface [45], which is in keeping with the mechanism for improved pitting resistance [44]. A further advantage of the addition of nitrogen is the prevention of precipitation of inclusions by decreasing chromium partitioning [46, 47].

The duplex stainless steels are distinguished by a dual phase structure, which includes a combination of approximately equal volume percentage of austenite ($\gamma$) islands in ferrite ($\alpha$) grains [40]. Both cast and rolled products have roughly equivalent volume portion of ferrite and austenite, which in the case of rolled components, contains a rolling structure obtained by hot working, followed by a solution treatment and rapid cooling. An optical micrograph of 2205 duplex stainless steel is shown in Figure 2.2, the light phase is austenite and the dark phase is ferrite with approximately equal volume ratio [40]. The finest phase structure for modern rolled products differs between producers, but overall a range of between 45% and 60% austenite may

be expected. The structure is obtained by instantaneous control of the chemical composition and thermal treatment [39].
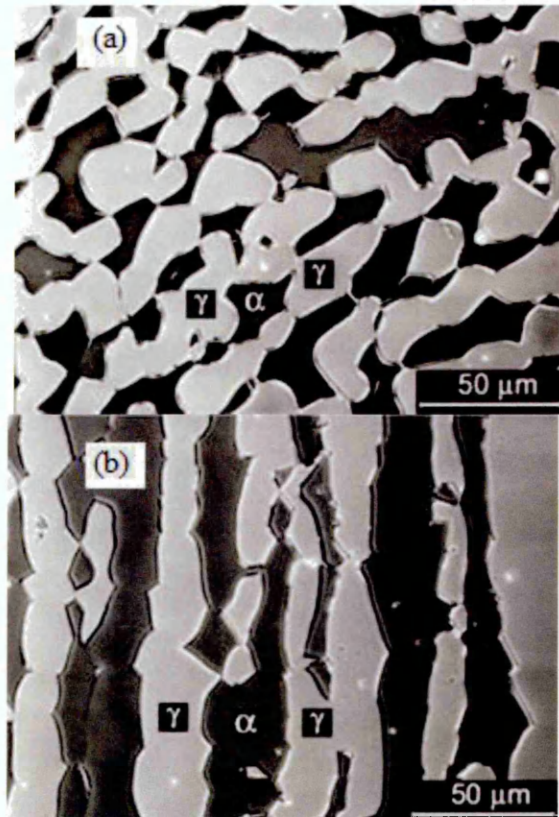


**Figure 2.2** Optical micrograph of 2205 duplex stainless steel; transverse (a), longitudinal (b) sections [40].

Duplex stainless steels have a low coefficients of thermal expansion, similar to carbon steels, thus reducing the requirement for expansion joints and rendering duplex alloys suitable for thermal cycling conditions [48]. Furthermore, the thermal conductivity is higher than for austenitic grades and this, combined with higher mechanical strength, allows for thinner walled components in many applications, such as pressure vessels and tubing [49], Table 2.1.2 presents the physical properties of duplex stainless steels. Finally, as duplex stainless steels contain about 50% ferrite, they show a degree of magnetism [50].

18

**Table 2.1.2** The physical properties of Duplex stainless steel [49].

| Density | kg/dm$^3$ | 7,8 |
|---|---|---|
| Modulus of elasticity | GPa | 200 |
| Thermal conductivity | W/m°C | 15 |
| Electric resistivity | μΩm | 0.80 |

Duplex stainless steels have higher ultimate tensile strength values than most ferritic and austenitic grades. Similar to all other metals and alloys, the mechanical properties depend on aspects such as grain size, texture and degree of segregation [51]. The mechanical properties of 2205 duplex stainless steel are presented in Table 2.1.3 The major characteristics of the duplex stainless steels is their high proof strength at room temperature, twice that of comparable austenitic grades. The ultimate tensile strength is also high, while the elongation is greater than 25%. This combination of these properties allow for duplex steels to be used in thinner sections than austenitic grades [52], which can lead to considerable savings in weight and capital investment.

**Table 2.1.3** The minimum mechanical properties values of 2205 DSS at 20°C [49]

| Proof strength Rp(0.2) MPa | Ultimate tensile strength MPa | Elongation A5 % |
|---|---|---|
| 460 | 660 | 25 |

The results of fatigue tests in air on smooth specimens [53] indicate a fatigue limit for all types of stainless steel about 50% of the ultimate tensile strength. However for materials with ultimate tensile strengths greater than 1000MPa, the fatigue limit is found to be less than 50%. Similar results obtained in sea water type environments appear to show marked scatter [54].

Some duplex steels have corrosion fatigue limits close to the average fatigue limit in air whereas others hardly attain values equivalent to 40% of average fatigue limit in air being equivalent to 20%

of ultimate tensile strength [20]. The drop in fatigue strength in a corrosive environment is clearly linked to the intrinsic resistance of the materials to the corrosion mechanisms encountered in the test medium employed [55]. Thus, for sea water, the ratio between the fatigue limit in the corrosive medium and the fatigue limit in air can be correlated with the pitting resistance. Fatigue limits in sea water to air percentage versus Pitting Resistance Equivalent Number (PREN) are plotted in Figure 2.3. This shows that alloys with greater PREN have higher fatigue limits in sea water. Normally, the fatigue limit in the corrosive environment will be reduced when the passive film is damaged by pitting [56].
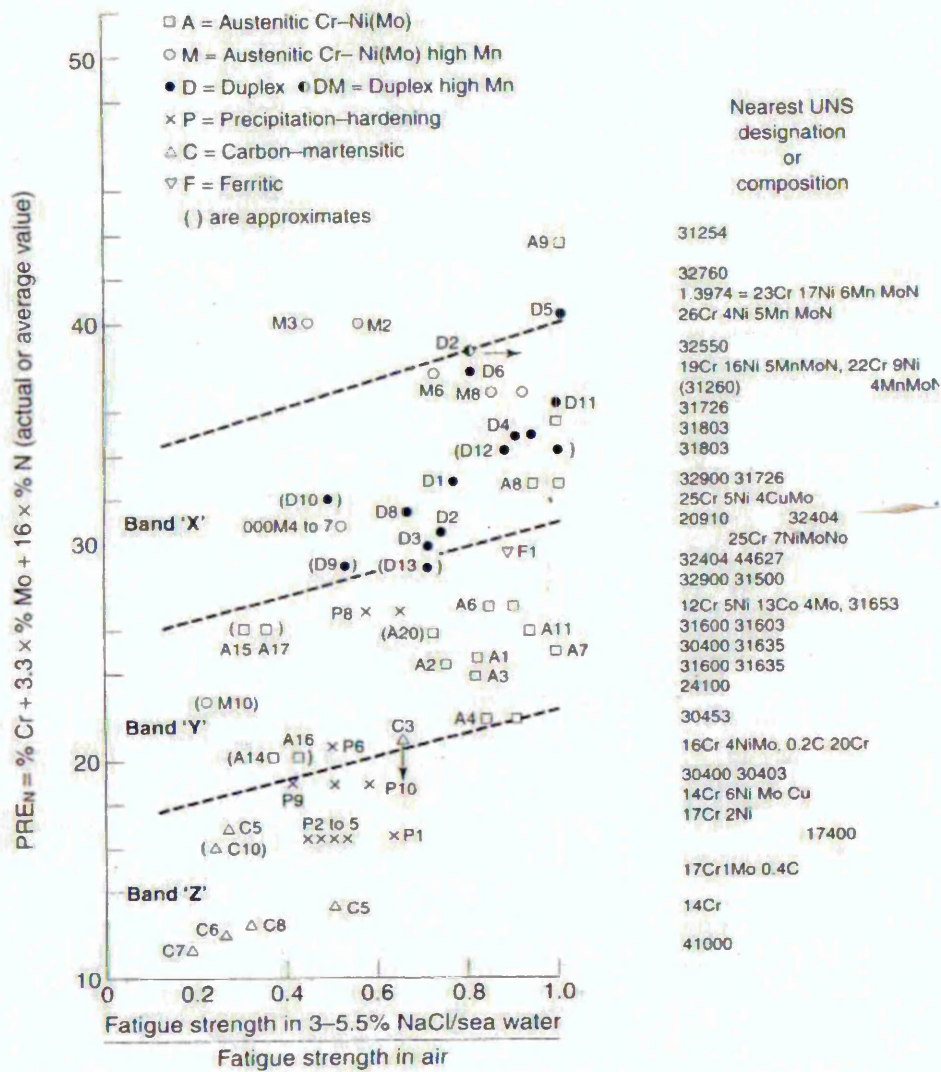


**Figure 2.3:** PREN versus the ratio of smooth fatigue strength in sea water-type solutions to that in air, for various stainless steels (ambient to 40°C). Values in parentheses have been estimated [53].

The effect of an applied potential on the fatigue corrosion properties is demonstrated in Figure 2.4 where the fatigue life is seem to reduce by increasing anodic polarisation, particularly at low stress ranges and high number of cycles.
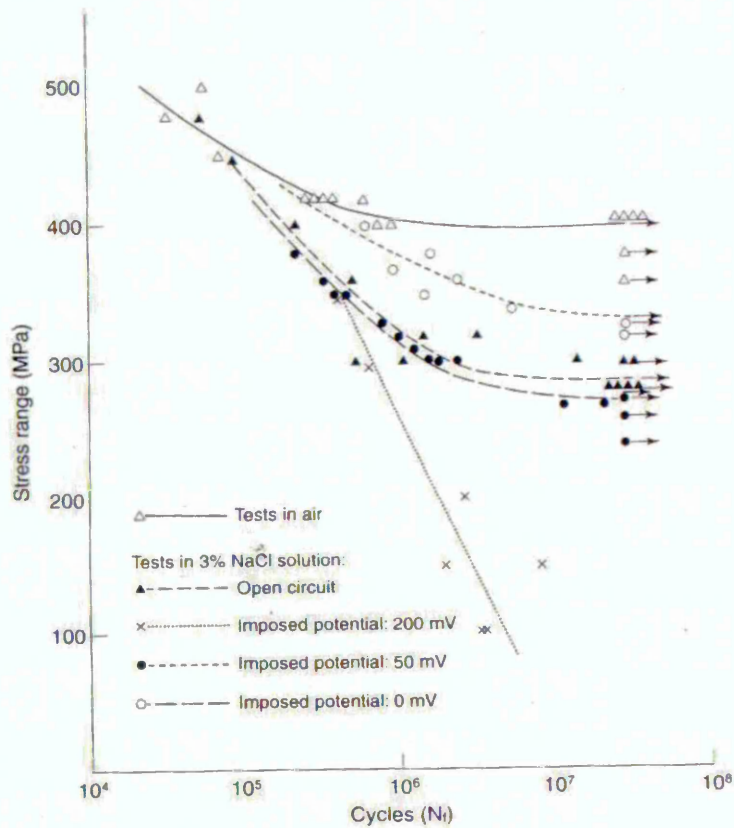


**Figure 2.4** Corrosion fatigue test results on alloy S32404 in 3% NaCl under applied potentials [56].

The *S-N* curves for 3RE60 and 2205 in a modified synthetic white water consisting of an acidic aluminium sulphate solution with 400 ppm chloride and 250 ppm sulphate and a pH of 3.5 at room temperature are shown in Figure 2.5 [57]. As shown in this figure, the corrosion fatigue strength of 2205 is about 15% higher than that of 3RE60. This difference has been

attributed to the higher strength of 2205 compared to 3RE60 [57]. However, the fact that 2205 also contains higher levels of chromium, molybdenum, and nitrogen (i.e., 22%Cr, 3.0%Mo, 0.13%N) than 3RE60 (i.e., 18.5%Cr, 2.7%Mo, 0.07N) also suggests that 2205 would be more readily repassivated at film rupture sites at persistent slip bands [24].
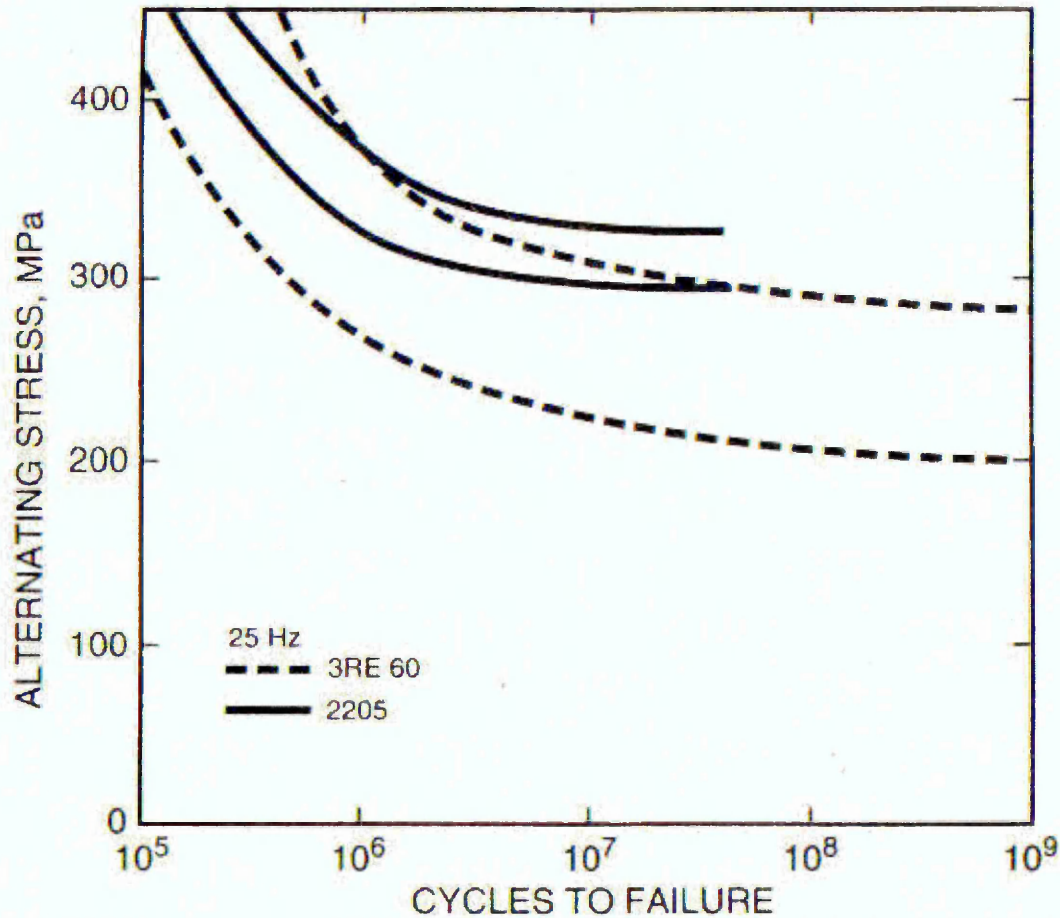


**Figure 2.5:** Corrosion fatigue behaviour of the duplex stainless steels 3RE60 and 2205 in synthetic white water. The upper and lower lines for each material represent the scatter in the data [58].

The corrosion fatigue crack growth rates show differing responses to the presence of aqueous environments, depending on the duplex stainless steel. The duplex stainless steel Uranus 50 shows some acceleration in the crack growth rate due to the presence of a 3% NaCl solution,

as shown in Figure 2.6 [56]. However, crack propagation rates at 10 Hz have been found to be the same in air and in acidic (pH = 3.5) chloride solutions for cast duplex stainless steels designated as alloy 63 (Fe-21.5Cr-10.0Ni-3.0Mo-0.08C-0.25N-0.5Ti;) [59].
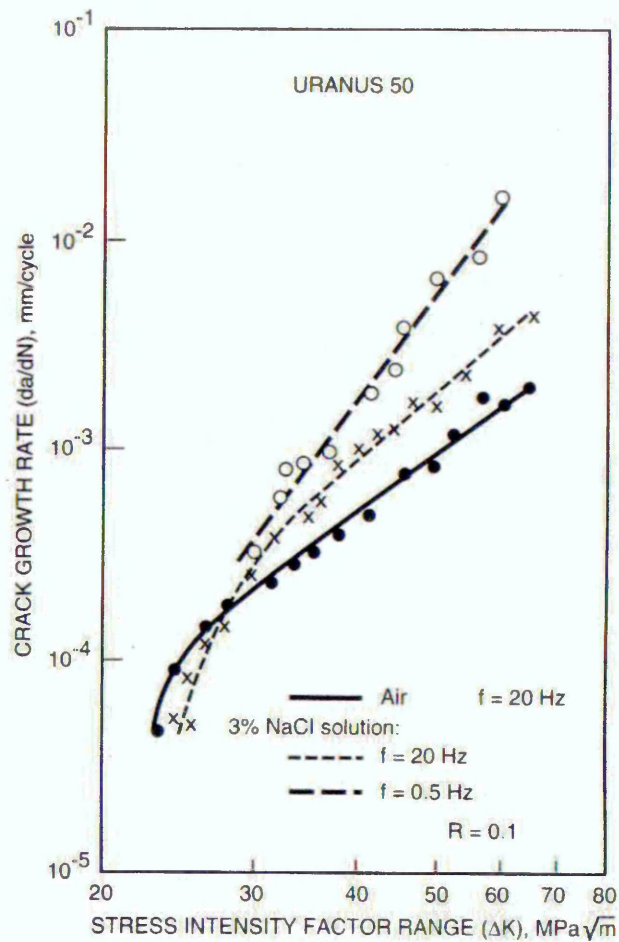


**Figure 2.6** Fatigue crack growth rates in air and in a 3% NaCl solution for stainless steel Uranus 50 [24].

Among the test and environmental variables that have been studied for stainless steels are the effect of notches, pH of the solution, deaeration of the solution, frequency of stressing, and applied potential. As shown in Table 2.1.4, for the duplex stainless steel 2205, the presence of notches and low pH is detrimental and the effect of deaeration is variable. The frequency of stressing has been found to have little effect on the corrosion fatigue crack growth rates at $2 \times 10^7$ cycles of 2205 [53]. However, for Uranus 50, decreasing the stressing frequency from 20 to

0.5Hz results in an increase in the crack growth rate in a 3% NaCl solution, as shown in Figure 2.6.

Table 2.1.4 Effect of pH on corrosion fatigue strength of stainless steels at 100 Hz in a 3% NaCl solution at 40°C [24].

| Alloy | Type of Specimen | Corrosion Fatigue Strength [MPa] | | | | | | |
|---|---|---|---|---|---|---|---|---|
| | | pH1 | | pH3 | | pH7 | | |
| | | Aerated | Deaerated | Aerated | Deaerated | Aerated | Deaerated | In Air |
| 304LN (1.4311) | Smooth | 138 | 47 | 200 | 165 | 290 | 269 | 320 |
| | Notched | 47 | 40 | 75 | 46 | 129 | 110 | 160 |
| 321 (1.4541) | Smooth | — | 127 | — | 219 | — | 317 | 320 |
| | Notched | — | 68 | — | 160 | — | 186 | 200 |
| 316LN (1.4429) | Smooth | 145 | 145 | 220 | 220 | 260 | 275 | 305 |
| | Notched | 83 | 83 | 122 | 130 | 139 | 150 | 220 |
| 316 + Ti (1.4571) | Smooth | — | 220 | — | 260 | — | 330 | 328 |
| | Notched | — | 131 | — | 229 | — | 240 | 210 |
| 317LMN (1.4439) | Smooth | 138 | 109 | 269 | 264 | 295 | 250 | 268 |
| | Notched | 64 | 70 | 87 | 87 | 195 | 195 | 189 |
| 2205 (1.4462) | Smooth | 210 | 190 | 365 | 330 | 420 | 425 | 458 |
| | Notched | 154 | 123 | 210 | 210 | 251 | 230 | 240 |

## 2.1.4 Applications

Due to their high strength and good corrosion resistance stainless steels alloys have been used in widespread applications in different fields such as; oil and gas, paper industry, chemical and petrochemical, power generation, and marine transportation.

The use of stainless steel alloys for offshore applications predominantly started in the early days of the North Sea developments [20]. The corrosive conditions which were encountered in this region negated the use of carbon steels and led to the selection of stainless steel. Stainless steel grades have been supplied for down-well and wellheads tools, process piping and vessel components, such as pump parts, compressors and valves.

Stainless steels have been used in the paper industry since the 1960s. Since 1974, it has been reported that more than 50 Kraft batch digesters have been built, with either solid or clad alloys, with no maintenance required over a six-year period [52]. Overall, stainless steel alloys find many applications in this industry section, including chemical pulping, bleaching, pulp storage tanks, paper machines, and steam plant [60].

Stainless steels have been used in the chemical and petrochemical industries. For example, for applications where higher chloride contents are present, brackish water, hot coastal conditions, both tubing and tube-sheets are made from stainless steel. They have also been used for reactors, heat exchangers and storage tanks in the production of detergent, comprising greasy amines and chlorides; in plastic production, e.g. polypropylene; steam sterilisation of bio-products and sodium cyanide production [61].

Due to the embrittlement of some stainless steel alloys during extended exposure to temperatures above $300^{\circ}C$, their applications are limited to temperatures below this. The main use of stainless steel in the power generation industry would appear to be where sea water cooling systems are employed or in the handling of geothermal fluids [62]. Applications for the standard stainless steel grades include centrifugal fans and absorbers [52]. Flue gas ducting expansion joints and heat exchangers in waste water treatment have also been made from stainless steels [63].

## 2.2 Fatigue

Fatigue in engineering materials is a topic which involves several scientific disciplines and which provides a rich variety of phenomena for fundamental and applied research. In this section of the literature survey a basic introduction of the fatigue process is given. The intention is to gain an understanding of both fatigue and corrosion before presenting the theories developed to explain the corrosion fatigue process. Figure 2.7 represents the parameters used in fatigue testing.

Metal fatigue has been studied for over 150 years, with the first study believed to have been conducted around 1829 by Albert who performed tests involving repeated loading on mine-hoist chains made of iron [64]. In a historical survey of the fatigue of metals Suresh [65] pointed out the work of Wöhler [66] who conducted systematic investigations of fatigue failure in Berlin from 1852 to 1869. Wöhler observed that the strength of steel railway axles subjected to cyclic loads was appreciably lower than their static strength. His work led to the characterisation of the fatigue behaviour in terms of stress amplitude-life (S-N) curves and to the concept of the fatigue endurance limit. The work of Gerber in 1874 is also mentioned as he began developing methods for fatigue design such as fatigue life calculations for different cyclic mean stresses levels [67].
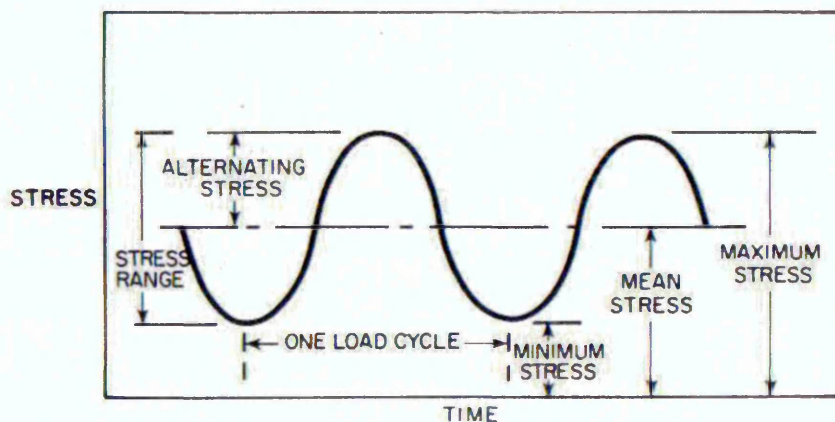


**Figure 2.7:** the parameters used in fatigue testing.

During the last 4 decades many aspects of fatigue damage in materials have been studied and reported, such as fatigue crack initiation, fatigue crack propagation, the fatigue limit, fatigue resistance, calculation of fatigue life and mathematical modelling of the fatigue process.
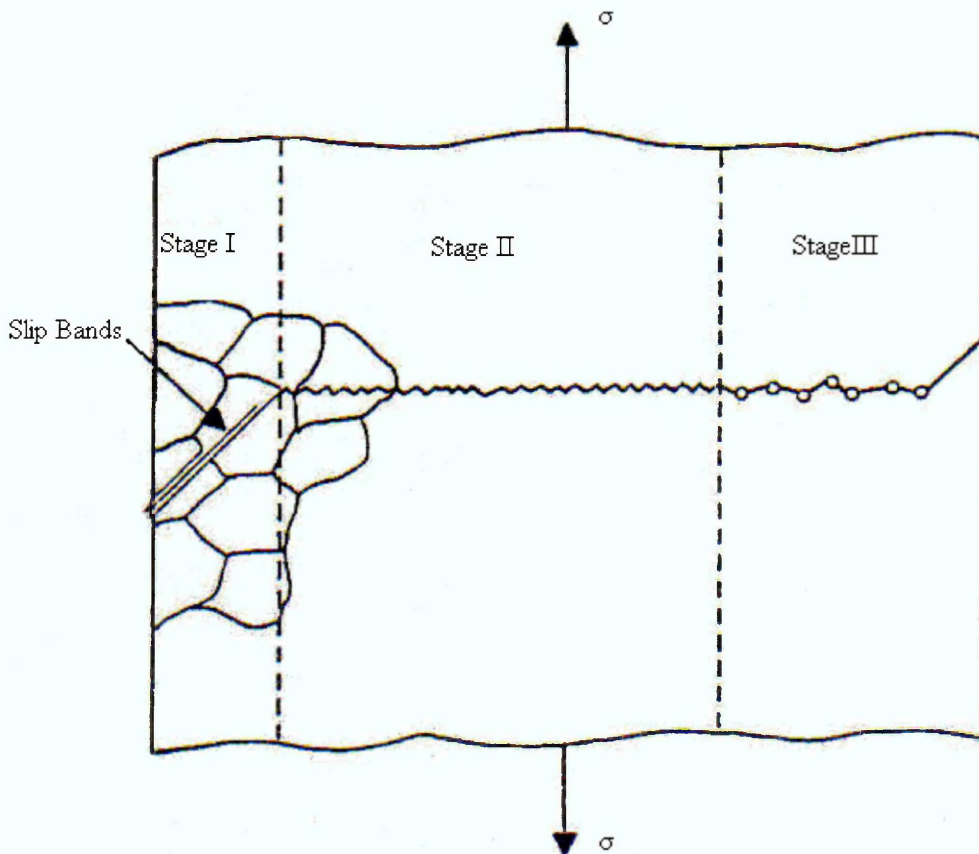


**Figure 2.8:** The different forms of crack behaviour as a function of the crack size.

In 1961 Forsyth [68] recognised and proposed the existence of two different forms of cracks, a stage I crack driven by shear stresses, and a stage II crack driven by tensile stresses, see Figure 2.8. The former occurs on a plane of maximum shear strain, the latter on a plane whose normal is the direction of the maximum tensile stress. Depending on the stress-state and its intensity, either stage I or stage II cracking will dominate the fatigue lifetime of specimens, component and structures.

As will be seen later in this section, before, during and after the transition zone from stage I to stage II the description of the fatigue crack growth will depend on the current crack length, the stress state and stress level. Once an initial crack is detected in a component or structure the next task is to determine and measure the crack growth rate for which the concepts of fracture mechanics are applied.

Figure 2.9 illustrates the three different forms of fracture mechanics applicable to the fatigue process. For long cracks propagating under low applied stresses, linear elastic fracture mechanics (LEFM) provides an adequate description of fatigue crack growth behaviour. But when the initial crack size is physically small, e.g. 500 microns or less, the stress level for propagation is necessarily high and the assumptions that were considered for LEFM analysis may be inappropriate. Consequently an elastic-plastic fracture mechanics (EPFM) description of the crack growth is necessary.

Finally, when considering extremely short cracks, the crack growth behaviour is influenced by the microstructure of the given material, therefore, requiring the implementation of microstructural fracture mechanics (MFM) to describe their growth [68].

Some models have been reported for the study of short cracks, for example Hobson [69] and Navarro-de los Rios [70]. The Brown-Hobson and the Navarro-de los Rios models to predict the short crack growth have been studied under corrosion fatigue conditions [71, 72].

It is well known that fatigue failure results in progressive localised and permanent structural change and may result in cracking and subsequent fracture of the structure or component after a sufficient number of loading cycles. Most of the work reported concerning fatigue research considers fatigue as a two-stage process. The first stage involves the development of a crack, i.e. crack initiation, and the second stage describes crack propagation.

Depending upon the level of the cyclic stress, a crack can be initiated at the surface of the component from pre-existing surface features such as grain boundaries, non-metallic inclusions or boundaries between two or more phases [19]. Alternatively cracks may be initiated at subsurface defects.
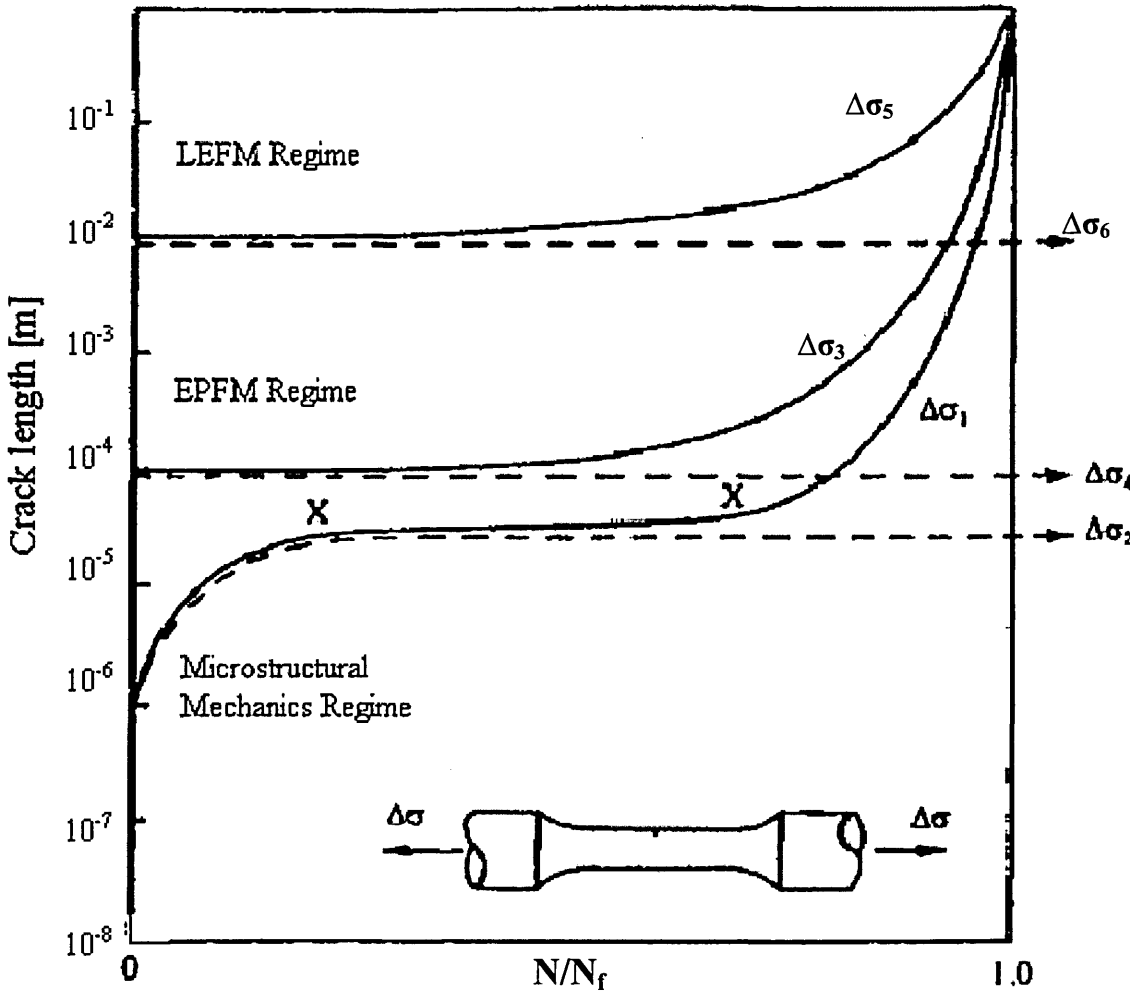


**Figure 2.9** The three basic forms of fatigue crack growth.

The presence of inclusions almost always has a deleterious effect on the fatigue and fracture resistance of materials subjected to loading in air as well as in corrosive environments. Inclusions introduce strain concentrations because of the mismatch of mechanical, physical and electrochemical properties with matrix material. The vast majority of cracks associated with fatigue start at a free surface, so, the nature of that free surface is an important factor [72]. It has been reported that the size and the shape of non-metallic inclusions have an important effect on fatigue crack initiation [73].

It is not necessary for the bulk of the grains in a piece of metal to deform plastically for it to fail by fatigue. Continued cyclic plastic deformation in one localised surface region is sufficient for fatigue failure to occur. Depending on the characteristics of the applied stress and the crack length, once initiated, cracks may either continue to propagating or arrest [74]. The arrest of cracks at sub-fatigue limit stresses occurs because the mechanical driving force associated with the crack is not large enough to overcome the arresting microstructural feature, for example, a grain boundary. Thus a fatigue limit can be defined as a limiting stress below which cracks once initiated are unable to propagate and produce failure, i.e. the crack growth rate being effectively zero [75].

Structures subjected to cyclic loading may fail as a consequence of the growth of a single crack or as a result of the coalescence of several cracks, which depends on the stress history-material strength relationship. It has been proposed that the fatigue fracture process can be divided in the following stages [76];

1- Cyclic plastic deformation prior to fatigue crack initiation,

2- Initiation of one or more micro-cracks,

3- Propagating or coalescence of micro-cracks to form one or more macro-cracks,

4- Propagation of one or more macro-cracks and

5- Final failure.

The tendency in recent evaluations has been to define a concept involving crack growth rates rather than to determine the total life to failure. It is assumed that cracks are present in the material before service or that cracks are initiated very early in the service history, these assumptions suggest that the crack growth controls fatigue behaviour [65]. Therefore, crack initiation and crack growth measurement is a very important part of material property studies.

## 2.2.1 Crack Initiation

The initiation stage of fatigue cracks is an event whose definition depends upon the size scale of observation. Materials scientists are expected to consider the nucleation of flaws or persistent slip bands as the initiation stage of fatigue failure; on the other hand designers and mechanical engineers normally associate the resolution of crack detection with the threshold for crack nucleation [74].

During cycling loading dislocations pile up and form structures called persistent slip bands. Figure 2.10 presents a schematic of a persistent slip bands in material surface. Persistent slip bands produce areas that rise above or fall below the surface of the component due to movement of material along slip planes. The former is called an extrusion and the later is called an intrusion. The extrusion and intrusion form tiny steps in the surface that produce stress concentration sites where fatigue cracks can initiate.
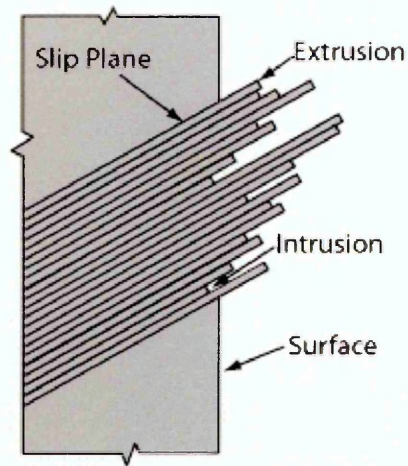
**Figure 2.10:** A schematic of crack initiation from persistent slip bands

In general it can be considered that crack initiation is strongly dependent on the ductility of the material, which is a function of the microstructure, and applied stress level. The fatigue limit can be considered as a limit of crack propagation. Miller [74] has described fatigue as a mechanism dominated by crack propagation. From this point of view it is suggested, that in polycrystalline metals it can be safely assumed that the crack initiation phase does not exist.

## 2.2.2 Short Fatigue Cracks

The data used to construct ($da/dN$)-$\Delta$K (crack growth rate – stress intensity factor) curves and hence predict crack growth rates rely on laboratory fatigue tests on specimens containing long cracks, typically of the order of tens of millimetres. Suresh [65] states "it has been shown that the growth rates of small flaws can be significantly greater than the corresponding rates of long flaws when characterised in terms of the nominal driving force" the short fatigue crack growth problem is seen as a breakdown of similitude. Similitude is fundamental to the use of fracture mechanics and states that cracked components of different dimensions exhibit the same crack growth rate when subjected to the same value of stress intensity factor. Short cracks have also been observed

32

to grow at values of stress intensity factor range below the threshold value predicted by laboratory testing of specimens contains long cracks.

Crack growth is almost exclusively described using fracture mechanics. When one considers a growing crack there are three basic modes of crack surface displacement, these are shown schematically in Figure 2.11 Under mode I loading the crack surfaces move directly apart, while mode II and III are shear (sliding) modes. For each mode of displacement there is a characteristic elastic stress field associated with the crack tip.



Mode I:
Opening

Mode II:
In-plane shear

Mode III:
Out-of-plane shear
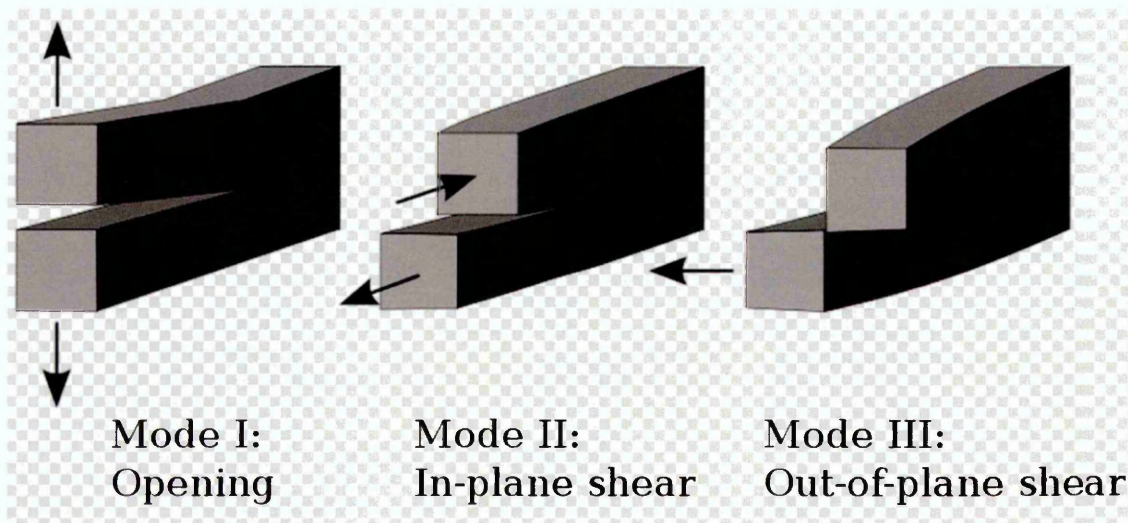
**Figure 2.11:** The three basic modes of fracture.

Stress intensity factor $\Delta K$ is used in fracture mechanics to predict the stress state "stress intensity" near the tip of a crack caused by a remote load or residual stresses. It is a theoretical construct applicable to a homogeneous elastic material and is useful for providing a failure criterion for brittle materials. The stress intensity factor range has been used to account for the role of pitting in defining threshold conditions for cracking using Linear Elastic Fracture Mechanics (LEFM) in the context of fatigue-limit based propagation.

Paris and Erdongan [77] suggested that as the stress intensity factor range describes the stress field around the crack tip the ($\Delta$K) should be proportional to the rate of fatigue crack propagation. This relationship is defined by the Paris law;

$$da/dN = C(\Delta K)^m \qquad (2.2.1)$$

da/dN = crack growth rate per cycle and C, m are material constants

Equation 2.2.1 assumes that the microstructure of a given material will be homogeneous. Where the rate of crack growth is appreciably affected by microstructural discontinuities such as grain boundaries the Paris law is no longer applicable. The stress field must also be predominately elastic. Figure 2.12 shows a plot of crack growth rate *(da/dN)* with respect to ($\Delta$K) where regimes A, B and C correspond to stage I, II and III in the previous section.
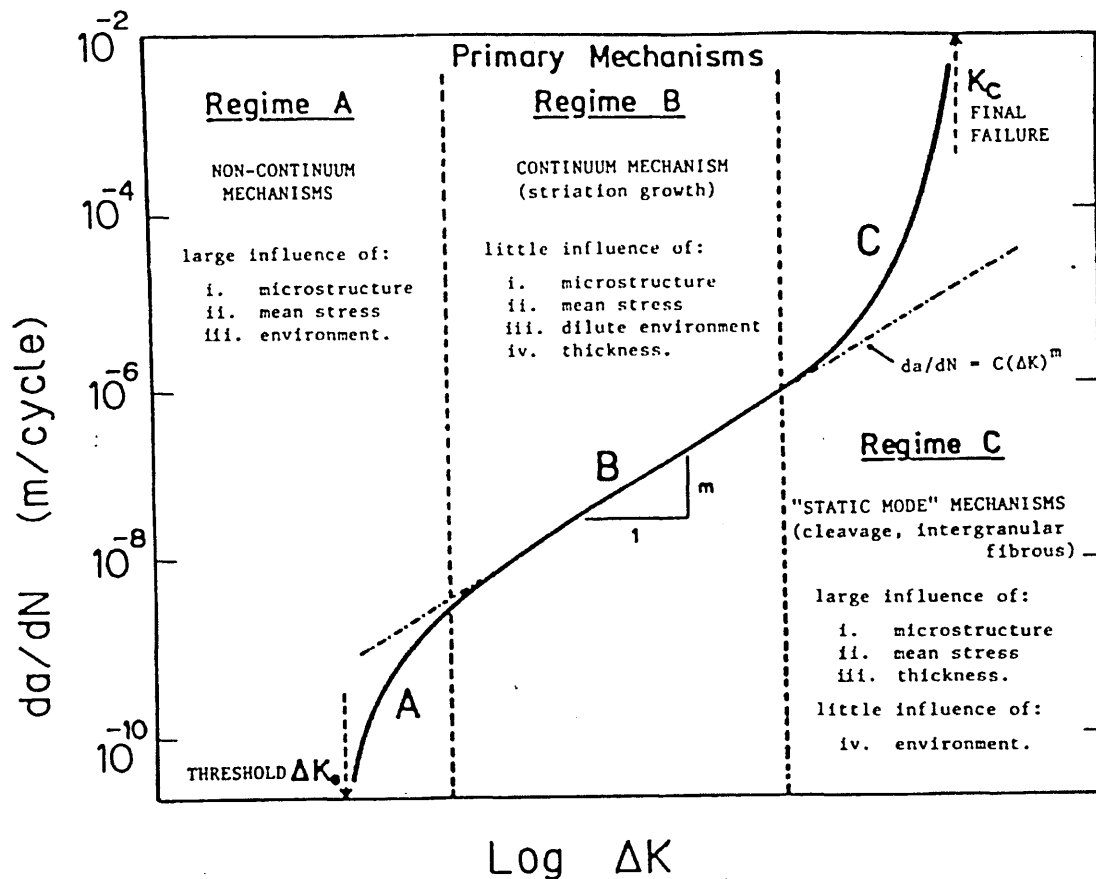
Figure 2.12: schematic illustration of the three regimes of crack growth.

## 2.2.3 Crack propagation

Crack propagation is the regime between crack initiation and complete fracture. In general this phase between initiation and fracture is broken into three convenient stages. Each with its own distinctive growth, Figure 2.12 illustrates each phase schematically:

- Stage I shear crack growth on crystallographic slip plane

- Stage II striation crack growth – crack growth on a plane normal to the applied stress

- Stage III unstable rapid crack growth; ductile tearing

Stage I fatigue crack growth is dominated by shear with micro-cracks growing along the plane of greatest shear. This is generally at $45^\circ$ to the applied nominal stress in uniaxially loaded polycrystalline material. Under low load high cycle fatigue this period of growth may account for up to 90% of the fatigue crack life. The behaviour of stage I and stage II cracks is extremely different. The transition from stage I to stage II crack growth is not immediate and generally takes place gradually over a few grains. Stage II crack growth is associated with the magnitude of the tensile strain range in the material just ahead of the crack tip. The crack grows perpendicular to the applied nominal stress as it is in this plane where the greatest amount of crack displacement is possible, leading to the greatest strain range in the material ahead of the crack tip. Stage II cracks are often referred to as macro-cracks or long cracks. It is within this relatively stable stage of crack growth that most engineering predictions are made.

Stage III crack growth is at a fast rate and characterised by static modes of fracture such as, cleavage or intergranular separation of the material until complete fracture. In most practical engineering design situations this period of crack growth is ignored due to the speed at which fracture may occur.

## 2.3 Corrosion

### 2.3.1 Introduction

In this section the basic aspects of corrosion and localised corrosion are presented. Pitting corrosion is presented in some detail due the implications that this type of localised attack has in the early stages of surface damage and subsequent fatigue.

Corrosion is the degradation of a metal by an electrochemical reaction within its environment. From this simple definition it should be appreciated that corrosion is a system property and not a material one. In order to understand a corrosion reaction one must know about the material and environment conditions.

Generally, it may be seen that there are two types of corrosion, generalised and localised corrosion. The type of corrosion is generally dependent upon the metal or alloy being considered. Localised or more specifically pitting corrosion will receive most attention as it is the most relevant when considering stainless steels. Under these conditions certain localised areas of the metal surface corrode at higher rates. These variable rates are attributed to the heterogeneity of the metal, the environment or the geometry of the structure.

Corrosion reactions taking place at the surface of a metal in contact with an aggressive environment affect its mechanical behaviour when subjected to cyclic or static stress. For example it has been reported that carbon steel does not present a fatigue limit when it is tested in a corrosive environment [78, 79]. Stainless steels which are susceptible to pitting corrosion in chloride containing environment, present failure by fatigue induced in the early stages of damage by corrosion pits as shown by Boukerrou et al. [80]. The same behaviour has been reported by Wu [81], in high strength steel and by Akid [78], in medium carbon steel in contact with chloride solutions.

## 2.3.2 Cost of Corrosion:

The degradation by corrosion of structural and functional components is a huge cost to modern industrialized economies. The cost is not simply the replacement value of a corroded component but also the indirect costs including any product and production loss, maintenance ...etc. The original [82] cost of corrosion survey, estimated that the cost to the UK economy is between 3-4% of Gross National Product (GNP) per year. Although more limited in scope this concluded that the cost is still of the order to 2-3% of GNP per year. On a more personal note, the corrosion costs around £600 per capita per year; it is equivalent to around 1-2p/£ for each tax-payer.

Similar surveys undertaken in the USA and Japan also arrived at a similar annual cost, with the total annual estimated direct cost of corrosion in the USA amounting to a staggering $276 billion; approximately 3.1% of the GNP. This suggests that, although corrosion management has improved over several decades, industry must find more and better ways to encourage, support, and implement optimal corrosion control practices [83].

## 2.3.3 Electrochemical corrosion measurements

Electrochemical corrosion measurements utilise the electrochemical nature of metallic corrosion. The relationship between voltage and its corresponding current is used to determine metallic corrosion behaviour, and estimate corrosion resistance.

Metallic corrosion occurs when metal atoms are oxidized and subsequently leave the metal lattice as ions. The oxidation of metal atoms to ions is referred to as an electrochemical reaction because it is a chemical reaction that involves generation and transfer of electrons to

electrochemically active species dissolved in the electrolyte. The transfer of electrons enables electronic measurement and study of metallic corrosion.

The oxidation reaction of the metal is referred to as the anodic reaction and areas on a metal surface where oxidation occurs are referred to as anodes. The reduction of electrolyte electrochemically active species is referred to as the cathodic reaction and areas where reduction occurs are referred to as cathodes. Both anodic and cathodic reactions must be present to initiate and sustain metallic corrosion.

The general equation of anodic reaction is written as follows:

$$M \rightarrow M^{+n} + n\mathrm{e} \qquad (2.3.1)$$

Where M is the metal element, which for stainless steels corroded in sodium chloride solution, M can be iron (Fe) or chromium (Cr), ($n$) is the number of electrons resulted from this reaction which is equivalent to the valance number of the metal ion resulted. Equation (2.3.1) is referred to as an anodic reaction because free electrons are produced.

The electrons produced from the anodic reaction reacts with electrochemically active species such as hydrogen ions. This reaction is termed a cathodic reaction, an example of this reaction being the reduction of hydrogen ions:

$$2H^{+} + 2\mathrm{e} \rightarrow H_2 \qquad (2.3.2a)$$

Another example of a cathodic reaction is oxygen reduction

$$O_2 + 2H_2O + 4\mathrm{e} \rightarrow 4\,OH^{-} \qquad (2.3.2b)$$
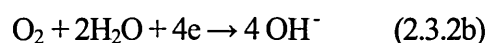
Therefore, iron and chromium atoms are oxidized to produce their ions and release electrons that cause reduction of hydrogen or oxygen ions from the electrolyte at the metal surface, forming hydrogen molecules or producing hydroxide ions.

Ohms law states that an electrical voltage is equal to the product of resistance and electrical current:

$$E = IR \qquad (2.3.3)$$

Hence it is reasonable to assume that applying a potential ($E$) to an electrode will produce an electrical current ($I$). Electrical corrosion current can be converted into a rate of material removed by corrosion using Faraday's Law.

$$\frac{W}{A} = \frac{ItM}{nF} \qquad (2.3.4)$$

Where;

W      weight removed [mg],

A      area of corroded surface [$cm^2$],

I      corrosion current [Amps],

t      time [sec],

M      molecular weight [mg/mol],

n      valance number and

F      Faraday's constant (96485.3383) [coulombs/mole].

Corrosion current can be measured using a potentiostat with a three electrode system which comprises a test and reference electrode with the aid of a counter electrode which is made predominantly from an inert material such as platinum. Figure 2.13 depicts a test potentiostat system schematic for measuring potential differences and current. This system consists of a test electrode which is typically a metal sample (working electrode) and the reference electrode often a saturated calomel electrode. The principal is that the potentiostat allows changes in the potential of the metal sample in a controlled manner and the current density is measured as a function of potential. A comparison can be made by a known standard potential produced from the reference electrode.
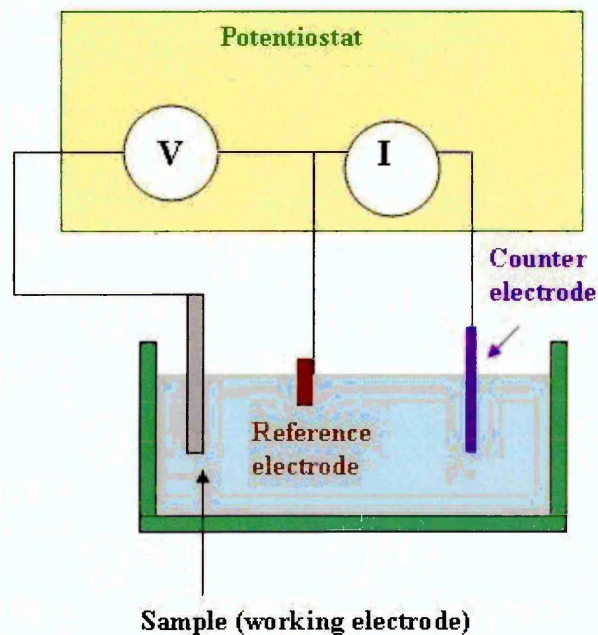


**Figure 2.13:** Schematic of 3-electrode test cell arrangement

The results can be used to produce a plot of current as a function of voltage, such as that shown in Figure 2.14. The shape of this curve is similar to curves obtained from direct current DC polarisation methods such as Tafel plots. The corrosion current can be estimated by extrapolating linear portions of the anodic and cathodic branches in Figure 2.14 to the Open Circuit Potential

(OCP), as shown by the continuous lines. An electrode becomes an anode or cathode when the over-potential is equal or more positive or negative than the natural OCP value respectively.
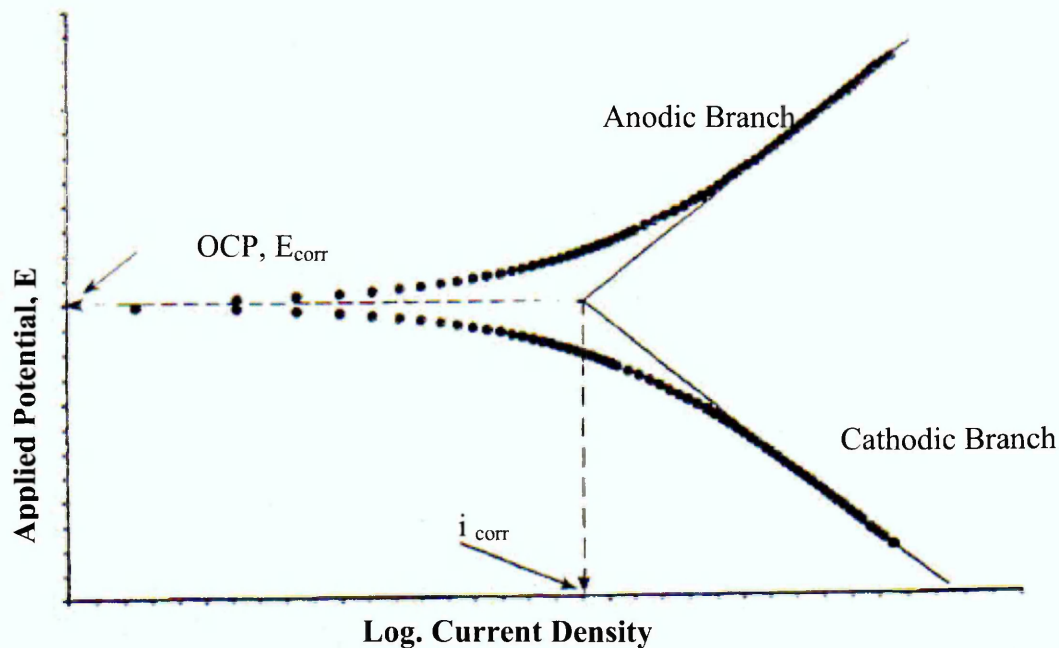


**Figure 2.14:** A schematic of polarisation curve ($i$-E).

Figure 2.14 shows, schematically, anodic and cathodic branches. The anodic reaction is the top branch and the cathodic reaction is the bottom branch. The OCP for the corrosion reaction occurs at the curve inflection point, which is also the potential where no net current flows to or from the electrode. Making an electrode entirely anodic or cathodic produces external current which can be measured. Being able to independently study half reactions is important for electrochemical corrosion measurement.

Therefore, when E is increased above the OCP value, anodic behaviour is expected. Increasing the applied potential leads to increase in the anodic current (active) as shown in Figure 2.15. The point at which active dissolution decreases is represented by the active-passive transition which corresponds to the primary passivation potential ($E_{pp}$). Exceeding this potential the measured current then starts to decrease to a low value which is expressed as passive current ($i_{pass}$). The

current remains close to this value with increasing applied potential. The extent of this range depends on the type of stainless steels and the environment (chloride concentration). For example the polarisation curves obtained in this study later are different from the curve shown in Figure 2.15 in the active passive transition behaviour.

The passive potential range is then terminated by a distinct point where the measured current starts to increase with increasing the potential. The potential at this point is called pitting potential ($E_p$) because pits begin to initiate and grow. So, the passive range can be defined as the potential between $E_{pp}$ and $E_p$. Defining the passive range for a material led to development of anodic protection technique for corrosion resistance.
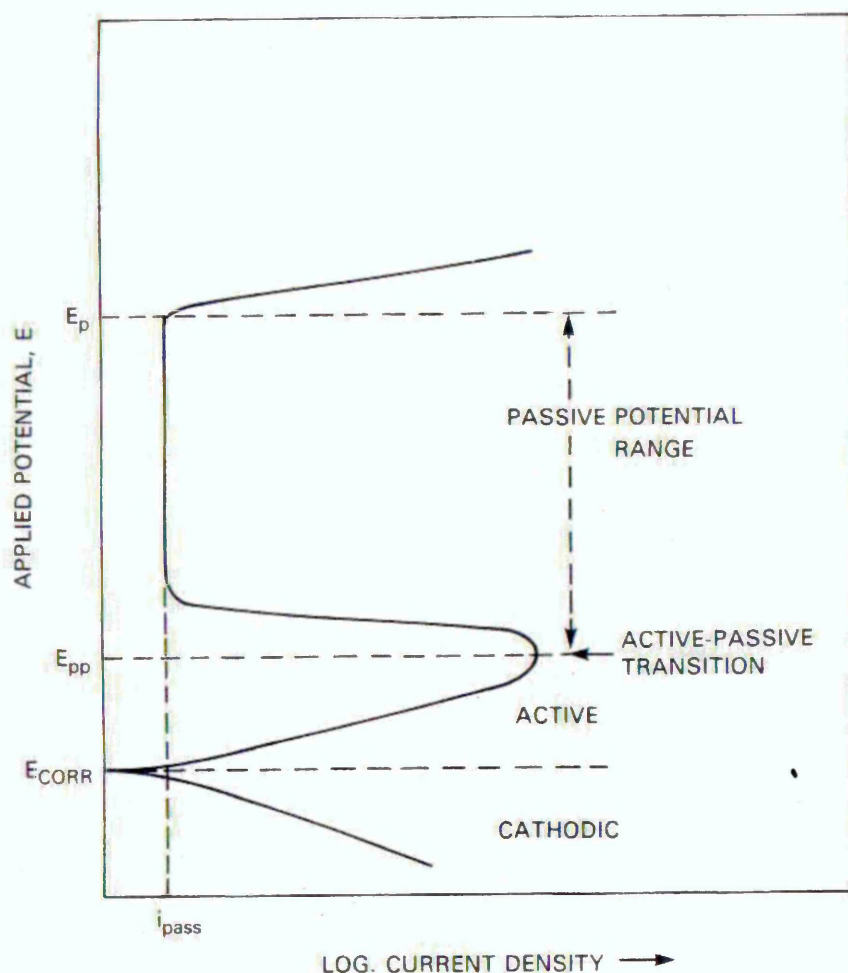


**Figure 2.15:** A schematic of polarisation curve for a stainless steel in a chloride solution.

## 2.3.4 Film Establishment and Breakdown

Many metals and alloys become covered with an oxide film on exposure to aqueous environments. Copper or tin and their alloys develop thick films, while metals which exhibit passive behaviour like stainless steels have a very thin film of the order of 9 to 20 nm. These films are cathodic to the metal matrix [84]. There is evidence of the structure of passive films in stainless steels that suggests a two-layer structure [85]. The inner layer is mainly composed of chromium oxide mixed with other chromium phases such as CrOOH which has a p-type semi-conductive behaviour. The outer layer is composed of iron hydroxide FeOOH and $\gamma$-$Fe_2O_3$ and has an n-type semi-conductive behaviour. Figure 2.16 shows a representation of this model of a passive film.

FeOOH + $\gamma$-$Fe_2O_3$ (n-semi-conductive)

6-15nm [Passive Film]

Cr(OH)3 or CrOOH (p-semi-conductive)

Metal Structure
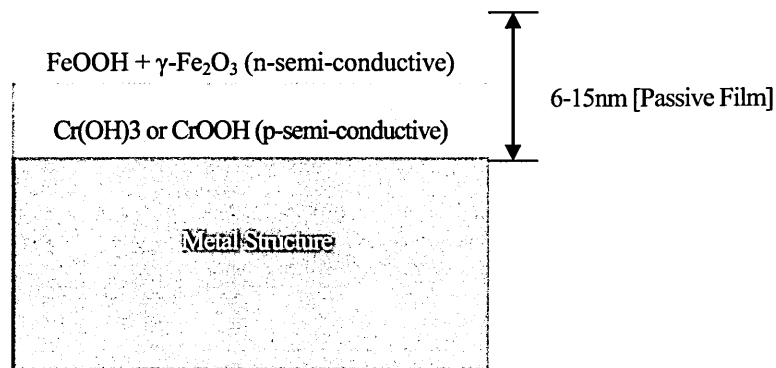
**Figure 2.16:** A two layer stainless steel passive film model. [85]

The same authors [85] suggested that the passive film formed on stainless steels has a structural amorphous nature due to the excellent bond flexibility of the chromium. Increasing the chromium content in the alloy enhances the amorphous degree of the structure. They also indicated that molybdenum alloyed with stainless steels enhances the passive film to be chemically more homogeneous and structurally amorphous. The porous film grows linearly with the amount of ions released in the solution and with the elapsed time, however the thickness was decreased rapidly after particular time [8].

There is also an indication that the increase of chromium in the alloy decreases the thickness of the passive film and is also responsible for its amorphous character [86].

The thickness of passive film of 316LN SS formed in 0.5 M NaCl at open circuit potential (OCP) increases as the immersion time increases. It was found for polarisation experiments that the thickness of the passive film increased when the potential was increased from the OCP to potentials 500 and 800 mV more positive [87]. Surface film breakdown is dependent on the nature of the film, the characteristics of the electrolyte, the electrochemical activity developed at the interface of the metal-electrolyte and the application of stresses.
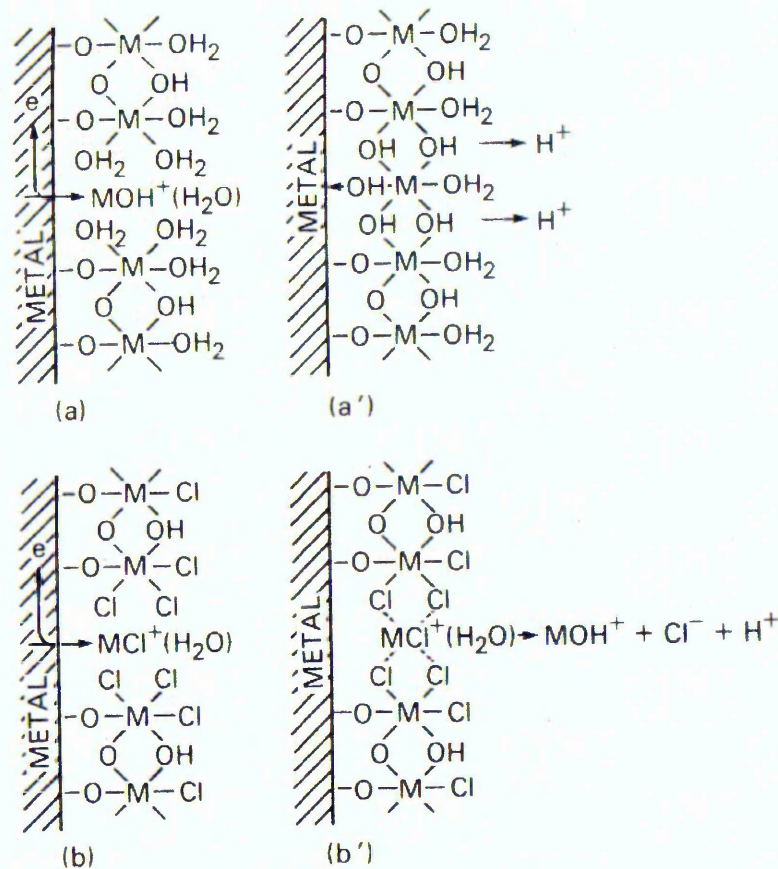


**Figure 2.17:** Metal ions dissolved through an undeveloped part of the film (a) are captured to form a film (a´) resulting from bridging with OH groups. Cl$^+$ replacing H$_2$O (b) prevent the bridging reaction (b´), resulting in breakdown of the film [88].

When the metal is subjected to cyclic loading the film is damaged mechanically due to the creation of slip steps from beneath. The breakdown of the film causes dissolution of the non-covered active metal in contact with the electrolyte, which acts as a small anode against the large cathodic film. A larger cathodic area will draw more electrons from the anode, resulting in more metal loss at the anode. The larger a cathodic area in relation to an anodic area, the larger will be the potential for corrosion and vice versa. To illustrate, if there is a very small anodic area, and a huge cathodic area, all the metal loss will occur in the small anodic area to satisfy the electron demand by the cathode, resulting in a localised or pitting corrosion. Conversely, if there is a large anodic area and a small cathodic area, given the same environment and conditions, corrosion rate will decrease, usually resulting in a general and uniform corrosion. The current density on the relatively large cathode is low, cathodic polarization is slight, and the voltage maintain a value close to the open circuit potential. At the same time, the current density on the small anode will be high and the consequent corrosion quite severe, giving rise to a particularly vicious form of corrosion called localised corrosion. This mechanism does not apply for all metal-electrolyte system undergoing corrosion fatigue, as is the case for acid solutions where oxide films can be soluble.

A model is proposed to explain the stability and rupture of the passive film of stainless steels [88]. In this model the passive film is assumed as a hydrated oxide film (Figure 2.17a). For a stable film it is suggested that the metal ions, which are produced from the anodic reaction on the uncovered part of the metal surface, form $MOH^+$. Then $H_2O$ molecules attract the produced $MOH^+$ ions to make a connection to the film and hydrogen ions are released (Figure 2.17a'). However, the presence of chloride ions in the solution replaces $H_2O$ molecules in the undeveloped part of the film (Figure 2.17b). This

45

replacement results in the formation of soluble metal chloride complexes and their removal from the film (Figure 2.17b'). This reaction explains the breakdown of passivity and the initiation of pitting.

## 2.3.5 Pitting Corrosion

Pitting corrosion is a highly localised form of corrosion that occurs at specific areas on a material surface. Pitting can be particularly damaging due the concentration of attack at a few sites. The reason stainless steels are so susceptible to pitting corrosion is that they depend upon the presence of a passive film for their good corrosion resistance [89]. Stainless steels are protected from corrosion by the passive film that is formed as the chromium content reaches approximately 11%. However, even some high chromium content stainless steels suffer from pitting corrosion in aqueous environments containing chloride ions.

Generally pitting corrosion is divided into two stages, pit initiation and pit propagation. If the passive film breaks down locally and does not re-form, pitting may develop. During pit initiation the passive film breaks down and active dissolution of the freshly exposed metal occurs. The location where a pits can initiate is influenced by many factors, for example variations in structure or composition of the metal surface, difference in the concentration of dissolved oxygen or the local breakdown of a passive film due to an applied stress being concentrated by some geometry. In his research Isaacs found that pits often tend to be located randomly around the metal surface [90]. Some research has been carried out to study the structural parameters involved in localised corrosion processes. From these, it has been demonstrated that defects in the metal structure, such as non metallic inclusions may act as sites for pit initiation on passive metal surfaces [91].

In these early stages pits grow in a metastable manner [92]. Metastable pit growth may be terminated at any time, in which case the pit surface repassivates and growth ceases [89]. The greater the corrosion potential difference across the pit the greater the chance of stable pit growth.

Pits propagate as a result of the development and maintenance of an aggressive local environment. The growth of pits is thought to involve the dissolution of metal and the maintenance of a high degree of acidity at the bottom of the pit by the hydrolysis of the dissolved metal ions [93].
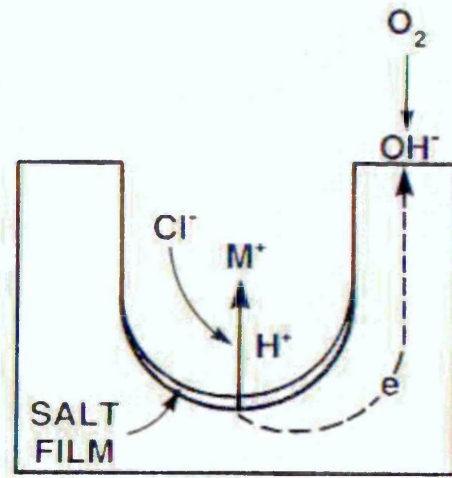


**Figure 2.18**: Schematic illustration of the pit growth mechanism [24].

The pit propagation process is illustrated schematically in Figure 2.18 for a stainless steel pitting in a neutral aerated sodium chloride solution. The anodic metal dissolution reaction at the bottom of the pit,

$$M \rightarrow M^{+n} + ne, \qquad\qquad (2.3.1)$$

is balanced by the cathodic reaction on the adjacent surface,

$$O_2 + 2H_2O + 4e \rightarrow 4OH^- \qquad\qquad (2.3.2b)$$

The increased concentration of $M^+$ within the pit results in the migration of chloride ions ($Cl^-$) to maintain neutrality. The metal chloride formed, $M^+Cl^-$, is hydrolyzed by water to the hydroxide and free acid:

$$M^+Cl^- + H_2O \rightarrow MOH + H^+Cl^- \qquad (2.3.5)$$
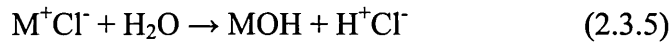
Corrosion pitting has been found to be related to an area of exposure, time of exposure, and the material-environment under consideration. In an experimental study on corrosion pit growth of low-alloy steel in 90 C deionised water, Kondo [14] found that the corrosion pit growth law can be formulated as:

$$2c = B\,t^{1/3} \qquad (2.3.6)$$

Where $2c$ is pit diameter,

$t$ is the time, and $B$ is a coefficient reflecting the effects of material/environment. Another formula was developed by Godard [94] taking into account the pit depth and the area of exposure:

$$d = BA^2 \qquad (2.3.7)$$

Where $d$ is pit depth and

$A$ area of exposure.

The general shapes of the corrosion pits are also worth mentioning. Figure 2.19 represents schematically typical shapes of stainless steels corrosion pits. As shown in this figure, corrosion pits shapes can be classified as follows:

1- In term of depth; narrow, elliptical or wide shallow.

2- In term of appearance from the surface; subsurface or undercutting.

3- In term of microstructural orientation; horizontal or vertical.
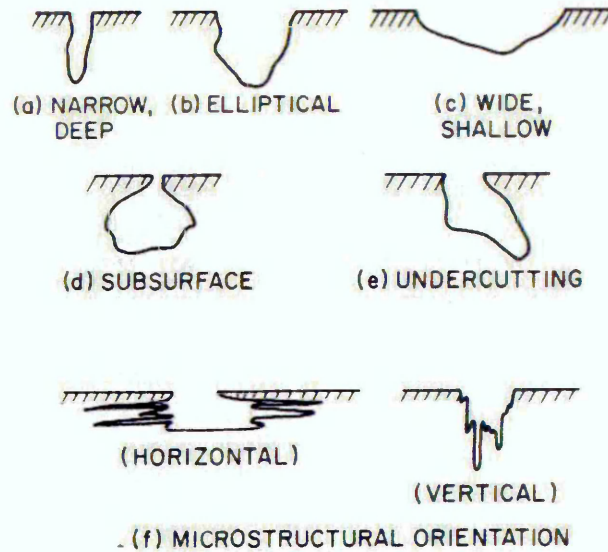


**Figure 2.19:** Schematic of the cross-sectional shapes of pits.

A common method of assessing pitting resistance is to calculate the Pitting Resistance Equivalent Number, PREN for the alloy. Table 2.3.1 represents pitting resistance equivalent number of some stainless steels grades.

There are various expressions for this but the most common is:-

$$PREN = (\% \ Cr) + 3.3 \ (\% \ Mo) + 16 \ (\% \ N) \qquad (2.3.8)$$

**Table 2.3.1** Pitting resistance equivalent number (PREN) of some of stainless steels grades [95].

| Grade | Type | Cr | Mo | N | PREN |
|--------|----------|-----------|---------|-----------|-----------|
| 1.4362 | SAF 2304 | 22.0-24.0 | 0.1-0.6 | 0.05-0.20 | 23.1-29.2 |
| 1.4462 | SAF 2205 | 21.0-23.0 | 2.5-3.5 | 0.10-0.22 | 30.8-38.1 |
| 1.4410 | SAF 2507 | 24.0-26.0 | 3.0-4.0 | 0.24-0.35 | 37.7-46.5 |
| 1.4501 | Zeron 100 | 24.0-26.0 | 3.0-4.0 | 0.2-0.3 | 37.1-44.0 |

## 2.4 Corrosion Fatigue

Corrosion fatigue (CF) is a degradation process involving the synergistic effect of electrochemical reactions (reactions in which charge transfer takes place at the metal-electrolyte interface), and mechanical cycle loading (fatigue). The combined effect of an aggressive environment, such as seawater, with a cyclic stress, or strain, is invariably more severe than the sum of the two individual effects of corrosion and fatigue acting separately. CF is the successive stages of metal damage that evolve with accumulated cycling loading, in an aggressive environment compared to inert or benign media, and resulting from the interaction of irreversible cyclic plastic deformation with localised chemical and electrochemical reactions. The most complicated aspect of CF is the combined nature of the process, as it has been shown by Gangloff [96] that neither cyclic stress in air nor environment attack applied separately produces the same damaging results as that of the simultaneous action. It is generally suggested that the presence of an aggressive environment enhances both crack initiation and crack growth for a number of specific metal-environment systems when subjected to cyclic loading [97].

Corrosion fatigue has been recognised since the beginning of the last century as a principal mechanism for material damage during service. The emphasis of much of this earlier work was placed upon the S-N behaviour, which is dominated by the initiation phase [98]. The majority of observed fatigue failures may be considered as CF failures, since only fatigue occurring in an absolute vacuum could be termed as pure fatigue. A study of the fatigue damage of machines and structures operating in corrosive environments is imperative, as it is known that such environments reduce the fatigue strength far below the typical fatigue strength determined in air. In some cases the environment eliminates the fatigue limit associated with air fatigue performance as reported schematically in Figure 2.20 [99, 100, 101, 102].

50

The analysis of the fatigue behaviour of metals and alloys in aggressive environments is much more complicated than that of the in air fatigue damage process. Figure 2.21 represents a schematic of Cowley et al [103] S-N data under three conditions; (i) fatigue in air, (ii) corrosion fatigue in 10% sulphuric acid and (iii) anodically protected corrosion fatigue, for three stainless steel alloys. Results of corrosion fatigue lifetime under anodic protection at high stresses showed a higher fatigue limit than the air fatigue limit. They related this to a large evolution of heat produced at these high stresses has produced very high local temperature in the air fatigue specimens, causing low endurance values. Where in the anodic protected tests the solution works as a cooling medium. Others explain this behaviour as a resistance of crack initiation as a result of the crack tip blunter [104].
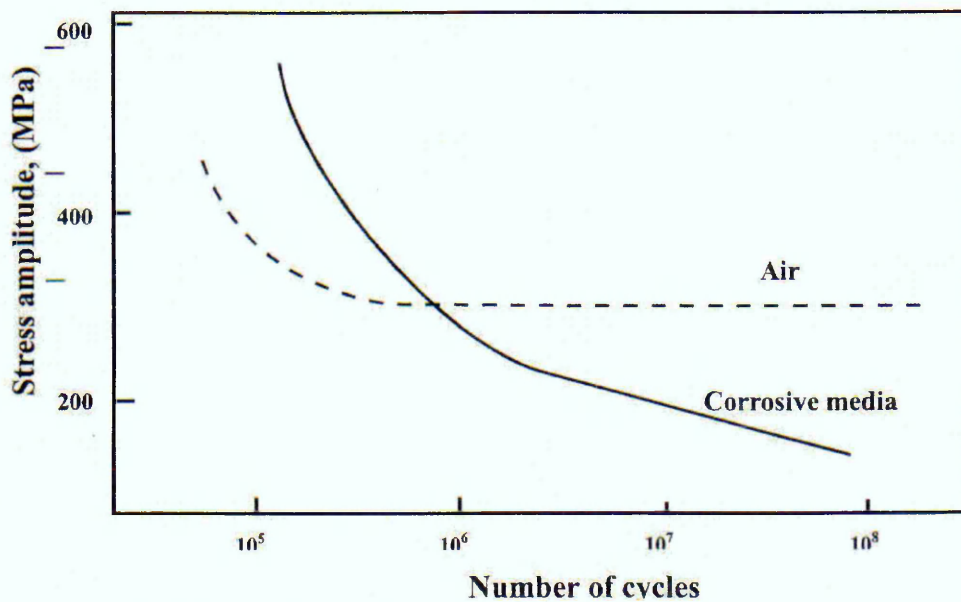


**Figure 2.20:** Schematic illustration of air fatigue and corrosion fatigue behaviour.

It is also possible that even where passive films are present, the stresses generated in high cycle fatigue experiments are either not high enough to break the surface films or slip band emergence is so slow that film repair takes place more rapidly than the possible corrosion damage [105]. This shows the important effect of the test frequency on the corrosion fatigue life time.

Retardation in the formation of corrosion pits as a consequence of a delay in film rupture results in the increasing of corrosion fatigue life of the metal.
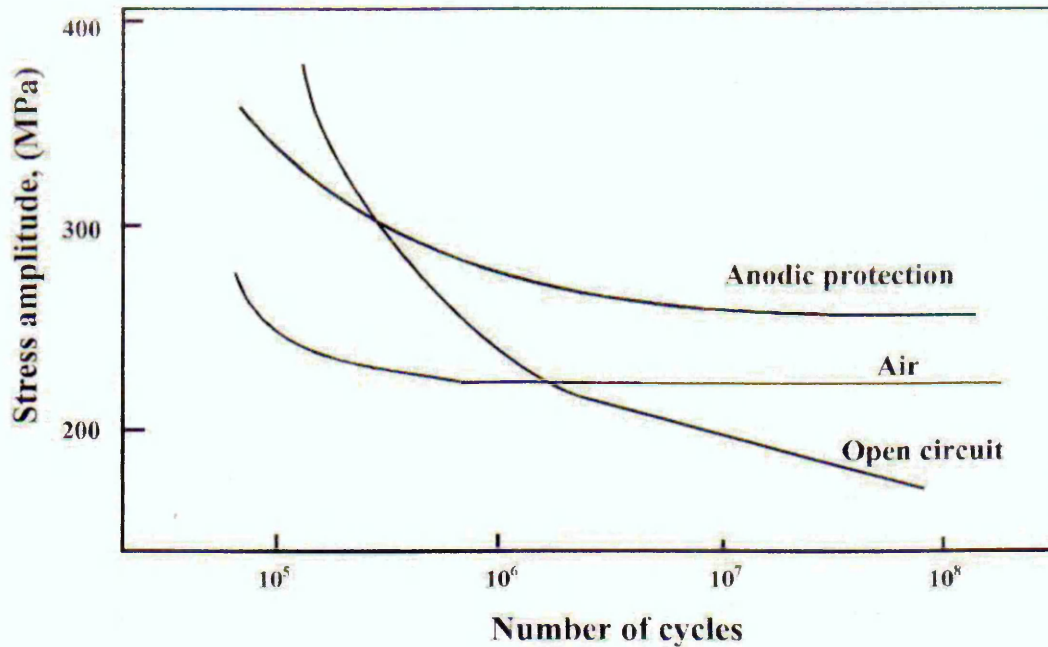


**Figure 2.21:** Fatigue and CF S-N curves for 18Cr-10Ni-Fe alloy under different conditions [103].

Corrosion pits that are produced in cyclic stresses in a corrosive environment, have often been the source of cracks. An example is aircraft components operating in fleets.

Once a pit or group of pits is formed, the rate of pit growth is dependent mainly on the material, environment, and on the type and state of stress [106]. Therefore, to estimate the total corrosion fatigue life of a component, it is of a great importance to develop realistic models which takes into account the early stages of damage, including corrosion dominated processes, i.e., pitting. These models can be used to formulate methods by which designers can assess the effect of pitting corrosion on fatigue life of components and structures, and apply that information to the design.

With the intention of understanding and controlling the phenomenon of corrosion fatigue failure, some models, based on pitting corrosion fatigue mechanisms, have been proposed in the past and others are emerging which will be presented later in this chapter. While it has frequently been stated that any metal or alloy that exhibits corrosion in a particular environment will also exhibit corrosion fatigue, such behaviour can not be generalised. It is not possible to establish a simple correlation between the extent to which different environments provoke different amounts of corrosion upon a given material and their relative influence upon the fatigue life time. Corrosion reactions may enhance crack growth if they produce metal dissolution at the crack tip maintaining crack sharpness or promoting the easy transport of hydrogen into the metal for those metals that are susceptible to hydrogen induced damage [107]. The aggressive environment acting simultaneously with cyclic loading promotes an increase in the density of cracks when compared to that observed in air [106].

The corrosion fatigue phenomenon is also considered to consist of two principles stages, like the process of air fatigue, namely crack initiation and crack propagation. The initiation stage, the period required for the nucleation of cracks has been estimated to be 10 percent of the total life time, whereas it is around 90 percent for the case of air fatigue [108]. The term initiation refers to a period that a defect takes to attain a detectable size. The minimum detectable size, and as a consequence, the duration of this period as a fraction of total life, is a function of the method used to detect the defect. The second stage, which corresponds to crack propagation, presents perturbations in the growth of short cracks due to microstructural obstructions such as grain and phase boundaries. This irregular behaviour only continues to a certain crack length after which the crack growth rate may have a linear relationship with crack length.

In both air and corrosion fatigue fracture processes, macroscopic cracks are termed long cracks and the initiation and growth of microscopic cracks in the submillimetre range precedes their

formation. The latter are termed short cracks and their growth can occupy the major percentage of the fatigue life.

During the corrosion fatigue process, damage accumulates with increasing number of load cycles (N) by the following stages [96, 109, 106]:

1- Cyclic plastic deformation (influence of pit initiation and growth)

2- Microcrack initiation, corrosion fatigue crack initiation can be the result of pitting.

3- Short crack growth to link and coalescence, and

4- Macrocrack propagation.

5- Failure of the component.

The mechanisms for corrosion fatigue may (in no particular order) involve hydrogen embrittlement; film rupture, dissolution and repassivation; enhanced localised plasticity; interactions of dislocations with surface dissolution, films or adsorbed atoms; and complex combinations of these processes [109, 110]. The contribution of each mechanism is controversial and depends on metallurgical, environmental and chemical conditions.

Theories of corrosion fatigue have generally relied on one or more of the following mechanisms [96, 111, 112, 113, 114]:

1- Stress concentration at the base of hemispherical corrosion pits created by the interaction with aggressive environment.

2- Electrochemical attack of plastically deformed areas of metal with non-deformed areas acting as cathode.

3- Dissolution of the metal due to the rupture of the protective surface film.

4- Surface energy reduction of the metal produced by adsorption of species mainly atomic hydrogen.

Fatigue crack initiation of components in an aggressive environment can take place as a result of diverse electrochemical phenomena such as localised corrosion processes. Pitting corrosion, preferential dissolution, film rupture and the lowering of the surface energy are the most studied mechanisms suggested to explain the phenomenon.

## 2.4.1 Pitting in Corrosion Fatigue

Pitting is considered as a major mechanism for crack initiation in corrosion fatigue. Many researchers [78, 84, 89, 97-112, 115] have studied corrosion fatigue of metals in a variety of environments and surface conditions. It has been suggested that the failure process of at smooth surfaces can include the initiation and growth of corrosion pits, the effect of corrosion products, dissolution and passivation of crack surface, and the coalescence of multiple cracks. Congleton et al [107] provided evidence of crack initiation associated with the pitting corrosion process where corrosion pits were clearly seen on the surface of the metal when subject to CF conditions.

Corrosion pit formation in metals and alloys in aggressive environments undoubtedly does lead to a reduction in fatigue life. Akid [115] demonstrated the effect of pH on the CF crack initiation, he showed that CF cracking arose from pitting at inclusions in pH 6 solutions and from the dissolution of slip bands in solutions with pH 2.

Duquete et al. [106] showed that carbon steels are highly susceptible to CF in acidic solutions, where pits are not detected, and additionally they observed that, reduced fatigue lives could be induced by the application of small anodic currents in de-aerated solutions where corrosion pits

do not form. On the other hand, fatigue tests carried out in 3% NaCl solution adjusted to pH 12 with NaOH, where only a few randomly distributed pits were found, showed fatigue limits very similar with those observed in air [105] is may be expected because corrosion pits formed in carbon steel in these conditions tend to have a hemispherical geometry and the stress concentration they induce is not very high [84].

Akid [116] observed that during the early stages of defect development in carbon steel in chloride solutions, pit development and stress assisted dissolution accelerate the transfer from a defect (pit/crack) to a stage II tensile fatigue crack.

In stainless steels, corrosion fatigue crack initiation is promoted by any surface defect that has the characteristics of a real stress concentrator. Mechanical notches are more dangerous in corrosive environments than in air fatigue, and the development of corrosion pits is particularly deleterious. Cyclic plastic deformation accelerated both the dissolution of slip steps and the pit initiation in 316L SS in chloride containing solution, thus groups of small crystallographic pits form and coalesce resulting in the creation of small cracks [117]. However, the presence of surface defects or pits is not necessary, as indicated by Magnin [118], who showed how the environment promotes CF crack initiation by enhancing the localisation of plastic strain.

## 2.4.2 Pit-crack transition

For defect free surfaces of metallic components, susceptible to pitting corrosion and subject to cyclic stresses in aggressive environments, a very important aspect of the corrosion damage process is the transition from a corrosion pit to a short crack. This transition step, which can be considered as the moment at which a crack is completely established at a pit site, is believed to have a marked effect on the resulting fatigue life time. The transition point depends on the applied stress level, the nature of the environment, the pit depth and on the loading frequency as

demonstrated by Akid [116]. The same author suggested that a model to determine the time for a pit to develop into a crack must incorporate both frequency and stress terms.

For a given metal electrolyte system that develops corrosion fatigue cracks from pits, stress-assisted dissolution enhances the crack development and reduces the influence of the microstructure on crack growth. Historically, much of the investigations carried out on fatigue and CF have focused on the behaviour of long cracks, although it is now well established that under specific circumstances fatigue life time is controlled by the nucleation and growth of microscopic defects [119, 120].

It has been stated that non-metallic inclusions have a significant effect on crack initiation stage in corrosion fatigue. Corrosion pits, which are initiated from surfaces containing sulphide inclusions, tend to eliminate the inherent resistance of the fatigue cracking of the microstructural barriers [121, 122].


## 2.4.3 Models of Corrosion Fatigue

Linear Elastic Fracture Mechanics (LEFM) concepts are widely used to assess the crack growth behaviour of pre-cracked components undergoing cyclic deformation in different environmental conditions. LEFM is however of limited use when considering development of damage from smooth surfaces. The pit growth rate theory is combined with the fatigue crack growth concepts to develop CF models. The number of cycles to nucleate a mode I crack from a pit, subjected to cyclic loading, could be modelled using LEFM concepts and in this respect some models have been proposed [14, 123, 124]. All of the models consider pits with hemispherical geometry and the corresponding stress intensity relation is used to assess the critical pit depth using the crack growth threshold ($\Delta K$), which is found empirically [125].

Hoeppner [123] proposed a model, which determines the critical pit depth to nucleate a mode I crack. This model applies to metal-environment systems susceptible to pitting corrosion fatigue. The number of cycles needed to develop a critical pit size that will produce a mode I crack is obtained by combining calculations of pit growth rate and fatigue crack growth curve fitting.

Akid and Miller [15] developed a model of corrosion fatigue based upon microstructural fracture mechanics. The model is based on the fact that the fatigue limit observed in ferrous materials in air is not, as had previously been thought, due to stress level being too low to initiate any fatigue cracks but that initiated cracks fail to propagate as a result of microstructural characteristics of the material, grain size, texture and phase distribution. In an aggressive environment the corrosion processes affects the ability of microstructural features to decelerate or arrest crack growth.

Akid and Miller's model [15] is based upon previous in-air crack growth models. The Hobson model [69] considers the growth of a fatigue crack in two regimes, before, and after that main microstructural barrier, shown schematically in Figure 2.22(a). The second model developed by Akid and Miller [15] is that of Navarro and de los Rios model [70]. The Navarro and de los Rios model Fig.2.22 (b) is based on the following concept of crack growth; a crack growing along an active slip band within a grain will have a crack growth rate that is controlled by the degree of plasticity ahead of the crack tip.
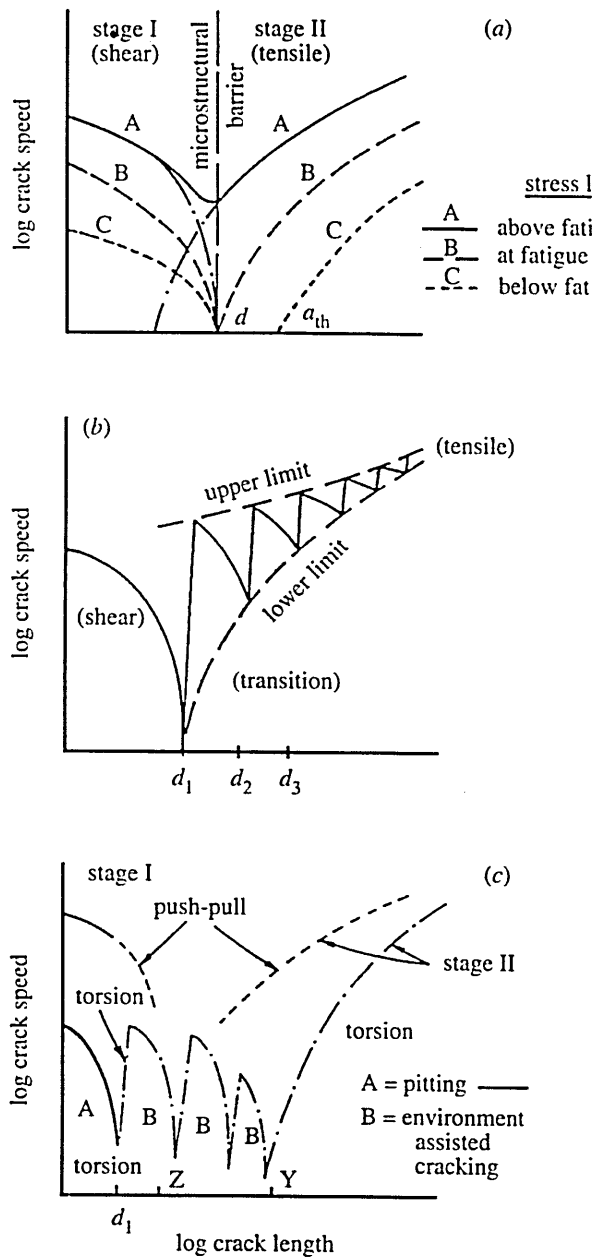
**Figure 2.22** Short fatigue crack growth models: (a) Hobson, (b) Navarro-de los Rios and (c) a modified Hobson model for corrosion fatigue [15].

As the crack approaches the first microstructural barrier (grain boundary) its growth rate will reduce, as the degree of plasticity ahead of the crack tip will be reduced by the presence of the boundary. When the crack reaches the grain boundary one of two things can occur, (a) if the applied stress is above the fatigue limit the stress ahead of the constrained plastic zone will eventually be high enough to initiate slip in the next grain, thus allowing crack growth to continue. As the crack grows in the new grain its rate will initially be high as the plastic zone

59

ahead of the crack tip increases to fill the new grain; (b) if the applied stress is below the fatigue limit the crack will arrest upon reaching the grain boundary. This process is shown in Figure 2.22b.

Akid and Miller [15] developed these models by using the superposition model to combine them with a corrosion term. Corrosion was included in these models by expressing the crack growth rate caused by corrosion in terms of metal dissolution using Faraday's law:

$$(da\backslash dN)_{CF} = (da/dN)_{diss} + (da/dN)_{AF} \qquad (2.4.1)$$

$$\frac{d_a}{dN_{(diss)}} = \frac{M\, i_{corr}}{zF\rho\omega} \qquad (2.4.2)$$

Where,

$(da\backslash dN)_{CF}$ = Total crack growth rate

$(da/dN)_{diss}$ = Corrosion rate (metal dissolution)

$(da/dN)_{AF}$ = Air fatigue growth rate

$i_{corr}$ = Anodic current density

$\omega$ = Cyclic frequency

$z$ = Valance

$F$ = Faraday's constant (96485,3383 [coulombs/mole]

$M$ = Molecular weight

$\rho$ = Material density

The affect that this metal dissolution term has on the crack growth models is to remove crack arrest at microstructural defects; this is due to the crack length extension that occurs as a result of metal dissolution. Figure 2.22c shows schematically the effect of including the metal dissolution term in the short crack growth models. Comparison of experimental results with crack growth rate values calculated using the modified short crack growth equations showed a reasonable correlation. Murtaza and Akid [18] modelled corrosion fatigue cracking by development of the environmentally assisted crack growth term to include both long and short crack growth within the environment. The effect of strain enhanced dissolution was also included in the environmentally assisted crack growth term.

## 2.5 X-ray Diffraction (XRD) Technique for Residual Stress Measurements

### 2.5.1 Introduction

There are different techniques used to measure residual stress. Some are destructive techniques such as hole drilling and others are non-destructive techniques like X-ray diffraction (XRD) and neutron diffraction [126, 127], where each technique has its own advantages and disadvantages. Out of these X-ray diffraction is one of the most commonly used non destructive techniques for residual stress measurement [128]. Although the term stress measurement is commonly used, stress is an extrinsic property that is not directly measurable. In XRD stress measurement, the strain in the crystal lattice is measured and associated residual stress which produces the strain is calculated.

When the X-ray beam is irradiated on a crystal structure, the beam is scattered or diffracted by the atomic planes. These diffracted wave fronts from various lattice planes travel different directions and distances, and they interfere constructively only where the difference in path length is an integral multiple of the X-ray wave length. This happens at specific angles, defined by Bragg's law of diffraction. XRD technique measures the residual stress from the shift in X-ray diffraction peak position $(2\theta^o)$, caused by the change of lattice spacing due to the presence of residual strain. If the X-ray detector moves around the irradiated specimen it will find peaks in intensity at certain angles. Typical examples of peaks at different diffraction angle are shown in Figure 2.23. From these $(2\theta^o)$ angles the spacing between the planes of atoms can be calculated. If the crystal lattice structure is altered by an external force, it will create residual stress within the material; as a result the lattice spacing will be altered. The change in lattice spacing will also change the angular position of the X-ray peak. Using Bragg's Law, the new atomic spacing can be calculated by the new

peak position and then the strain can be calculated by the difference between the old and new atomic spacing. Using calculated strain values the respective stress values can be calculated.
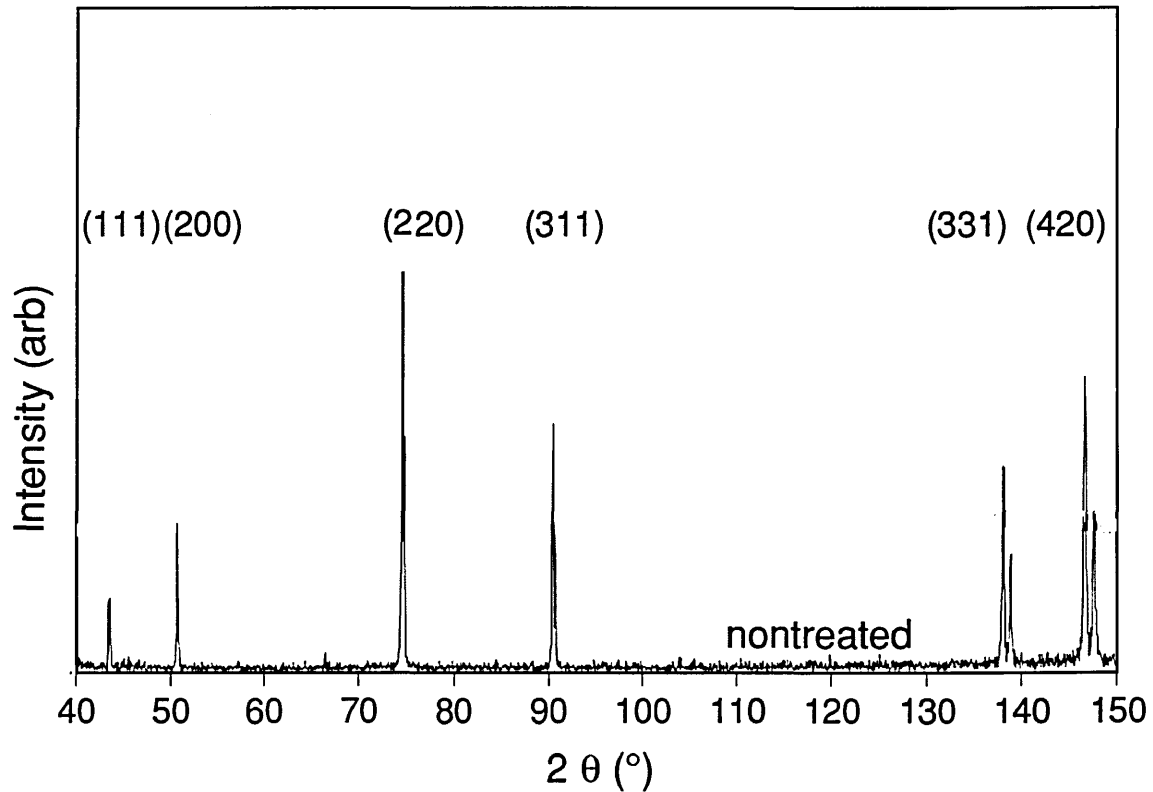


**Figure 2.23:** An example of X-ray diffractometer chart of intensity of the reflected beams vs. $2\theta$ angle for 316L foil specimen [129].

The elastic constants of the material are used for the calculation, assuming linear elastic distortion of the crystal lattice. The technique of measuring residual stresses in a component using XRD is firmly established and explained in literature [128, 130].

## 2.5.2 Bragg's Law

In order to measure the stress using X-rays, the X-ray beam should diffract in an appropriate manner. X-ray diffraction relies on the fundamental interaction between the wavelength of the X-ray beam ($\lambda$) and the crystal lattice spacing ($d$). The diffraction of the X-

ray beam on crystalline materials was initially studied by the British scientist W.L Bragg in 1912 [130], and is called Bragg's law. This expression defines conditions necessary for diffraction of X-rays to occur and Bragg's law is commonly known as the fundamental basis for all X-ray diffraction measurements. Figure 2.24 illustrates the incident and reflected X-ray beam and the notations used. Any change in the lattice spacing, $d$, results a corresponding shift in the diffraction angle $2\theta$.
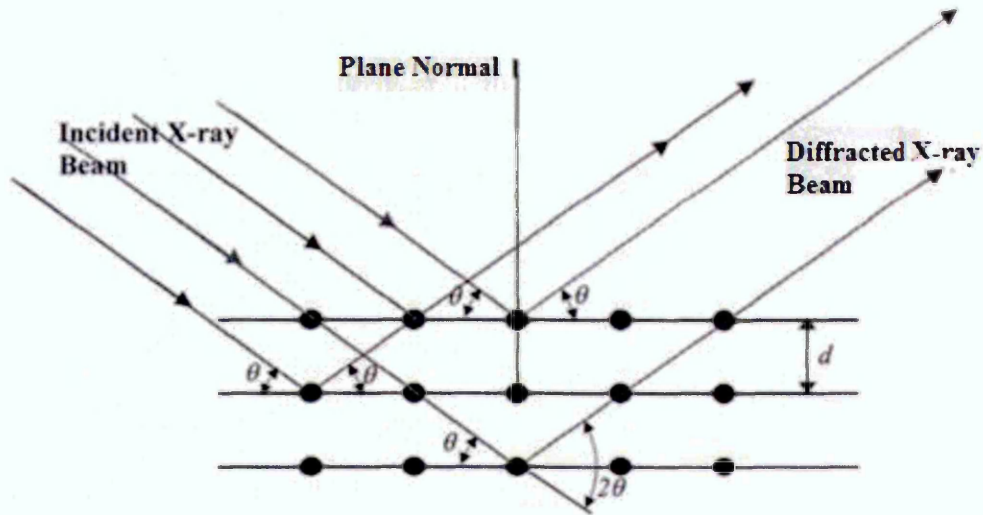


**Figure 2.24:** Illustration of X-ray diffraction by a crystal lattice [131].

Bragg's Law can be stated as,

$$n\lambda = 2d \sin\theta \qquad (2.6.1)$$

where;  $\lambda$- wave length

$d$- lattice spacing

$\theta$- incident/diffraction angle

n- integer denoting the order of diffraction.

## 2.5.3 Measurement of Residual Stress

To perform strain measurements the component is placed in an X-ray diffractometer and exposed to an X-ray beam that interacts with the crystal lattice to cause diffraction patterns. When the material is stressed (strained) the crystal lattice will elongate and contract accordingly. This changes the inter-planer spacing, $d$, which will cause a shift in diffraction pattern. By accurate measurement of the peak shift, the change in the inter-planar spacing can be evaluated and thus the strain within the material can be obtained. If the unstrained inter-planar spacing is $d_0$, strain ($\varepsilon$) can be expressed as,

$$\varepsilon = \frac{d - d_0}{d_0} \qquad (2.5.2)$$
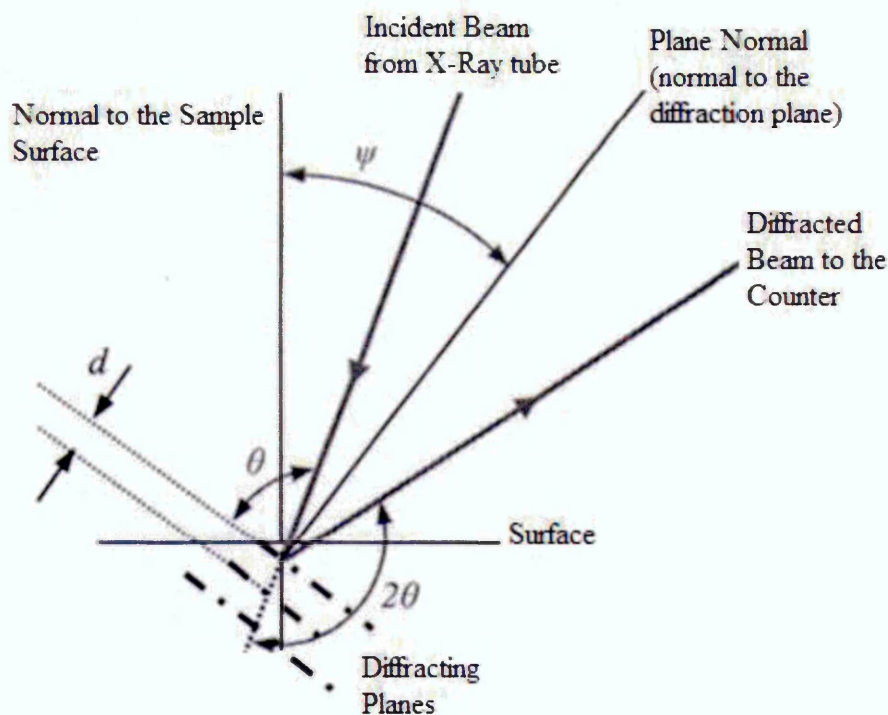


**Figure 2.25:** Incident and diffracted beams with angular notations; the plane normal which is the normal to the lattice plane is at an angle of $\Psi$ to the normal to the surface of the component.

As shown in the Figure 2.25 the angle between the normal to the sample surface to plane normal i.e. the normal to the measuring diffraction lattice plane is represented by $\Psi$. By altering the tilt of the specimen or by tilting the X-ray tube and detector within the diffractometer, measurements of planes at a different $\Psi$ angles ($d_\Psi$) can be made, and strains ($\varepsilon$) along respective directions can be calculated using,,

$$\varepsilon = \frac{d_\Psi - d_0}{d_0} \qquad (2.5.3)$$

The respective stress ($\sigma$) values can be calculated using Hooke's law which is in general terms given by,

$$\sigma = E\varepsilon, \qquad (2.5.4)$$

Where $E$ is the Young's modulus of the material. It is obvious that any tensile or compressive stress producing a strain in a particular direction will also create, not only linear strain in that direction of the stress, but also strains in the transverse directions. These components can be calculated using Poisson's ratio ($v$) which is the ratio of the transverse to longitudinal strain. Using the strain in terms of inter-planar spacing the stress can be evaluated from the following equation:

$$\sigma = \frac{E}{(1 + v)sin^2\Psi}\left(\frac{d_\Psi - d_n}{d_n}\right) \qquad (2.5.5)$$

where,          $E$ - Young's modulus,

                $v$ - Poisson's ratio,

                $\Psi$- orientation of the plane normal to the normal to the sample surface,

                $d_n$ - interplanar spacing measured at plane normal (when $\Psi = 0$) and

                $d_\psi$ - interplanar spacing measured at different $\Psi$ angles.

In XRD, several methods have been used in residual stress measurements. Some of them are single angle technique, two angle technique and $\sin^2\Psi$ technique [127]. The common method used for stress determination is the $\sin^2\Psi$ method, where several XRD measurements are made at different $\Psi$ angles and inter-planer spacing $(d)$ is measured for respective $\Psi$ angles. The $d$ against $\sin^2\Psi$ is plotted which is a straight line as shown in Figure 2.26.
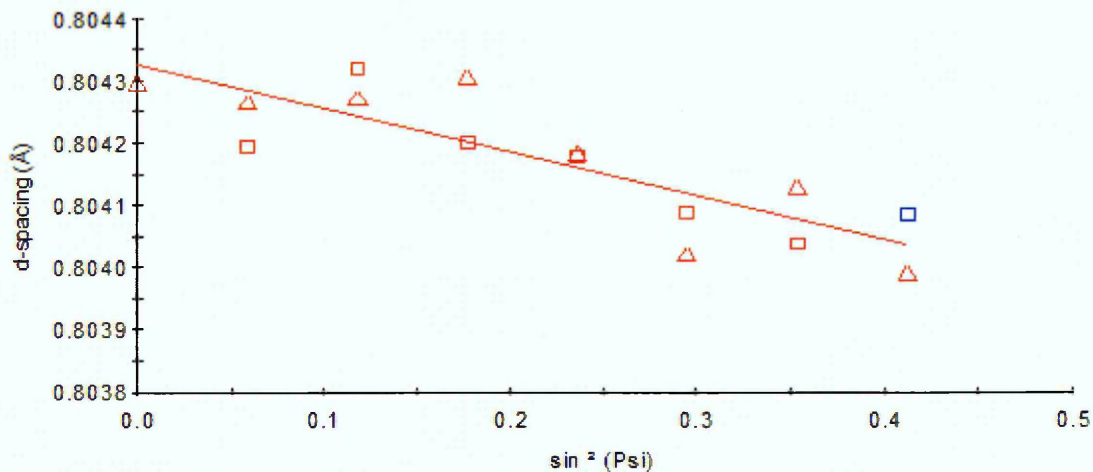


**Figure 2.26:** Example of an inter-planer spacing $(d)$ vs. $\sin^2\Psi$ plot measured for a 316L SS sample [132].

Using the value of the gradient (m) of the straight line the stress can be evaluated. This method assumes a zero stress at $d = d_n$, where $d$ is the intercept of the $y$ axis when $\sin^2 y = 0$. Thus the stress can be evaluated by,

$$\sigma = \left(\frac{E}{1+v}\right) m \qquad (2.5.6)$$

A comprehensive explanation of the methodology with complete mathematical derivations is well documented and established [133].
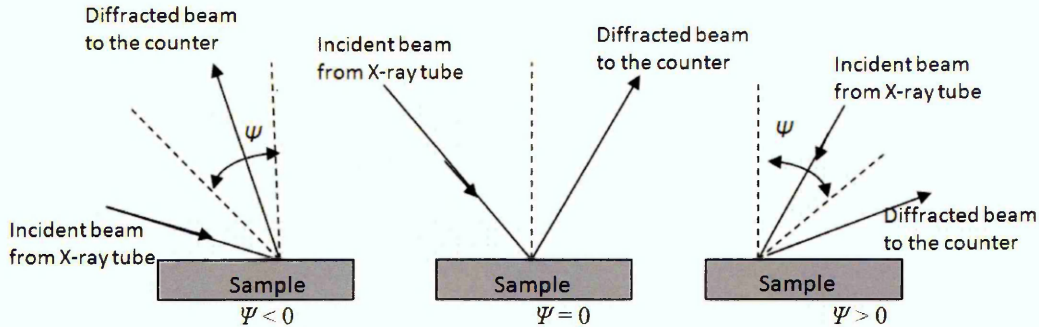


**Figure 2.27:** Different positions of the diffractometer with different stages of $\Psi$ offsets.

## 2.5.4. Different Positions of Diffractometer Movements

According to the different positioning of X-ray tube and detector the $\Psi$ angle varies. Figure 2.27 shows three positions of the diffractometer with positive, negative and zero $\Psi$ angle values.

## 2.5.5 Sample Preparation

Generally the sample surface should be clean free from dirt, scale or grease. Any cleaning or removal of material must be done by a process that does not influence the residual state which thereby changes the stress to be measured.

## 2.5.6 Irradiated Area on the Sample by the X-ray Beam

The irradiated area can be varied by focussing the X-ray beam at the tube exit by means of rectangular slits and masks. When measuring residual stress of cylindrical samples it is important to optimize the irradiated area of the X-ray beam. Hence using slits and masks,

the area must be controlled. The intensity can be improved by elongating the beam in the axial direction. The main problem in reducing the irradiated area is the simultaneous reduction of the number of X-ray counts of which results in a weak peak and the stress measurements will have a considerable amount of error. In this kind of situation the scan duration should be adjusted accordingly to obtain an accurate stress measurement.

The X-ray beam convergent slits and masks must be selected to optimize the irradiated area to keep the error margin as low as possible within the finalized scan duration. The length of the area on the sample that is irradiated by the incident beam is dependent on the divergence of the X-ray beam. The divergence of the X-ray beam can be adjusted by using different type of divergence slits and masks. Slit size controls the irradiated length ($L$) and the mask size controls the irradiated width ($w$).

The irradiated length can be calculated using [134],

$$L = \frac{R\ (sin\omega\ sin\delta)}{(sin^2\omega - sin^2\left(\frac{\delta}{2}\right))} \qquad (2.5.7)$$

where, $L$ - irradiated length of the sample,

$R$ - radius of the goniometer,

$\delta$- divergence angle,

$\omega$- angle between incident beam and sample surface.

Vignal et. al in a study using XRD techniques on 316L austenitic stainless steel under applied stress below the yield stress, have correlated the corrosion susceptibility to the nature of the surface stresses [4]. In other study using Auger electron spectroscopy they

studied the role of elastic stresses and the cold-worked layer on the corrosion potential value [135]. They found a linear relationship between the local residual stress and the corrosion potential as the corrosion potential becomes higher with increasing compressive stresses where increase in the chromium content in the passive film was observed.

Using XRD technique to measure residual stress and investigate its influence on fatigue life it has been suggested that the main relaxation of residual stresses normally takes place in the first cycle, followed by further gradual relaxation during the life time [136]. The relaxation during the first cycle depends on the monotonic yield strength of the material in tension and compression, while relaxation during successive cycles is related to the cyclic yield strength. Since the relaxation is associated with dislocation movement, it is then correlated to the plastic strain amplitude and the number of fatigue cycles.

## 2.6 X-Ray Photoelectron Spectroscopy (XPS)

XPS is a surface analysis technique that probes the first ten to twenty atomic layers of the surface of a material. XPS is used to determine quantitative atomic and chemical composition. It is a surface technique with a sampling volume that extends from the surface to a depth of approximately 50-70 Angstroms. XPS is an elemental analysis technique that is unique in providing chemical state information of the detected elements.
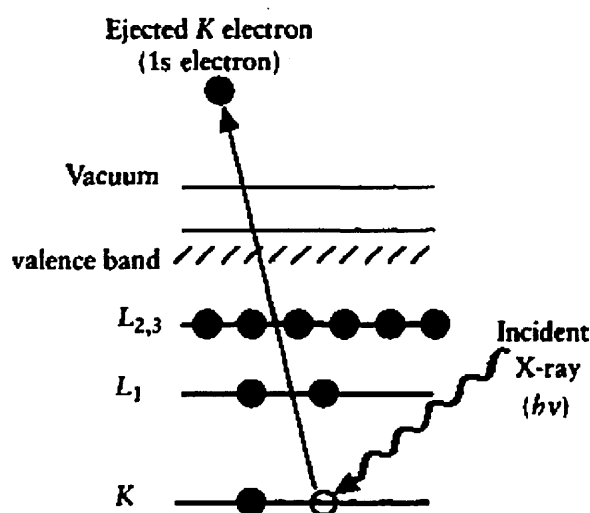


**Figure 2.28** Incident photon and correspondence emission of electron

In this technique [137], a photon is absorbed by an atom, leading to ionization and emission of an electron from the core levels as shown in Figure 2.28. The energy of the emitted photoelectrons is then analysed by the electron spectrometer and the data presented as a graph of intensity versus electron energy. Photoelectron spectroscopy uses monochromatic sources of radiation. The process of photoionization can be considered in several ways: one way is to look at the overall process as follows:

$$A + h\nu = A^+ + e^- \qquad (2.6.1)$$

Where          h - Planck constant ($6.62 \times 10^{-34}$ J s)

v - Frequency (Hz) of the radiation

A - Atom

$A^+$ - Excited atom

Conservation of energy then requires that:

$$E(A) + h\nu = E(A^+) + E(e^-) \qquad (2.6.2)$$

Since the electron's energy is present as kinetic energy (KE) this can be rearranged to give the following expression for the KE of the photoelectron:

$$KE = h\nu - (E(A^+) - E(A)) \qquad (2.6.3)$$

The final term in brackets represents the binding energy (BE) of the electron,

$$KE = h\nu - BE \qquad (2.6.4)$$

For each element, there will be a characteristic binding energy associated with each atomic orbital, and the presence of peaks at particular energies indicates the presence of that element in the sample. Moreover, the area under the peaks represents the concentration of the element within the sample. Therefore, the XPS technique provides qualitative and quantitative analysis of the sample surface.

Most elements have major photoelectron peaks below 1100 eV, and therefore a scan range from 1100-0 eV binding energy is usually sufficient to identify all detectable elements (a survey scan). For the purpose of chemical state identification, for quantitative analysis of elements and for peak deconvolution, detail scans are obtained (high-resolution scans or multiplex scans). The abundance of elements is calculated

from peak heights or peak areas, and identification of chemical states of elements is made from exact measurements of peak positions and separations, as well as from certain spectral features such as shape of the peaks. The depth distribution of the elements can be obtained by acquiring spectra at different angles of X-ray beam. The variable angle of the X-ray beam frees photoelectrons from different depths. The higher the value of the emission angle (or take-off angle), the deeper the penetration of the X-ray beam into the sample, *i.e.* the greater the escape depth of photoelectrons. An alternative approach is the sputtering of the sample with an inert gas such as Argon, which allows collection of spectra from varying depths by controlling both the intensity and time of sputtering.

# Chapter 3- Objectives

## 3.1 Introduction

Austenitic stainless steel materials have been used in variety of applications where good resistance to corrosion and high mechanical strength are required. However, they are susceptible to localised corrosion in aggressive environments in particular when they subjected to cyclic loading. Therefore, the objective of industries is to enhance the resistance of these materials by introducing manufactories techniques to modify the material surface structure and composition. Development of a homogenous oxide film is one of the objectives to obtain a novel surface function of metallic materials. Recently, the alternating voltage passivation process (AVPP) was reported to enhance the corrosion resistance of stainless steels as a result of increasing the oxide layer thickness and changing in its composition.

The main aim of this study was to assess the influence of AVPP treatment of the 316L SS native oxide film on the local electrochemical behaviour and the mechanical properties.

## 3.2 Objectives

The following specific objectives were set;

➢     Perform material characterisation studies to investigate the changes in the material composition structure and thickness of the native oxide film and compare it with the modified oxide film using IFM, SEM and XPS.

➢ Investigate the local electrochemical behaviour of the modified and unmodified oxide film applying a local electrochemical measurement technique (scanning droplet cell), through different experiments such as; potentiodynamic polarisation curve, potentiostatic polarisation, linear voltammetry and electrochemical impedance spectroscopy.

➢ Compare the electrochemical behaviour of the modified 316L SS surface and duplex stainless steel 2205.

➢ Generate and monitor the growth of corrosion pits on the surface of material using the scanning droplet cell technique and assess the effects of varies factors (e.g. flow rate, surface finish, and applied stress) on pit initiation and growth.

➢ Determine the material mechanical properties by conducting tensile strength tests on the designed samples.

➢ Study the effects cycling loading on changes in residual stress state of the native and modified oxide films using an X-Ray Diffraction technique.

➢ Investigate the hardness properties of the oxide film before and after film modification using nano-indentation hardness tests.

➢ Configure of a test system to measure the pit and short fatigue crack growth behaviour, to investigate each stage of the corrosion fatigue damage process occurring at the 316L SS surface and compare this with the modified film surface.

➢ Understand the effects of corrosion on cracking behaviour during the different stages of fatigue crack growth.

# Chapter 4- EXPERIMENTAL WORK

## *4.1 Material Characterisation*

Two stainless steels materials were used in the experimental work, austenitic stainless steel (316L SS) and duplex stainless steel (2205 DSS). The later was used only for electrochemical experiments for comparison with the 316L SS.

### 4.1.1 Chemical Composition

The chemical composition of the stainless steels materials is presented (in weigh percent) in table 4.1 as reported by the manufacturer.

**Table 4.1**: Chemical composition of stainless steel materials (wt. %)

| Material | C | Cr | Ni | Mo | Mn | Si | P | S | Co | N |
|----------|-------|-------|-------|------|------|------|-------|-------|------|-------|
| 316L | 0.017 | 16.72 | 10.06 | 2.03 | 1.26 | 0.40 | 0.035 | 0.005 | 0.16 | 0.04 |
| 2205 | 0.019 | 22.29 | 5.73 | 3.17 | 1.44 | 0.42 | 0.02 | 0.001 | 0.1 | 0.179 |

### 4.1.2 Samples Preparation

Figure 4.1 shows flat tensile fatigue samples used in this study. Samples were ground using water-cooled silicon carbide papers of 600, 800 and 1200 grit size. Samples were then polished in two steps, starting with rough polishing with 6μm diamond abrasive paste followed by a second polish step using 1μm paste. Electrolytic etching was used for revealing the microstructure. This method gave the best results compared to the non-electrolytic method. The etching was performed immediately after the surface polishing process.
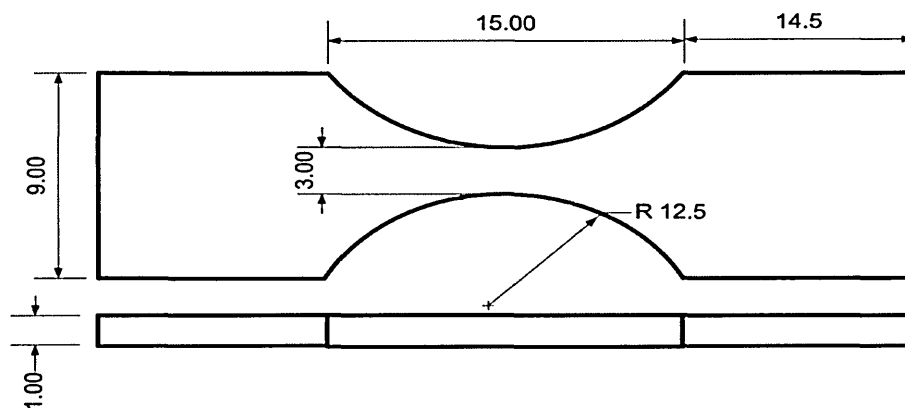
**Figure 4.1**: Dimensions of tensile fatigue sample used in this study (dimensions in mm).

The specimen was subjected to anodic polarisation, 400mV above the open circuit potential for periods of 10 sec until the microstructure was completely developed. Each material was etched with different agent and procedures as following:

Duplex Stainless steel 2205

The material surface was etched using (25ml HCl, 75ml $H_2O$, 0.7g Sodium Metabisulphite) to reveal the microstructure of the material. In order to develop the microstructure it was necessary to use a potentiostat and a three electrode cell with a platinum mesh as auxiliary electrode and saturated calomel electrode (SCE) as a reference. Samples were subjected to anodic polarisation, 400 mV above the open circuit potential for periods of 10 seconds until the microstructure was completely revealed.

Austenitic Stainless Steel 316L

The material surface was etched using (60 ml $HNO_3$, 40ml $H_2O$) to reveal the microstructure of the material. A platinum electrode was used as the cathode, the applied voltage was 0.8 V DC for periods.

In order to reveal the possible presence of inter-metallic compounds, such as delta ferrite ($\delta$) and sigma phase ($\sigma$) in the 316L SS, samples were subjected to electrolytic etching in 10% aqueous NaOH for periods of 15 seconds until the phase was clearly distinguishable. EDX analysis was carried out in order to determine the presence of inter-metallic compounds, which were observed in 316L samples after etching.

### 4.1.3 Microstructure Investigation Using IFM

An infinite focus microscope (IFM) equipped by image analysis software was used to study the microstructure of the two stainless steel materials. The infinite focus microscope is a digital light microscope which has 3D measurement and image analysis capabilities. IFM allows capturing and calculation of sharp images with virtually infinite depth of focus. It can capture images with almost 1000-times enlarged depth of focus. IFM can capture surfaces topographic specimens with large height and profile differences quickly and produces high resolution digital colour images [138].

The *alicona®* *Infinitefocus* IFM equipped with an *alicona®* software was used to investigate the surface topography, microstructure analysis, pits profile and to detect and measure fatigue cracks in direct measurement.

### 4.1.4 Scanning Electron Microscope (SEM)

The SEM is one of the most versatile instruments for investigating the microstructure and details of fractured surfaces of materials. It provides high resolution images with a

magnification with extends beyond x10000 up to x150000 with a depth of focus ranging from 1μm at x10000 to 2mm at x10 [139].

The Philips XL40 Analytical Scanning Electron Microscope with an Oxford Instruments ISIS 300 energy dispersive analyser was used. Samples were placed on aluminium stubs using a conductive adhesive media and mounted on the sample stage situated inside the chamber, which were then ready for SEM investigation.

Three modes of SEM were used which includes secondary electron (SE) mode, backscattered electron (BS) mode, and x-ray spectroscopy mode. For surface topography investigation, material contrast and microstructure, SE and BS modes were used. Where x-ray mode was used for elemental distribution measurements. SE and BSE modes were used for imaging and EDX analysis was conducted to identify specific features such as inclusions.

The average grain size was determined using the mean linear intercept (MLI) method in accordance with BS 4490:1989 [140]. According to the MLI method the number of grain boundaries intercepting linearly *(N)* for a total length of *(L)* were counted. The mean number of intercepts *(Ni)* was determined evaluate the mean number of intercepts over the total distance, i.e. *(NL)*.

$$N_L = \frac{Ni}{L} \qquad \text{Eq. (4.1)}$$

The grain size *(d)* was expressed as the mean value of the intersected segment since the material microstructure is equiaxed.

$$d = \frac{1}{N_L} \qquad \text{Eq (4.2)}$$

## 4.1.5 X-ray Photoelectron Spectroscopy

Analysis was performed on two samples 316L and 316L AVPP. The first was unmodified stainless steel and the second stainless steel which had undergone an electrochemical treatment by AVPP. The goal was to determine what effect this had on the surface oxide layers of the sample. X-ray photoelectron spectroscopy (XPS) was used with technical details as following:

- Instrument: VG Escalab 250 XPS

- X-Ray source: Monochromated Al Kα

- Spot size and power: 500 μm, 150 W

- Ion miller: Focussed Ion beam milling a 3x3mm square concentric with the X-Ray spot.

- Sample current 1 μA.

To this end, depth profiles were taken by scanning the sample and then etching small amount of material from the surface using an argon ion miller and rescanning. In total, 11 layers were studied on each sample. It was expected that the oxide layers were extremely thin (~ 5 nm), so very short etch times were used. The etch rate of this argon ion miller is approximately 0.2 nm/s, however this can vary a great deal depending on the material being etched. Therefore, reliable thicknesses cannot be determined. However, it is safe to assume that the etch rate is constant for both samples, so relative thicknesses can be assessed. Both samples were etched for 100s (very roughly, about 20 nm).

Survey scans were taken at each depth. These reveal the presence of carbon, oxygen, Iron and Chromium peaks. As well as a survey scan, detailed scans were taken of the Chromium $2p_{3/2}$, Iron $2p_{3/2}$, Oxygen 1s and Carbon 1s peaks (these being the strongest

peaks for each element). Typically, XPS spectra are charge normalized by shifting the spectra such that the C 1s peak is at 284.5 eV. However, in this case the C1s peak became quite weak with etching, and the existence of a carbide species complicated matters, so it was decided to normalize the spectra to the Fe 2p3 peak corresponding to metallic iron, as this was a very strong peak at all levels. This was set to be equal to 706.8 eV, the average value from 12 examples in the literature. All other peaks were shifted accordingly.

## 4.1.6 Depth profiles

The relative atomic percentages of the elements (Fe, Cr, O, C) could be determined at each layer using the following formula:

$$Re lAt\% = \frac{\dfrac{A_{Fe2p3}}{RSF_{Fe2p3}}}{\dfrac{A_{O1s}}{RSF_{O1s}} + \dfrac{A_{C1s}}{RSF_{C1s}} + \dfrac{A_{Cr2p3}}{RSF_{Cr2p3}} + \dfrac{A_{Fe2p3}}{RSF_{Fe2p3}}} \qquad Eq\ (4.3)$$

Where A is the area under the peak and RSF is the Relative Sensitivity Factor, an empirically derived factor which describes the relative sensitivity of XPS to the different peaks and elements.

These relative atomic percentages can then be plotted as a function of etch time to give a depth profile. The simplest depth profile is just to take the areas under all the peaks and compare (ignoring the fact that each peak is split into two representing two different species).

## 4.2 Alternating Voltage Passivation Process

The main objective of this study was to determine the influence of AVPP treatment on the native oxide film's electrochemical and mechanical properties. Therefore, some of the samples are subjected to surface film modification by applying an Alternating Voltage Passivation Process. In this process samples are immersed in a solution containing 0.02 M NaCl, pH 3 and room temperature. A potentiostat is used, operating in three electrode cell mode, with a platinum counter electrode, the sample as the working electrode, and saturated calomel (SCE) as a reference electrode. Pulses are applied with amplitude (+ 0.4 - 0.4 )V) vs. SCE, Pulse width 29 ms, anodic to cathodic time ratio is 4:1 for 16h as shown in Figure 4.2.
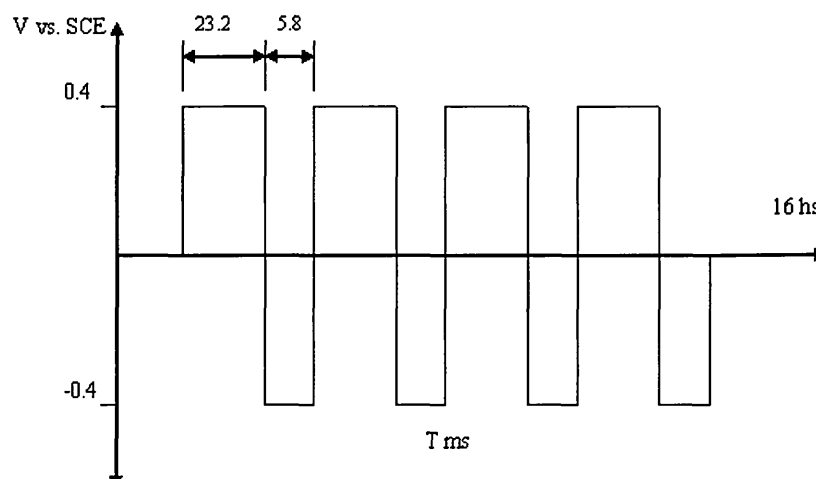


**Figure 4.2:** Amplitude and width of the pulses used in the AVPP treatment. The amplitude is ±0.4V vs. SCE, pulse width is 29 ms, anodic to cathodic time ratio is 4:1 for 16h in 0.02M NaCl, pH3.

## 4.3 Surface Profiles Measurements

Surface profiles were measured using a Taylor-Hobson Talysurf-120L, Stylus type apparatus with a 2µm stylus tip radius. Measurements were taken over a nominal *5mm* length using *0.8mm* cut off filter. Three measurements were taken along the longitudinal direction as shown in Figure 4.3, and these positions are numbered as 1, 2, and 3. Five readings were taken in transverse direction, which are numbered as positions I, II, III, IV and V in Figure 4.3. A typical surface profile of a machined sample obtained from the Talysurf is shown in Figure 4.4. The surface roughness was noted as measuring parameter of the average roughness, *Ra*.
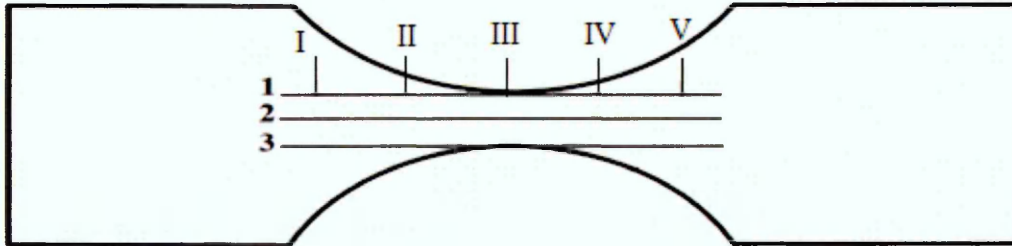


**Figure 4.3:** Locations where surface profile measurements take place on a fatigue sample.
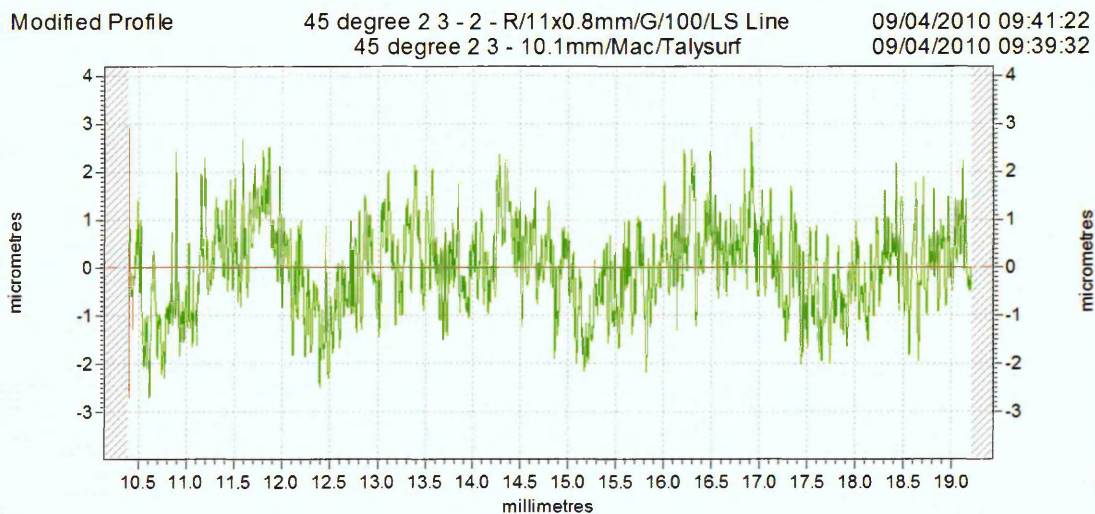


**Figure 4.4:** Typical surface profile of a machined sample obtained from *Talysurf.*

## 4.4 Electrochemical Testing

### 4.4.1 Introduction

The fast and precise measurement of electrochemical activity is important for a variety of studies, not only for research, but also in practical applications. It is possible to measure effects such as corrosion rate by direct analytical methods, for example weight loss measurements or solution analysis by spectroscopy; however, these methods are often slow, time consuming and inefficient. Additionally, they are limited to systems in which the products formed by the process do not form adherent layers.

As the processes under consideration are electrochemical, it is possible to evaluate them using electrical methods based on Faraday's law, which relates the change in mass per unit area to the current flow. The advantages of this approach are a relatively short measuring time, high accuracy and the possibility of monitoring the process continuously.

However, there are also disadvantages, namely the system under investigation has to be perturbed from its normal state by an external signal, which inevitably changes the properties of the system. The DC technique has been widely used for corrosion rate measurement, but the method generally requires a relatively large perturbation (or polarisation) signal and can, in fact, fail when the corrosion measurement required the use of a low conductivity medium. AC methods are finding increasing applications in electrochemical research, because only small perturbation signals (which do not disturb the electrode properties) can be used and low conductivity media can also be investigated [141].

### 4.4.2 Potentiodynamic Polarisation test

Electrochemical experiments were carried out in order to determine the susceptibility of the duplex stainless steels 2205 to pitting corrosion in 3.5 wt% NaCl (pH=6.5), the value of

the pitting potential (Ep) was the most important parameter to be determined from potentiodynamic experiments. Its value was used to determine the level of anodic polarisation applied during the scanning droplet cell technique.

An acrylic cylinder with a cross sectional area of approximately $5cm^2$ was clamped to the specimen, gaining an effective surface area of $5cm^2$ as shown in Figure 4.5. The electrolyte was 3.5 wt% NaCl prepared with de-ionised water. A saturated calomel reference electrode (SCE) and Platinum counter electrode were used along with the duplex stainless steel 2205 specimen (working electrode) in a conventional 3-electrode test cell arrangement. Electrochemical tests were performed using a computer controlled Potentiostat (EG&G).

The electrolyte was at ambient temperature and the pH was 6.5. During the tests the electrochemical cell was open to the atmosphere. Samples were changed after each of the potentiodynamic tests and the cell was filled with fresh solution. Electrochemical tests included potentiodynamic polarisation at potentials more negative and more positive than the corrosion potential were conducted to evaluate the cathodic and anodic behaviour of the material. Potentiodynamic polarisation was commenced from a potential 250 mV below $E_{corr}$ at a scan rate of 0.166 mV/sec, in the anodic direction. Polarisation was continued until breakdown of passivity occurred. The measuring frequency of the applied potential and the induced current was one second in the potentiodynamic polarisation experiments. For the evaluation of the pitting potential 4 tests were carried out.

**Figure 4.5:** An acrylic cylindrical with three-electrode cell used in the potentiodynamic polarisation

tests.

## 4.4.3 Scanning Droplet Cell

The Scanning Droplet Cell (SDC) is shown schematically in Figure 4.6. An electrolyte droplet is dispensed and positioned on the surface passing through a plastic capillary. The wetted circular area of the surface forms the working electrode (WE). The capillary contains a miniature reference (RE) of Ag/AgCl and a platinum counter electrode (CE). The diameter of the capillary is 1mm. The contact angle between the capillary and specimen is 90° which allows a precise delineation of the wetted area (droplet).
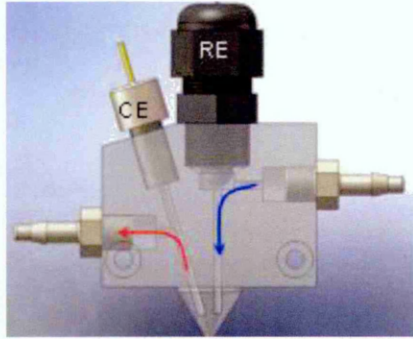
**Figure 4.6:** Schematic view of the scanning droplet cell. (Courtesy UniScan Instruments Ltd)

Measurements were made within the wetted area of the specimen. The electrolyte circulation was controlled through the system using a peristaltic pump. The specimens tested were from 316L SS and 316L SS with a modified passive film achieved using AVPP. The electrolyte used for these experiments was 3.5% NaCl. Electrochemical tests including potentiodynamic polarisation at potentials more negative and more positive than the corrosion potential were conducted to evaluate the cathodic and anodic behaviour of the material. Potentiodynamic polarisation was commenced from a potential 250 mV below the corrosion potential Ecorr at a scan rate of 0.166 mV/sec, in the anodic direction. Polarisation was continued until breakdown of passivity occurred. The measuring frequency of the applied potential and the induced current was one second in the potentiodynamic polarisation experiments. Tests were carried out in order to evaluate the pitting potential and to compare it with the typical potentiodynamic tests.

## 4.4.4 Effects of Flow-Rate on Pitting

In this work the effects of flow rate and surface finish on pitting behaviour were investigated using the scanning droplet cell (SDC). This technique was chosen as it has been demonstrated to be a useful tool for the investigation of localised corrosion

providing quantitative information regarding electrochemical processes [142, 143, 144, 145]. The electrochemical tests were conducted under different flow rates ranging from 10 to 90 $mm^3/s$ using % wt 3.5 NaCl at room temperature and potentiostatic control 1V vs. Ag/AgCl for 1hr. The electrolyte circulation was controlled through the system using a peristaltic pump. Measurements were taken under different flow rates. The resulting current was then used to obtain the material removed during dissolution using Faraday's law. Results of these calculations were compared with the measurement of pit volume using the IFM.

## 4.4.5 Effect of Surface Finish on Pitting

The present investigation is an attempt to quantify the effects of surface finish parameters on the localised corrosion behaviour of 316L SS. The specimens are prepared with three different roughness values namely Ra = 0.68, 1.89 and 3.56 μm. They were mechanically polished using silicon carbide paper with 800 and 1200 grits to produce Ra 3.56 and 1.89 surface finish respectively. Water cooling was used during polishing to prevent overheating of the specimens. In order to produce 0.68 Ra surface finish samples were further polished using 6μm then 1μm diamond paste. Electrochemical tests were conducted using SDC technique applying 1V vs. Ag/AgCL voltage for 1hr. Current was recorded during the potentiostatic polarisation time. The resulting current was then used to obtain the material removed during dissolution using Faraday's law. Results of these calculations were compared with the measurement of pit volume using the IFM.

## 4.4.6 Effects of Applied Stress on Pitting

The objective of the use of the potentiostatic polarisation test in the present work was to quantify the degree of localised electrochemical activity involved in the nucleation of corrosion pits in terms of current. In order to determine localised current directly from potentiostatic measurements the SDC technique was used. Prior to testing, the samples were polished to 1200 grit in cold water. The potentiostatic polarisation tests were performed using the Scanning Droplet System and a tensile fatigue rig set up used shown in Figure 4.7. In this study, uniaxial tensile stress was applied simultaneously with potentiostatic polarisation in order to evaluate the kinetics of localized corrosion at a fixed potential, 1V vs. Ag/AgCl, over a 1 hr period. Current was recorded during the holding time. The resulting current was then used to obtain the material removed during dissolution using Faraday's law. Results of these calculations were compared with the measurement of pit volume using the IFM.



Reference electrode
Electrolyte outlet
Electrolyte inlet

Capillary tip

Video camera

Specimen fitted
in the fatigue-rig
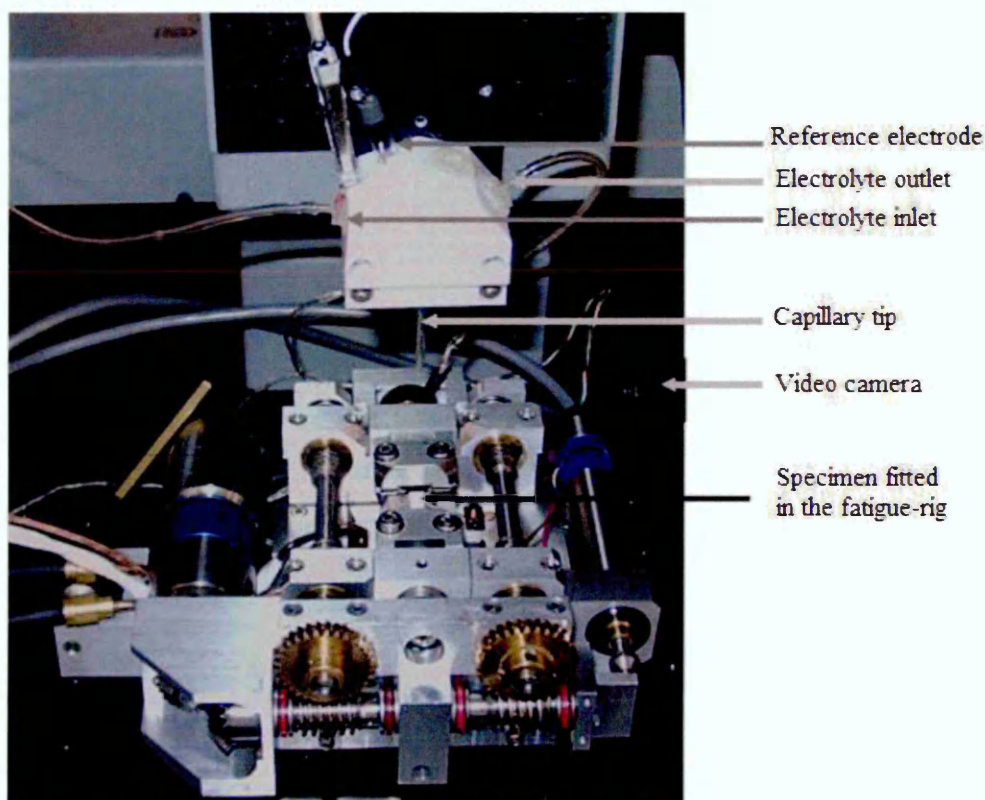
**Figure 4.7**: Stress rig and scanning droplet cell set up system.

## 4.4.7 Pit Geometry Measurement

Volume (V), area (A) and roughness (Ra) analysis were performed using the Alicona[TM] IFM to obtain the profiles of the corroded material surface. The volume obtained from these measurements was converted to weight loss W by considering the material density ($\rho$).

$$W = \rho V \qquad \text{Eq (4.4)}$$

## 4.4.8 Pits Growth Law

A wide variety of pit growth laws has been reported [14, 94] for different metal-electrolyte systems, however these laws based on typical corrosion cell where generation of many pits are expected. The objective of this part of the experimental work was to generate corrosion pits using SDC and IFM to obtain the pit growth law. Pits were generated on 316LSS samples in 3.5 wt% NaCl at pH 6.5 and room temperature. The depth of the generated pits was measured using IFM. The sample surface was wet ground to 1200 grit finish and then polished to 1 $\mu$m using diamond paste. Samples were polarised at different periods typically, at 30, 60, 90,...,360 min. Pits were generated by controlling the applied anodic potential at value around the pitting potential namely 0.5V. It was possible to generate pits of different depths as were reported in the literature [84, 146, 147].

### 4.4.9 Linear Voltammetry

Linear voltammetry was used to characterize the 316L SS surfaces prior to and after the modification by the AVPP. The study makes it possible to compare the current peaks and the corresponding electrochemical processes taking place on the material investigated as well as the influence of the potential scan rate. These tests were applied using a macro-sized sample ($2cm^2$) with a typical three electrode cell for 316L and 316L-AVPP-treated samples at room temperature at different scan rate (from 0.005 to 0.1 V/s). A series of linear sweep voltammograms were recorded at different scan rates within an electrolyte solution of 3.5% NaCl, pH 6.

The linear voltammograms for the stainless steels were also recorded using micro-sized samples in scanning droplet cell SDC. The linear voltammograms were recorded at different scan rates in the potential range from 0.005 to 0.1 V/s.

### 4.4.10 Electrochemical Impedance Spectroscopy

Electrochemical impedance spectroscopy (EIS) uses a range of low magnitude polarizing voltages, much like linear polarisation. However, EIS uses a voltage cycle from peak anodic to cathodic magnitudes (and vice versa) using a spectrum of alternating current (AC) voltage frequencies [148].

If a potential is applied across an electrochemical cell, a current is caused to flow through the cell, with a value determined by the processes taking place at the electrode. If the applied potential is sinusoidal ($\Delta E \sin(\omega t)$) then the subsequent current will also be sinusoidal, with a value ($\Delta I \sin(\omega t+\Phi)$) as shown in Figure 4.8 where $\Phi$ is the phase angle.
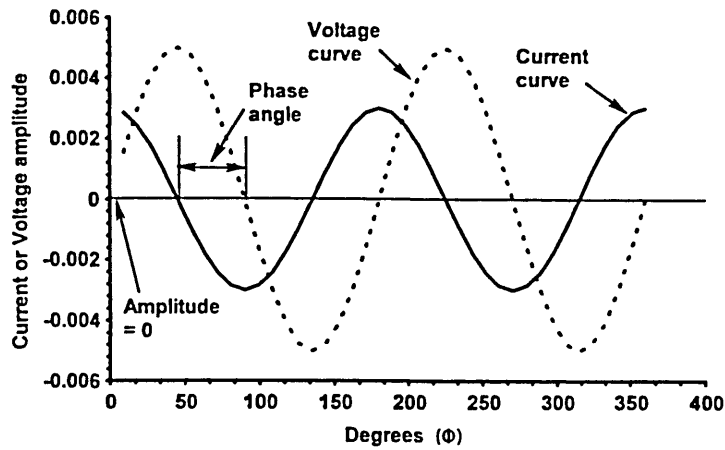
**Figure 4.8:** AC voltage-current phase angle [148].

The relationship between the applied potential and the current flow is known as the impedance. The impedance can be expressed in two ways;

1) Cartesian co-ordinates (Nyquist plot):

| | | |
|---|---|---|
| Impedance: | $Z = a - jb$ | Eq (4.5) |
| Resistive component of impedance: | $a = r \cos \theta$ | Eq (4.6) |
| Capacitive component of impedance: | $b = r \sin \theta$ | Eq (4.7) |

2) Polar co-ordinates (Bode plot):

| | | |
|---|---|---|
| Modulus of impedance: | $r = |Z| = \sqrt{(a^2 + b^2)}$ | Eq (4.8) |
| Phase angle: | $\theta = \tan^{-1} (-b/a)$ | Eq (4.9) |

Resistance and capacitance values are obtained at each frequency, and these quantities can provide information on corrosion behaviour and rates, diffusion, and film properties. Capacitive and resistance properties of an electrified interface produce time constants. Time constants produce a) semicircles in Nyquist plots b), inflections in Bode phase diagrams, and c) negative values for Bode magnitude plot slopes. There are a number of

factors and processes that can produce multiple time constants on the same test electrode [141].
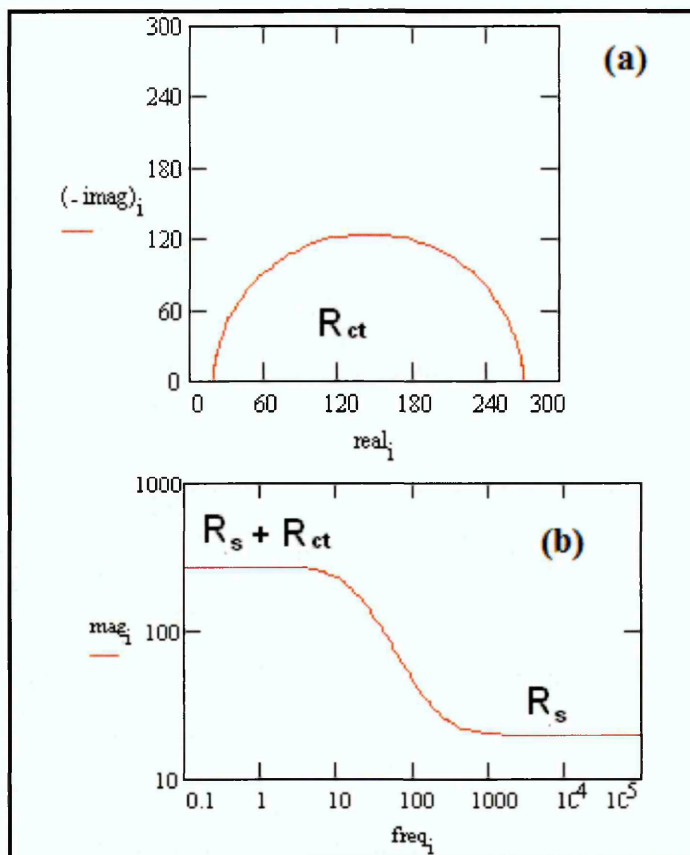


**Figure 4.9:** Nyquist plot (a) and Bode plot (b) of metal [149]

Every metal immersed in a solution has an electrical Double Layer (DL) interface with the solution. The corresponding electrical circuit of a DL consists of: solution resistance ($R_s$), charge transfer resistance ($R_{ct}$) and DL capacitive reactance ($C_{dl}$) as shown in Figure 4.10.
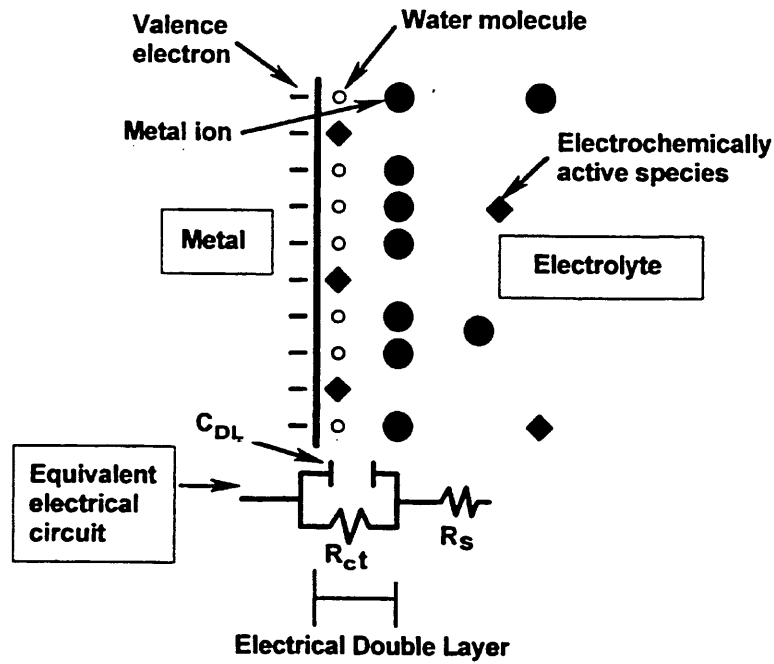
**Figure 4.10:** Electrical double layer and its equivalent circuit [148]

This circuit would be represented by one semi-circle on the Nyquist plot and its radius represents the charge transfer resistance as shown in Figure 4.9a. Bode plot, where a single time constant and two resistances represent the metal as shown in Figure 4.9b.

## 4.5 Residual Stress Measurements using X-ray Diffraction Technique

### 4.5.1. Introduction

The XRD technique is used, prior to fatigue testing and after every 1k cycles up to 10k cycles, to measure the residual stress status on the surface of tensile fatigue test samples. The critical area where the maximum stress is expected is shown in Figure 4.11. Samples prior to testing were ground to 1200 grit and then polished to 1μm using diamond paste. Before every scan samples were cleaned thoroughly with acetone.
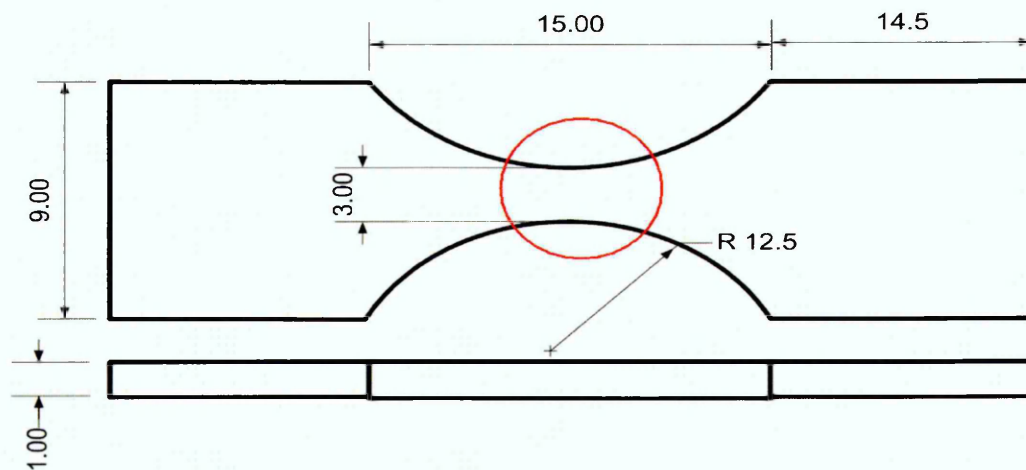


**Figure 4.11**: Dimensions of tensile fatigue sample, the circle represents the area of the specimen where residual stress measurements take place (dimensions in mm).

### 4.5.2 Samples dimensions and preparation

Figure 4.11 represents dimensions of tensile fatigue sample which was used in this study, for fatigue and residual stress measurements. Samples were ground using water-cooled silicon carbide papers of 600, 800 and 1200grit size. Then samples were polished in two steps, starting with rough polishing with 6μm diamond abrasive paste followed by a second polish step using 1μm.

### 4.5.3 Miniature Fatigue Rig

Figure 4.7 shows the miniature tensile fatigue rig used in this study. This miniature rig can fit inside scanning electron microscope and capable of performing uniaxial tensile, compression and bending fatigue tests. The MTW906S material testing system is provided from ADMET Inc. to control experiments and collect data. This package provides an interface to set system test parameters and analyze data. Results are provided in real time and stress-strain curves generated while tests are in progress. Some other parameters such as peak load/stress, offset yield, modulus of elasticity and other measurements are also reported.

### 4.5.4 Fatigue tests settings

Two samples of 316L SS with a native oxide film and two others with modified oxide film by AVPP were used for residual stress measurements after fatigue cycle loading. Two maximum stresses value were used, 250MPa and 350MPa. The stress ratio R was 0.1 and test frequency $f$ 0.2Hz. The residual stress of the samples were measured using XRD prior to the oxide film modification introduction and after. Samples were subjected to cycling loading for intervals of 1k cycles for XRD measurements. Cycling was stopped after every 1k cycles to perform XRD measurements up to 10k cycles where it was found that all samples became compressive residual stress free.

### 4.5.5 Summary of Fatigue Test Procedure

Figure 4.12 shows a test setup window for the miniature fatigue rig menu. The steps for setting the fatigue test condition can be summarised as following:

**Step 1:** Selection of the TEST SETUP button from the Live Screen Toolbar.

**Step 2:** The DISPLAY Tab allow the selection of the engineering and time units plus test/sample information.
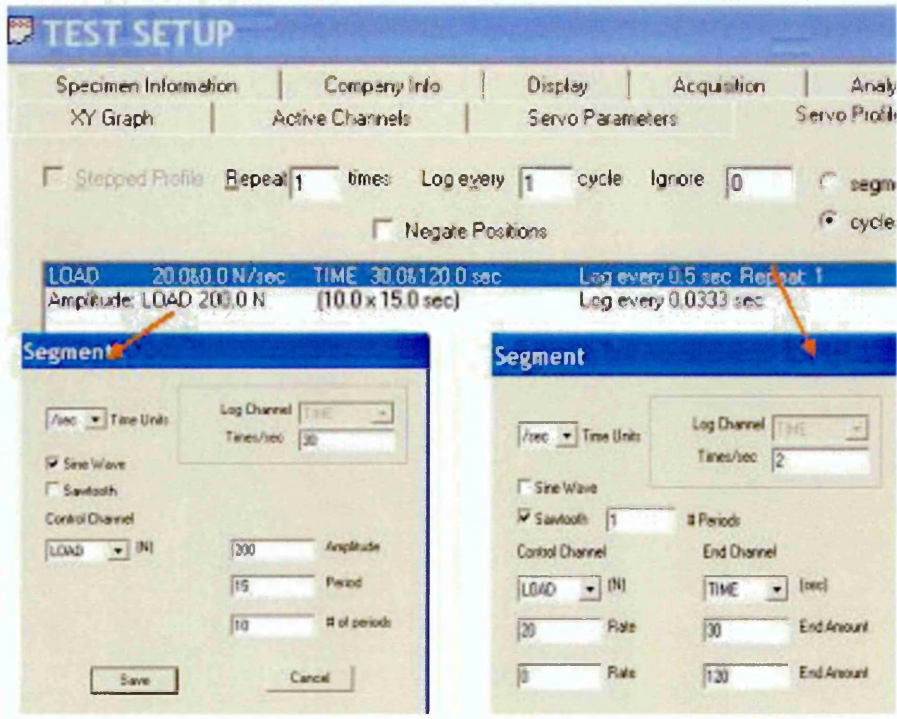
**Figure 4.12:** Miniature fatigue rig software test setup menu.

**Step 3:** The ACQUISITION Tab for input the start test Threshold (should be greater than Preload value, if Servo is active), end of test Sample Break and desired Log Rate(s). To zero all displacements at threshold, place a checkmark next to Zero Displacements @ Threshold.

**Step 4:** The ACTIVE CHANNELS Tab to select which channels to turn on. Also to select the active transducer for each active channel and it's Rate Units.

**Step 5:** The ANALYSIS Tab to select the desired analyses for the test procedure.

**Step 6:** The COMPANY INFO Tab and input the information which will appear above all reports and XY Plots.

**Step 7:** The SPECIMEN INFORMATION Tab to select the specimen geometry and dimensions.

**Step 8:** The XY GRAPH Tab to define the axes type and scaling for the live graph.

**Step 9:** The SERVO PARAMETERS Tab to input the Preload Amount and Rate, also to input the Home Rate and the Post Test Action.

**Step 10:** The SERVO PROFILE Tab to define the desired control profile.

### 4.5.6. X-ray Diffraction Apparatus

The Philips *PW3040 X'Pert Pro* XRD apparatus shown in Figure 4.13 with *X'Pert Stress* software housed in the Materials Engineering Research Institute, was used for stress measurement. The apparatus is subjected to periodic calibration to test the movement of the goniometer, measuring position with rotation, coincidence of the beam at the centre of rotation, and other important hardware settings. A Copper X-ray tube was used, since copper tube gives more depth of penetration compared to *Cr, Fe* and *Co* tubes, which do not exceed $10\mu m$. Philips *X-Celerator* type detector was used, which is most suitable for shorter wave lengths, texture measurements and rapid data collection.
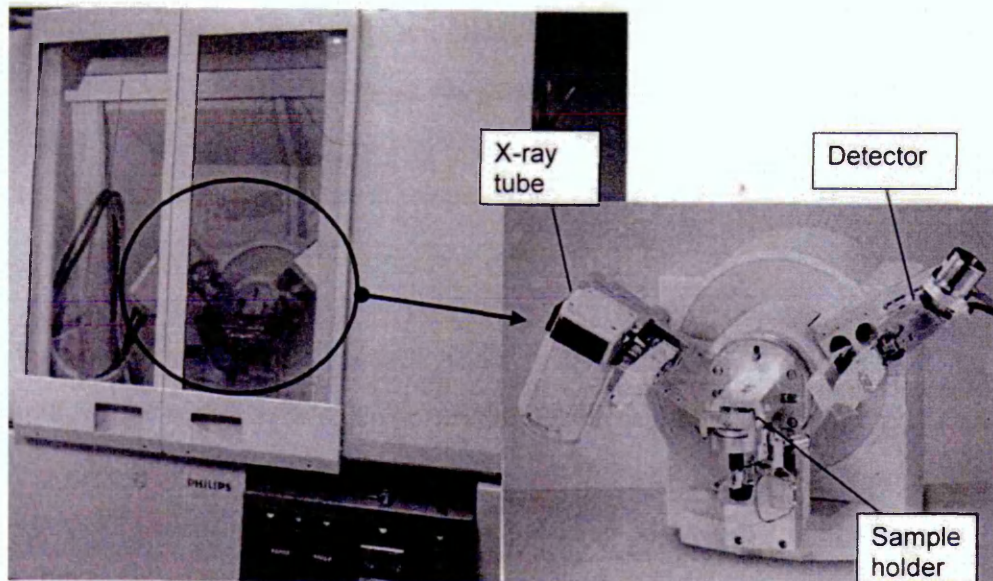


**Figure 4.13:** Philips PW3040 X'Pert Pro XRD apparatus.

### 4.5.7 Hardware Parameters Used for Stress Analysis

The uniaxial $\sin^2\Psi$ method was used for stress analysis. To find the most appropriate $2\theta$, a full scan was conducted over $180°$. The recommended angle is $\geq 140°$ and the lattice plane ($hkl$) (331) [150]. However after complete scan it was identified that for 316L implant grade alloy, the corresponding peak is slightly shifted to around $146.7°$. Therefore the $2\theta$ scan was adjusted to start from $146.3°$ to $147.2°$ in order to cover the peak at $146.7°$. To reduce the uncertainty within residual stress measurements and to improve the accuracy of the fit, 9$\Psi$ measurements were utilized for measurements where the $\Psi$ tilts were chosen to give equal $\sin^2\Psi$ steps. A $\sin^2\Psi$ range of 0.5 was used; the recommended range is 0-0.6. The main hardware parameters used for XRD measurements can be listed in Table 4.2.

**Table 4.2:** Hardware settings used with X'pert XRD apparatus for stress measurements.

| Parameter | Setting |
|---|---|
| Diffractometer type | X'PERT PRO |
| Detector type | X'Celerator |
| Anode material | Copper K-alpha |
| Scan axis | 2 theta-Omega |
| Tilt axis | Omega |
| Tilt range | Positive and negative |
| Divergence slit | 5 |
| Masks | 1/2 |
| Monochromator usage | yes |
| Generator voltage | *40kV* |
| Tube current | *40mA* |
| Pre set counts | 10000 |
| Scan axis | gonio |
| Data angle range ($2\theta$) | 146 to 147.3° |
| Maximum $\Psi$ | 45° |
| Maximum $\sin^2\Psi$ | 0.5 |
| No. of $\Psi$ steps | 9 |
| No. of scans | 9 |
| Step size | 0.040 |
| Scan type/mode | continuous |
| Time per step | 28sec |
| Scan speed | 0.02°/sec. |
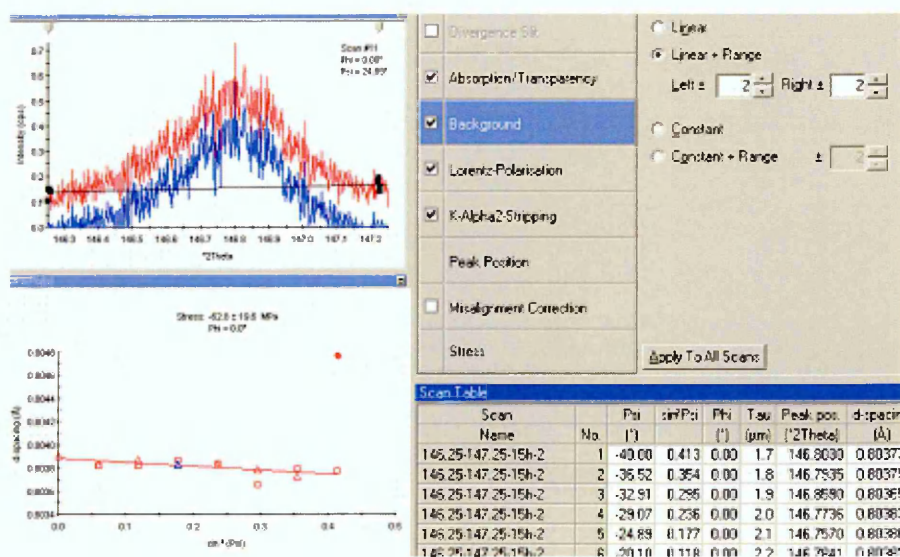


**Figure 4.14:** The operating window of *X'pert stress* analysis software with parameters.

### 4.5.8 Stress Analysis Software

Brief descriptions of the settings involved under each software parameter are given below.

*Absorption/ Transparency*

Diffracted intensities are influenced by absorption, which is directly related to path length of the incident and diffracted beams traverse in the specimen for a given geometry [151]. The results were corrected according to the information depth and position correction. Linear absorption coefficient for 316L SS was calculated as 2025.57 $cm^{-1}$ [152].

*Background adjustment*

This function is used to subtract unnecessary background intensity from a measurement. The background was adjusted by default, but fine adjustments needed to be carried out in order to obtain more accurate stress values. The graphical representation of peaks is shown in scan peak representation area shown in Figure 4.14 and the scan peak is displayed by the top graph and corrected peak by bottom graph. The background was adjusted accordingly to optimise the results.

*Lorentz polarization (L-P) factor*

Lorentz-polarization factor is an important experimental quantity that control X-ray intensity with respect to diffraction angle. Its evaluation is essential to any analysis that depends on the intensities of X-ray diffraction maxima. Practical examples of such applications include three features:

1) number of grains which are oriented in order to give $2\theta$ diffraction,

2) diffraction intensity per unit length,

3) Relationship of diffraction intensity to one crystallite on $2\theta$, which define the L-P factor. For the adjustment of the L-P factor a weak texture and large structural broadening were selected

and the default value of monochromator factor was used.

*K-Alpha2 stripping*

This parameter eliminates that part of the data originating from the K-Alpha2 wavelength induced from the X-ray tube. As a result the overlap problems are eliminated before calculating the peak position and this simplify the stress analysis. This filter is specific to the tube anode. When selected, the K-alpha 2 stripping parameter the software consists of default setting to perform the filterisation related to radiation from copper tube.

*Peak position correction*

This function allows selection of the most appropriate fitting method to determine the position of the peak. Correct identification of the peak position from the curve is important. The software offers the option of selecting the most suitable method out of nine methods. Considering the accuracy and consistency, the most appropriate method for stress analysis is the *Pearson VII* method and this was selected for stress measurements.

### 4.5.9 Optimising Scan Duration

To reduce the uncertainty within residual stress measurements and to improve the goodness of fit, rather than the statistical quality of the diffraction peaks, the most suitable method is to increase the number of $\Psi$ measurement tilts rather than the scan time within each peak. However the scan time of the peak also needs to be optimized to obtain an accurate stress measurement. A total number of nine $\Psi$ angles were used. These angles were selected to cover both positive and negative quadrants. Tests were carried out to investigate the optimum time duration in order to obtain a more stable and accurate stress reading. Therefore, 15hrs time was chosen as the suitable scan time.

## 4.5.10   Repeatability Tests

After optimising the scan duration for 15 hrs, the repeatability of XRD measurements was investigated. Measurements were taken at the same location of the sample using identical software and hardware settings as used in all other stress measurements. An example of the results is given in Figure 4.15. The error of repeatability of residual stress measurements is very good since it is about 0.4%.
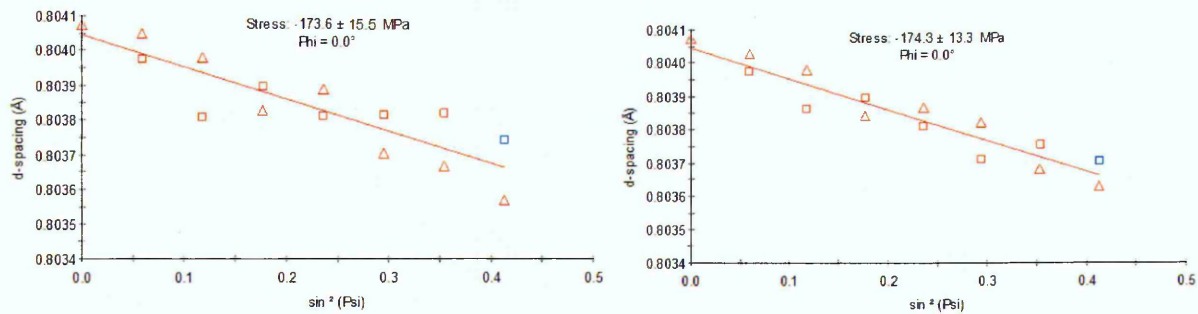


**Figure 4.15**: Example of residual stress results showing the repeatability of the measurements.

## 4.6 Tensile Testing

The tensile test is the most common type of mechanical test which can be carried out on a material in order to obtain its mechanical properties. Tensile tests are multi-purpose in character, in the sense that the results are typically applied in a variety of contexts. For example, the fatigue limit of a material may be related to the ultimate tensile strength [53]. The quantities derived from a tensile test are best considered by reference to the deformation behaviour of a test piece when subjected to a continuously increasing tension load until it breaks. The typical behaviour of the stainless steel, obtained by plotting the increase in length of a reference length of a test piece of a uniform cross-section (strain/ε) against the applied stress, is shown in Figure 4.16.

Shortly after initial yield, narrow bands of plastically deformed material can be seen clearly in contrast with the generally undisturbed surface. These bands extend from one edge of the test piece to the other, inclined at $45°$ to the axis of tension, along the two directions in which the shear stresses have their maximum value.
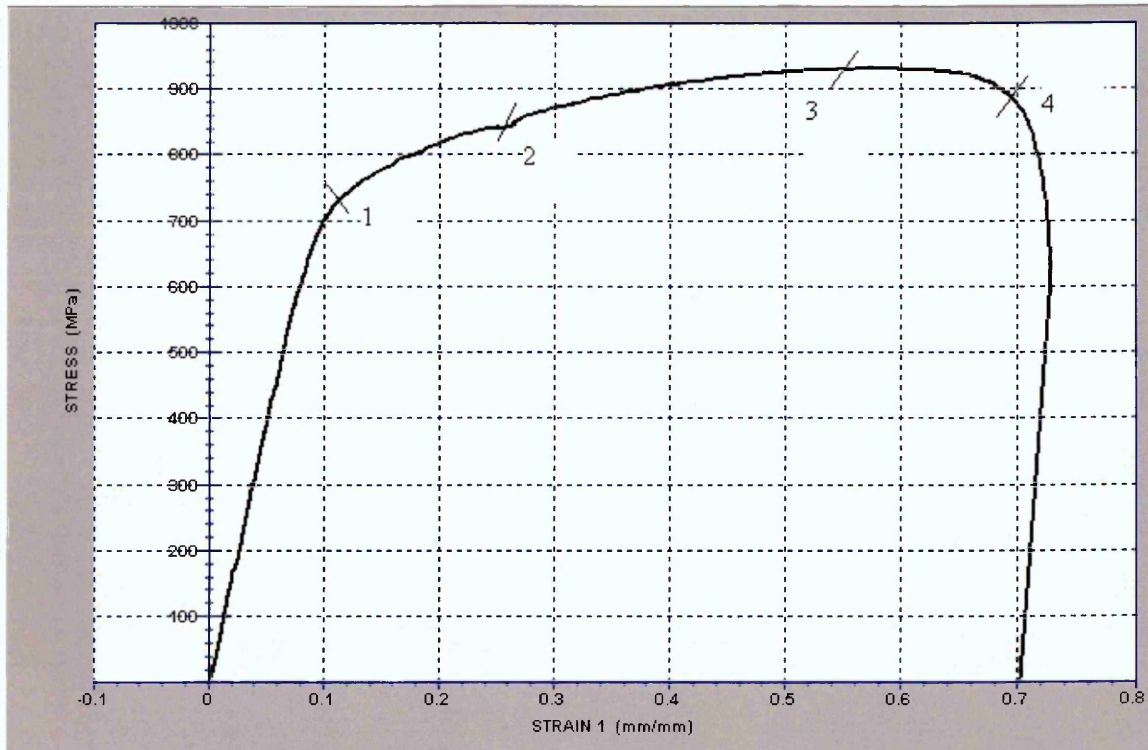


**Figure 4.16:** An example of stress strain curve for DSS 2205.

When yielding is complete (at 2) the load begins to rise again until it reaches a maximum value at 3. After this point load falls off steadily while a more localized elongation takes place in one part of the test specimen, where it is said to "neck". Load continues to fall while necking proceeds, until the reduction in cross-section is appreciable and fracture occurs at a load represented by the point (4).

In the present work, tensile specimens with a flat cross-section have been manufactured having dimensions as shown in Figure 4.11. Testing was carried out using a mechanical stage as shown in figure 4.7. The stage can be used inside the Faraday cage which contains the scanning droplet cell. The maximum applied load of this rig is 4.5KN. The Specimens were machined in order to have a cross-section of $(1 \times 3)$ mm$^2$ and a gauge length of 16 mm. The specimens were designed to be axially stressed in the rolling direction. Tensile tests are performed in this study in order to obtain the mechanical properties of the materials.

## 4.7 Nano-hardness test

The hardness and Young's modulus (E) of the surface films of 316L sample and 316L-treated samples by AVPP were measured using the CSM indentation tester. Samples were ground and polished to a mirror finish. An indenter tip (Berkovich) is driven into the sample normal to the sample surface, by applying an increasing load up to the designated maximum load. The load is then gradually removed until partial or complete relaxation of the material occurs. The applied force and depth are measured dynamically during a load-unload cycle. Hardness and Young's modulus are calculated directly from the resultant force-displacement curve, by the software based on the procedure and equations shown in Figure 4.17 [153]. Three different load values were applied which were 3, 2 and 1mN. In the first test a 3mN load was applied and the resulting load displacement curves for both samples were almost equal. However it was noticed that the indentation depth exceeded the expected thickness of the surface films. Therefore, lower applied loads were applied notably, 2mN and 1mN.
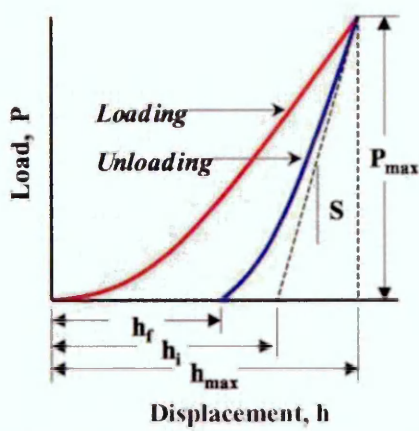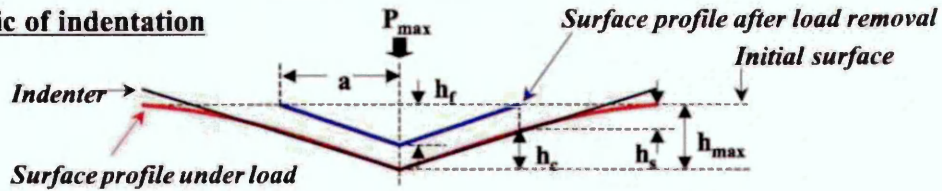
**Figure 4.17:** Nano-hardness instrumented calculations [153].

Where $P_m$ = maximum applied load

ht = depth from the original surface

Ap = projected contact area which is determined from the contact depth, he

S = contact stiffness (tangent to the unloading curve)

$v$ = Poisson ratio of measured material (0.3 was used in the experiment)

## 4.8 Corrosion Fatigue Tests Using SDC

### 4.8.1 Introduction

SDC measurements were conducted on 316L SS and 316L SS treated by AVPP whilst simultaneously being subjected to cycling loading using a servo-hydraulic horizontal stress rig shown in Figure 4.18. These tests were carried out in order to determine the influence of the AVPP on corrosion fatigue life of 316L SS material. One of the main objectives of this project was to utilise the scanning droplet cell simultaneously with a fatigue rig in order to measure the degree of localised corrosion activity via corrosion current measurements involved in the nucleation of cracks from corrosion pits. Three series of tests were performed namely three air fatigue tests on 316L SS samples ; three corrosion fatigue tests on 316L SS and three corrosion fatigue tests on 316L SS treated by AVPP samples.
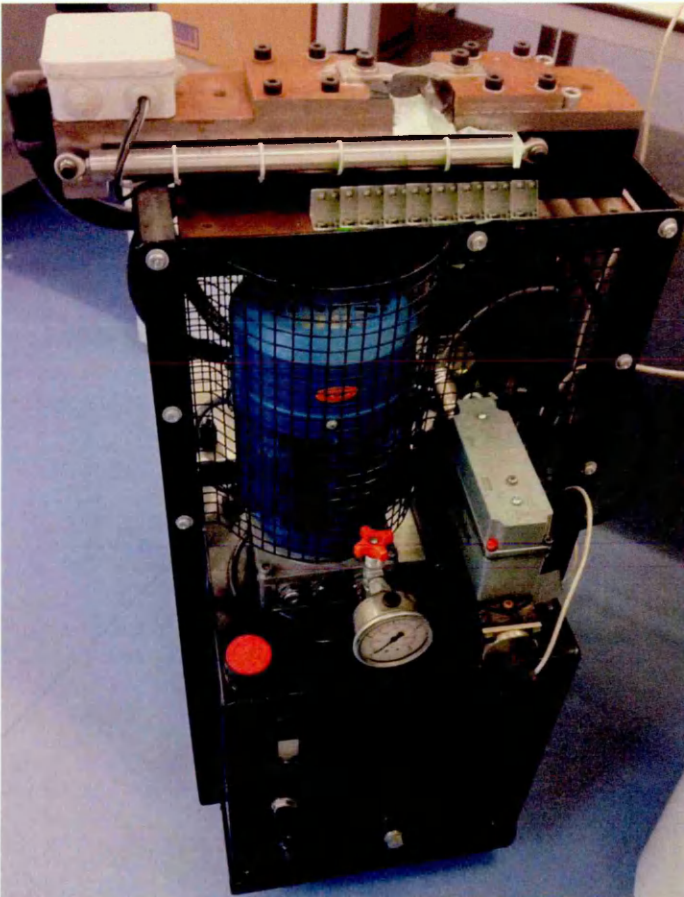


**Figure 4.18** The servo-hydraulic horizontal stress rig used for fatigue testing.

## 4.8.2 Fatigue Samples

Flat test specimens were machined from 316L stainless steel plate with dimensions as shown in Figure 4.19. The axis of the specimen is parallel to the rolling direction of the plate. The gauge area was carefully polished with a series of finer grade emery papers to 1200 grit. Three of the specimens were subjected to AVPP treatment as explained in section 4.1.
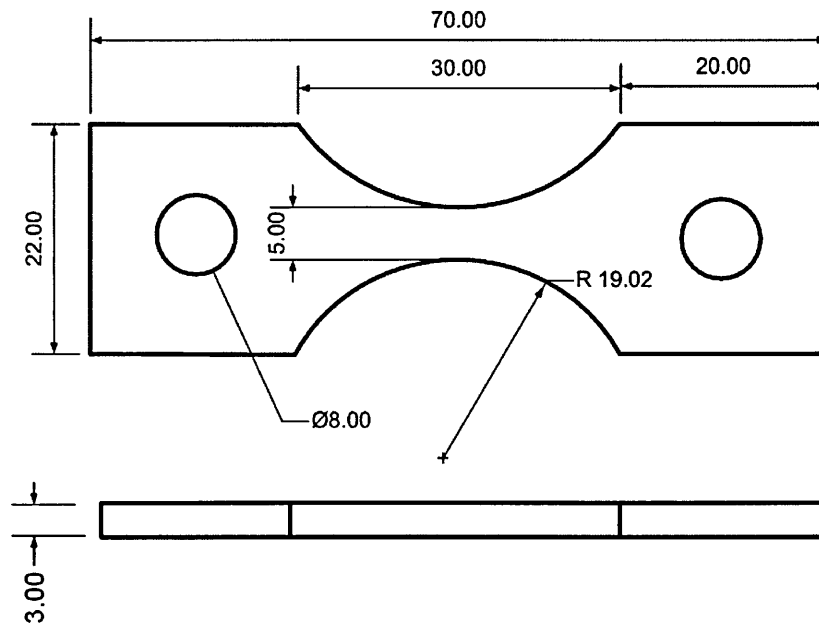


**Figure 4.19:** Fatigue sample dimensions.

## 4.8.3 Testing System Set up

Figure 4.20 shows corrosion fatigue testing system set up which includes the Scanning Droplet Cell (Model 370), the stress rig and their operating accessories. As previously stated the SDC incorporates a technique which confines a liquid in contact with a sample surface in order to measure electrochemical and corrosion reactions over a limited region where the droplet is actually in contact with the sample. This offers the ability to spatially resolve electrochemical activity and to confine it exclusively to a quantifiable area of the sample. The technique previously reported in the scientific literature [154] employs a glass theta capillary to deliver the drop to the surface

however in this set up we have introduced a new PTFE SDC head. The counter and reference electrode are contained within the PTFE capillary block as shown in Figure 4.20 (sec1).
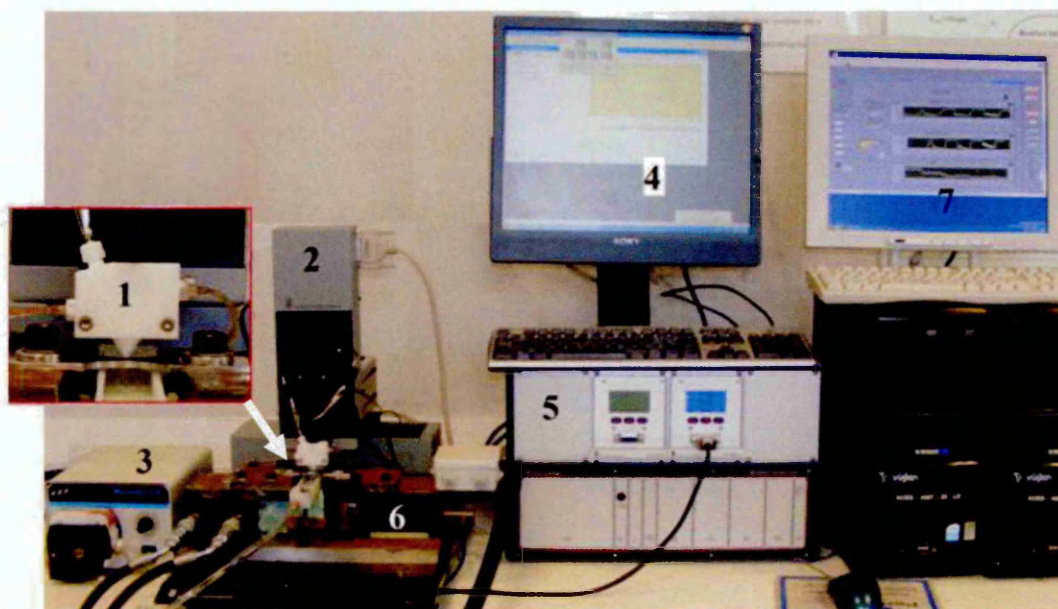


**Figure 4.20:** Corrosion Fatigue System: SDC head (1); positioning system (2); peristaltic pump (3); UniScan M370 software (4); UniScan potentiostat (5); stress rig (6); STRESS software (7).

The Model 370 utilises a fast and precise, closed loop x, y, z positioning system (2) with nanometer resolution, along with a flexible data acquisition system enabling the selection of the configuration most suited to the experiments. The system is designed with flexibility to ensure convenient cell, sample and probe access. The SDC uses a peristaltic pump (3) to deliver precise amounts of electrolyte to the sample surface. The UniScan M370 application and analysis software (4) was used to complete control of the UniScan potentiostat (5) and efficient current-time data processing. The software allows definition of scan parameters (displacement, velocity, step size, number of data points).

The corrosion fatigue testing set up includes also a servo-hydraulic horizontal stress rig (6). This machine was designed particularly to be suitable for corrosion fatigue testing using the SDC. This is because the capillary needs to be vertical on the specimen axis to allow precise steady delineation of the wetted area (droplet). The stress rig is controlled by STRESS TEST software (7) which can be set for static and cyclic loading.

## 4.8.4 Fatigue Machine Commissioning and Calibration

It was necessary to demonstrate the capability of the stress rig to apply a steady pressure into the sample panel. The pressure must be controlled by the servo-hydraulic machine position control facilities. Therefore static tests were used to determine the applied displacement range necessary to achieve a certain pressure range in the panel.

Applying a variety of pressures to the panel ensured the rig could achieve and maintain the required pressures. The applied pressure was monitored using the software provided. The displacement was independently measured using a strain gauge. The stress was calculated from the strain values obtained from a strain indicator.
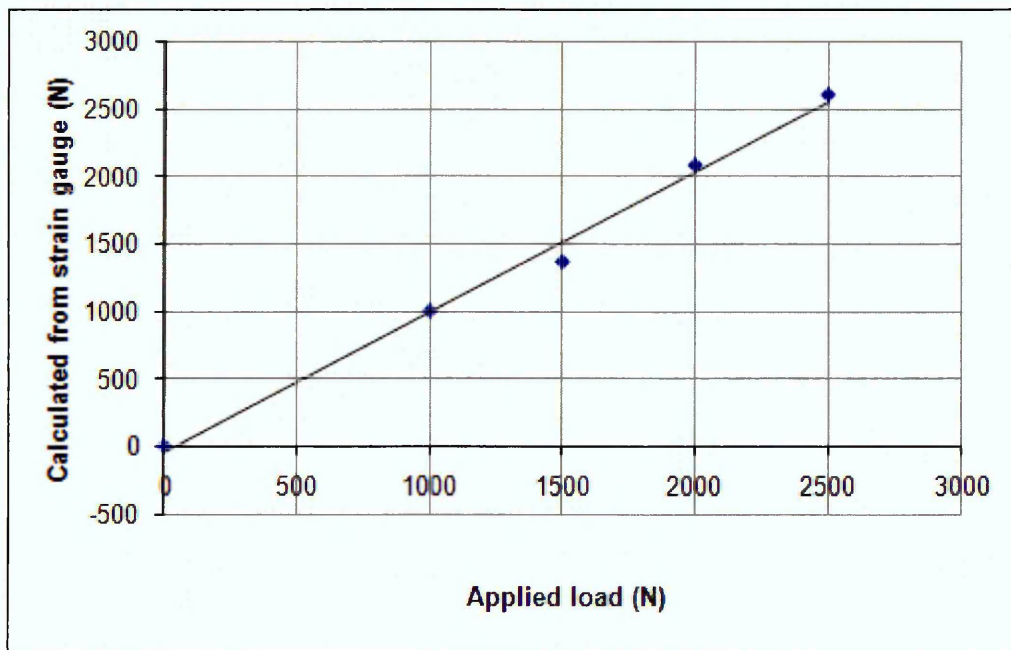


**Figure 4.21:** Applied load vs. measured load from strain gauge for stress rig commissioning.

Two static tests were performed, increasing the maximum applied pressure in each to 50bar. Figure 4.21 plots the applied load, calculated from the applied pressure against the load calculated from the measured strain gauge. This shows that for the two tests the applied load linearly related to the measured load. The plots from the two tests show the same slope demonstrating that the rig is capable of providing a consistent loading and the reliability of the rig for application of accurate loading.

## 4.8.5 Corrosion Fatigue Procedure

Three specimens were subjected to cyclic corrosion fatigue loading using the servo-hydraulic horizontal fatigue testing machine as shown in figure 4.20. The general test conditions were as follows:

The stress ratio, R = minimum stress/maximum stress = 0.1;

frequency, f = 0.5 Hz;

sinusoidal waveform.

The value of stress level is the maximum load at the minimum cross-section $\sigma_{max}$ = 260 MPa. The same stress amplitude was applied in all the fatigue tests.

Three specimens of 316L SS were tested in air to compare the fatigue life with the corrosion fatigue life of 316L SS with and without AVPP treatment in 3.5%NaCl solution at room temperature.

The solution was continuously circulated between the SDC and the tank at a rate of about 20 mm$^3$/s by means of a peristaltic pump. The solution was renewed for each test. Tests were carried out under applied anodic polarisation at the potential of 0.5V vs. AgCl, a scanning droplet cell and a potentiostat (Figure 4.20) were used to control the potential of the specimens. The wetted part of the fatigue specimen is in contact with the

droplet forming the working electrode (WE), the reference electrode is a Silver Chloride Electrode (Ag/AgCl) and an auxiliary electrode (AE) made of Platinum is used to supply the current from the potentiostat. Current-time curves were recorded during the corrosion fatigue tests using the Uniscan potentiostat. Observations of fatigue damage on the specimen surface and measurements of crack length were made via Infinite Focus Microscope at certain intervals during the tests. These intervals occurred at particular number of cycles or when noticing any distinctions in the current-time curve.

# Chapter 5- Results

## 5.1 Alternating Voltage Passivation Process

A number of the samples were subjected to surface-film modification by applying an Alternating Voltage Passivation Process (AVPP). In this process, samples are immersed in a solution containing 0.02 M NaCl, pH 3 at room temperature. A potentiostat is used, operating in three electrode cell mode, with a platinum counter electrode, the sample as the working electrode, and the saturated calomel (SCE) as a reference electrode. Pulses are applied with amplitude ± 0.4V vs. SCE, the pulse-width is 29 ms, and the anodic to cathodic time ratio is 4:1 for 16h. Figure 5.1 shows the current-time curve resulting from one of the AVPP experiments on 316L SS sample.
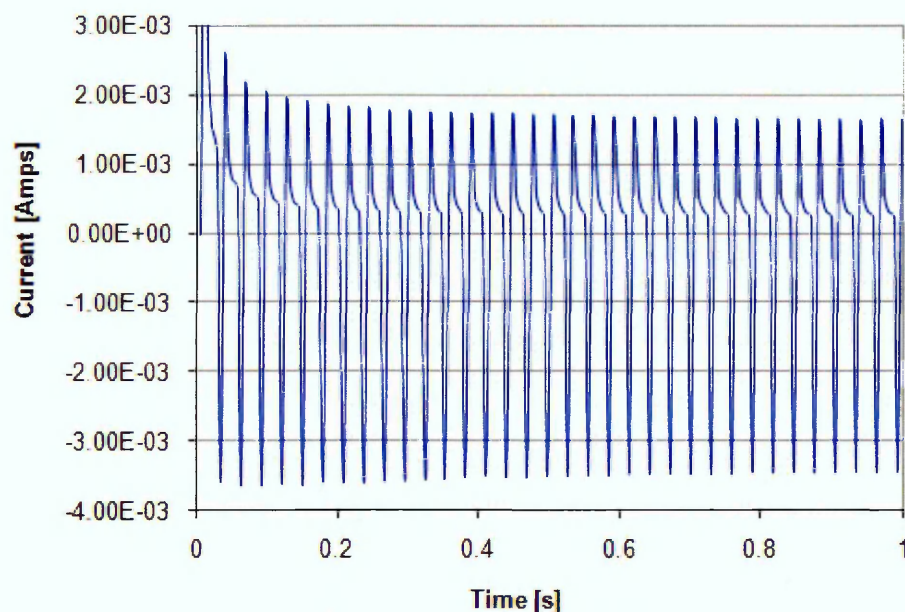


**Figure 5.1:** Current-Time curve results of AVPP (amplitude ± 0.4V vs. SCE, pulse-width = 29 ms, and the anodic to cathodic time-ratio is 4:1 for a total duration of 16h).

The film grows linearly with the elapsed time [155]. At the lower potential which is the active potential region of Fe and Cr. Fe and Cr ions are dissolved in the electrolyte. Then $Cr^{+2}$ ions in the solution adjacent to the surface of the alloy are re-oxidised to

deposit as $Cr^{+3}$ oxide at the upper potential which is the passive region of Cr. The main objective of this study is to determine the influence of AVPP treatment on the native oxide-film electrochemical and mechanical properties as discussed later.

## *5.2 SEM and IFM Characterisation*

In this section the characterisations of the materials used in this research are presented. These include 316L stainless steel, AVPP-treated 316L and 2205 duplex stainless steel. The three surfaces were analysed using an infinite-focus microscope (IFM) and scanning-electron microscope (SEM) including its Energy Dispersive X-ray Spectrometer (EDX). X-ray Photoelectron Spectroscopy (XPS) was used for further investigation of the surface oxide films for the 316L stainless steel with and without film-modification.

### 5.2.1 SEM and IFM for 316L Stainless Steel and AVPP

Figure 5.2 presents optical micrographs from IFM of the microstructure of the 316L before and after AVPP treatment. The microstructures of the two surfaces are presented also in SEM images in Figure 5.3. It is shown that the microstructure of the material containing single phase austenitic (γ) includes grains with average size of 23μm. The electrolytic etching revealed the presence of delta ferrite (δ) distributed in the grain boundaries. In addition to presence of black dots which are inclusions. Investigation of some of these inclusions shows that they are from Al as shown in Figure 5.4. The EDX results from SEM showing the composition of the material-surface are presented in Figure 5.5 and in Table 5.1. Investigations include microstructure features such as grain-size and grain-orientations. The average grain size of 316L SS samples was to be 23 μm. No noticeable changes were detected in the microstructure of the surface after the AVPP. So it was decided to carry out further investigation using XPS.
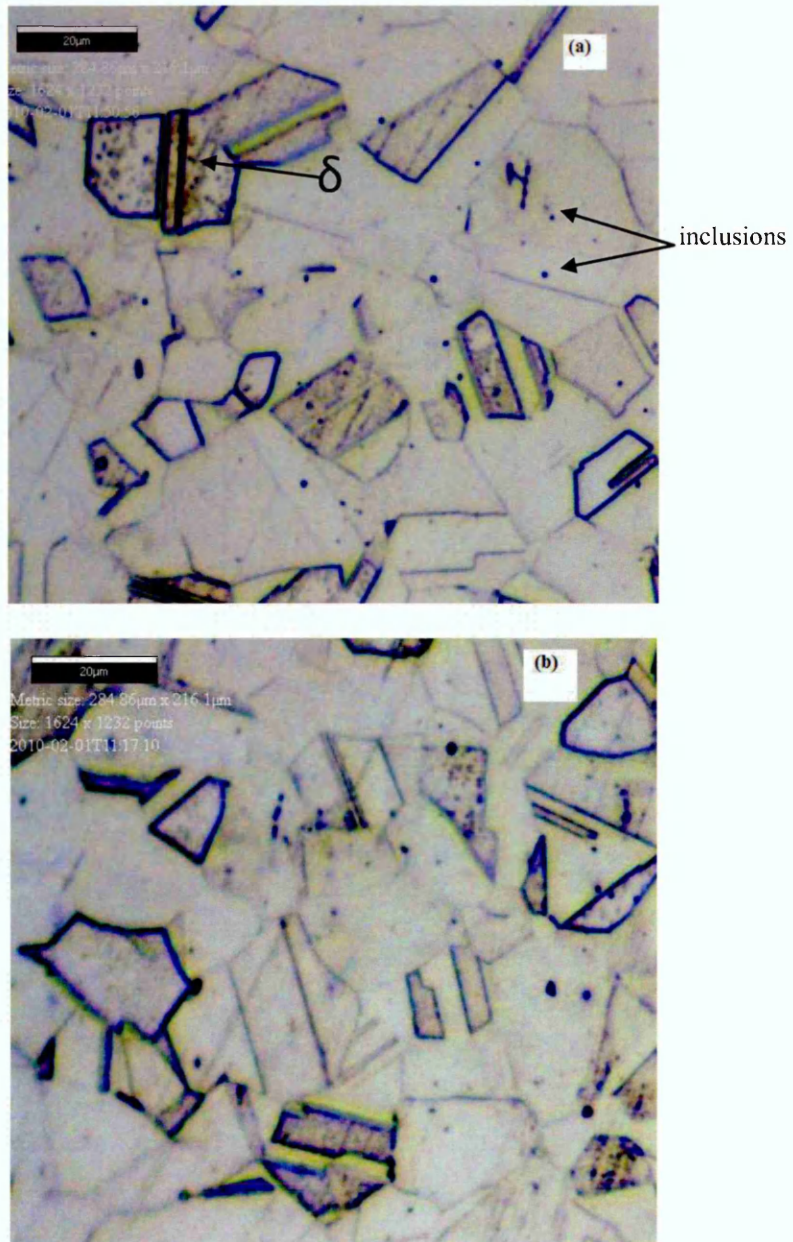
**Figure 5.2:** Microstructure of (a) 316L SS, and (b) 316L-AVPP. The images were provided by optical focus microscope (IFM).
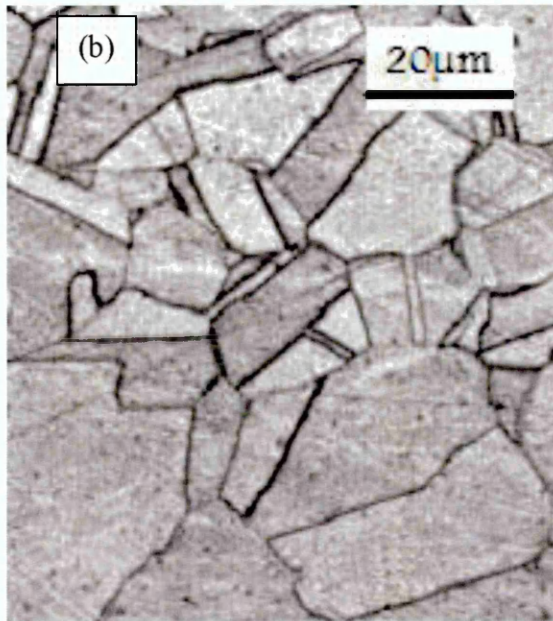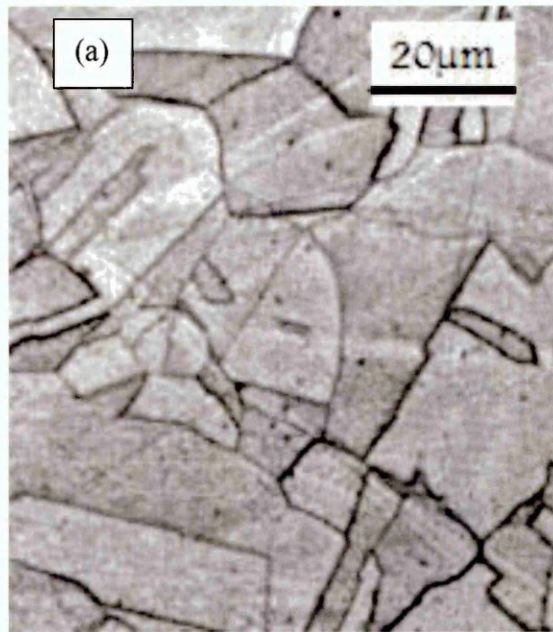
**Figure 5.3:** SEM images showing the microstructure of (a) 316L and (b) AVPP.
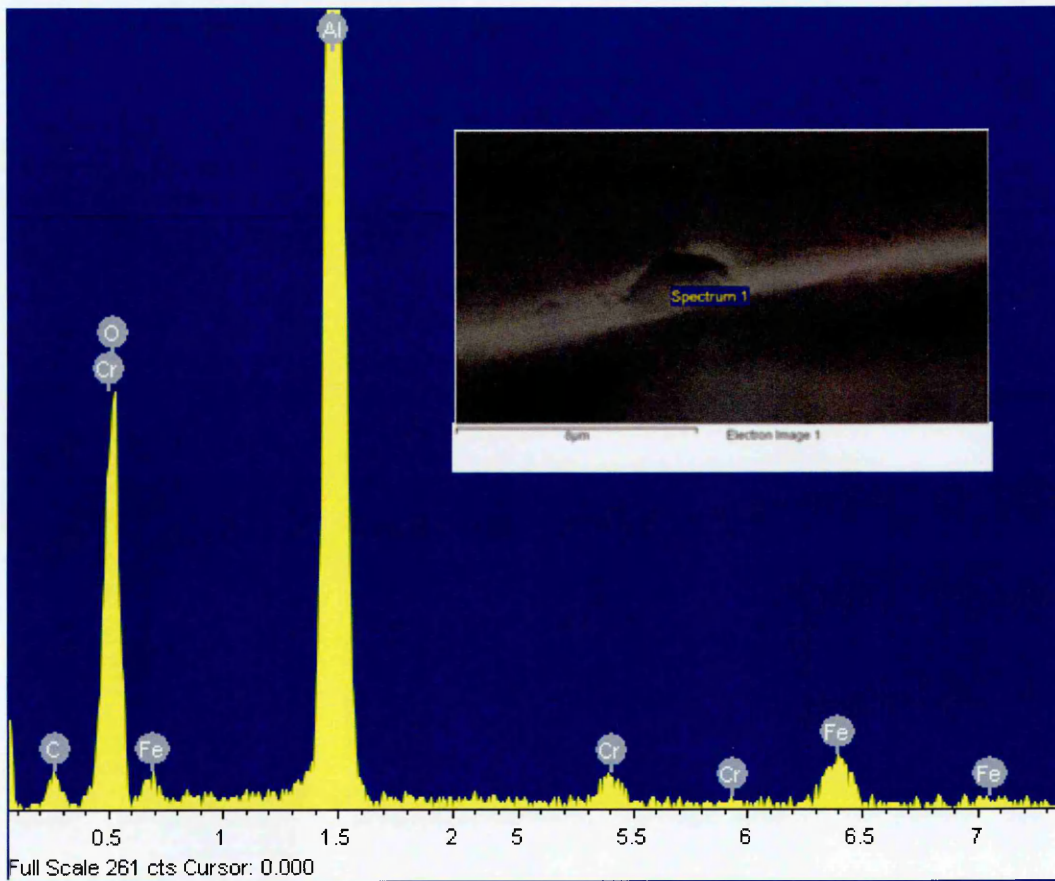
**Figure 5.4:** EDX spectrum of an inclusion on 316L SS surface.
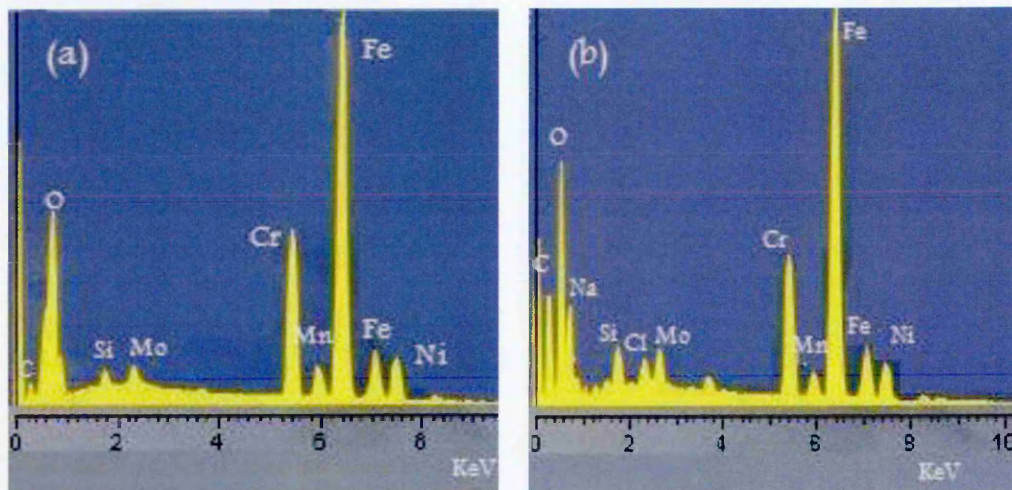


**Figure 5.5:** EDX spectrum of 316L SS (a), AVPP (b).

118

**Table 5.1:** Chemical composition of materials 316L and AVPP resulting from EDX measurements

| Element | Fe | Cr | Ni |
|---|---|---|---|
| 316L AVPP | 66.8 | 24.6 | 6.0 |
| After AVPP | 66.3 | 24.8 | 6.6 |

## 5.2.2 SEM and IFM for 2205 Duplex Stainless Steel

Figure 5.6 and Figure 5.7 show IFM and SEM images of the two-phase microstructure of the duplex stainless steel 2205 revealing approximately equal amounts of austenite and ferrite. The continuous dark phase is the Ferrite ($\alpha$), and the Austenite ($\gamma$) is distributed as lighter islands. The chemical composition of the material- surface were examined using the EDX; results are revealed in Figure 5.8.
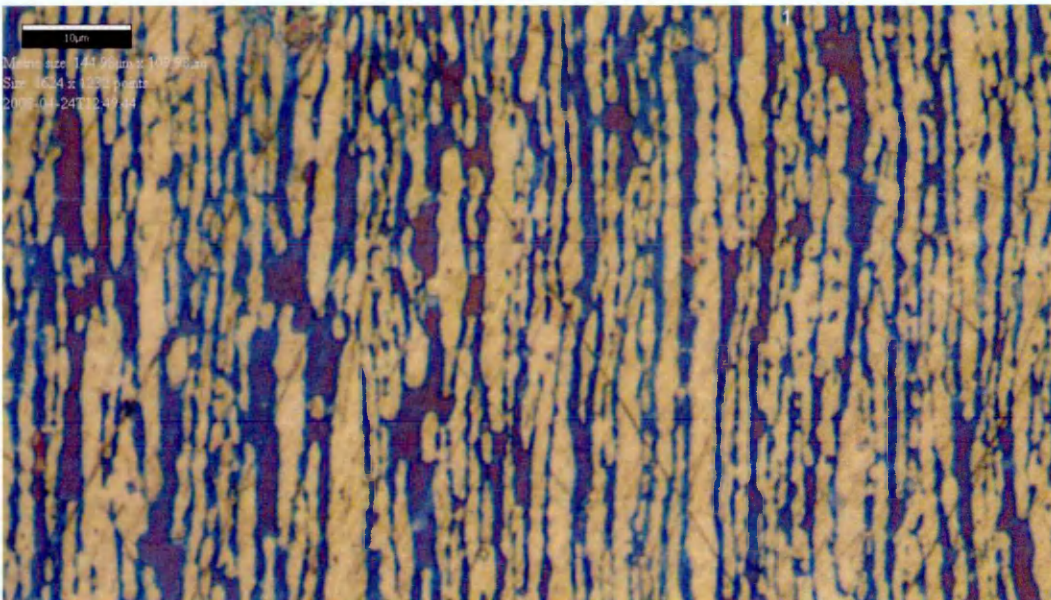


**Figure 5.6:** DSS2205 optical microscope (IFM) image of the longitudinal surface side.
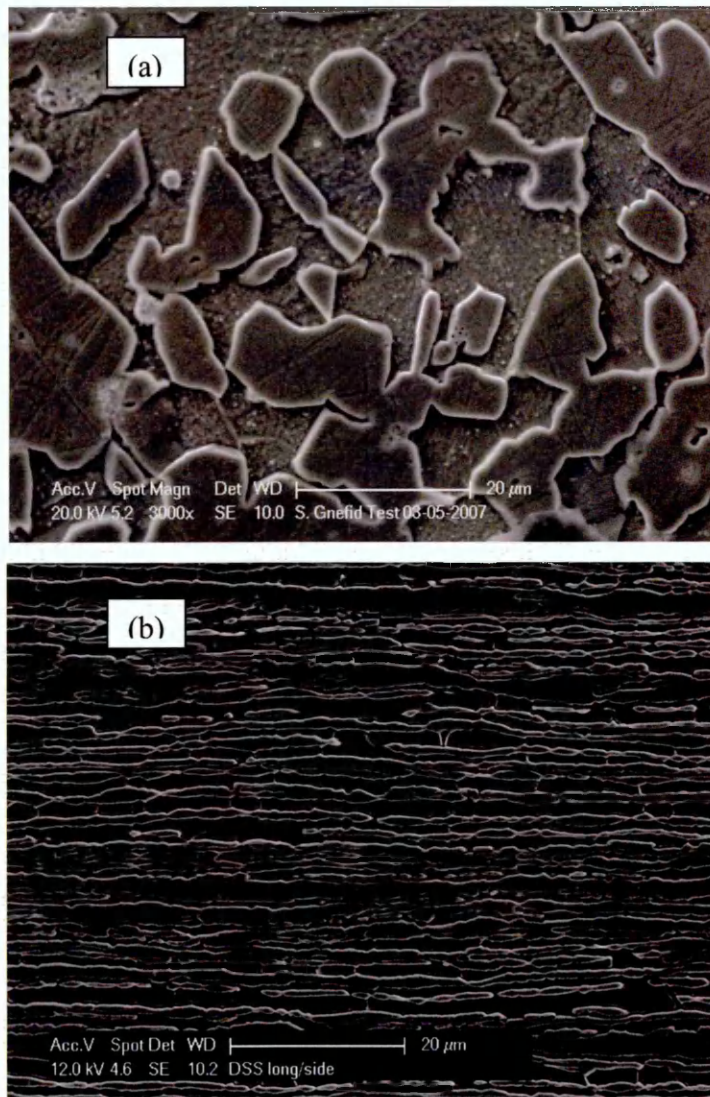
**Figure 5.7:** DSS2205 SEM image of the transverse surface (a) and SEM image of the longitudinal side (b).
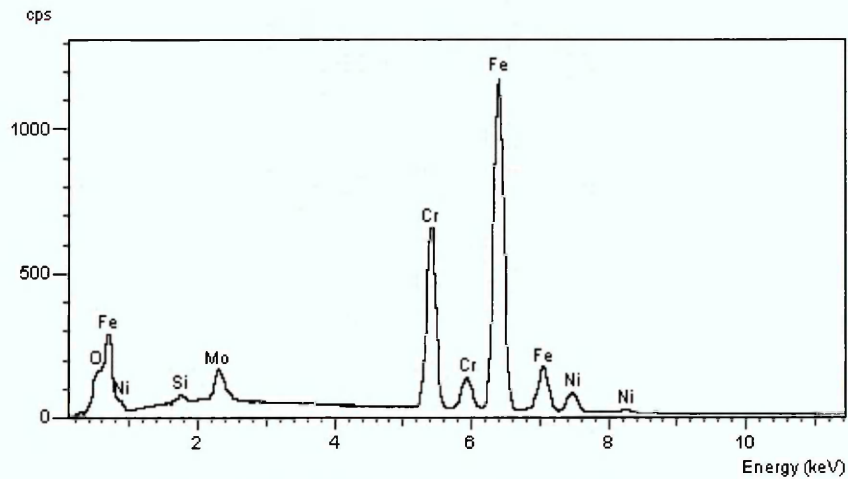


**Figure 5.8:** EDX spectrum of 2205 DSS.

120

## 5.3 XPS analysis

### 5.3.1 The 316L Sample

Survey scans were taken at individual depths. These revealed the presence of Carbon, Oxygen, Iron and Chromium peaks. The graph in Figure 5.9 below shows the survey scans at each depth for the 316L sample.
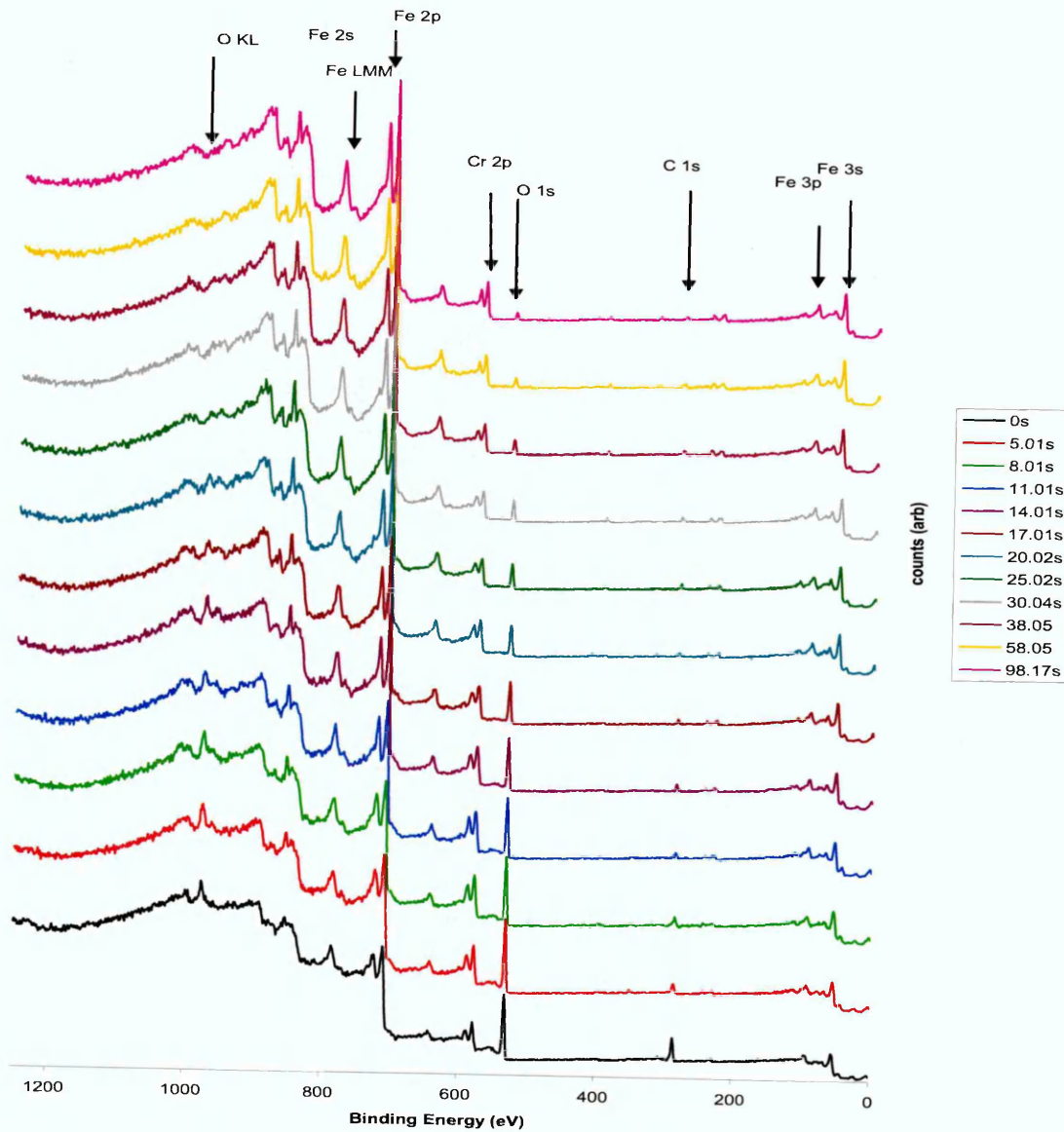


**Figure 5.9:** Survey scan for the 316L sample

These surveys show that the Carbon and Oxygen peaks both diminish with etching-time and the Iron and Chromium peaks increase. The XPS surface-scan did not detect the existence of Ni Oxide in the film. Therefore, detail concerning Ni is not described in this study, although a small amount of Ni Oxide might be incorporated in the film. As well as a survey scan, detailed scans were taken of the Chromium $2p_{3/2}$, Iron $2p_{3/2}$, and Oxygen 1s peaks (these being the strongest peaks for each element), see Figures 10, 11 and 12. Typically, XPS spectra are charge-normalized by shifting the spectra, so it was decided to normalize the spectra to the Fe 2p3 peak corresponding to metallic Iron, as this was a very strong peak at all levels. This was set to be equal to 706.8eV, the average value from 12 examples in the literature. All other peaks were shifted accordingly.
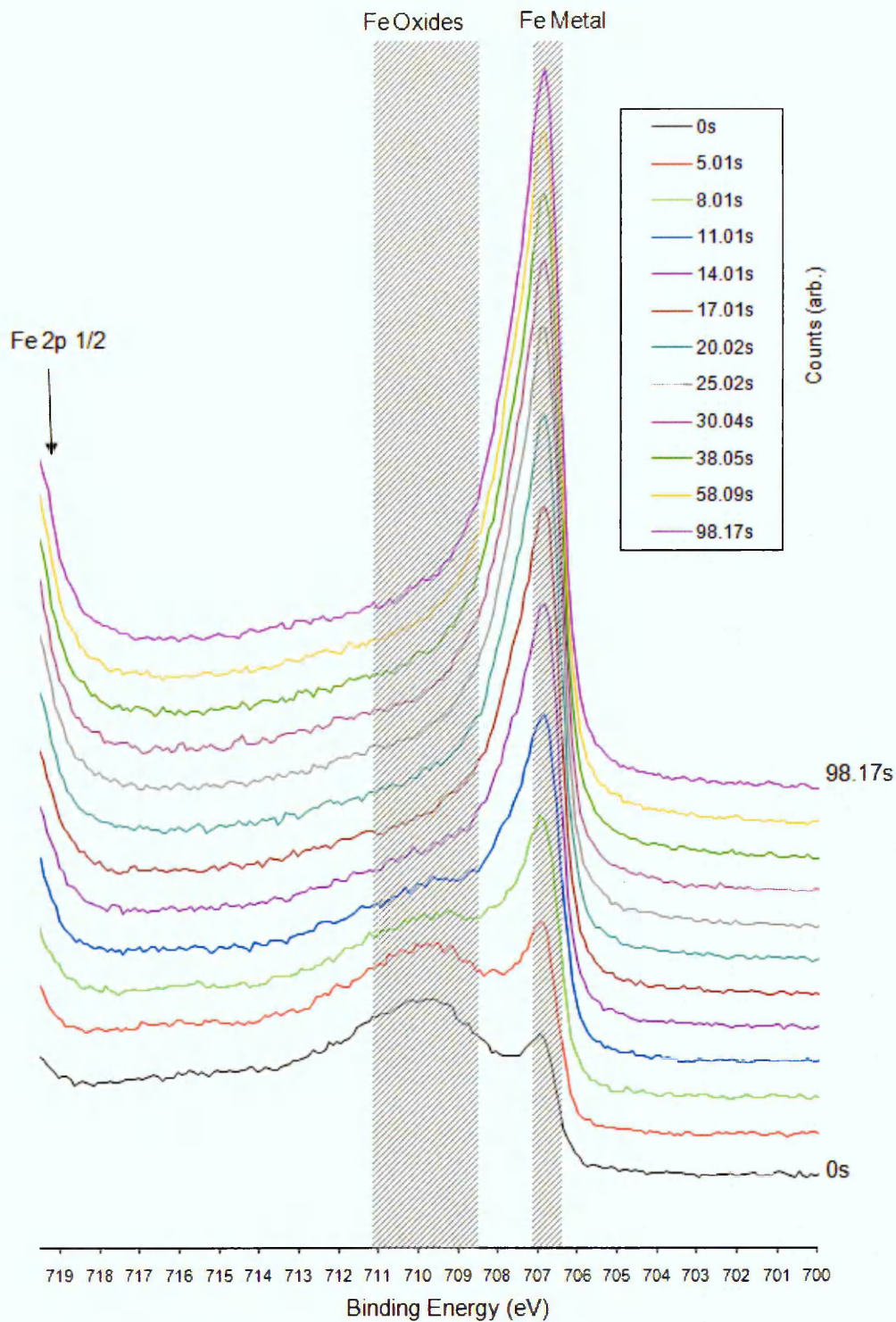
**Figure 5.10**: Depth profile of Fe 2p3 for the 316L sample.

As can be seen from Figure 5.10, the Fe2p3 peak changed dramatically with depth. Close to the surface, the peak consisted of one sharp peak at 706.8 and a broad peak at

about 710. With etching, the broad peak rapidly disappeared, leaving only the sharp peak. These features were indentified with chemical states by looking up energies for various Iron species on an online XPS database [156]. The 2p3 peak in metallic Iron has been reported at energies ranging from 706.4 to 707.1 eV, and Fe 2p3 in Iron Oxide has been reported at energies from 708.5 to 711.1 eV. Superimposing these ranges on the above plot and the origin of both peaks, it becomes clear that the first peak is metallic Iron and the second Iron Oxide. The oxide layer disappears very rapidly, leaving Iron only as the surface is etched. Hence, if we examine at which layer the Iron Oxide disappears completely, which in this case is the 5th layer we can determine the depth of this layer. This was found to be around 3nm according to the estimation of the spallation rate of 0.2nm/s.
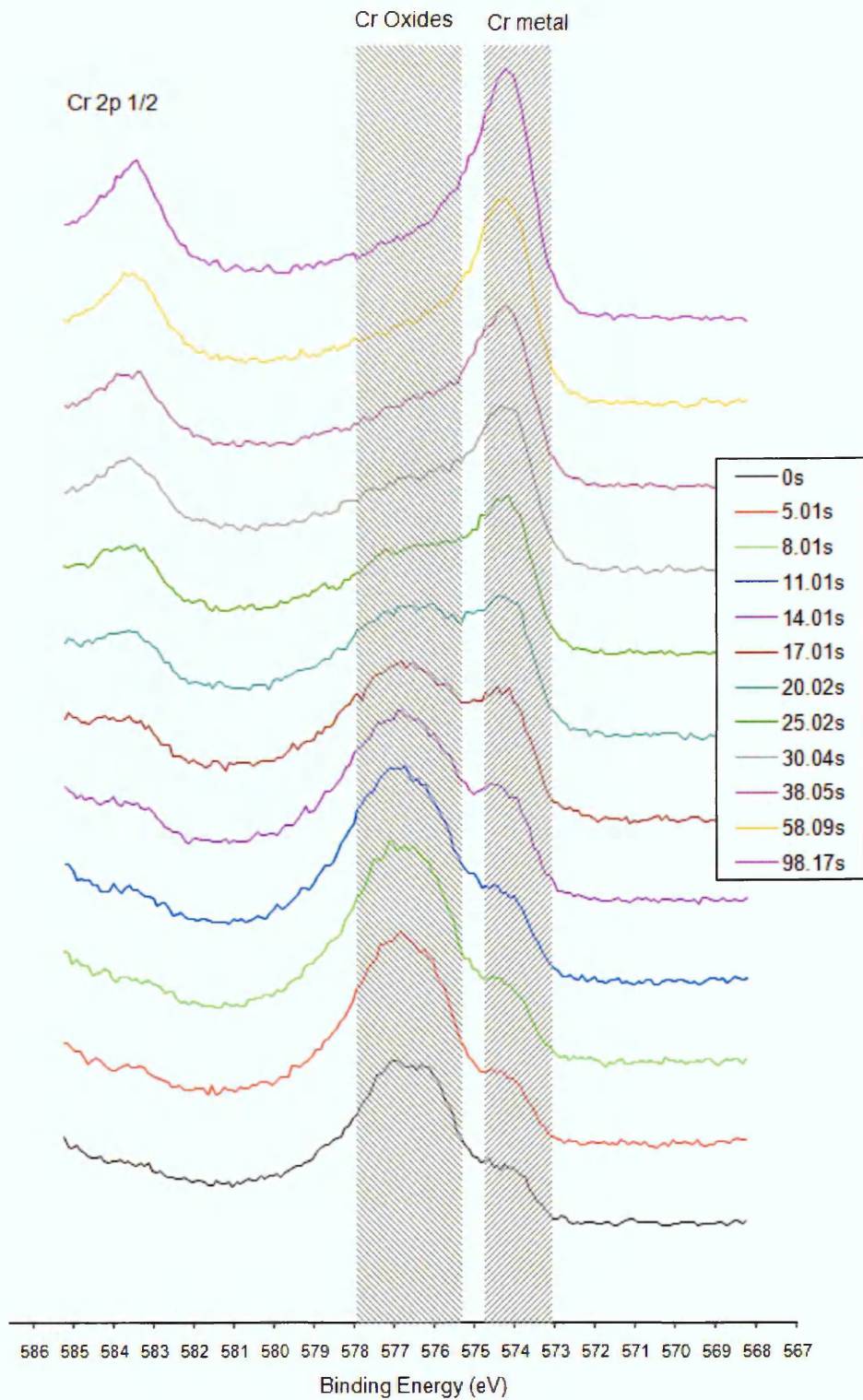
**Figure 5.11:** Depth profile of Cr 2p3 for the 316L.

The Chromium peak also consisted of two components, a narrow peak and a broad peak.

Also like the Fe, the broad peak (Chromium Oxide) disappeared with depth (although it

took much longer to do so hence at greater depth) revealing metallic Chromium. Figure

5.11 presents an overlaying of the reported values for Chromium metal and Oxide.
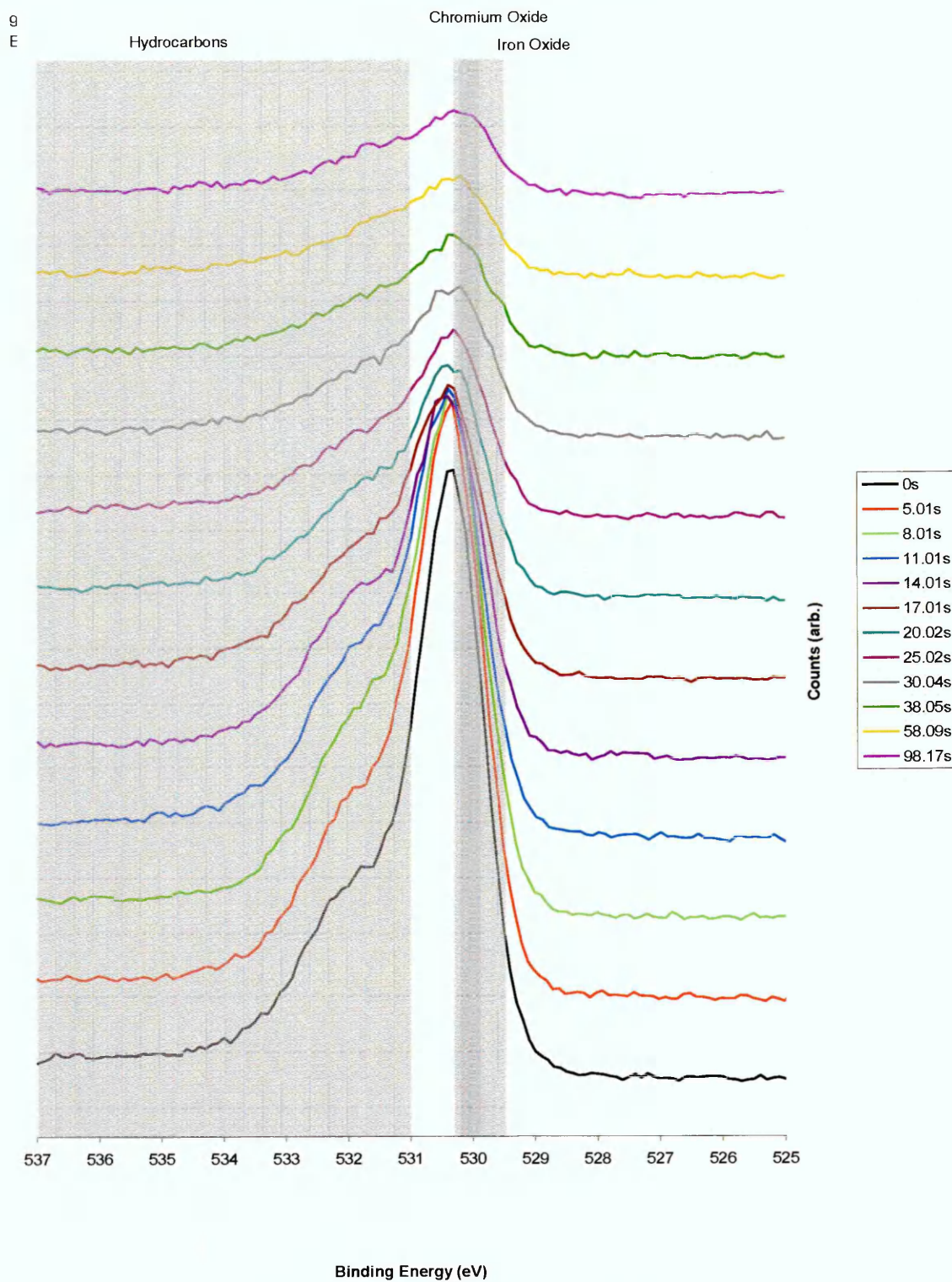


**Figure 5.12:** Depth profiles of O 1s for the 316 L.

The Oxygen peak again decreased with etching-time. It also had two components, one at roughly 530 eV and one at 532 eV. The range of energies for Oxygen associated with hydroCarbons and Oxygen in Iron and Chromium Oxide was overlaid in Figure 5.12. Whilst it is impossible to distinguish between the ranges of Chromium and Iron Oxide overlap, but it is clear that the small shoulder is due to hydrocarbons and the main peak is due to metal oxides.

## 5.3.2 Depth-profile for the 316L Sample

The relative atomic percentages of the elements (Fe, Cr, O, C) could be determined at each layer using the following formula:

$$\mathrm{Re}lAt\% = \frac{\dfrac{A_{Fe2p3}}{RSF_{Fe2p3}}}{\dfrac{A_{O1s}}{RSF_{O1s}} + \dfrac{A_{C1s}}{RSF_{C1s}} + \dfrac{A_{Cr2p3}}{RSF_{Cr2p3}} + \dfrac{A_{Fe2p3}}{RSF_{Fe2p3}}} \qquad \text{(Eq. 5.1)}$$

Where A is the area under the peak and RSF is the Relative Sensitivity Factor, an empirically-derived factor which describes the relative sensitivity of XPS to the different peaks and elements. These relative atomic percentages can then be plotted as a function of etch-time to give a depth-profile. The simplest depth-profile is obtained by taking the areas under all the peaks and comparing them (ignoring the fact that each peak is split into two representing two different species):
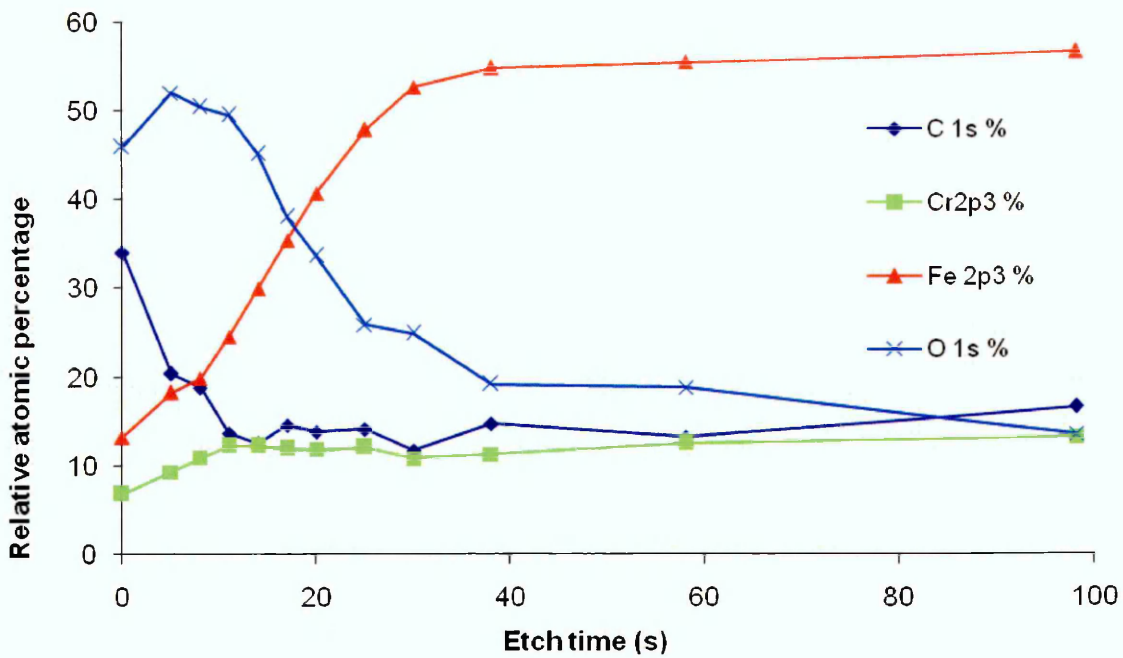
**Figure 5.13:** Depth-profile for the 316L.

Figure 5.13 shows that Carbon and Oxygen decrease as etch-time increases and Chromium and Iron increase. This is as expected. The Iron percentage plateaus at 40s, implying that all the Oxide is gone at this depth. What is curious is that the C and O percentages are not zero at this point. To better understand the structure of the oxide layer, a depth-profile of just the two Iron and two Chromium species can be plotted as shown in Figure 5.14.
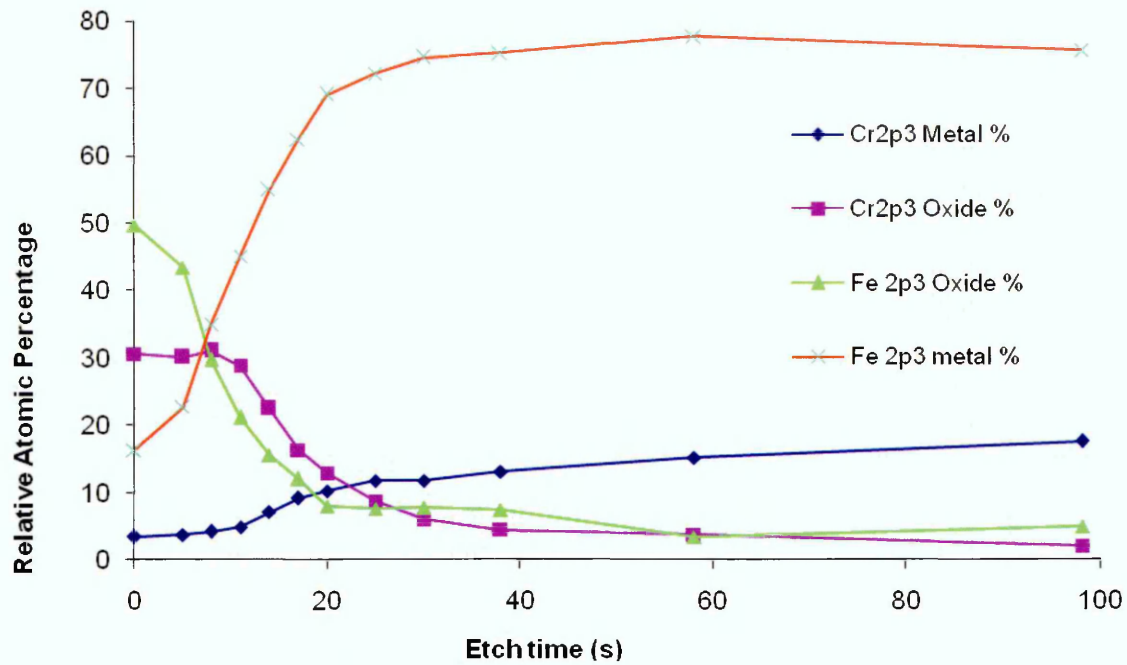
**Figure 5.14:** Iron vs. Chromium for the 316L

This is an interesting observation, as initially the Iron Oxide percentage drops and the Chromium Oxide is unaffected. It is only after about t = 12s that the Chromium Oxide percentage begins to drop. This drops to effectively zero by 40s. This appears to suggest the presence of a multilayer system with a thinner layer of Iron Oxide on top of a thicker layer of Chromium Oxide.

### 5.3.3 AVPP Sample

Figure 5.15 shows a survey-scan of the AVPP sample. This specimen had the same compositions as the 316L sample. Comparing the AVPP survey-scans to the ones for the 316L there appears to be much more Carbon in this sample, probably reflecting additional contamination picked up during the extra processing steps.
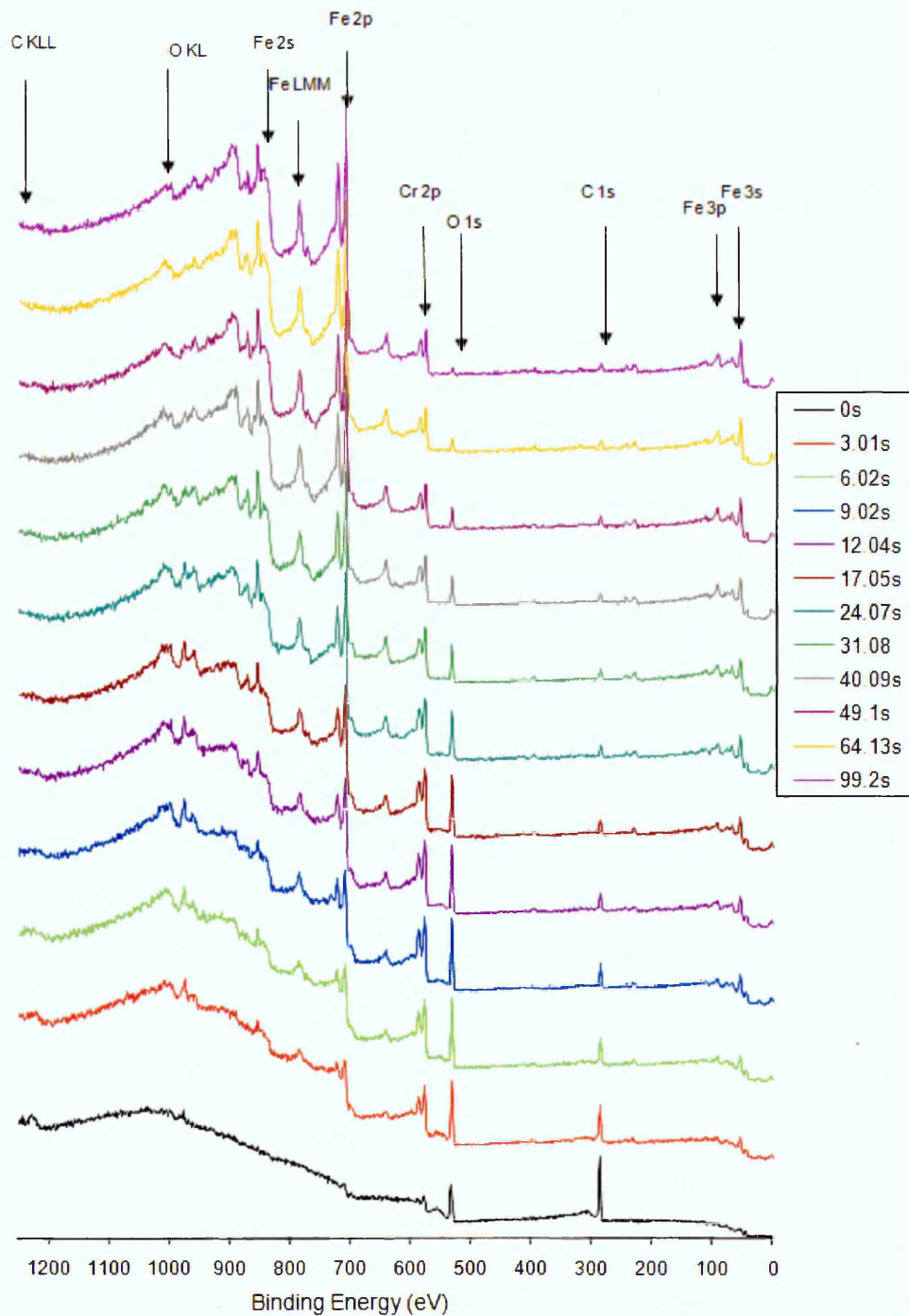
**Figure 5.15:** Survey-scans for the AVPP sample.

The detailed scans in this sample contain the same species as in Sample 316L, namely Iron, Iron Oxide, Chromium, Chromium Oxide, hydrocarbons and metal (probably Iron) carbide. The data is fitted in the same way and the peaks follow the same general trend with etching, so they have not been included in this Chapter.

## 5.3.4 Depth-profile for the AVPP Sample

The depth-profile obtained using the simple peak area approach is shown in Figure 5.16 below:
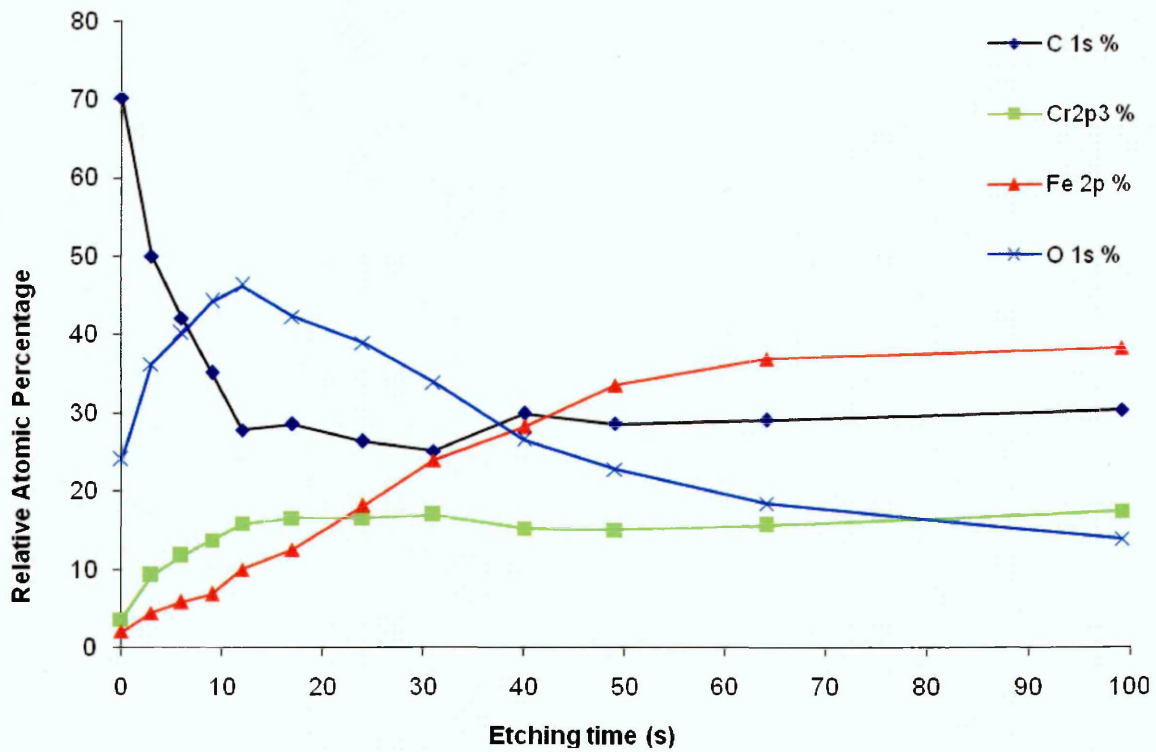


**Figure 5.16:** Depth-profile for the AVPP sample

All the elements follow the same trend as in the 316L sample, with two key differences:

1)    The Fe & Cr take much longer to plateau, about 60-70s instead of 40.

2)    There is a lot more Carbon, even at the deepest level.
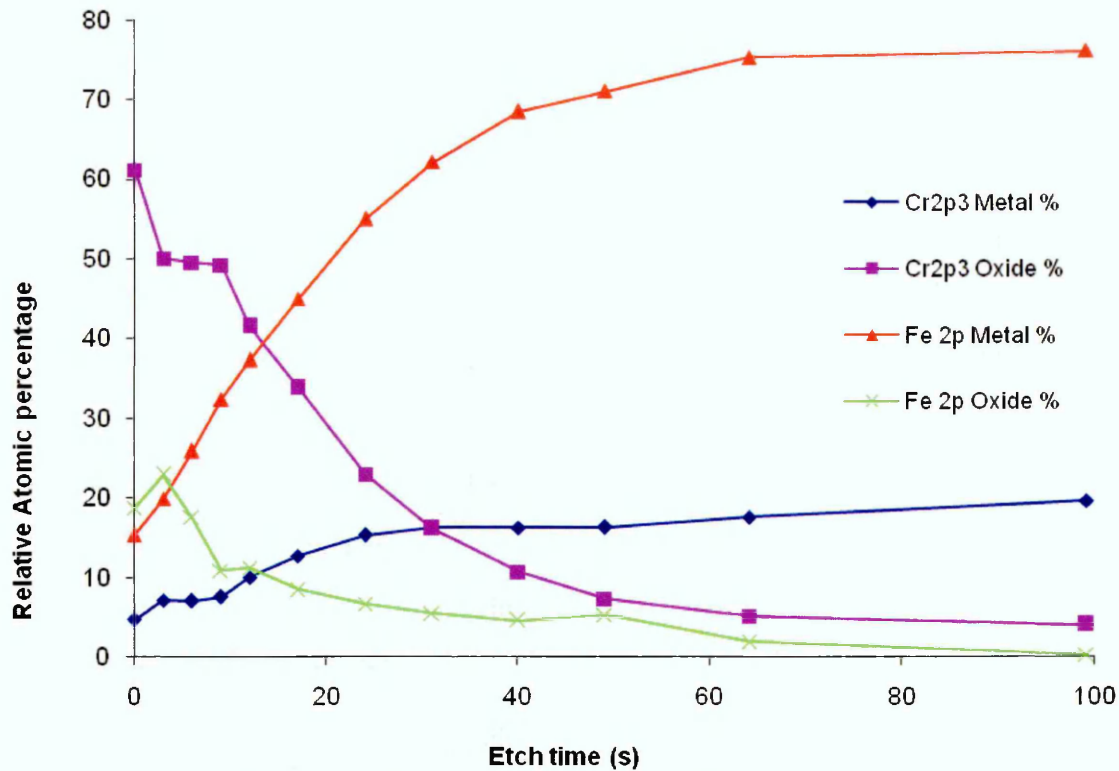
**Figure 5.17:** Iron vs. Chromium for AVPP sample

## 5.3.5 Summary of the XPS analysis

1)      By comparing the Cr vs. Fe depth-profiles for each sample it appears that the Iron Oxide layers are roughly the same thickness. However the Chromium Oxide layer is substantially thicker in the Sample 316L- AVPP (Figure 5.18)

2)      The two samples are chemically identical, as there are no species that have been indentified which exist in the 316 sample but not the 316L- AVPP sample.

3)      The structure of both samples from the surface towards the bulk is; Iron Oxide, Chromium Oxide, metallic Fe and Cr.

4)      A rough estimate is that the Chromium Oxide layer is 50% thicker in the sample 316L- AVPP than the 316L.

5)      Hydrocarbon contamination is present at all levels of both samples; however it is substantially worse in the 316L AVPP.
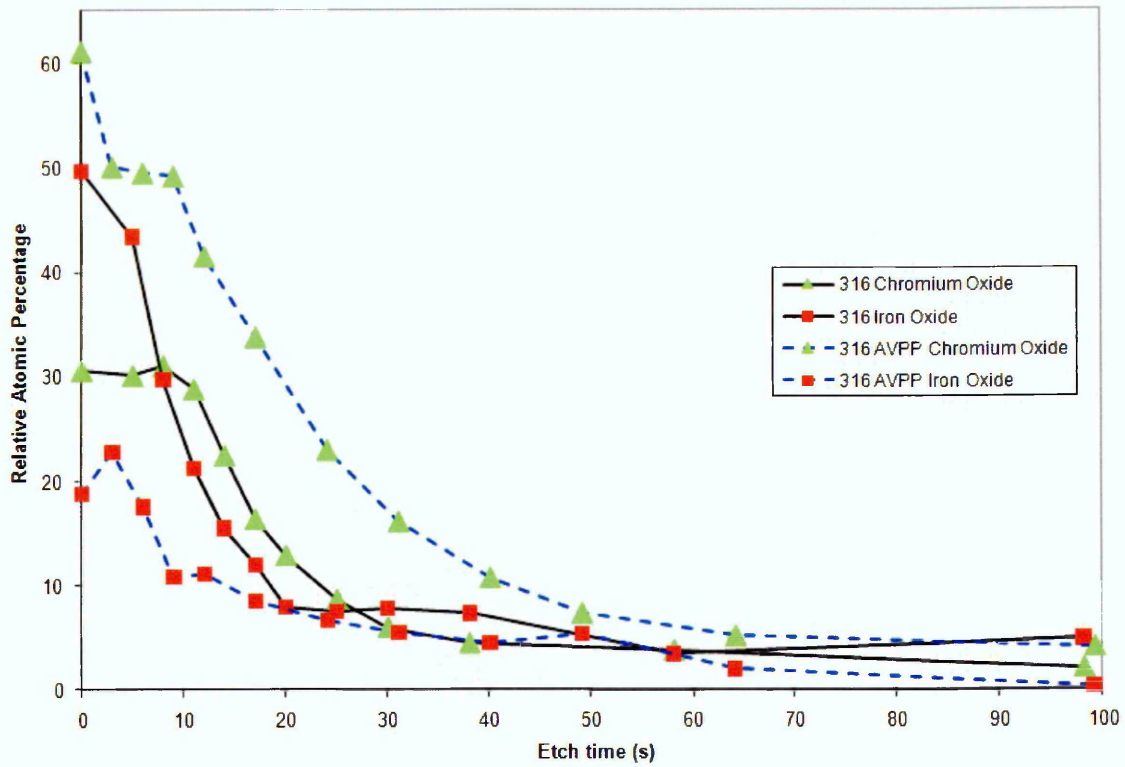
**Figure 5.18:** Comparison of Oxide layers between the 316L and 316L-AVPP Samples.

## 5.3 Surface-profiles

According to the experimental procedures mentioned in the last Chapter, samples were polished up to 1200 grit for corrosion-fatigue tests. Some were polished to 800 grit, 1200 grit and to 1μm diamond paste (mirror finish) for residual-stress measurements and for electrochemical testing. Therefore, three different surface-profiles resulted as shown in Figure 5.19 and Figure 5.20.

## 316L Samples
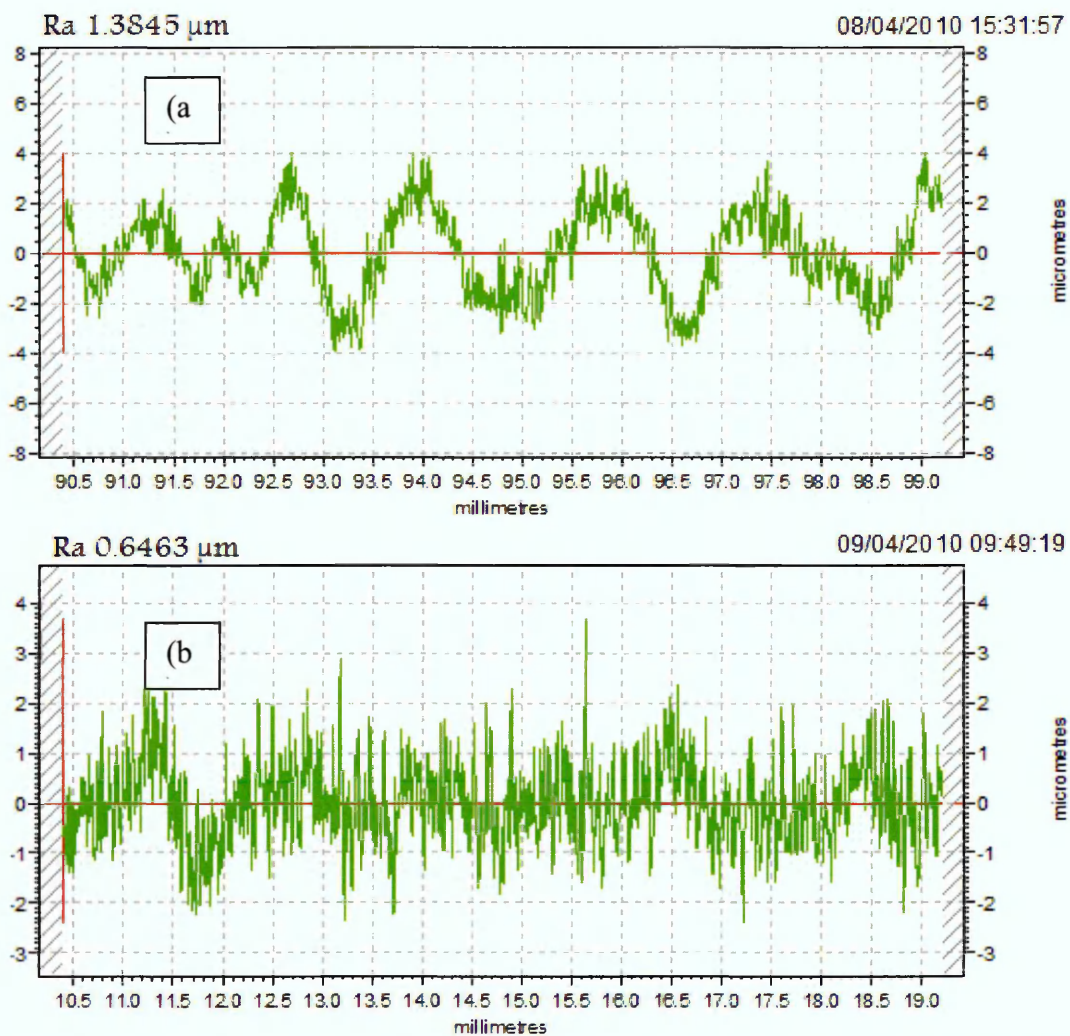


**Figure 5.19:** Typical results of surface-profile for the 316L surfaces polished to (a) 1200 grit CF and (b) 1 μm diamond paste for XRD analysis (b).
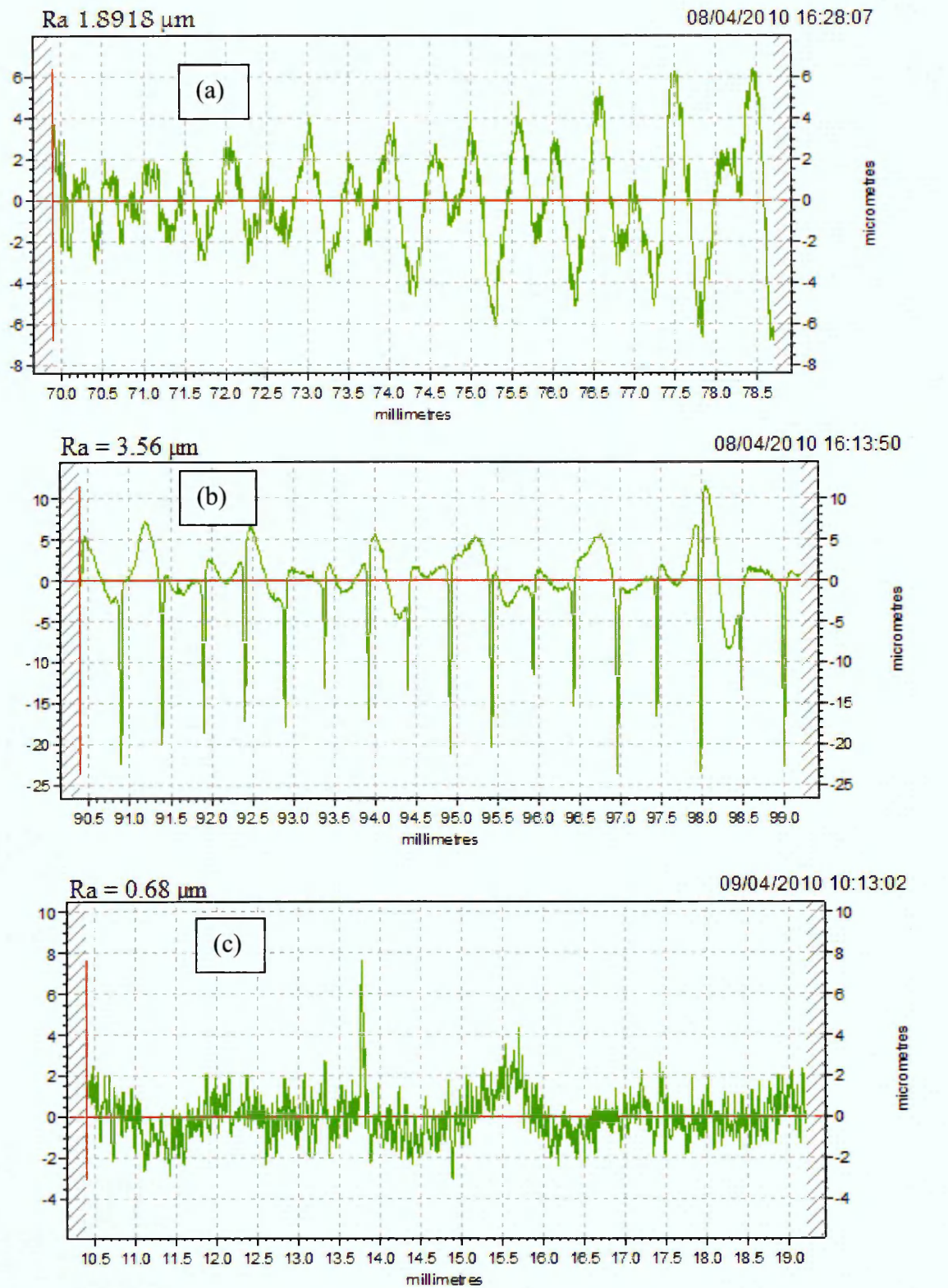
**Figure 5.20:** Typical results of surface-profile for the 316L SS surfaces polished to (a) 1200 grit CF, (b) and (c) 800 grit and 1μm diamond paste for electrochemical measurements.

## 5.4 Electrochemical Properties

### 5.4.1 Potentiodynamic Polarisation

Experiments were carried out to evaluate the electrochemical behaviour of the materials 316L, 316L SS treated by AVPP and DSS2205 in 3.5 % NaCl. To begin with, experiments were carried out on DSS 2205 in classical method to compare it with the results from SDC in same conditions. A typical polarisation curve for the 2205 material is shown in Figure 5.21. This polarisation curve represents an average of 4 potentiodynamic polarisations performed on different samples of the material under the same experimental conditions. The values of corrosion potential $E_{corr}$ and pitting potential $E_p$ for the material in macro cell (5 $cm^2$) are 55 mV and 975 mV respectively, versus Ag/AgCl. From the polarisation curves it is possible to see that the duplex stainless steel 2205 exhibits a high pitting potential in 3.5 % NaCl.
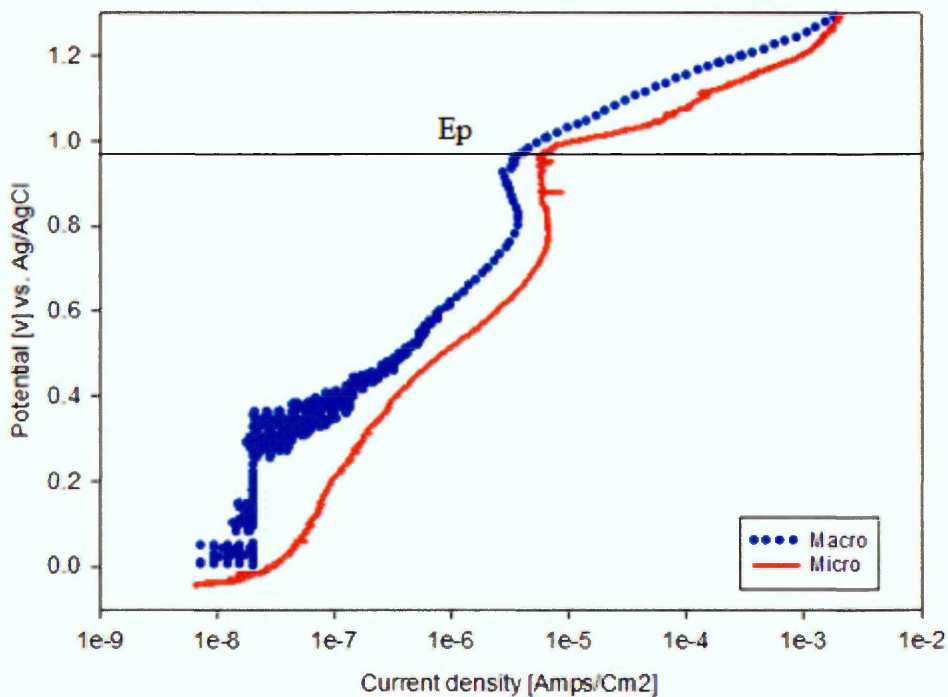


**Figure 5.21:** Potentiodynamic polarization curve of DSS2205 on 3.5 wt% NaCl in macro (5 $cm^2$) and in micro (6.36E-05 $cm^2$) dimensions.

The pitting potential "E$_P$" was determined as the potential value at which the current density increased abruptly for one order of magnitude or more. The polarisation curve for this material is presented in Figure 5.21, where it can be seen that this alloy undergoes active dissolution during anodic polarisation up to a potential of around 0.5V. This is followed by a transition to passive behaviour. The passive region is semi-stable over the potential range of E = 0.5 to E = 0.95V. Once the pitting potential was reached, the anodic current increased rapidly as a consequence of the nucleation and growth of corrosion pits.

At potential levels more positive than 0.95 V, the passive behaviour was not stable; and a more gradual transition to pitting was observed as the current increased two orders of magnitude in a potential range of 200 mV following the onset of pitting. The pits found in the sample following the polarisation test presented a shallow shape. Figure 5.22 represent the material surface image obtained after potentiodynamic experiments and in more focus Figure 5.23 show a 3D optical IFM microscope image.
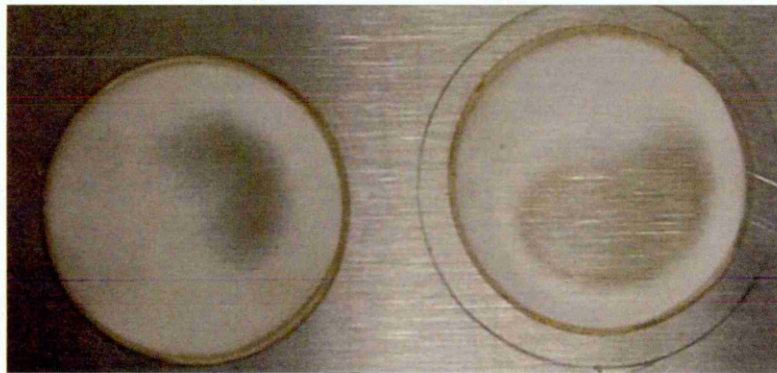


**Figure 5.22:** Image of two specimens of DSS2205 (5cm$^2$ area) in 3.5NaCl, after potentiodynamic experiments.
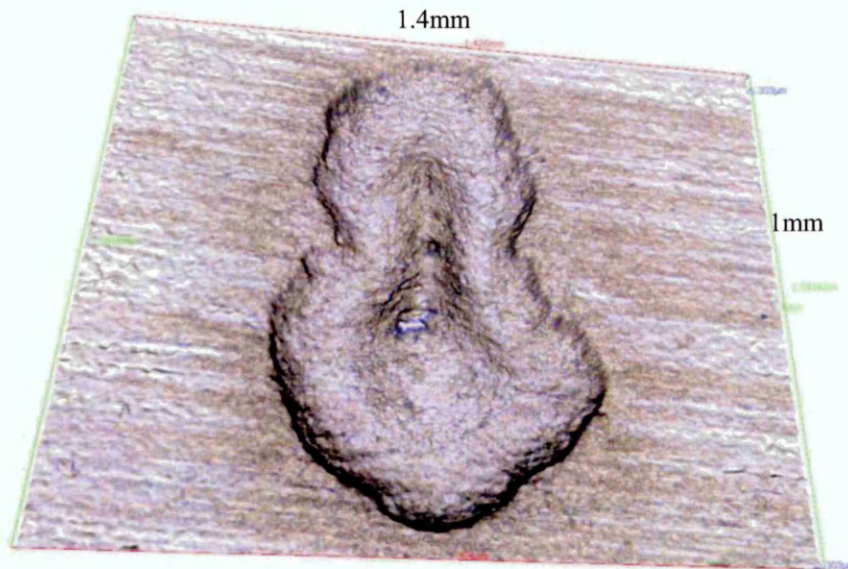
**Figure 5.23:** 3D image of a large pit for DSS2205 after potentiodynamic test of 5cm$^2$ area in 3.5% NaCl.

Figure 5.21 shows also the potentiodynamic curve (micro) obtained from the SDC test for comparison. Both curves show similar trends but with a slight difference in the pitting potential. In the micro size the $E_{corr}$ and $E_p$ are 60 mV and 1035 mV versus Ag/AgCl respectively. From the polarisation curves it is possible to see that the duplex stainless steel 2205 exhibits a high pitting potential in 3.5 % NaCl. Figure 5.24 shows typical pitting response from the SDC tests.
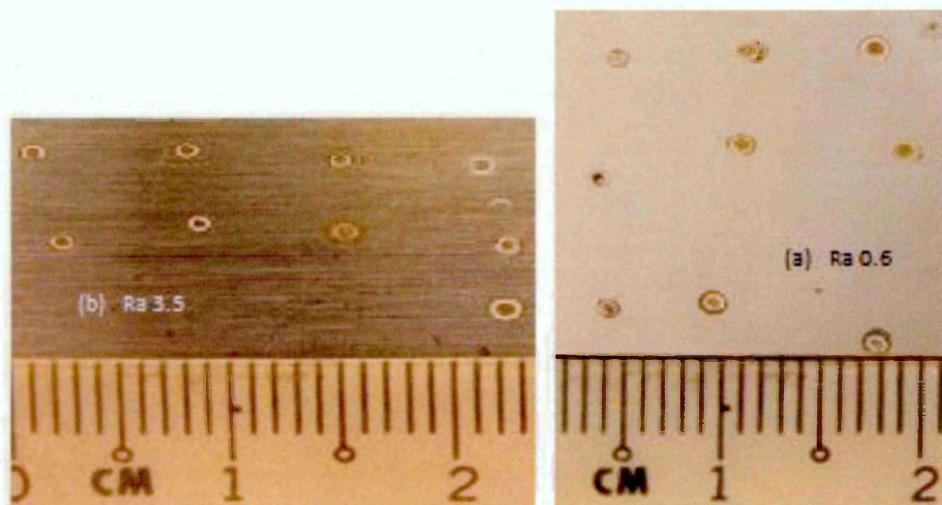


**Figure 5.24:** Results of the SDC showing roughness for two surfaces of DSS2205 in 3.5NaCl, (a) Ra 3.5 and (b) Ra 0.6.

## 5.4.3 Potentiodynamic polarisation for the 316L, AVPP and 2205 Samples

Figure 5.25 shows the polarisation curves obtained for the 316L material without surface-film modification (316L) and with surface-film modification (316L-AVPP), in addition to the polarisation curve for 2205. The potentiodynamic curve for the 2205 material, which is very similar to the 316L-AVPP curve, is presented in the last section. The cathodic region of the polarisation curve for the 316L matches well with the 316L-AVPP having a slightly higher corrosion potential. However, it illustrates a huge difference in the pitting potential E$p$, where the E$p$ for the 316L-AVPP (1000 mV) is twice the E$p$ for 316L (450 mV). This indicates that the passive film stability of the 316L stainless steel surface is enhanced remarkably with the formation of the modified film using AVPP.
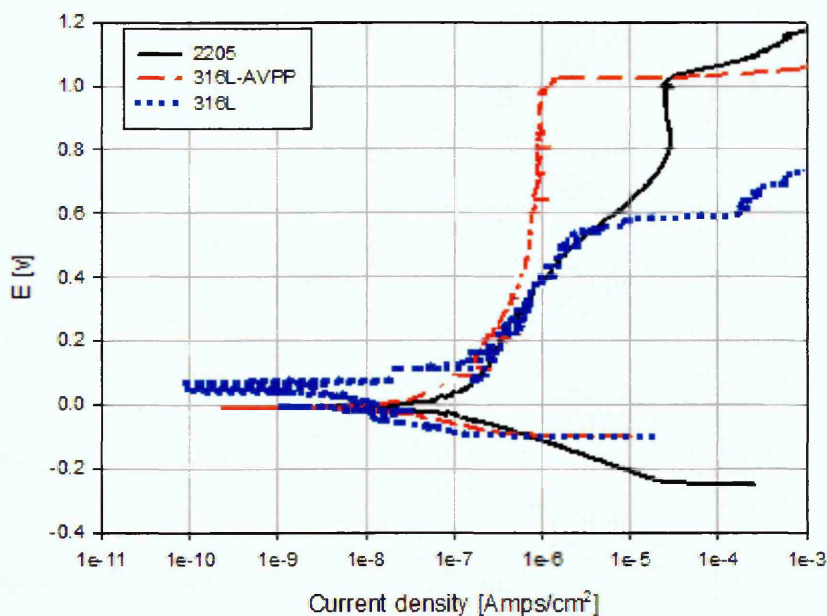


**Figure 5.25:** SDC potentiodynamic polarisation curves for 316L, AVPP and 2205 stainless steel samples in 3.5 wt% NaCl, the SDC tip diameter is 1mm.

## 5.4.4 Potentiostatic Polarisation Results

Figure 5.26 presents Current-Time potentiostatic polarisation results for the 316L and 316L-AVPP-treated surface using SDC with 3.5% NaCl 6.5 pH at potential 0.35 V vs. Ag/AgCl. This potential corresponds to the passive region for both samples and was chosen from the potentiodynamic curve. The 316L curve represents more corrosion activity and goes to the highest level of current for a short time, where the AVPP current increases gradually with time to reach its highest level which is about half of the 316L highest level.
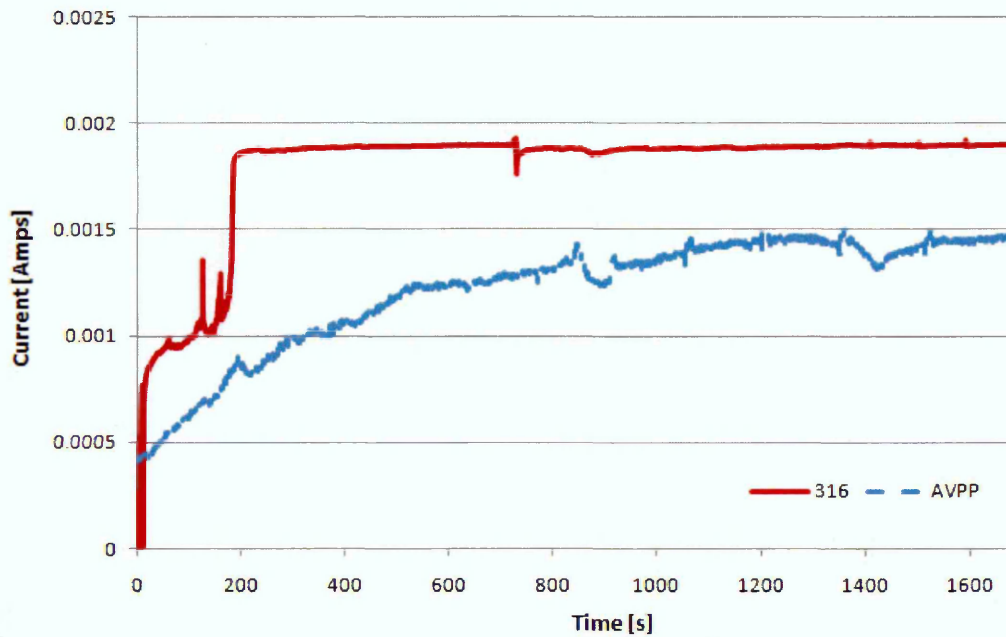


**Figure 5.26:** SDC current-Time potentiostatic polarisation results for 316L and 316L-AVPP treated surface in 3.5% NaCl, 6.5 pH at a fixed potential 0.35 V vs. Ag/AgCl.

## 5.4.5 Linear voltammetry

Acquisition of linear voltammograms of 316L SS and 316L-AVPP-treated measured in %wt 3.5 NaCl solution make it possible to compare the current peaks and the corresponding electrochemical processes taking place on the material investigated as well as the influence of the potential scan rate. The linear voltammograms were recorded at different scan rates in the potential range from 0.005 to 0.1V/s from -1V to 1V. As can be seen in Figures 5.27 and 5.28, the main features of the linear voltammograms are similar, with some differences between both surface-films. For both samples each curve has the same trend but it is apparent that the total current increases with increasing scan-rate. For the 316L surface-film sample (Figure 5.27) two peaks are observed. The first peak is at a potential –0.4V which can be ascribed to the oxidation of Fe (II) to form Fe (III) on the sample surface. It is followed by a region with a constant current density, up to 0.4 V. Another peak is then formed at the transpassive region at a potential of 0.65 V, and this is associated with the oxidation of Cr (III) to Cr (VI) [157]. The Ni (II) species formed during the Passivation process might also have been oxidised to Ni (IV) Oxide ($NiO_2$) in this potential range [158].
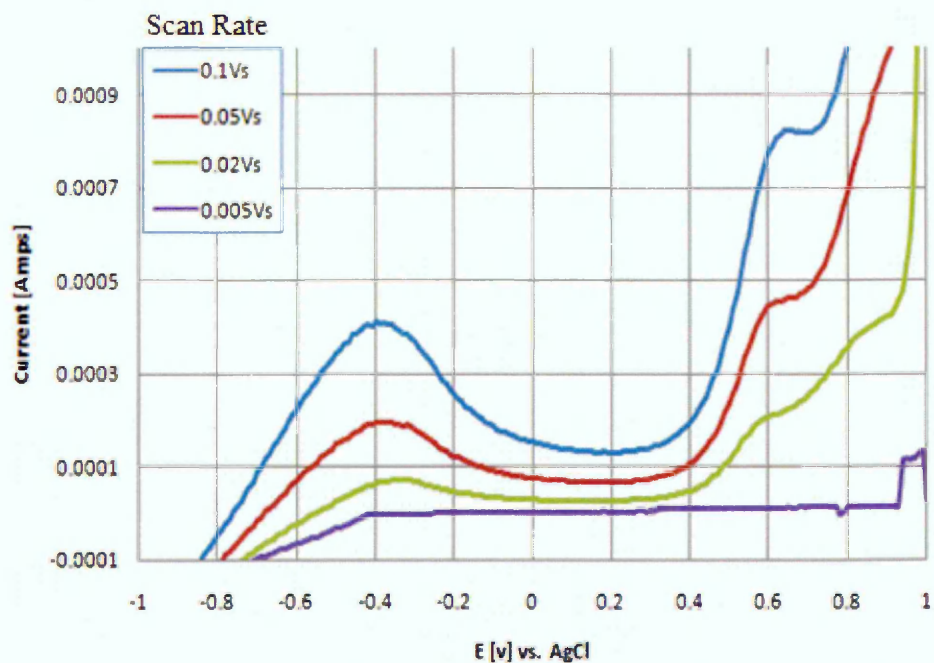
**Figure 5.27:** Linear voltammograms of the 316L SS (5cm$^2$) sample at different sweep-rates on wt % 3.5 NaCl, pH 6.

Figure 5.28 shows the linear voltammograms of the AVPP film. The curves have the same trend as the 316L sample with deviations in the peaks' positions and in their current size. Therefore, the first peak moved from -0.4 V in the 316L sample to be at -0.3 V and the current decreased from 0.0004 Amps to 0.0002 Amps. The second peak was at 0.65 V potential to 0.85 V potential; however the current increased from 0.0008 to 0.0009 Amps.
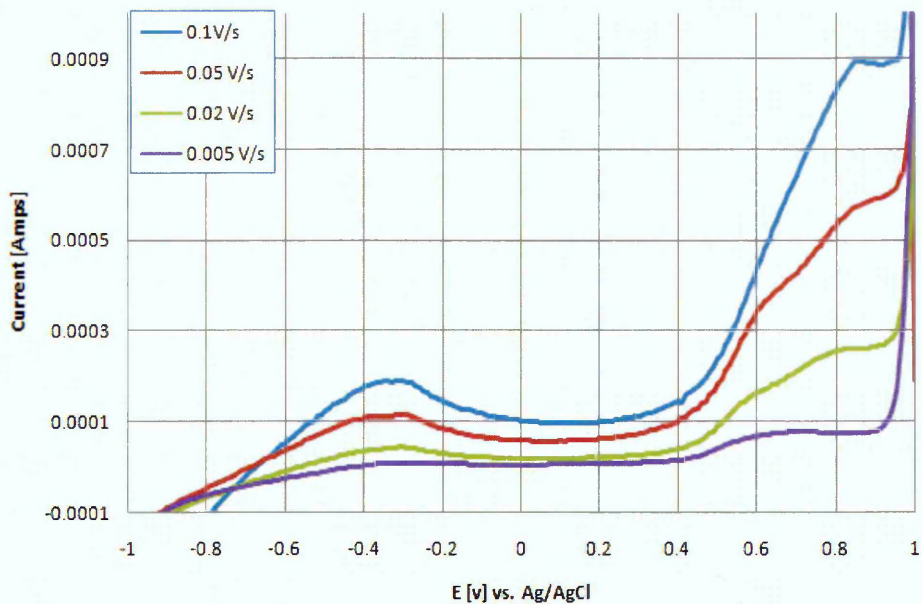
**Figure 5.28:** Linear voltammograms of the AVPP ($5cm^2$) sample at different sweep-rates on %wt 3.5 NaCl, pH 6.

SDC linear voltammetry tests were repeated for both the 316L and AVPP samples under the same conditions. Their results are presented in Figures 5.29 and 5.30. Similar results were obtained with differences in the magnitude of the current because of the electrode area size.
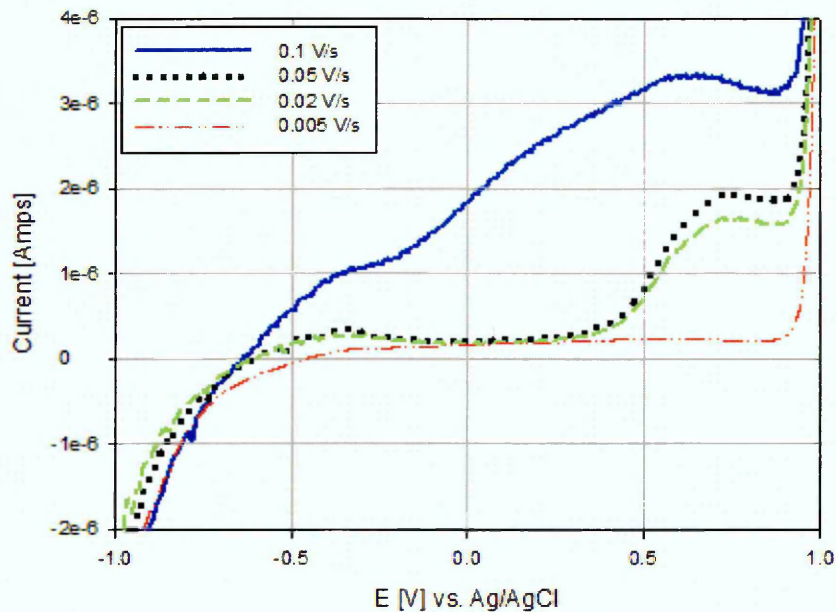


**Figure 5.29:** SDC linear voltammograms of the 316L (0.78 $mm^2$) sample at different sweep-rates in %wt 3.5 NaCl, pH 6.
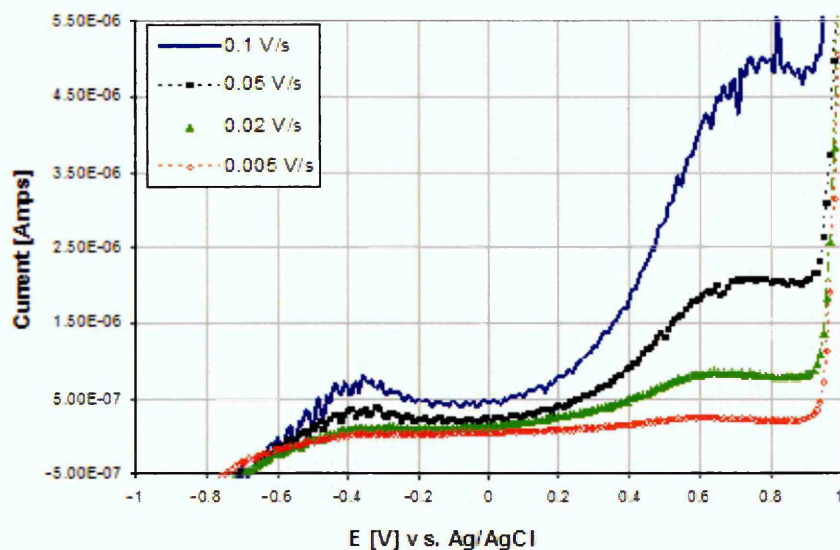
**Figure 5.30:** SDC linear voltammograms of the 316L-AVPP (0.78 mm$^2$) sample at different sweep-rates in %wt 3. NaCl, pH 6.

## 5.4.6 Electrochemical Impedance Spectroscopy

The Bode plots of the 2205, 316L and 316L-AVPP-treated samples are shown in Figure 5.31. It can be seen that the impedance response shows stable impedance for the three samples. However the 316L-AVPP modified surface-film sample shows a film-resistance approximately one order of magnitude higher than the unmodified film. The 2205 surface-film sample has an equivalent impedance response to that of the modified surface-film sample. This supports the observation of high pitting potentials obtained from the polarisation plots.
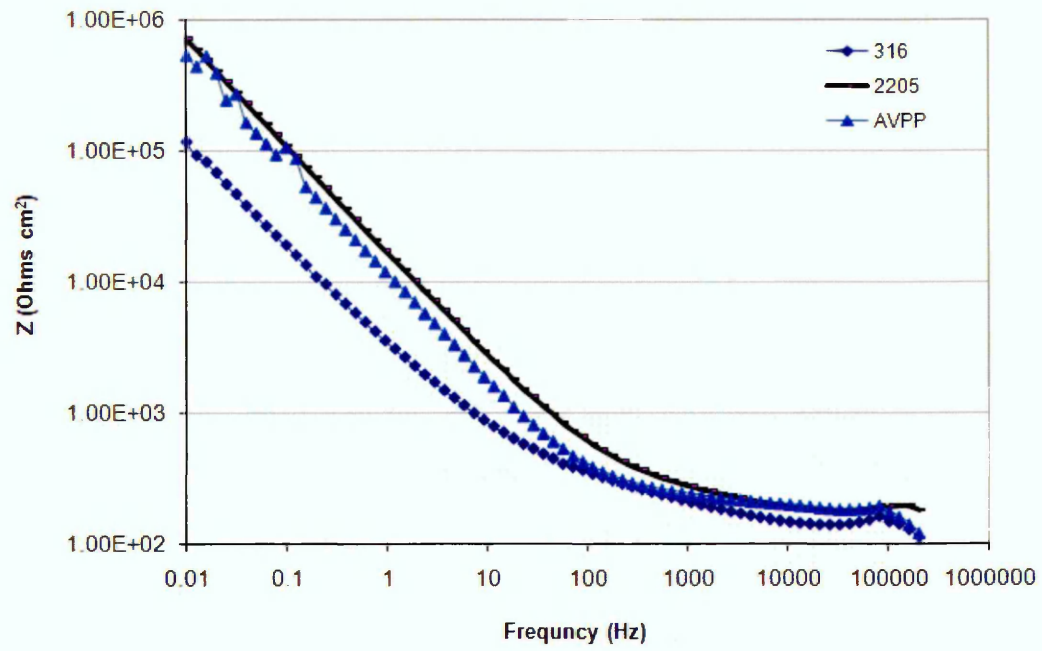
**Figure 5.31:** Electrochemical Impedance Spectroscopy (EIS) for the 316L, 316L-AVPP-treated and 2205 specimens immersed into 3.5 M NaCl pH 6.5.

## 5.5 Pitting

### 5.5.1 Pit Geometry measurements

Unexpectedly the typical profile of the material removed was that of a circular groove. The central area inside the circle appears to form an island which includes intact material with distribution of few undeveloped pits. Figure 5.32a shows an IFM image of a typical shape of a corroded surface obtained after a SDC potentiostatic. However, some of the localised corrosion takes the shape shown in Figure 5.32b where the pit grows in the middle. A more detailed examination of the profile is given in Figure 5.33 which shows an IFM cross section image of the pit profile. It is noteworthy that the groove formed varies in depth, where the groove at the solution inlet side is deeper than at the outlet side. This behaviour is considered to be the result of increased availability of Oxygen, and subsequent increased dissolution, on the inlet side. Furthermore it might be reasonable to assume that the actual flow dynamics are slightly different on the inlet and outlet sides, with the outlet side being somewhat more quiescent.
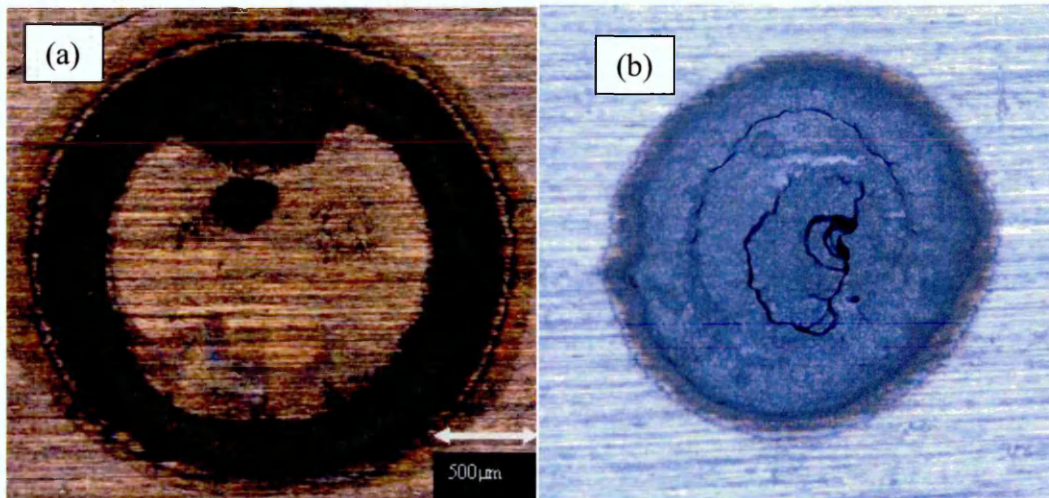


**Figure 5.32:** IFM optical microscope images showing two different typical localised corrosion shapes obtained using the SDC. DSS2205 in 3.5%NaCl, 1V vs. Ag/AgCl for 2 Hr.
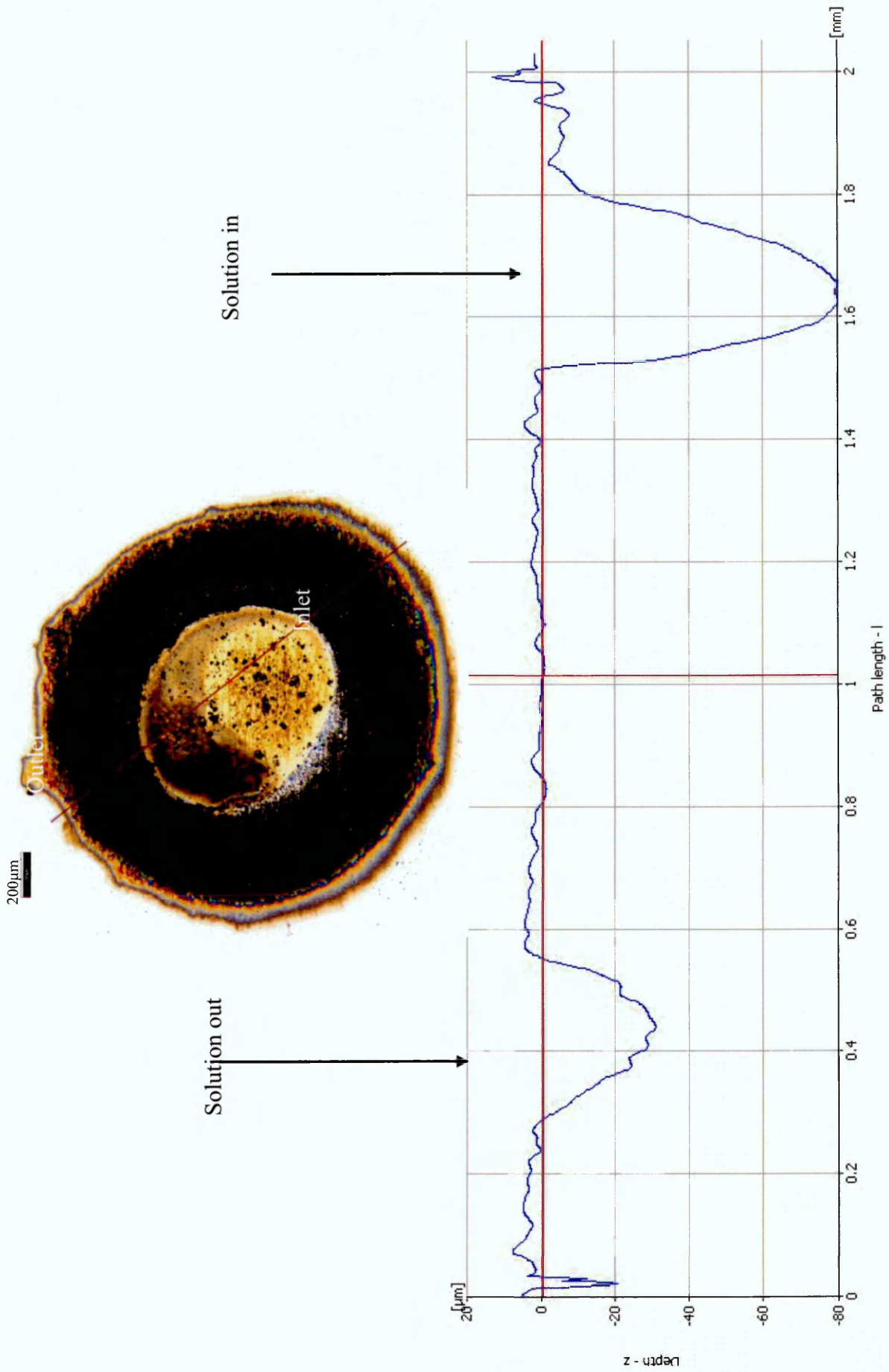
**Figure 5.33:** Image of a pit obtained from IFM after an SDC test against its cross sectional

## 5.5.2 Comparison of SDC and IFM Measurements

Figure 5.34 represents results from SDC tests in terms of material mass, as calculated using Faraday's law, compared to mass calculated from the volume of material removed measured using IFM. In the low flow-rate regime (below 25 mm$^3$/s) there is reasonable correlation between the SDC and IFM results. However, when higher flow-rates were applied the difference between the two results increased. Pits produced at low flow-rates were found to be more shallow than pits produced from higher flow-rates. Shallow pits on the surface can be measured more precisely than deeper pits with IFM because of the increase in the possibility of hidden undercutting of pits. Confirmation of this could be evaluated by conducting metallographic cross-sections of the pit-profiles.
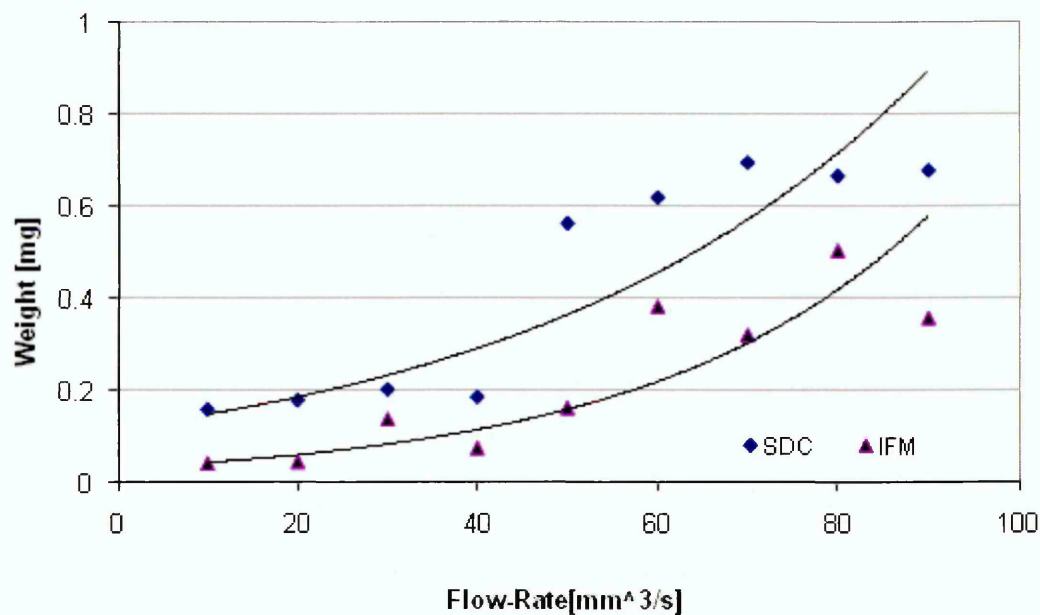


**Figure 5.34:** Weight of material removed as calculated from Faraday's law using SDC current-time measurements and as measured with IFM.

## 5.5.3 Effects of Flow-Rate on Pit Growth Rate

Figure 5.35 shows examples of current-time curves obtained from potentiostatic measurements for 316L SS samples in 3.5%NaCl obtained from the SDC with 1mm diameter capillary and test duration of 2 hours. The applied potential is 1V vs. Ag/AgCl. For the same test conditions with a changing flow-rate, it is found that the current density increases with the increase in flow-rate. The increase in flow-rate leads to an increase in Oxygen supply and mass transport of species, thus accelerating the corrosion process. The form of the current-time responses obtained from this series of tests is similar to that obtained with 0.9 capillary tests for both surfaces in term of the effect of flow-rate.
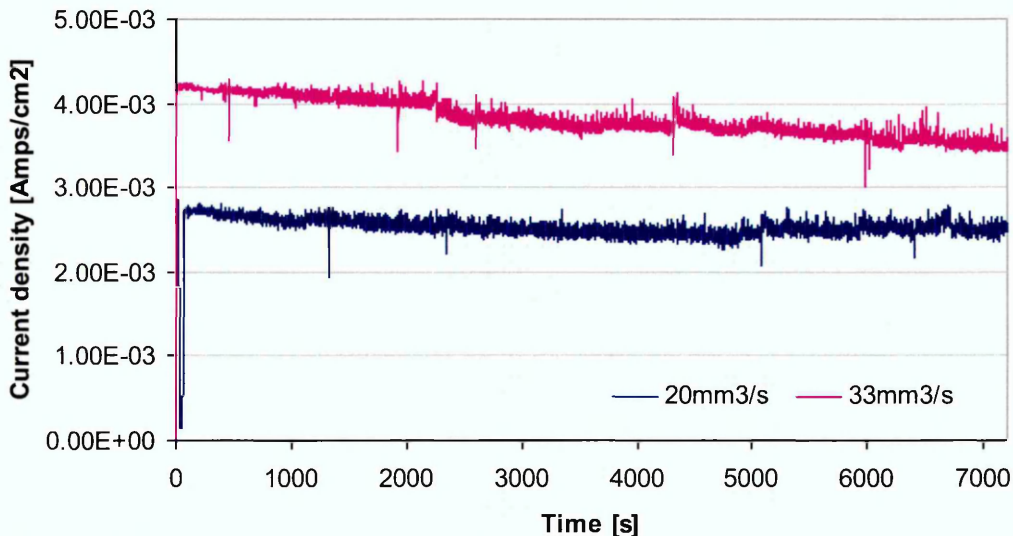


**Figure 5.35:** SDC current density-time for potentiostatic polarisation tests for the 316L SS Sample in 3.5%NaCl, 1V vs. Ag/AgCl for; 2hs for two different flow-rates.

## 5.5.4 Effect of Surface Finish on Pitting

The results also show differences between the three surfaces, where there is a higher material loss for 3.5µm Ra surfaces than 1.8 and 0.6µm surfaces, as shown in Figure 5.36. In this Figure the effects of flow-rate on the material-loss are presented as a function of

surface-finish. It is shown that the material-dissolution increases with the increase in flow- rate.
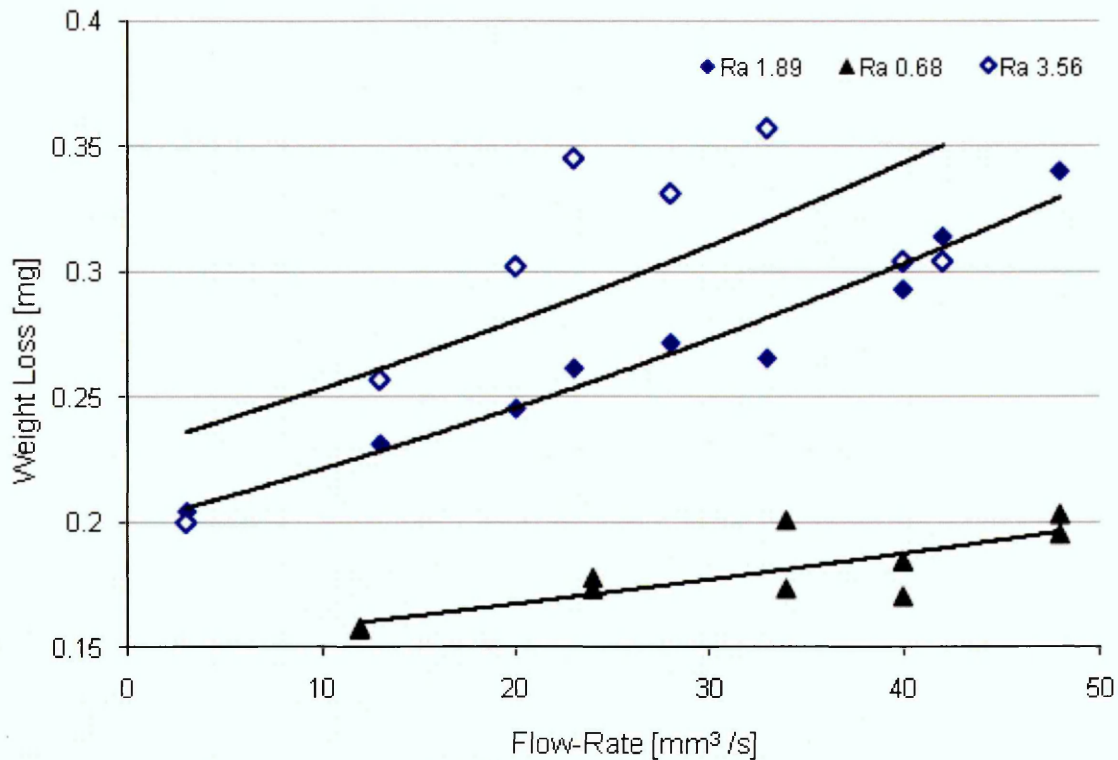


**Figure 5.36:** Flow-rate vs. weight loss (calculated from the charge obtained during SDC tests) for the 316L SS Samples in 3.5%NaCl under potentiostatic 1V vs. Ag/AgCl for 2hs.

## 5.5.5 Effects of Applied Stress on Pitting

The localised corrosion-rate of the stressed sample during potentiostatic polarisation, shown in Figure 5.37, is found to be much larger than that of the unstressed (at 0 MPa) sample. However, a slight increase in the corrosion-rate was observed as the applied stress increased through steps to about 1.33 of yield-stress of the alloy. Figure 5.38 also shows current density for 316L SS samples potentiostatically polarised at 1V vs. Ag/AgCl. These samples were polarised under tensile stress at 0 and at 100 MPa (0.33 of yield stress) of the alloy.
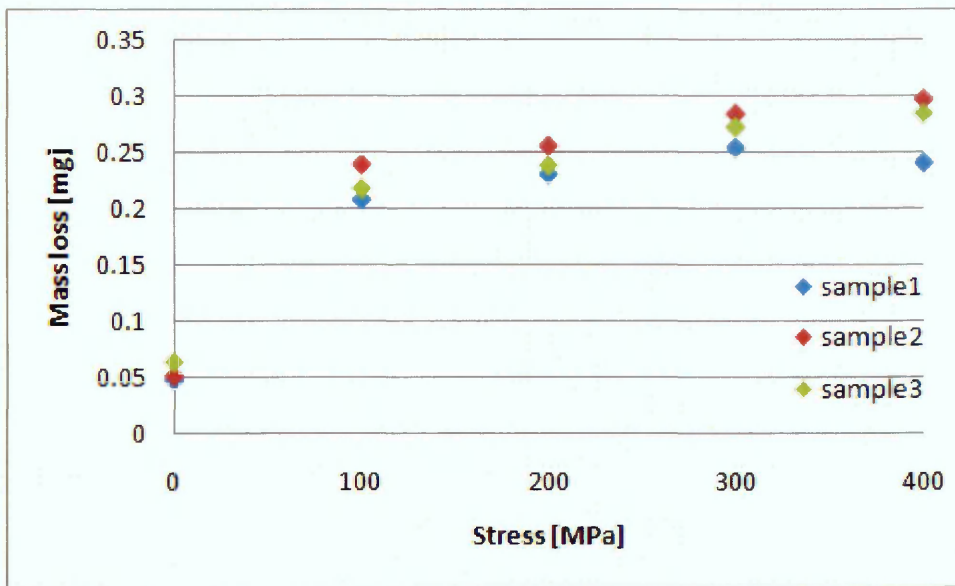
**Figure 5.37:** Weight loss, calculated from Faraday's law using SDC current-time measurements, as a function of stress for the 316L SS Samples in 3.5 wt% NaCl, 1V and 30min.
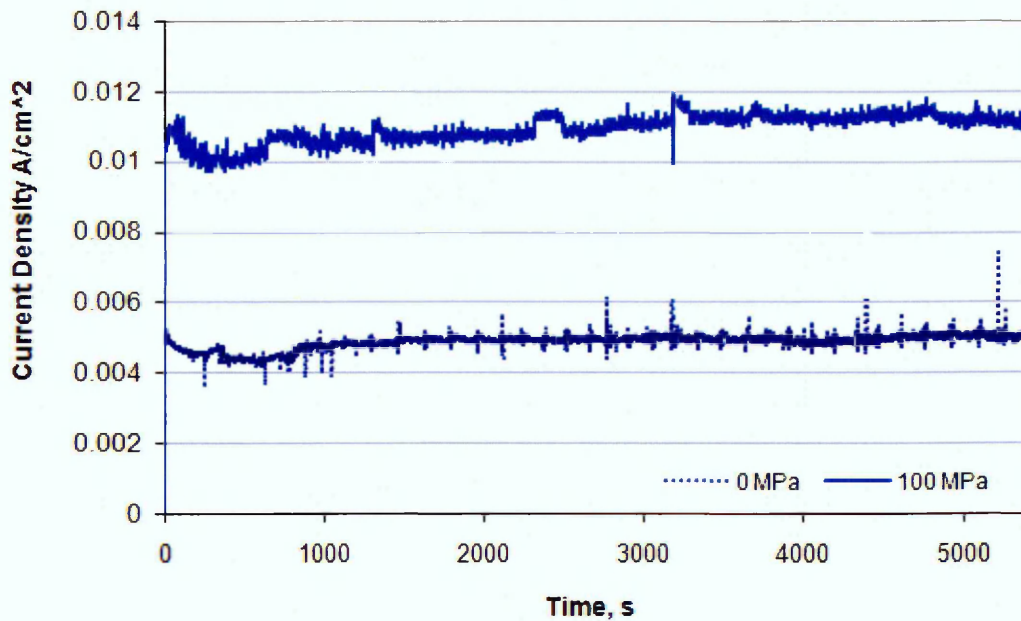


**Figure 5.38:** Current Density for the 316L SS Samples potentiostatically polarised at 1V vs. Ag/AgCl at 0 and at 100 MPa, for 2hs.

## 5.5.6 Pit Growth Law

The results from the electrochemical potentiostatic polarisation using SDC method is shown in Figure 5.39. This Figure represents a plot of the pits depth and pits diameter against the polarisation time. As can be seen the pits depth increases regularly with

polarisation time, however it is not so for the pits diameter. From Figure 5.40 a pit growth law of the form:

$$D = C\ T^b\ (D = 2.2\ T^{0.8}) \qquad (5.2)$$

was obtained for 316L SS. Where D represents the pit depth in (µm), T is time of anodic polarisation in (minutes) and C and b are empirical constants obtained from the analysis of the experimental data.
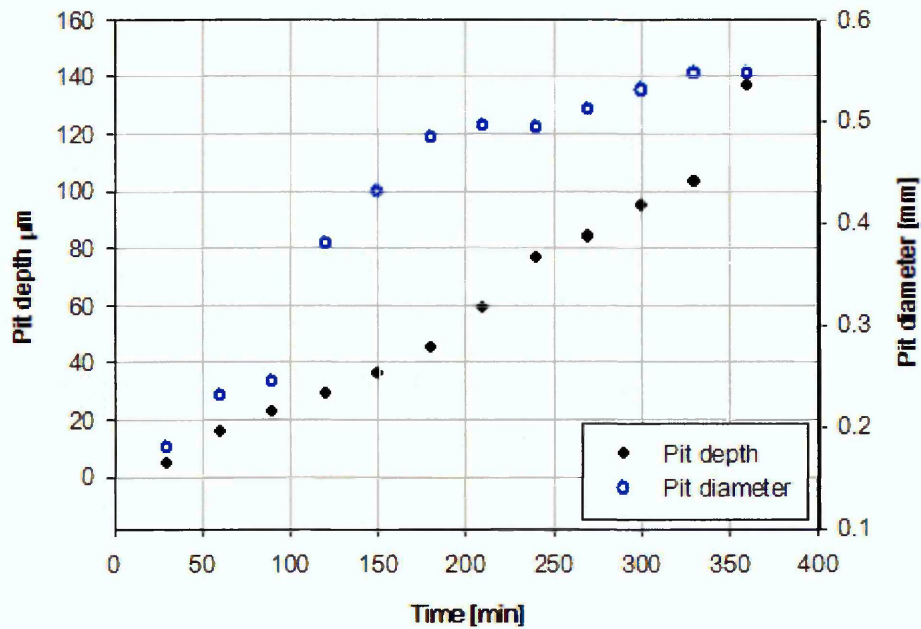


**Figure 5.39:** Pit diameter and pit depth as function of polarisation time results from IFM for 316L SS in 3.5%NaCl and 0.5V vs. Ag/AgCl.
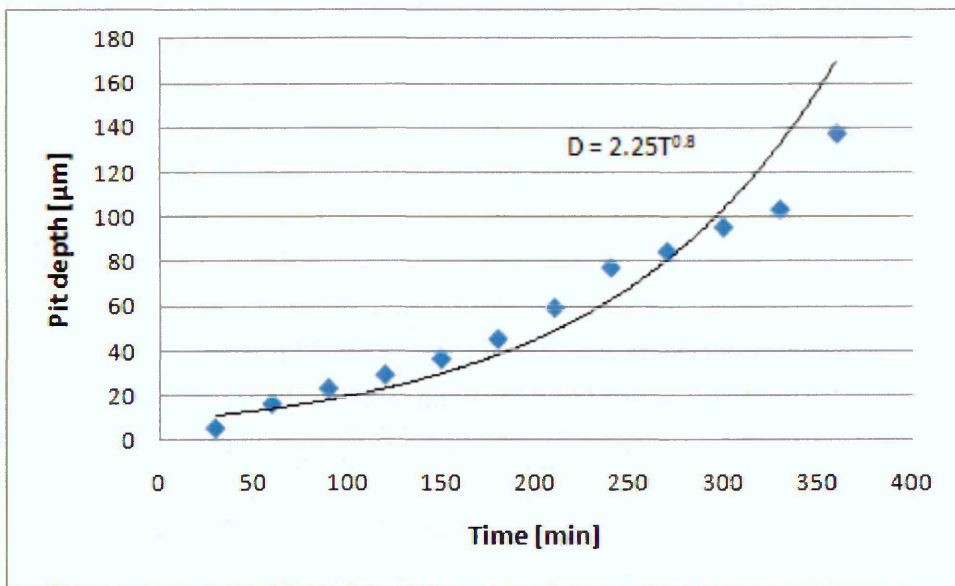
**Figure 5.40:** Pit depth as function of polarisation time results from IFM for 316L SS in 3.5%NaCl and 0.5V vs. Ag/AgCl.

## 5.6 Tensile Testing

Tensile tests were performed in order to obtain the mechanical properties of the duplex stainless steel 2205 and 316L SS samples. Figure 5.41 presents the stress-strain curves for DSS 2205. The tensile strength was found to be 920 MPa. The yield strength was about 600 MPa. This shows the alloy to be a high strength material. The results of elongation were between 25 to 26%, indicating a highly ductile material.

Figure 5.41 also presents the stress-strain curve for 316L SS. The tensile strength was found to be 670 MPa. The yield strength was 300 MPa. Therefore, the 316L alloy has less strength than the DSS 2205 alloy. The results of elongation were about 35%, indicating a highly ductile material.
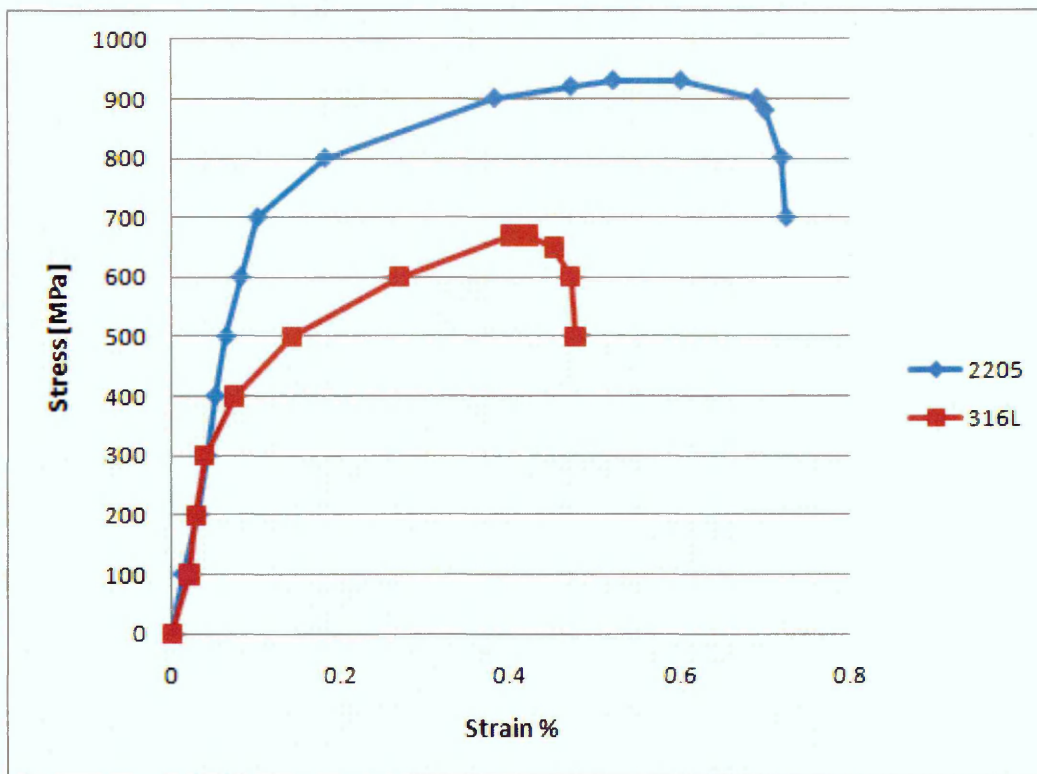
**Figure 5.41:** Stress-Strain curves for the DSS 2205 and 316L SS Samples.

## 5.7 Nano-Hardness Tests

### 5.7.1 Nano-hardness for the 316L and AVPP Samples

The results of nano-hardness tests for the 316L and 316L-AVPP-treated samples are presented in Figures 5.42, 5.43 and 5.44. These figures represent the curves of loads vs. indentation depth at 3 mN, 2 mN and 1 mN respectively. As can be seen in Figure 5.42, the loading and unloading curves of the two materials are almost equal, and the resulting indentation depth exceeds the thickness of the oxide-film. As the applied load is reduced to 2 mN (Figure 5.43), the indentation depth decreased which resulted in greater deviation between the two curves. More importantly, the indentation depth of the modified surface-film in the AVPP sample is larger than in the 316L sample. Moreover, when the applied load decreased to 1 mN (Figure 5.44) the indentation depth was further reduced to about 45 nm for the 316L oxide-film and to 60 nm for the AVPP oxide-film. This indicates that the 316L oxide-film has a higher hardness compared to

the AVPP oxide-film. Fluctuations appeared in the first 20nm depth of the AVPP surface which could be related to the difference in hardness between the AVPP layer and the bulk material. The values of Young's modulus (E), Vickers hardness (Hv) and Poisson's ratio ($v$) for the 316L and for the 316L-AVPP-treated samples, obtained from nano-hardness tests, are presented in Table 5.2.

**Table 5.2:** Nano-indentations hardness results

|  | 316L | AVPP |
|---|---|---|
| E [GPa] | 178 | 133 |
| Hv | 464 | 354 |
| $v$ | 0.3 | 0.3 |
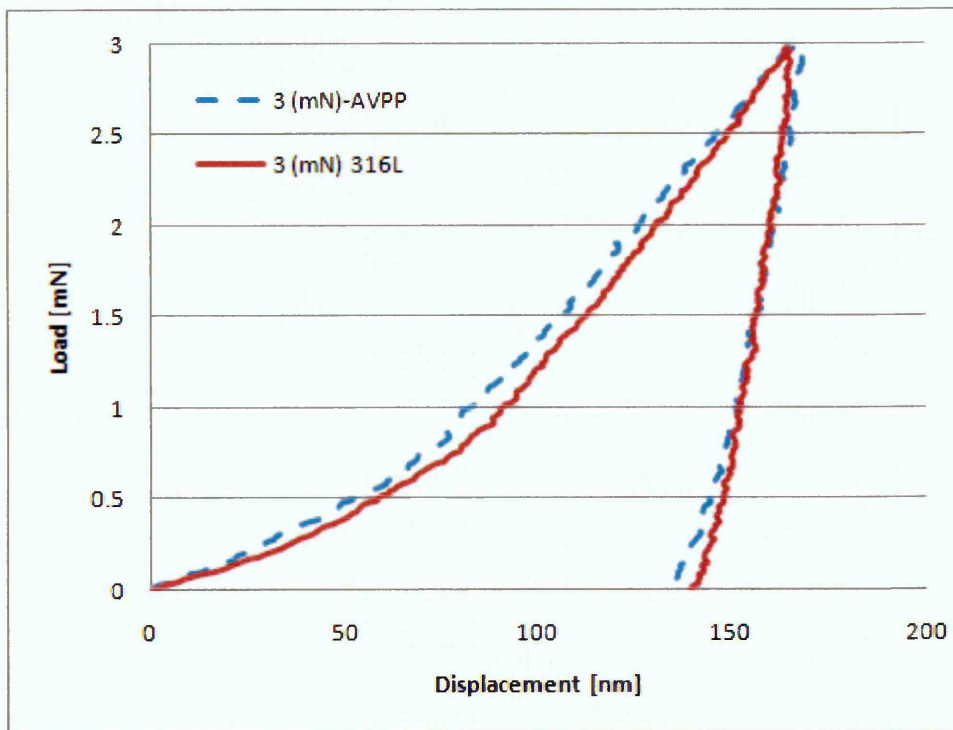


**Figure 5.42:** Load-Displacement curve at 3 (mN) maximum load for the 316L and 316L AVPP-treated samples.
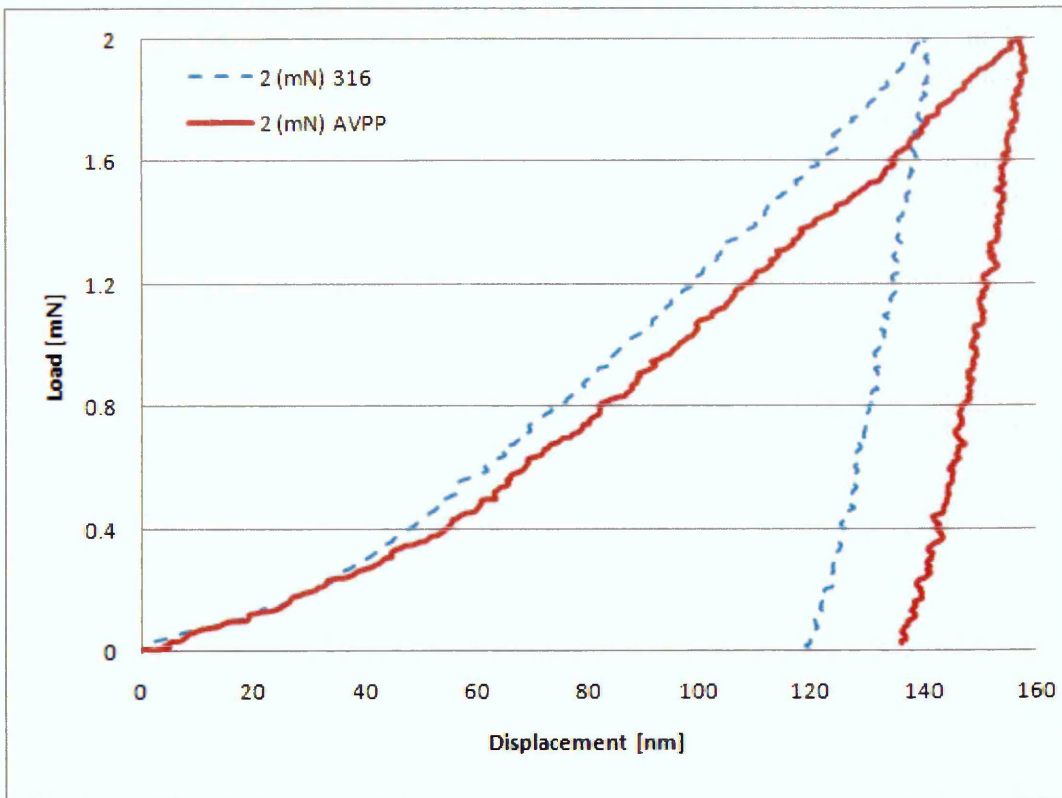
**Figure 5.43:** Load-Displacement curve at 2 (mN) maximum load for 316L and 316L treated sample by AVPP.
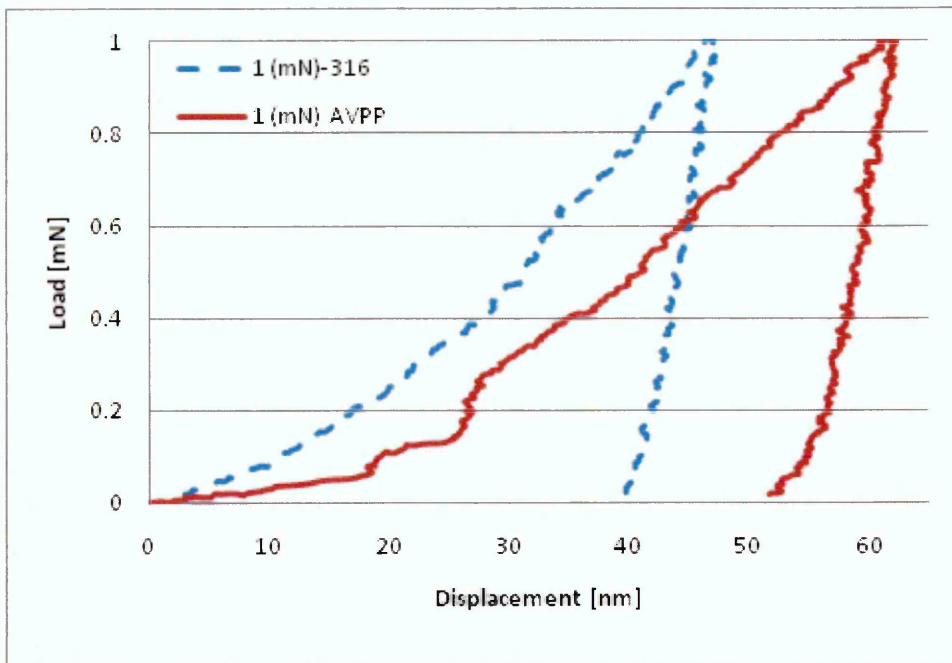


**Figure 5.44:** Load-Displacement curve at 1 (mN) maximum load for 316L and 316L AVPP-treated samples.

## 5.8 Residual Stress Measurement using XRD after Fatigue Loading

Residual stress measurements presented in (Figure 5.45) show that the compressive residual stress is reduced in the first sample from -130 to -110 MPa before and after AVPP treatment respectively. The same result obtained in the second sample where the negative residual stress decreased from -90 to -70 MPa before and after AVPP respectively. This indicates that the AVPP treatment decreases the residual surface stress. However, both sample stress states (treated and untreated) show similar trends after applying fatigue cycles, with the exception that the treated samples become residual compressing stress-free after the first 1000 cycles. The residual stress then becomes tensile and increases by a rate that is dependent on the applied stress.
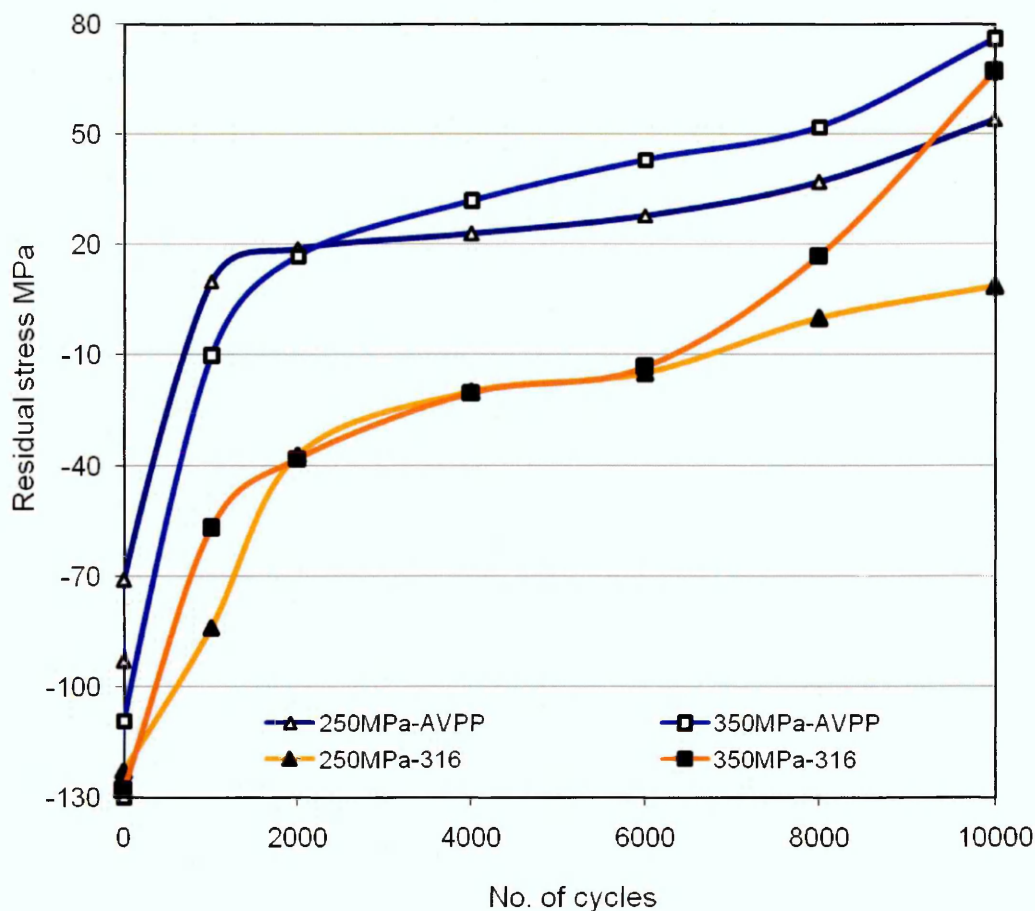


**Figure 5.45:** Residual stress for untreated two (316L) and two treated (316L-AVPP) samples at no. of stress cycles at σmax 250MPa and 350MPa, R0.1, test frequency 0.2 Hz.

## 5.9 Corrosion Fatigue Testing

### 5.9.1 Fatigue Life

Three corrosion-fatigue tests were conducted in 3.5% NaCl, at room temperature for both 316L SS and 316L-AVPP-treated. In addition fatigue tests were conducted in air for 316L for fatigue life comparison. Corrosion-fatigue tests were conducted using a fatigue-rig machine in combination with SDC with 3.5%NaCl solution under anodic polarisation with an applied potential of 0.5V vs. Ag/AgCl. The solution flow-rate was 20 mm$^3$/s. Samples of 316L SS and 316L-AVPP-treated were tested under the same maximum applied cyclic stress, notably 260 MPa. This represents around 0.87 of the yield strength of the material. The stress rate R was 0.1, and the loading frequency 0.5Hz.

Figure 5.46 shows a bar-chart for the average of fatigue-life of the three samples of each material under different environmental conditions shown in table 5.9.1. As can be seen from the bar-chart, the fatigue-life to failure for 316L in air is larger than the fatigue-life in 3.5%NaCl for both 316L and 316L-AVPP-treated samples. It also shows that the fatigue-life for 316L treated by AVPP in 3.5%NaCl is larger than that of the 316L in 3.5%NaCl. This indicates that the fatigue-life of the 316L material is reduced to about 30% when the same test is conducted in the presence of 3.5%NaCl. However, the fatigue-life of 316L in 3.5%NaCl increased to about 18% as a result of introduction of AVPP treatment.

**Table 5.9.1:** Fatigue life of the three different test conditions

| Test condition | Total fatigue life (No. of cycles) | | | Average |
|---|---|---|---|---|
| 316L in air | 32703 | 33808 | 31761 | 32757 |
| 316L in 3.5%NaCl | 22466 | 23102 | 23731 | 23099 |
| 316L-AVPP in 3.5%NaCl | 26450 | 29655 | 30708 | 28937 |
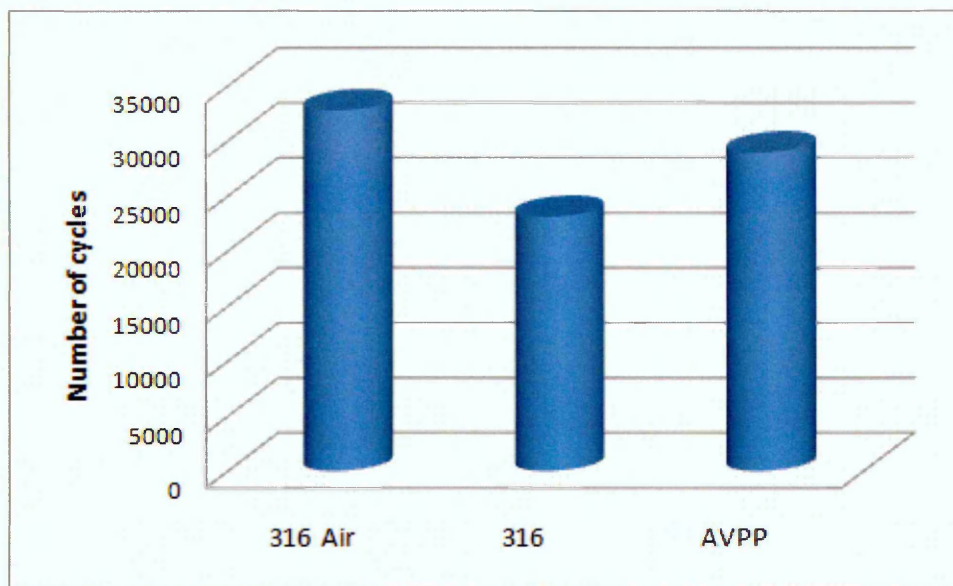
**Figure 5.46:** Fatigue life in air for the 316L Samples, and in 3.5%NaCl, for both the 316L and 316L-AVPP-treated Samples. Applying fixed potential 0.5V vs. Ag/AgCl, 20mm$^3$/s flow rate. R = 0.1, $\sigma_{max}$ =0.87 $\sigma_y$, $f$ = 0.5Hz.

## 5.9.2 Electrochemical Current Analysis

This study includes the initiation and the propagation of corrosion-fatigue cracks. The corrosion-fatigue testing using a scanning droplet cell was conducted in the 316L SS and 316L-AVPP-treated samples. This study was achieved by analysing the resulting electrochemical current behaviour and monitoring the surface-profile changes using an Infinite Focus Microscope IFM.

The behaviour of the resulting current in the 316L and 316L-AVPP-treated samples can be divided into four stages. These stages relate to electrochemical and mechanical processes. The electrochemical process comprises film-dissolution and localised corrosion including pit-initiation and pit-growth. The mechanical processes include micro-cracks initiation, early corrosion-fatigue crack-growth and main crack-growth to final failure. Figure 5.47 shows an example of the resulting current transient in the initial stage of a corrosion-fatigue test for the 316L SS sample and the applied cycling loading.
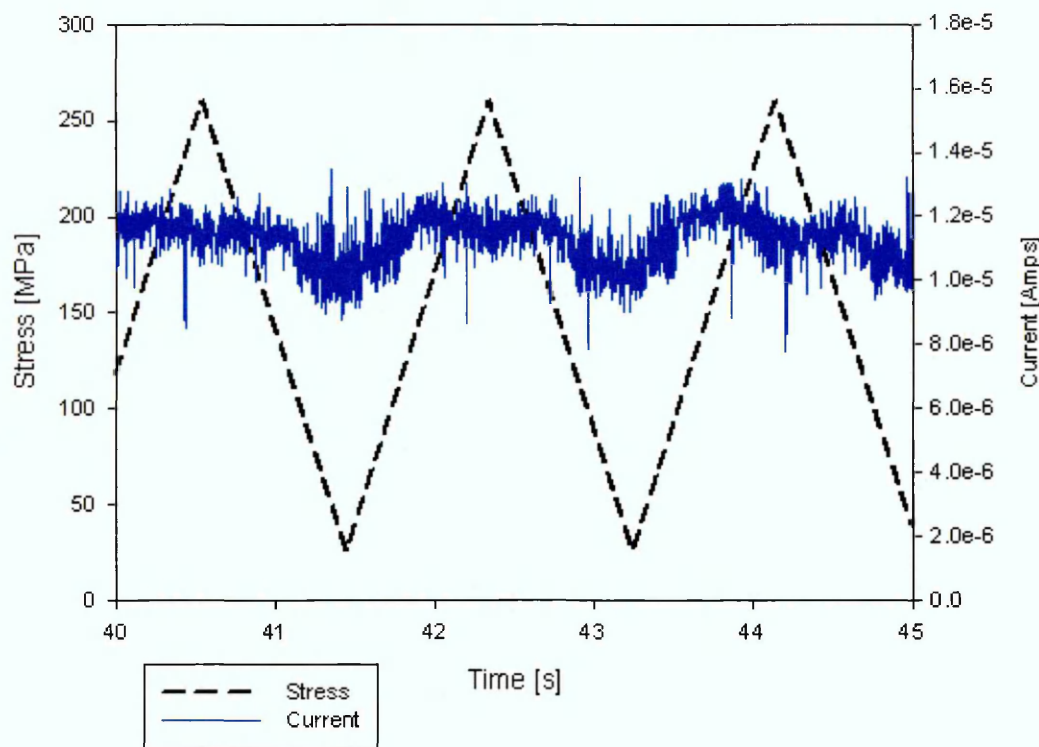
**Figure 5.47:** Stress cycles and current transient curve vs time in the initial stage of one of the corrosion-fatigue tests for the 316L Sample in 3.5% NaCl at 0.5V using SDC.

## 5.9.3 316L SS Results

As can be seen in Figure 5.48, in the first stage the current remained relatively stable, with a low value. This stage generally lasted around 0.3 of the fatigue life for the 316L SS samples from the start of cycling. It was then followed by a rapid increase in the current, which, it is suggested is related to the film-breakdown and pitting-process, as shown in Figure 5.49. During this stage the current increased continuously to about 0.35 of the fatigue life then a sudden decrease in the current occurred for a short time forming a distinct peak. This peak represents the micro-crack initiation stage after which the current increased again. The increase in the current may be attributed to the formation of fresh bare metal in the micro-cracks.
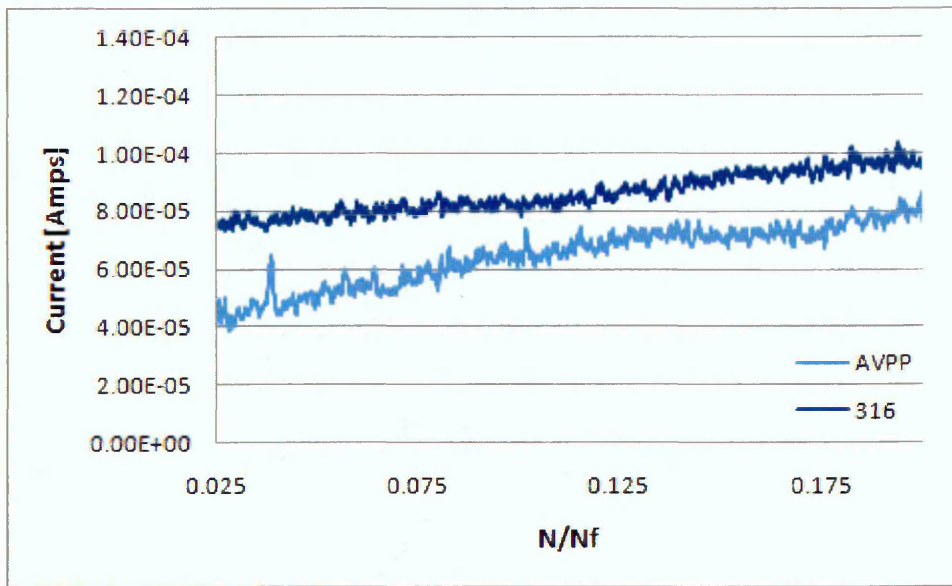
**Figure 5.48:** Current transient curve vs. fatigue life fraction in the initial stage of corrosion-fatigue tests for 316L and AVPP samples in 3.5% NaCl at 0.5V using SDC, maximum applied stress 260MPa, R 0.1, and $f$ 0.5 Hz.
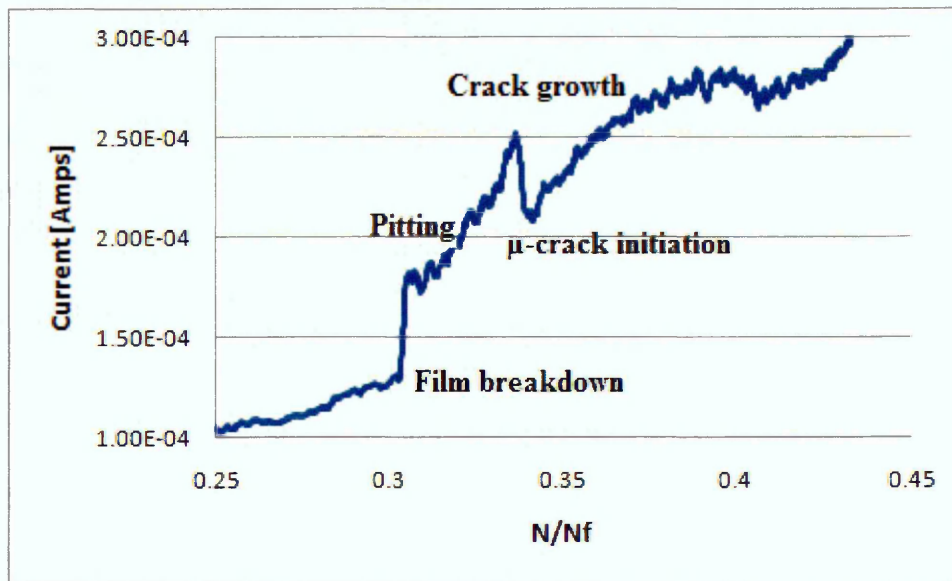


**Figure 5.49:** Current transient curve vs. fatigue life fraction in the second and third stages of corrosion-fatigue tests for the 316L Sample in 3.5% NaCl at 0.5V using SDC, maximum applied stress 260MPa, R 0.1, and $f$ 0.5 Hz.

Most of these micro-cracks are consumed by dissolve pit growth except for one or two cracks which propagate until the final failure. This localised electrochemical activity in the micro-cracks resulted in the development of the pit diameter. During localised

161

corrosion the current increased until all the micro-cracks are dissolved with the exception of the main crack which continued to grow simultaneously with current to the final failure as shown in Figure 5.50. Over all, the resulting current from corrosion fatigue tests for the 316L SS sample continued to increase during all the test stages regardless of the relatively stable low current during the first stage which corresponded to film dissolution before breakdown.
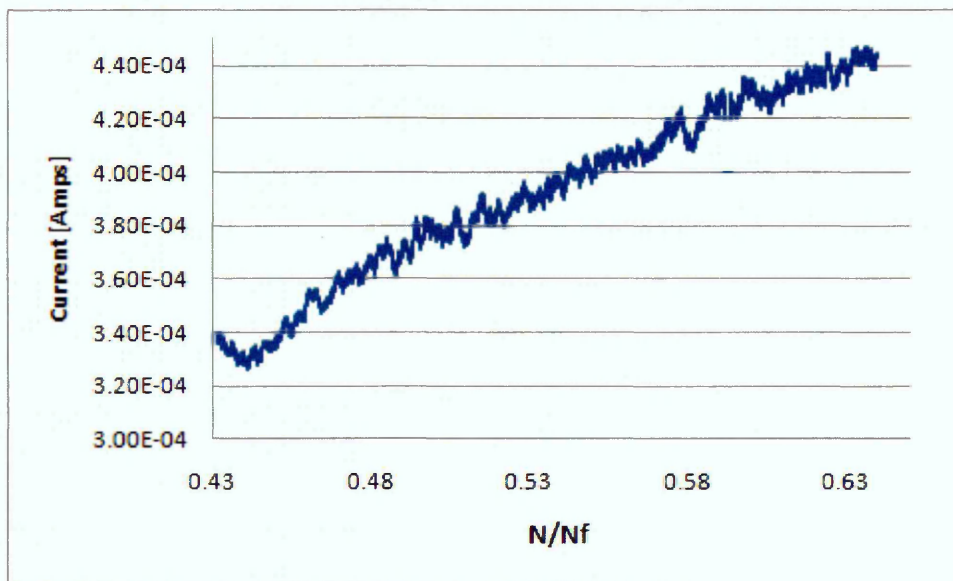


**Figure 5.50:** Current transient curve vs. fatigue life fraction in the fourth stage of corrosion-fatigue tests for the 316L Sample in 3.5% NaCl at 0.5V using SDC, maximum applied stress 260MPa, R 0.1, and $f$ 0.5 Hz.

## 5.9.4 316L-AVPP Results

Similarly the current generated from the corrosion-fatigue tests for 316L-AVPP-treated samples can be divided into four stages which reflect the electrochemical and mechanical activities. As shown in Figures 5.48, 5.51 and 5.52, the first stage of the current generated for the 316L-AVPP-treated samples remained relatively stable with a value even lower than the 316L sample first stage current value. However, this stage lasted longer than the first stage for the 316L samples, at about 8700 cycles compared to 6900 cycles for the 316L samples. Furthermore, it is difficult to characterise whether this slight change in the current value is an extension of the first stage or initiation of the next stage. This current range remains stable for quite a long time (to around 49% of the fatigue life) before it exhibits a marked change where it increases sharply, as shown in Figure 5.53. The first stage represents the film-dissolution stage which is followed by the pit-formation stage.
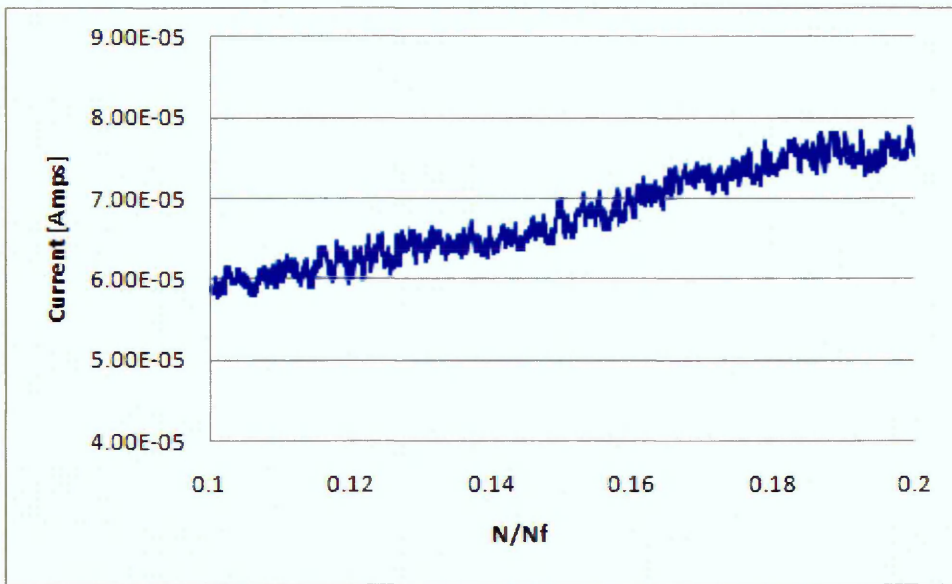


**Figure 5.51:** Current transient curve vs. fatigue life fraction in the initial stage of corrosion-fatigue tests for the 316L Sample treated by AVPP in 3.5% NaCl at 0.5V using SDC, maximum applied stress 260MPa, R 0.1, and $f$ 0.5 Hz.

The increase in current was associated with micro-crack initiation. The current further increased due to micro-crack growth and dissolution resulting in the development of the pit. This stage ended (around 0.53 of the fatigue life) in a peak which introduced the final stage where the current increased further until the final failure of the samples as shown in Figure 5.53.
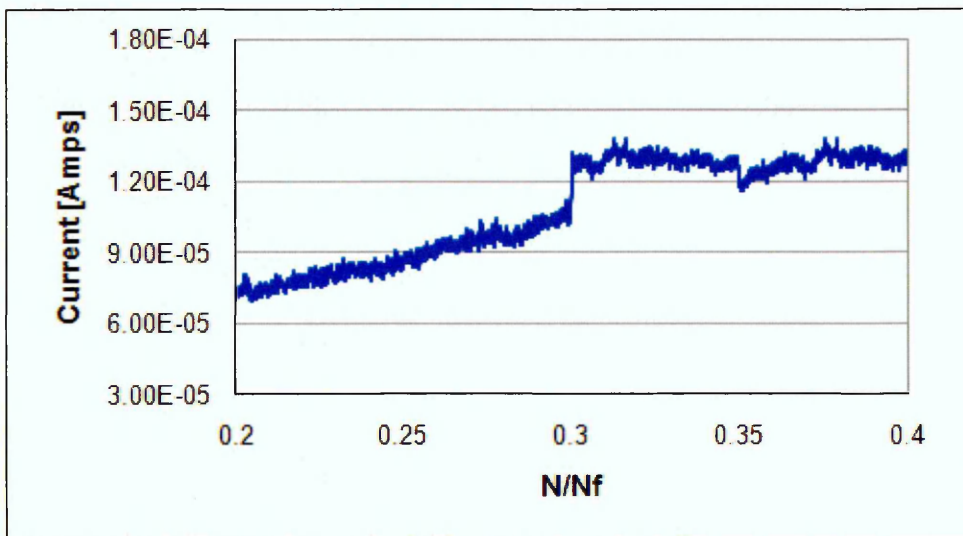


**Figure 5.52:** Current transient curve vs. fatigue life fraction in the second stage of corrosion-fatigue tests for the 316L Sample treated by AVPP in 3.5% NaCl at 0.5V using SDC, maximum applied stress 260MPa, R 0.1, and $f$ 0.5 Hz.
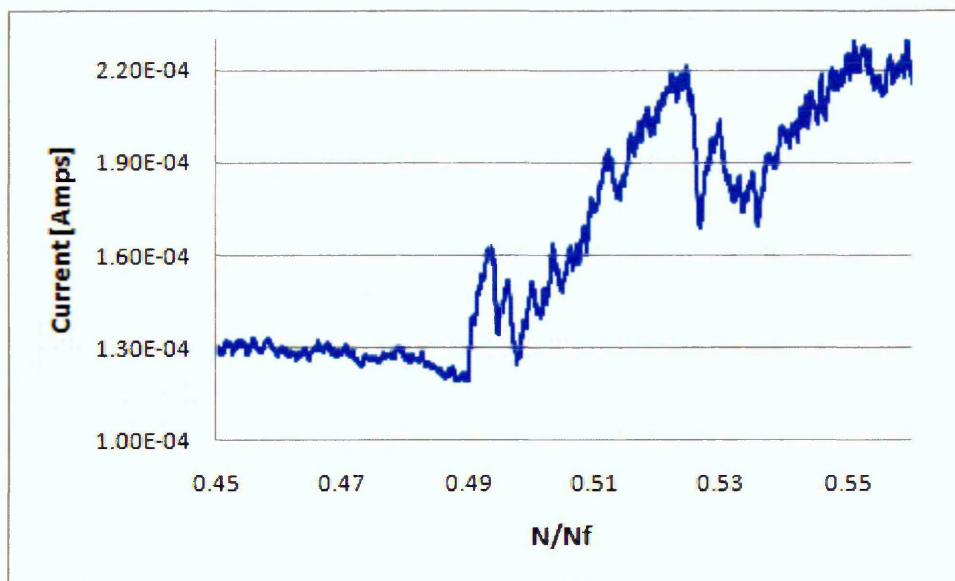


**Figure 5.53:** Current transient curve vs. fatigue life fraction in the fourth stage of corrosion-fatigue tests for the 316L Sample treated by AVPP in 3.5% NaCl at 0.5V using SDC, maximum applied stress 260MPa, R 0.1, and $f$ 0.5 Hz.

## 5.9.5 Pit Initiation and Growth

The corrosion-fatigue tests were stopped after a particular number of cycles or where noticeable changes in the current had occurred. The pit-profile generated during the corrosion- fatigue tests was measured using the Infinite Focus Microscope. A plot of pit-depth versus the number of cycles is presented in Figure 5.54 for the 316L SS samples and for the 316L-AVPP-treated samples. These results show that pits developed during the corrosion-fatigue tests grow gradually to a particular size for a number of cycles and then continue to grow rapidly until complete failure occurs. The maximum pit-diameter is generally equal to the SDC tip diameter which represents the droplet size. However, sometimes pit grew further to contain micro-defects generated because of cycling stress. Figure 5.55 shows an example of pit-growth during the corrosion-fatigue test for the 316L SS sample from 90μm diameter and 20μm depth at 5.5% of the fatigue-life to 800μm diameter and 500μm depth at about 80% of the fatigue-life. The latter includes the main corrosion-fatigue crack.
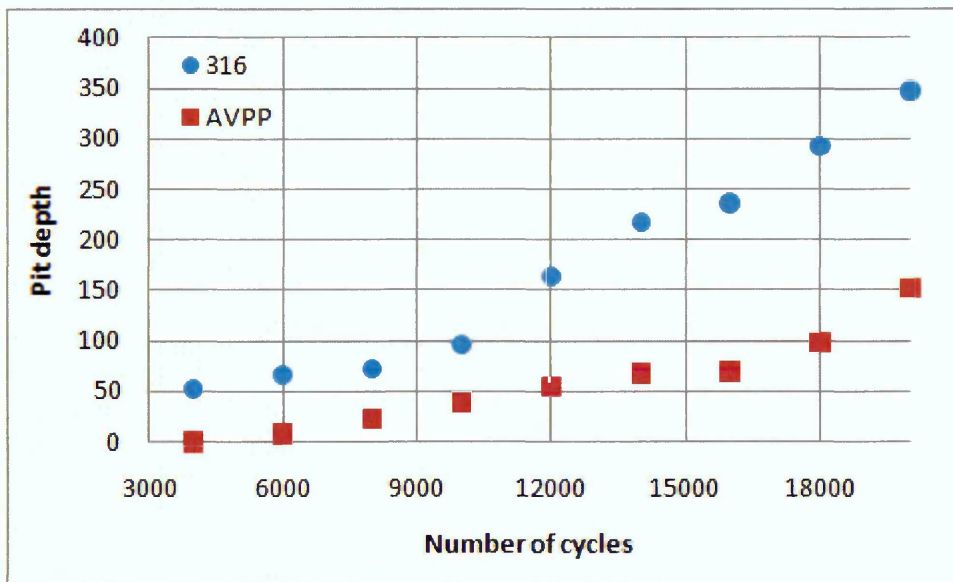


**Figure 5.54:** Pit depth vs. number of cycles for Samples 316L, and 316L with AVPP, during CF tests.
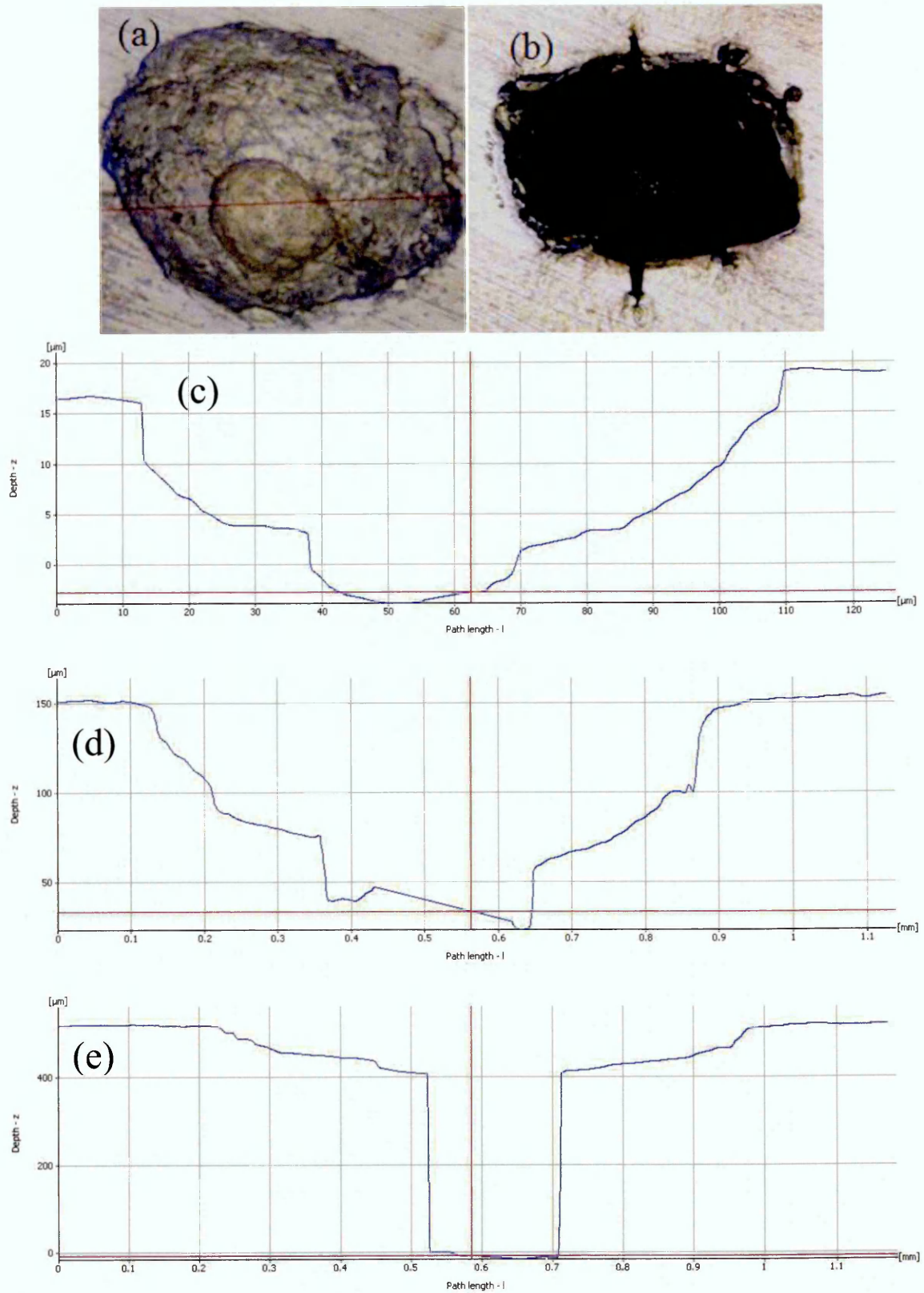
**Figure 5.55:** An optical micrographs of pit for the 316LSS Sample during CF tests at (a) 5.5% FL(22,600 cycles)  and (b) at 90%FL. It is growth profile (c) at 5.5% FL, (d) at 67%FL and (e) at 90%FL.

## 5.9.6 Corrosion Fatigue Crack Initiation and growth

This section represents the results of the corrosion-fatigue tests which were conducted for 316L SS and 316L-AVPP-treated at a stress level of 260MPa which represents approximately 87% of yield stress. These results include the crack growth which was obtained by Infinite Focus Microscope. This optical microscope allows the measurement of pit-profiles and cracks, and the taking of 3D images. Corrosion-fatigue cracks for both surfaces tested behaved in a similar manner regardless of the delay in crack-initiation which was caused by the delay in pitting for the 316L-AVPP-treated samples. Crack initiation was associated with a localised electrochemical pitting-process. As cycling continued, pits grew in diameter and in depth, resulting in the formation of a stress concentration site. Stress concentration from the pits causes the metal close to the pit to deform plastically as shown in Figure 5.56. It was found that micro-cracks were initiated at two locations. Some micro-cracks were initiated inside the pits and others were initiated at the perimeter of pits. Figure 5.57 shows the process of initiation and propagation of a corrosion- fatigue crack inside a pit generated by SDC. Those micro-cracks that initiated inside the pit were propagated to form a main crack which developed outside pits and led to failure.
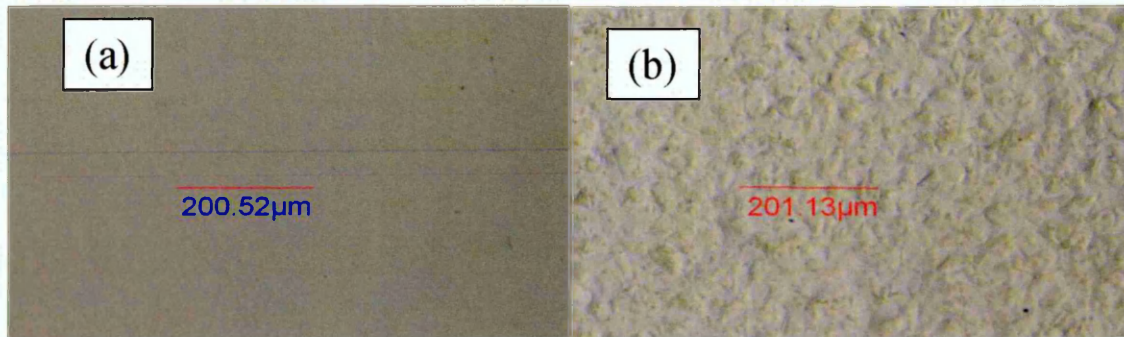


**Figure 5.56:** The 316LSS Sample's surface (a) before corrosion-fatigue and (b) a surface near to a pit after 5k cycles during corrosion-fatigue testing.
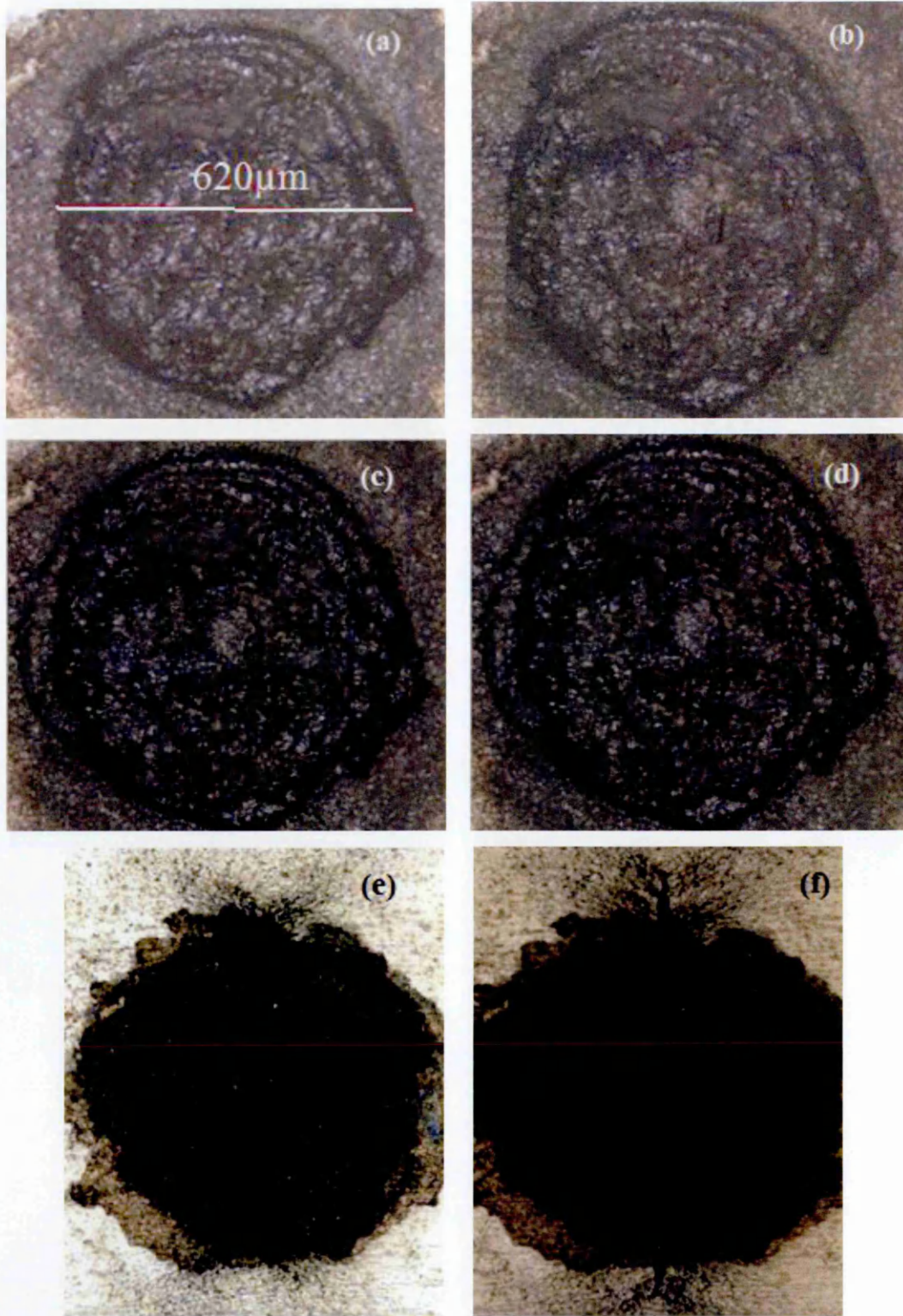
**Figure 5.57:** The corrosion-fatigue crack initiation and propagation process in association with corrosion pits, 260 MPa, 3.5% NaCl solution (a) 30% , (b) 35% (c) 45%, (d) 62%, (e) 76% and (f) 85% of fatigue-life.

168

Intergranular corrosion took place inside the pits at the grain-boundaries; as cyclic loading continued, these grain-boundaries formed micro-cracks see Figure 5.58. These micro-cracks were due to combination of stress and corrosion. Therefore, an increase in the current was noticed (section 5.9.2) for a while and then returned to its normal rate. The electrochemical activities inside the micro-cracks because of the increase of the solution's concentration can result in the production of new pits which become a stress concentration zone by increasing the pit's depth or diameter. The main crack grew from both ends of the pit at 90° to the tensile axis (mode I) and the crack growth was perpendicular to the applied load direction. The crack growth continued to final failure after overcoming the microstructural barriers for example grain-boundaries. When the crack encountered these barriers, the crack direction changed, forming two branches (secondary cracks) and producing a large plastic deformation zone. However, due to the fact that resolved stress is lower acting on the secondary cracks, overall propagation of the crack remained at 90° to the tensile axis (mode I) as can be seen in Figure 5.59.
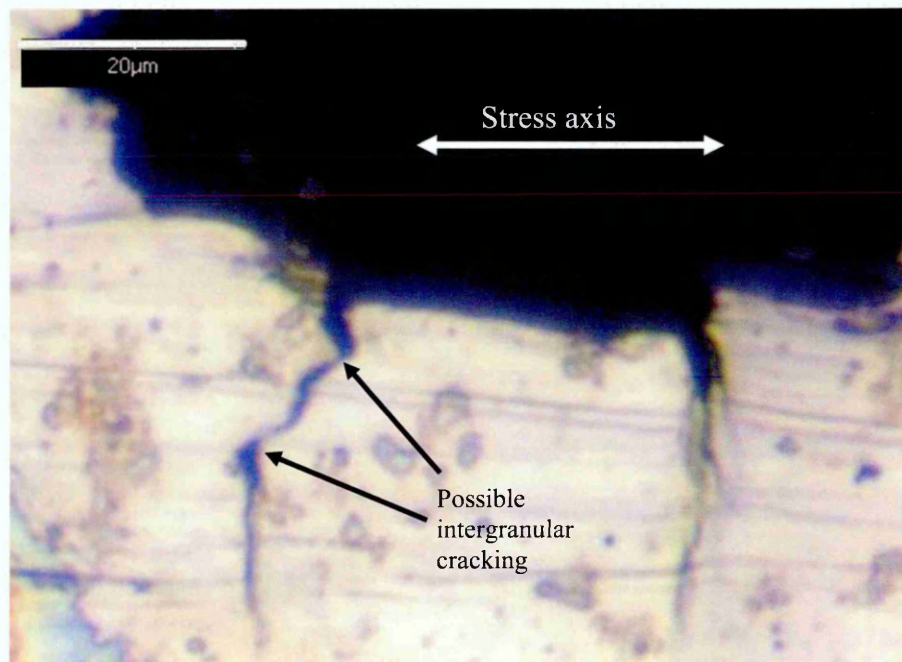


**Figure 5.58:** Corrosion-fatigue crack initiation in association with corrosion pit, 260 MPa, 3.5% NaCl solution at 45% of fatigue-life.

The other observation of crack initiation that has been observed is crack initiation from the pit-ends as can be seen in Figure 5.58. Some of these cracks dissolved electrochemically and some continued to grow to the final failure. The dissolving of the micro-cracks led to a widening of the pit, as a result decreasing the stress-concentration produced from the pit. Other cracks which continued to grow outside the pit were subjected to retardation of their growth because of grain-boundary barriers. As can be seen from Figure 5.59, this retardation resulted in the formation of large plastic zones after which cracks continued their growth. In the first type of crack initiation, it was seen that the crack grew from the inside of the pit to the outside until the failure. However in the second type, two major cracks were initiated at the edges of the pit; and these grew perpendicularly to the applied stress axes outside the pit to a particular size prior to coalescence. Before coalescence, the two main cracks grew towards the pit-centre assisted by dissolution of the growing crack see Figure 5.55.



**Figure 5.59:**
The Corrosion-fatigue crack initiation and propagation process in association with corrosion pit, 260 MPa, 3.5% NaCl solution (a) 45% , (b) 62% and (c) 93% of fatigue-life.
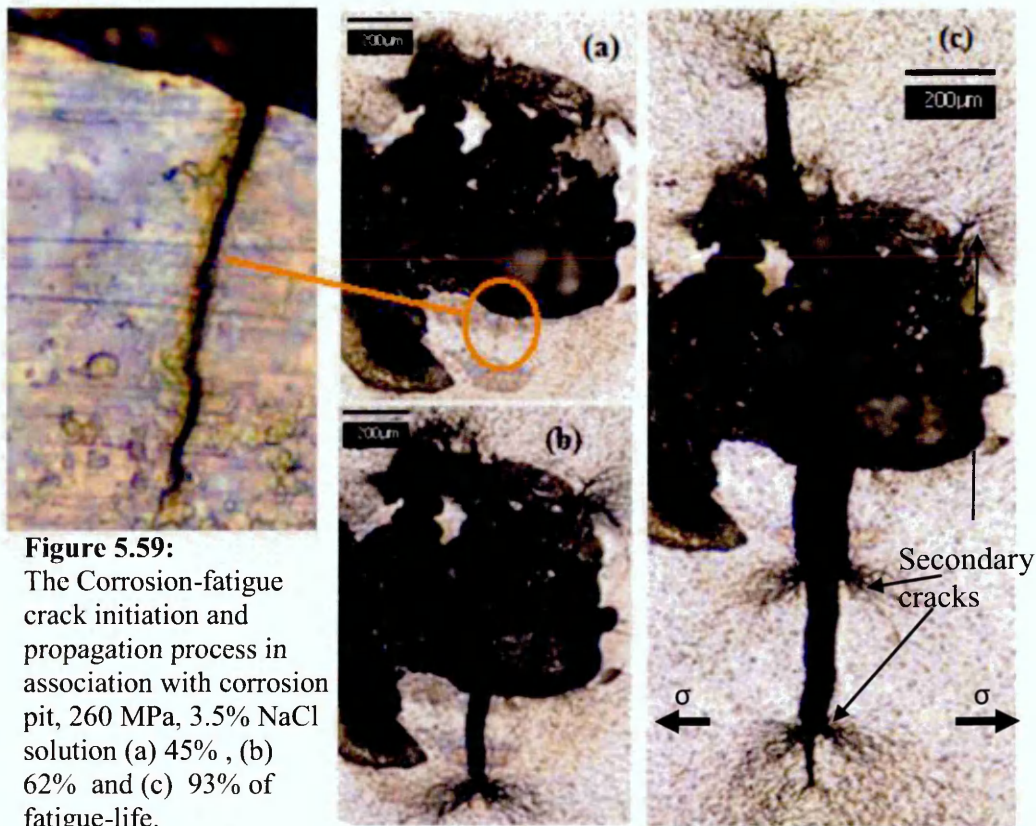
Crack growth behaviour was studied by measuring crack-length corresponding to a particular number of applied loading cycles. After collecting data from a test, a plot of surface crack-length versus fractions of fatigue life was obtained, as shown in Figure 5.60.
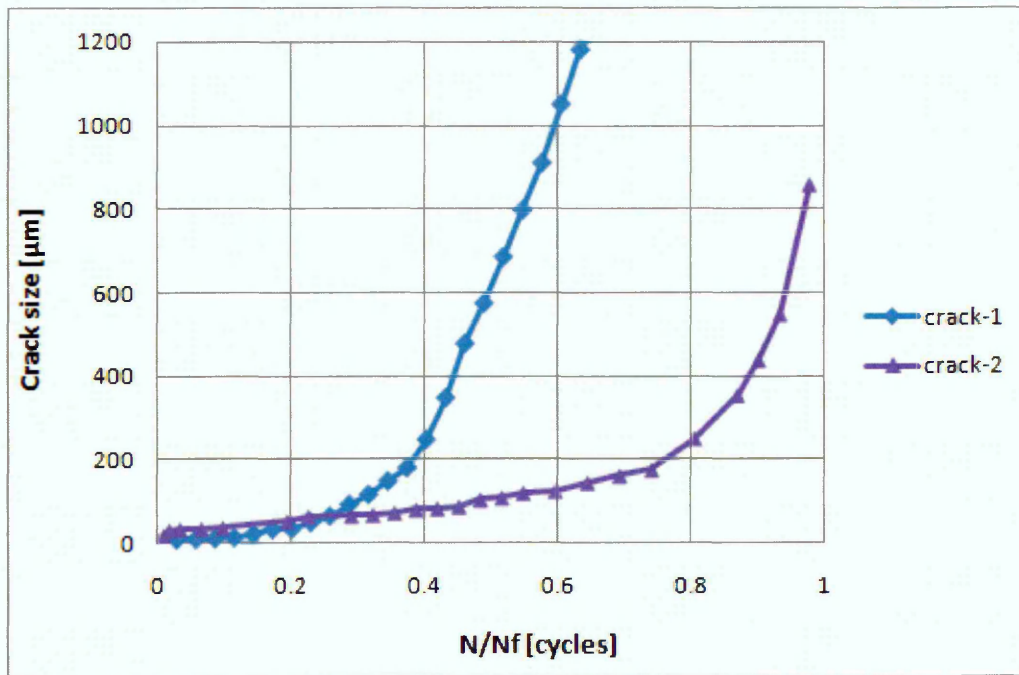


**Figure 5.60:** Corrosion-fatigue crack- length vs. fractions of fatigue life for the 316L SS Sample.

Once initiated micro-cracks from the end of a pit propagated in mode I tensile cracks perpendicular to the applied load axis. Initially these cracks showed high growth rate followed by deceleration in growth because they may have reached a grain boundary. After overcoming the first grain boundary cracks accelerated and showed another deceleration in growth on reaching the next grain boundary. This behaviour repeated for several times (6 or 7 grains as grain size estimated to be 23µm, section 5.3) and they

shown as cycles in Figure 5.61. This took about 160µm after which crack grew rapidly. This increase in crack growth rate continued up to the complete failure of the sample. However, when cracks initiated inside a pit almost no retardation was observed as shown in Figure 5.61 (crack1). This difference in growth behaviour may be caused by the difference in the environmental conditions for the two cracks. Cracks initiated inside the pit their growth enhanced by electrochemical dissolution because of solution contact. However cracks outside pits grew in dry condition i.e. not in contact with SDC droplet.
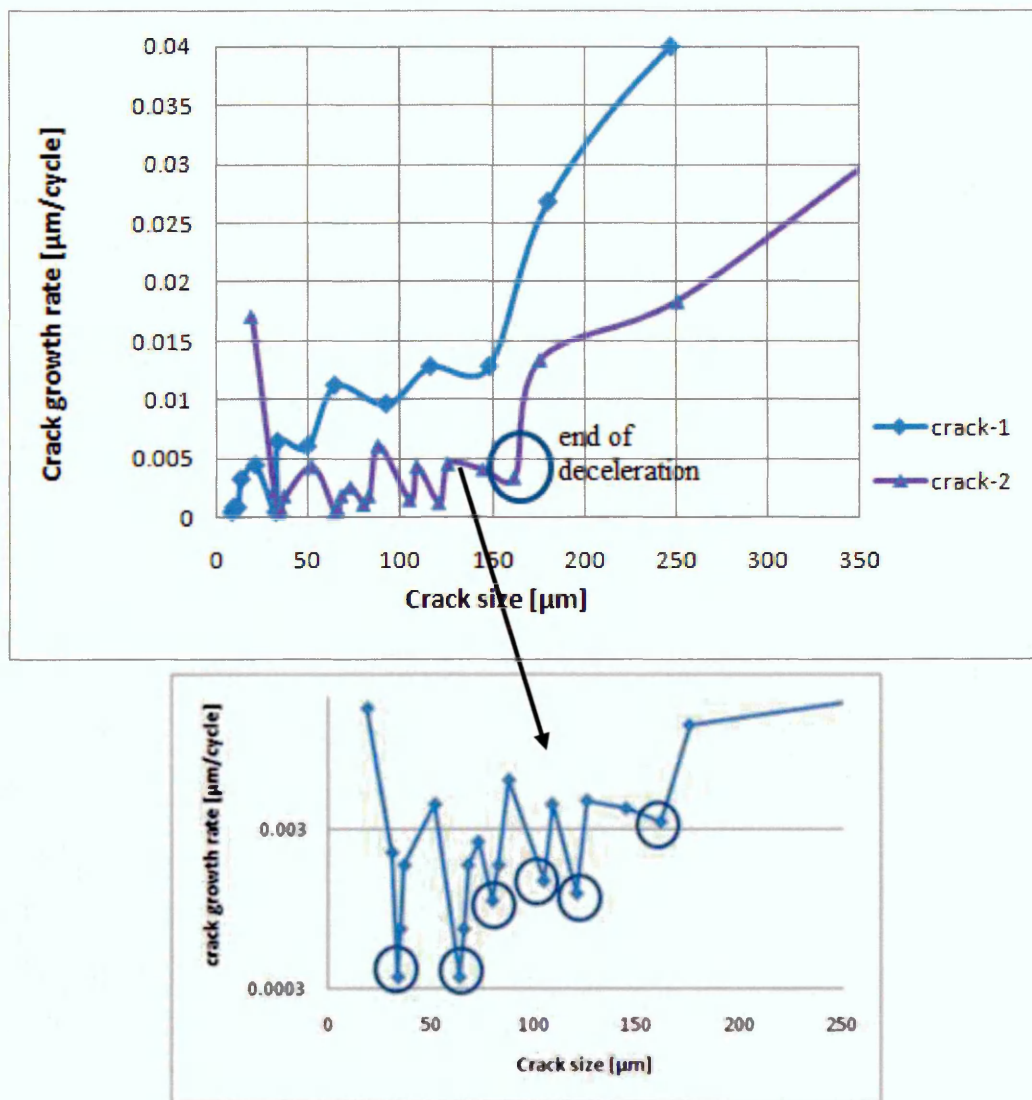


**Figure 5.61:** Crack growth-rate vs. crack size for crack-1 inside a pit, crak-2 outside a pit.

### 5.9.7 Fracture Surface Morphology

The fatigue fracture surface morphology of 316L specimens tested using SDC in 3.5%NaCl solution is shown in Figure 5.62. Approximately 75% of the fracture surface appeared relatively smooth and associated with a ductile growth of fatigue crack stage I and stage II. The remaining 25% of the surface had a rough texture associated with the final brittle fracture of the sample. Noticeable deformation of the sample exists in the area of final failure. On the fracture surface, several cracks were initiated from the pit to the depth direction, with one main crack that led to failure. It is worth noting for all the testing samples that all the cracks were initiated from corrosion pits.
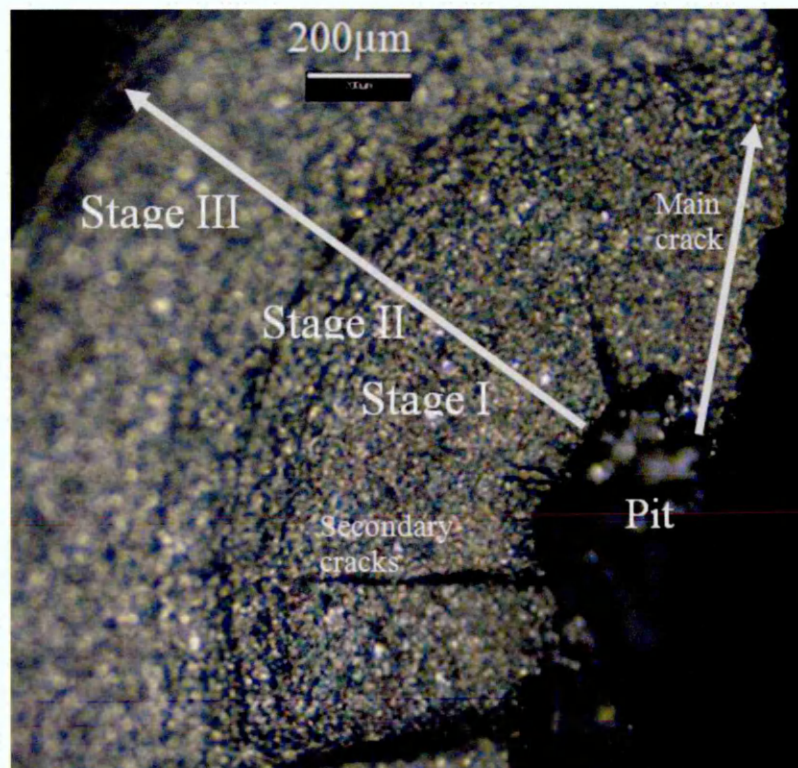


**Figure 5.62:** IFM fracture surface morphology for 316L SS after corrosion fatigue test, the axial tensile cycling loading direction is perpendicular to the image.

# Chapter 6- Discussions

## 6.1 Introduction

The main aim of this study was to evaluate the influence of surface film modification on the mechanical and electrochemical properties of 316L austenitic stainless steel. The alternating voltage passivation process was used as the modification technique for this material, as this had been reported to enhance the corrosion resistance of stainless steels as a result of increasing the oxide film thickness and changing in its composition [4, 5, 6]. However, no study has previously been reported with regard to the mechanical properties of this modified film, in particular the corrosion fatigue behaviour. Therefore, this study was focused on characterising the oxide film structure and chemical composition in order to understand the changes in the corrosion resistance of the modified surface film. These changes were mentioned in the literature and were confirmed in this study.

The mechanical behaviour of the modified surface film was also investigated. Therefore some mechanical tests were conducted, including residual stress measurement using XRD. Greater attention was given to the novel use of the SDC technique in conjunction with corrosion fatigue loading to assess stress-corrosion synergy effects on the modified surface film. The corrosion fatigue study attempted to characterise the pitting process, corrosion fatigue crack initiation and early crack growth behaviour. Results showed noticeable improvement in the corrosion fatigue life of AVPP-316L SS compared to the native 316L SS.

## 6.2 Material Characterisation

The microstructural characterisation of the 316L SS used in this study, indicated the presence of delta ferrite ($\delta$). The delta ferrite was found as isolated elongated grains with the major axis parallel to the rolling direction as shown in Figures 5.2 and 5.3. The delta ferrite phase consists of ferrite formed on solidification and is a phase rich in chromium which is ferrite-stabilising element and lean in nickel which is austenitic-stabilising element. The presence of delta ferrite is known to decrease the pitting corrosion resistance of the steels and, when present as a continuous grain boundary network, can decrease the resistance to sensitisation. The main problem with presence of delta ferrite in austenitic stainless steels, particularly when these steels are subjected to high temperature for a long time for example during welding or heat treatment, the delta ferrite transforms to sigma phase which is hard and brittle and reduces the ductility of the steel.

The 316L SS revealed also the presence of inclusions such as Al as presented in figure 5.4. Inclusions are preferential place for crack initiation in fatigue crack in air and for pit initiation in corrosion fatigue testing. Fatigue crack initiation in inclusions on the material's surface may occur through the isolation of the inclusion from the matrix interface, separation of internal boundaries or through fracturing of the inclusion itself. Under corrosion conditions these inclusions can act as sites for particle-induced pitting and serve to eliminate the fatigue crack initiation period of its fatigue life [18, 159]. The effects of inclusions on the fatigue life in air or in corrosion environment are not the objective of this because many researchers have previously investigated this area in details. An example being Giordani et al. [160] in their study of fatigue and corrosion–fatigue crack initiation mechanisms in stainless steel, where they confirmed the

relevance of the coarse precipitates usually associated with Al-rich inclusions in fatigue crack initiation, particularly in an aggressive environment.

Chromium carbides did not appear to be present along the grain boundaries of the alloy surface therefore this alloy can be considered as non-sensitized. This is because of the low carbon content of this alloy. It is known that austenitic stainless steel alloys containing less than about 0.03 weight% carbon should be stable while other austenitic alloys which contain carbon in excess of 0.03 wt % can precipitate $M_{23}C_6$ when cooling below the solubility line.

The duplex stainless steel 2205 presented a microstructure of 50% ferrite and the 50% austenite, which is the expected microstructure for this grade of stainless steel, see Figures 5.6 and 5.7. The two phases are distributed along the rolling direction with the grains in each phase following the same direction. This steel did not develop pitting during the electrolytic etching and generally the etching in this stainless steel was easy compared with the 316L stainless steel. The microstructure of the duplex stainless steel 2205 revealed a very low number of inclusions causing the material to exhibt high resistance to general and localized corrosion.

## 6.3 Surface oxide film

### 6.3.1 Compositions

The enhanced corrosion and mechanical resistance of the AVPP-modified oxide film was examined, based on a characterisation of the alloy surfaces prior to and after the modification procedure. X-ray photoelectron spectroscopy (XPS) and linear voltammetry were conducted in order to characterise the oxide film composition and structure and corrosion resistance response. XPS survey scans were taken at individual depths which revealed varying compositional levels of Carbon, Oxygen, Iron and

Chromium. The graph in Figure 5.9 shows the survey scans at individual depths for the 316L native oxide film. These surveys show that the Carbon and Oxygen peaks both diminish with etch- time while the Iron and Chromium peaks increase with etch- time. As can be seen from Figure 5.10, the Fe2p3 peak changed dramatically with depth. Close to the surface, the peak consisted of one sharp peak at 706.8 units and a broad peak at about 710 units. With etching, the broad peak rapidly disappeared, leaving only the sharp peak. It was identified that the first peak is metallic Iron (Fe 2p3) and the second Iron Oxide (Fe 2p3). The oxide layer disappears very rapidly, leaving Iron only as the surface is etched. Hence, if we examine the point at which the Iron Oxide layer disappears completely, in this case the 5$^{th}$ layer, we can determine the depth of this layer. This was found to be around 3nm.

Similarly the Chromium peak also consisted of two components, a narrow peak and a broad peak, and like the Fe signal, the broad peak (Chromium Oxide) disappeared with depth (although it took much longer to do so hence was found at greater depths) revealing metallic Chromium. Figure 5.11 presents an overlaying of the reported values for Chromium metal and Oxide.

It was mentioned in section (2.3.4) that stainless steel alloys exhibit passive behaviour and become covered with a thin oxide film on exposure to aqueous environments. The structure of passive films in stainless steels consists of a two-layer structure [85]. The inner layer is mainly composed of chromium oxide mixed with other chromium phases such as $Cr(OH)_3$ or $CrOOH$. The outer layer is composed of iron hydroxide $FeOOH$ and $\gamma$-$Fe_2O_3$. As can be seen in Figure 5.14 the depth-profile of the two Iron and two Chromium species were plotted. On the surface the Iron Oxide percentage drops and the Chromium Oxide is unaffected. It is only after about t = 12s that the Chromium Oxide percentage begins to drop. This drops to effectively zero by 40s. This appears to suggest the

presence of a multilayer system with a thinner layer of Iron Oxide on top of a thicker layer of Chromium Oxide. This is in agreement with what was found in literature [85, 161].

However, a different oxide film structure and composition was found in 316-AVPP-treated samples as can be understood see Figure 5.18. The 316L-AVPP-treated oxide film thickness was increased to more than two thirds of the native oxide film. Where Chromium Oxide represents most of the percentage of this oxide layer. Typically the Chromium Oxide percentage was doubled from 30% in the native layer to 60% in the 316L-AVPP treated sample. On the other hand the Iron Oxide percentage in the 316L-AVPP-treated oxide layer reduced from 50% to 30% and its thickness reduced slightly. Therefore it can be concluded that the thickness of the Chromium Oxide layer was increased after the AVPP treatment. In order to understand the process of 316L-AVPP-oxide film formation a model is summarised in Figure 6.1 [8].
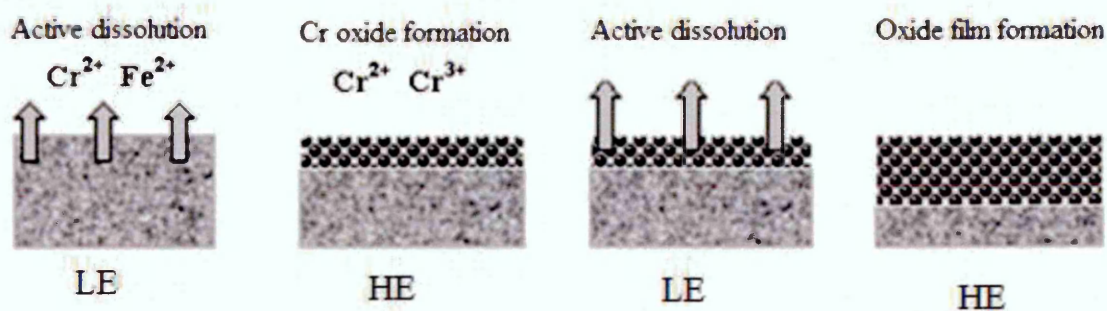


**Figure 6.1:** Schematic of Alternating voltage Passivation process at the low (LE) and high (HE) potentials [8].

In this process, at the low potential ionic species such as $Cr^{2+}$ and $Fe^{2+}$ ions are actively dissolved into the electrolyte adjacent to the surface of the substrate alloy. At the higher potential the dissolved ions, mainly $Cr^{2+}$ are re-oxidised to produce oxide particles, which grow to form thin continuous passive film. A low potential is then applied again

in the active region, where active dissolution takes a place at the surface. As a result of the repetition of this process a thicker oxide film is formed. The film thickness is dependent on the amount of ions released at low potentials and on the time of the process, however the thickness was decreased rapidly after particular time [8].

### 6.3.2 Film Hardness

Oxide film hardness was investigated using nano-hardness testing at different applied loads. However it was not possible to distinguish between the loading and unloading curves of 316L and 316L-AVPP samples until the applied load was reduced to 1mN. When the applied load decreased to 1mN (Figure 5.44) the indentation depth was further reduced to about 45 nm for the 316L oxide-film and to 60 nm for the AVPP oxide-film. This indicates that the 316L oxide-film has a higher hardness compared to the AVPP oxide-film. Although the AVPP oxide film is harder than the 316L oxide film, the fatigue life of 316L-AVPP is found longer than the fatigue life of 316L. This shows that the AVPP film improves the resistance to the pitting corrosion and consequently the corrosion fatigue life of the material. Further fatigue tests in air for 316L-AVPP may be needed to investigate their effects on the fatigue life.

## 6.4 Electrochemical Results

The electrochemical tests in this study were conducted in order to determine the corrosion resistance of 316L SS before and after the AVPP. The important properties examined were passivation behaviour and the pitting response for the untreated and treated surfaces. The pitting potential was used to investigate pit growth and its role in the corrosion fatigue behaviour of the materials. All the tests were carried under the same conditions such as test time, electrolyte concentration, environment temperature

179

and pH, as all these parameters affect the pitting corrosion behaviour. Therefore the study was restricted to a comparison of behaviour between the two surfaces.

The conventional technique of polarisation curve measurements for pitting corrosion determination was used in this work to evaluate the polarisation curve measurements obtained from SDC technique. The range of pitting potential values obtained for repeat tests conducted was not more than 50mV Ag/AgCl. It was assumed that the values of pitting potential obtained in this investigation were not combined by crevice events during the polarisation curves measurements. Figure 5.21 shows the polarisation curves obtained from the conventional (macro) and SDC (micro) techniques. These results showed that, despite the large difference in the electrode area of the two techniques, no noticeable variation were found between their polarisation curves. However, this is not the case for other studies using a micro-electrochemical technique. For example it was found that the current noise increased linearly with the exposed area, being ascribed to the dissolution of a set of small inclusions [162].

Figure 5.25 represents the potentiodynamic polarisation curves which were recorded for the 316L SS, 316L-AVPP-treated and DSS2205 in a 3.5%NaCl solution using SDC technique. A comparison of the stability of the passive layers can be obtained from these potentiodynamic polarisation curves. As can be seen the three polarisation curves exhibit active-passive behaviour. The corrosion potential $E_{corr}$ of the three samples was found to be around 0 mV vs Ag/AgCl. The pitting potential of the unmodified 316L surface showing the onset of active-passive behaviour at between 420 to 450 mV vs. Ag/AgCl. Using a scan rate 0.33 mV/s Cheng et al. [163] reported a pitting potential around 600 mV which is more positive than was found in this study. This might be attributed to : *i)* the higher concentration of the electrolyte used in the present study that

is 3.5NaCl wt% compared to 0.1wt % NaCl used by Cheng; and *ii*) the difference in the scan rate as the scan rate applied in this experiment was only 0.166 mV/s.

However the pitting potential of the 316L-AVPP-modefied samples was found to be around 1000mV vs. Ag/AgCl being associated with an extremely wide passive region, which shows that AVPP-modified surfaces have a greater ability to resist localized corrosion. Mansfeld et al. [5] showed such improvement in 304 austenitic stainless steel after AVPP treatment, He et al. [6] however reported, for a treated duplex stainless steel an increase in corrosion potential where the pitting potential remained unchanged. Generally all these results indicate that the alternating passivation process provide an improvement to the passive properties of stainless steel alloys exposed to aggressive environments. Mansfeld et al. [5] suggest that it is unlikely that significant changes have occurred in the Cr content of the passive film as a result of AVPP. However He [6] and in this work using XPS analysis show that significant enrichment in chromium occurs in an AVPP passive film compared to an unmodified passive film.

The industrial demand to use DSS2205 is increasing over that of 316L for a wide range of applications [164], the most important reason being the dramatic increase in corrosion resistance. Therefore, DSS2205 was used in the present work for comparison particularly in regard to the corrosion resistance. As can be seen in the polarization curves in Figure 5.25 the pitting potential of DSS2205 is almost the same as the 316L-AVPP-treated surface. Therefore the AVPP treatment could be effective in developing highly protective surface films particularly in the presence of environments containing chloride ions.

The results of electrochemical impedance spectroscopy confirmed the findings of the potentiodynamic polarisation curves as shown in Figure 5.31. It can be seen that the impedance response shows stable impedance for the three samples. The 316L-AVPP

modified surface-film sample shows a film-resistance approximately one order of magnitude higher than the unmodified film. The 2205 surface-film sample has an equivalent impedance response to that of the modified surface-film sample. This supports the observation of stable passive film and high pitting potentials obtained from the polarisation plots and appears in agreement with the literature [6]. In the EIS comparative study between the passivity state of 316L and DSS2205, the difference in the impedance was associated with an increase in the film resistance as a result of increase in the film thickness [163].

Linear voltammograms in %wt 3.5 NaCl solution for 316L SS and 316L-AVPP-treated samples were obtained in order to compare the current peaks and the corresponding electrochemical processes taking place on the material surface films as well as the influence of the potential scan rate. Thus linear voltammograms were recorded at different scan rates from 0.005 to 0.1V/s in the potential range from -1V to 1V. As can be seen in Figures 5.27 and 5.28, the main features of the linear voltammograms are similar, with some differences between both surface-films. For both samples each curve has the same trend but it is apparent that the total current increases with increasing scan-rate. The potentials of the positive and negative peaks move slightly, with increasing scan rate, towards more positive and negative values, respectively. Furthermore the current increases with increasing scan rate and is ascribed to the fact that a slow scan rate allows more time for diffusion and oxidation to take place on the material surface [165].

As it can be seen for the 316L surface-film sample in Figure 5.27 two peaks are observed. The first peak is at a potential of $-0.4$ V which can be ascribed to the oxidation of Fe (II) to form Fe (III) [166]. It has been understood that this is due to the

formation of $Fe_2O_3$ [167, 168], while others reported that $Fe(OH)_2$ oxidises to FeOOH to form a Fe(III) hydrous film on the $Cr_2O_3$ film [169, 170].

It is followed by a region with a constant current density, up to 0.4V. where another peak is formed in the transpassive region, at a potential of 0.65V. This peak is associated with the oxidation of Cr (III) to Cr (VI) [167]. However, there are different views on whether or not the Cr(VI) phase is soluble [167-170]. It is suggested that there are two kinds of Cr(III) species in the passive film; one in the outer layer, which oxidizes to soluble Cr(VI) and the other in an inner layer, which oxidises to Cr(VI) that is retained in the passive film [170]. These authors further suggested that with increasing polarization time, Fe-chromite will form, which prevents any further oxidation of Cr(III) to soluble Cr(VI). Using XPS results Langevoort *et al.* [171] suggested that an $FeCr_2O_4$ layer forms at the interface between iron and chromium oxide. The Ni (II) species formed during the passivation process may have been oxidised to Ni (IV) Oxide ($NiO_2$) in this potential range [158].

Figure 5.28 shows the linear voltammograms of the AVPP film. The curves have the same trend as the untreated 316L sample with deviations in the peaks' positions and in their current size. It is seen the first peak moved from -0.4 V to -0.3 V and the current decreased from 0.0004 Amps to 0.0002 Amps. This may be associated with the change in the oxide film form from Fe (II) in the native oxide film to Fe (III) in the 316L-AVPP-treated passive film. The Fe (III) oxide is more stable than Fe (II) which leads to reduce the diffusion rate i.e. the current.

The second peak at 0.65V potential moves to 0.85 V potential; however the current increased from 0.0008 to 0.0009 Amps. As this is a chromium oxidation peak, the movement to more noble direction and the increase in current can be both ascribed to the enrichment in chromium in the AVPP oxide film.

## 6.5 Pitting Behaviour

Localised corrosion including pitting corrosion is classified as one of the major damage mechanisms affecting the integrity of many materials and structures in a variety of applications. Corrosion pits generally initiate due to some chemical or physical heterogeneity at the surface, such as inclusions, second phase particles, flaws, mechanical damage, or dislocations [172].

### 6.5.1 SDC Studies

To further understand the mechanism of pitting corrosion in stainless steel alloys the scanning droplet cell (SDC) technique was used to generate corrosion pits under controlled potential. The use of microcapillary technique in evaluation of localised corrosion has previously been reported [142, 143, 162, 173, 174, 175]. In the case of the SDC studies presented here, the pit profile for a given flow rate, surface finish and applied static stress was measured using an infinite focus microscope (IFM). Typical pits obtained by this technique are shown in Figure 5.32. The shape of the removed material in Figure 5.32a was a circular groove which appears dark in the image because of the difference in depth. The central area inside the circle appears to form an island which includes intact surface with disruption of few undeveloping pits this is clearly seen in Figure 5.33. This phenomenon was reported in other work [176]. It is noteworthy that the groove formed varies in depth, where the groove at the solution inlet side is deeper than at the outlet side. This behaviour is considered to be the result of increased availability of oxygen, and subsequent increased dissolution, on the inlet side. Furthermore it might be reasonable to assume that the actual flow dynamics are slightly different on the inlet and outlet sides, with the outlet side being somewhat more quiescent.

However, the pit shown in Figure 5.32b is the most common observed. The cross-section of this kind of pit having a large diameter on the surface and becoming gradually more narrow towards the bottom of the pit to give a (V) shape and in some cases a (U) shape. Examples of pit cross sections obtained using the SDC in 3.5% wt NaCl are given in Figure 6.2.
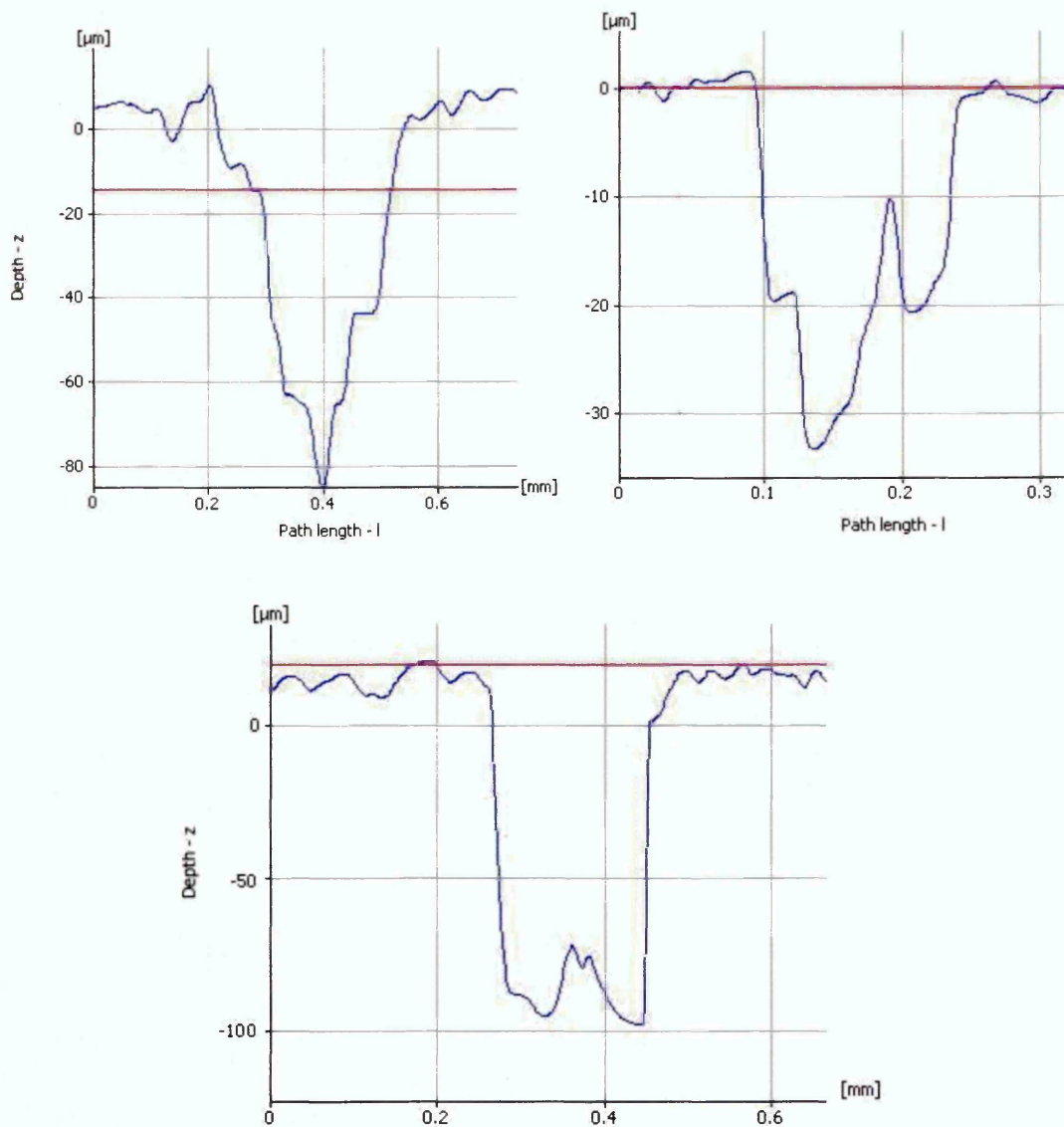


**Figure 6.2:** Typical shapes of pits generated on 316L SS surface using SDC in 3.5wt%NaCL, obtained by IFM.

The mechanisms of pit growth are generally measured by electrochemical or metallographic methods, however a combination of the two methods is usually preferred. Figure 5.34 represents results from SDC tests in term of material weight, as calculated using Faraday's law, compared to weights calculated from the volume of material removed measured using IFM. In the low flow rate regime (below 25 mm$^3$/s) there is reasonable correlation between the SDC and IFM results. However, when higher flow rates were applied the difference between the two results increased. Pits produced at low flow rates were found to be more shallow than pits produced from higher flow rate. Shallow pits can be measured more precisely with IFM than deeper pits because of the increase in possibility of hidden undercutting of pits.

In electrochemical measurements, the value of the flow rate is important as flow plays an important role in transporting oxygen and active species to the metal surface and promotes the removal of the products of corrosion away from the site thereby changing the diffusion characteristic of the corrosion cell. In this study for the set electrochemical conditions, it was found that the current density increases with the increase in flow-rate as shown in Figure 5.35. It has already been suggested that increasing the flow rate increases the rate of oxygen release from the electrolyte to the metal surface which increases the rate of corrosion [177]. Krawiec et al. [178] studied the parameters responsible for affecting the mass transport and the distribution of species in micro-capillaries close to the specimen surface, they reported enhancement in cathodic current with increasing electrolyte flow rate. However in a previous study [179] it was found that there was no effect on corrosion rate of 304 stainless steel when the flow velocity of natural water containing ozone increased from 0.05 to 1.7 m/s. However, the pitting potential was decreased in a potentiodynamic scan test when the flow rate increases for same material in 3.5% NaCl [180].

The results of this experimental study also show differences between the three surface conditions, where there is a higher material loss as the surface roughness increases from 0.68μm to condition 1.8 and 3.5μm Ra as shown in Figure 5.36. This behaviour has also been observed for different surface conditions and is reported in other studies [177, 180, 181, 182]. Hong at el. [183] investigated the effects of surface roughness on early stages of pitting corrosion of type 301 stainless steel suggesting that metastable pit growth on smooth surfaces is more difficult than that on rougher surfaces.

## 6.5.2 Influence of Strain Rate on Pitting

Many research studies have been presented in the past in regard to the role of stress on the localised corrosion [184, 185]. However, only a few researchers have investigated the role of stress on the pitting mechanism on passive materials with the local probes [186]. One of the objectives of the use of the potentiostatic polarisation test in the present work was to quantify the degree of localised electrochemical activity involved in the nucleation of corrosion pits in terms of pit current. In order to determine localised current directly from potentiostatic measurements the SDC technique was used. In this study, uniaxial tensile stress was applied simultaneously with potentiostatic polarisation in order to evaluate the kinetics of localized corrosion at a fixed potential, 1V vs. Ag/AgCl, over a 1hr period. Current was recorded continuously over time at fixed potential. The resulting current was then used to obtain the material removed during dissolution using Faraday's law.

The localised corrosion-rate of the stressed sample during potentiostatic polarisation, shown in Figure 5.37. it was observed that the mass loss hence pit current, increased as the applied stress increased. However it was also noted that the rate of increase, changed with increasing applied stress, a slight increase in the corrosion-rate Figure 5.38 also

shows current density for 316L SS samples potentiostatically polarised at 1V vs. Ag/AgCl, for samples under tensile stress at 0 and 100 MPa (0.33 of yield stress) of the alloy. Vignal at el. [187] used microcells and image analysis method to determine the behaviour of stainless steel under straining conditions. They observed stable pits in grains with a high density of slip bands at 650 mV/SCE.

Although 316L SS is a very widely used alloy, it has not been amenable to reproducible pit growth measurements in neutral NaCl solutions at open circuit potential. This is basically because of the tendency for expected repassiviation of the pits when the stainless steel is at open circuit potential [188]. This is the reason for the kinetic studies of potentiostatic controlled pit growth in variety of metal-electrolyte systems. The pit growth law reported in this study, equation 5.2 is not applicable to the behaviour of 316LSS in 3.5 wt% NaCl at open circuit potential. The relationship given in this study is for pit depth as a function of time for pits growing under high potentiostatic conditions. It has been reported that the rate of pit growth is characterised by a gradual increase in the current at constant potential, which is proportional to $t^2$ or $t^3$ [189]. For instance at controlled applied anodic potential, the pit growth in terms of the pit dept as a function of time of polarisation has been described as a power formula $P_d = kt^b$ where k and b are experimentally derived empirical constants [14, 94]. Gonzalez [84] generated pits on 316L stainless steel in artificial seawater solution using a conventional corrosion cell under cycling loading, reporting a pit growth law that can be expressed as: $D = 26\ t^{0.6}$, where D is the maximum pit depth in µm and t is the polarisation time in minutes.

## 6.6 Corrosion Fatigue

One of the main objectives of this work was to utilise the scanning droplet cell technique simultaneously with a fatigue rig in order to measure the degree of localised corrosion activity via corrosion current measurements involved in the nucleation of cracks from corrosion pits. The SDC measurements were conducted on 316L SS and 316L-AVPP-treated samples whilst simultaneously being subjected to cycling tensile loading using a servo-hydraulic stress rig. These tests were carried out in order to determine the influence of the AVPP on corrosion fatigue life of 316L SS material. The testing system was commissioned and calibrated to ensure its capability to obtain accurate results.

In order to investigate the pit initiation and growth behaviour, successive observation of the specimen surface during the corrosion fatigue process were performed. The observations of fatigue damage on the specimen surface and the measurements of the profile of corrosion pits were made using IFM.

Figure 5.46 shows the fatigue life bar-chart in air for 316L SS and in 3.5%NaCl environments for 316LSS and 316L-AVPP-treated samples. The fatigue life to failure in 3.5%NaCl solution is smaller than that in air and interestingly the fatigue life of 316L-AVPP-treated sample is higher than the fatigue life of 316L SS in 3.5%NaCl using SDC technique. The results show that alternating voltage passivation process in 3.5%NaCl solution restores the fatigue life of the 316L to values near those obtained in laboratory air. Therefore in this study it was found that the fatigue-life of the 316L material is reduced to about 30% when the same test is conducted in the presence of 3.5%NaCl. Although results of XRD showed that AVPP reduced the compressive surface residual stress compared to untreated 316L, the fatigue-life of 316L in 3.5%NaCl increased to about 18% as a result of the introduction of AVPP treatment. The passive film produced

by AVPP enhanced the resistance to pitting and pit growth rates were smaller when compared to untreated samples. The smaller pit depth leads to a lower stress concentration and as a result delay in crack initiation with the resulting effect being an increase in total fatigue life. The influence of cyclic stress in the relaxation of compression stress is greater for the AVPP sample than for untreated sample (Figure 5.45). This would have the effect of increasing the effective applied stress and would be expected to reduce fatigue life. However it can be seen that the AVPP lifetime is 18% greater thereby indicate the important role of the passive film in limiting the development of crack initiating pits.

Ebara [190] reported a reduction of fatigue strength of austenitic stainless steel to less than 20% due to 3% NaCl. Akid [116] showed that adding oxidizing agents to the solution in the form of $NaNO_2$ led to a more resistant passive film and an increase in the time for film breakdown as subsequent corrosion-fatigue life time. When considering damage accumulation under the conditions of corrosion fatigue, it is necessary to determine the role of the passive film and its subsequent breakdown, which leads to localized corrosion [191].

It has been demonstrated that the fatigue environment interaction can be assessed from transient current curves recorded during cyclic deformation, which can provide valuable information of the damage mechanisms of corrosion fatigue [84, 191, 192 ]. Electrochemical noise was measured for both 316L and 316L-AVPP-treated austenitic stainless steel in 3.5%NaCl aqueous solution.

During the corrosion fatigue test, the development of the electric current can be divided into four stages. These stages relate to electrochemical and mechanical processes. The electrochemical process comprises film-dissolution and localised corrosion including pit-initiation and pit-growth. The mechanical processes include micro-cracks initiation,

early corrosion-fatigue crack-growth and main crack-growth to final failure. As can be seen in Figure 5.48, in the first stage the current remained relatively stable, with a low value. This stage generally lasted around 0.3 of the fatigue life for the 316L SS samples from the start of cycling. The only electrochemical process occurred in this stage is oxide film dissolution, its stability depend on the capability of the oxide film to resist dissolution. It was shown in this study using XPS, this stainless steel alloy exhibits high chromium contents on the oxide film with less iron. Therefore the resulting current remains low during this period. Small fluctuations on the current were observed in the very early part of this stage which may be associated to the mechanical cycling loading as shown in Figure 5.47.

Figure 5.49 shows the development of corrosion current as a function of fatigue life. It was found that corrosion pit initiates when current start to increase. It is known that for stainless steels, compositions can be quite different between the surface and the interior under corrosion conditions and that the chromium content is much higher than that of the Fe on the specimen surface. Therefore the increase in current is an indication of the breakdown of the passive film (surface) where the solution becomes in contact with the bulk metal. This increase in current continued simultaneously with the pit growth to around 35% of the fatigue life of the specimen where sudden decrease in the current was observed. This sudden decrease in current may be related to the initiation of corrosion fatigue crack. This is an important feature as it may be used to assess pit depth at the pit to crack transition. In this case corresponded to around 8050 cycles with a pit depth 72μm. Gonzalez [84] in a corrosion fatigue study using 316L stainless steel has provided experimental data to suggest that the transition from a pit to a crack may be related to a change in the local electrochemistry, as observed through a decrease in the

local pit current density at 175μm pit depth. This behavior was also observed for a low-carbon steel tested under tension–tension loading in artificial seawater [193].

Finally, in the last stage the current increased continuously until final failure of the sample. The increase in current is related to the revealed of bare metals to the solution. Li [192] has attributed this increment to the plastic deformation which created areas from which dissolution of atoms occurred more readily than that from the relatively unstrained surface. This stage occupied about 60% of the total fatigue life where the passive film dissolution and pitting took about 40% of the total life. The behavior of 316L-AVPP-tereated sample is very similar to the behavior of 316L sample. However a significant difference was that the passive film dissolution stage took longer than the 316L samples. The passive film formed in these treated samples was thick enough to prevent the surface material from dissolving leading to an increase in the total fatigue life see Figure 5.53. A plot of pit-depth versus the number of cycles for the 316L SS samples, with and without AVPP treatment during corrosion fatigue, is shown in Figure 5.54. In this figure a power relationship between the pit diameter and time appears to exist for the plots. The maximum depth of corrosion pit increases with increasing number of cycles as shown in Figure 5.54.

It was found that enhanced dissolution at the metal surface occurred during the application of stress, and it was suggested that plastic deformation created areas from which dissolution of atoms occurred more readily than that from the relatively unstrained surface. This can be seen in Figure 6.3 where pit depth developed in an unstressed sample compared to that obtained from a corrosion fatigue sample.
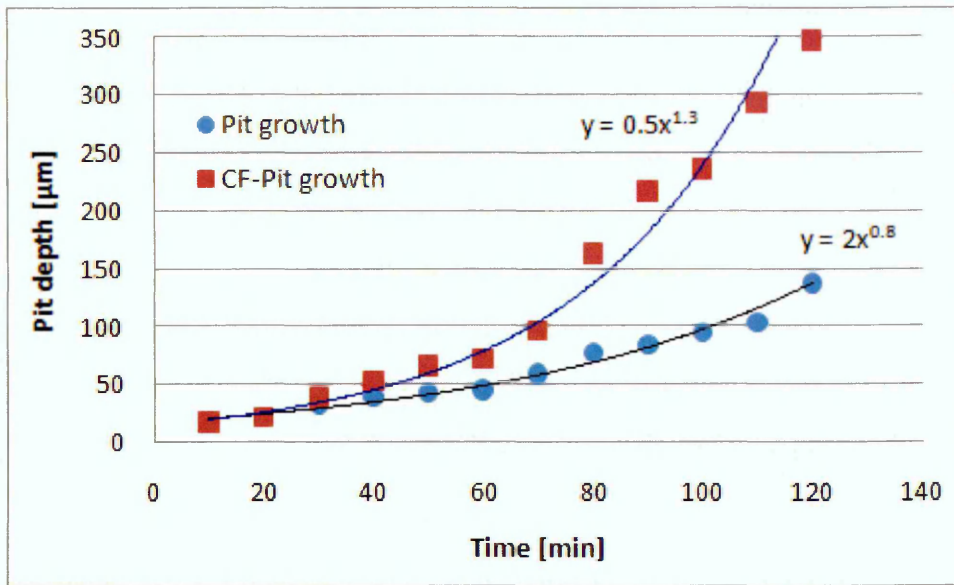
**Figure 6.3:** Pit depth vs. time for Samples 316L, and 316L with AVPP, with (CF-pit growth) and without cycling loading (pit growth).


## 6.7 Determining of Threshold Stress Intensity Factor

The stress intensity factor can be calculated using the pit depth size corresponding to the pit-crack transition. The stress intensity factor range $\Delta K$ has been used [146], to account for the role of pitting in defining threshold conditions for cracking using Linear Elastic Fracture Mechanics (LEFM) in the context of fatigue-limit based propagation, using equation 6.1.

$$\Delta K_{th} = \alpha\ \Delta\sigma_{th}\sqrt{\Pi a} \qquad (6.1)$$

Where a is the pit depth, $\alpha$ is a geometric factor. For semi-circular surface cracks, $\alpha$ is approximated by 0.67 [146] and $\Delta\sigma_{th}$ is the threshold fatigue strength is 220 MPa for 316L SS in environments containing chloride ions [24]. Using equation 6.1 and the pit depth (at the pit-crack transition) obtained from the IFM the threshold stress intensity factor range was found to be: $\Delta K_{th}$ = 2.23 MPa√m. The range of the pit depth in the crack transition for 316L SS samples at around 30% was found to be from 70 to 95µm. Therefore the value of threshold stress intensity factor range vary according to these pit

193

depths for the pit-to-crack transition and were found to be: $\Delta K = 2.18$ to $2.55$ MPa$\sqrt{m}$. Similarly the range of the pit depth in the crack transition for 316L- AVPP samples at about 53% of the fatigue life was found to be from 67 to 100μm, and hence the stress intensity factor range is $\Delta K = 2.1$ to $2.6$ MPa$\sqrt{m}$. From studies of the effect of pitting on the corrosion fatigue crack nucleation, Zhou et al. [146] reported values of 5.06 to 6.16MPa$\sqrt{m}$ for the threshold stress intensity factor range for cracks nucleated from pits of 110μm depth in 12 Cr martensitic steel in 0.1 M NaCl solution. Masaki [194] stated threshold value of the stress intensity factor range of Type 316L and Type 304 stainless steels, which were obtained by the crack propagation test using a CT specimen, having values of 3.5 and 2.5 MPa $\sqrt{m}$ respectively. In a corrosion fatigue study in 316L SS Gnozalez [84] for cracks nucleating at 175μm pit depth reported a $\Delta K = 3.4$ MPa$\sqrt{m}$.

# Chapter 7- Conclusions and Future Work

## 7.1 Conclusions

The influence of material surface condition, notably passive film condition and surface residual stress and the effect of applied surface stress on the development of corrosion pits has been assessed in relation to their role on the fatigue behaviour of stainless steel materials, in particular the early stages of corrosion fatigue. Several experimental techniques have been used to quantify changes in material response during stress and corrosion interactions. The original surface film of 316L austenitic stainless steel was modified electrochemically using an alternative voltage passiviation process (AVPP) to study the effects of this modification on the mechanical and corrosion properties. The following conclusions were made:

- Chromium enrichment in the modified passive film surface was observed, as was increase in the passive film thickness for the modified surface.

- Potentiodynamic polarization and electrochemical impedance spectroscopy (EIS) tests were performed in artificial seawater on the original and the modified passive. Results show that the impedance and pitting potential $E_p$ of the modified film is higher than the original film.

- Potentiostatic measurements using the scanning droplet cell system showed that localised corrosion rate increased as the flow rate and surface roughness increased.

- Changes in surface residual stress state of the native and modified oxide films during cyclic loading were studied using X-Ray Diffraction technique which showed that

195

surface compressive residual stress decreased as a result of the introduction of a new oxide film.

- Nanoindentation tests using a Berkovich diamond indenter were performed to explore the differences in mechanical properties between 316L SS oxide film before and after AVPP treatment. It was found that the 316L oxide-film has a higher hardness compared to the AVPP oxide-film.

- Tensile tests revealed that the yield strength and the tensile strength of 316L SS samples were around 300 MPa and 600 MPa respectively.

- The effect of corrosion pits on the fatigue behaviour of stainless steel materials in particular the short crack regime was investigated using the SDC in combination with a fatigue rig. Results showed an improvement in the corrosion fatigue life in the AVPP modified 316L SS surface compared to the native surface due to a delay in film breakdown and pit initiation. Based on the size of the pit at the crack-pit transition the stress concentration threshold factor range, for 316L in corrosion fatigue using SDC technique, was found to be from 2.1 to 2.5 MPa √m.

## 7.2 Recommendations for Future Work

This work involved different experimental techniques in order to assess the effects of AVPP on the 316L surface mechanically and electrochemically. However additional experimental work is needed particularly concerning corrosion fatigue using SDC such as:

- Conducting corrosion fatigue tests using SDC technique to evaluate the effects of the applied potential including open circuit potential covering all the corrosion fatigue damage characteristics particularly the pitting at pit crack transition stages.

- It is shown in this study that the flow rate has effects on the localised corrosion process and hence it maybe useful to examine its role on corrosion fatigue behaviour using SDC technique under different parameters such as temperature, solution concentrations and pH.

- Assessing the influence of applied stress on the corrosion fatigue crack initiation and growth mechanism using SDC technique to establish fatigue limit from the material S-N plot.

- Modifying the SDC technique to allow application of different fatigue testing modes such as bending which needs more movement flexibility of the SDC probe tip during cycling load.

- Developing a multi-stage damage accumulation corrosion fatigue model incorporating corrosion (pitting) and fracture mechanics (microstructural and continuum) damage laws. Damage regimes to be identified for given environmental and loading conditions and to construct damage maps based on the corrosion fatigue tests results obtained.

# References

1 Strehblow H.H." Combined surface analytical and electrochemical studies for
2 Schultz, J. ; Lohrengel, M. "Stability, Reactivity and Breakdown of Passive Films, Problems of Recent and Future Research" Electrochimica Acta 45 (2000) 2499-2513

3 Olsson, CO A. ; *Landolt, D.* Passive films on stainless steels-chemistry, structure and growth Electrochimica Acta, 48 (2003), 1093-1104.

4 Vignal, V. ; C. Valot, ; R. Oltra, ;M. Verneau, ; L. Coudreuse "Analogy between the effects of a mechanical and chemical perturbation on the conductivity of passive films" Corrosion Science 44 (2002), 1477–1496.

5 Mansfeld, F; Lin, S.; Kwiatkowski, L. "The effects of process parameters on alternating voltage (AV) passivation of 304SS", Corros Science 34 (1993). 2045-2058.

6 He H.; Zhang, T.; Zhao, C.; Hou, K.; Meng, G.; Shao, Y.; Wang, F. "Effect of alternating voltage passivation on the corrosion resistance of duplex SS"
J Appl Electrochem 39 (2009). 737–745

7 Chambreuil-Paret A. A. and Magnin T., "Improvement of the resistance to stress corrosion cracking in austenitic stainless steels by cyclic prestraining", *Metall Trans A – Phys Metallurgy Mater Sci* 30A (1999), 1327–1331.

8 Fujimoto S., Tsujino K. and Shibata T., "Growth and properties of Cr-rich thick and porous oxide films on Type 304 stainless steel formed by square wave potential pulse polarisation", *Electrochim. Acta*, Vol. 47, (2001), 543–551.

9 Miller K. J. & de los Rios Eds ER. (1986), Short fatigue Cracks, ESIS Puln.

10 Akid R., "in Corrosion and the Environment", NACE conference, Bath (UK), (1998)18th April, p41.

11 McEvily R. and Wei RP. "Fracture Mechanics and Corrosion Fatigue," (1971), Proc. Int. Conf. on Corrosion Fatigue, NACE, 409.

12 Austen I. and Walker EF. "Quantitative understanding of the effects of mechanical and environmental variables on corrosion fatigue crack growth behaviour. The Influence of Environment on Fatigue" (1977), Conf. Inst. Mech. Eng, London, 1.

13 Lindley TC., McIntyre P. and Trant PJ., "Fatigue Crack. Initiation at Corrosion Pits" (1982), Metals Tech. Vo19, 135.

14 Kondo Y., "Prediction of Fatigue Crack Initiation Life based on Pit Growth", (1989) Corrosion Science Vol. 45, No. 1, 7

15 Akid R. & Miller KJ. "Short Fatigue Crack Growth Behaviour of a Low Carbon Steel Under Corrosion Fatigue Conditions" (1991) Fatigue Fract. Engng. Mater. Struct. Vol 4. 637.

16 Atkinson ID & Chen ZY. "The Effect of Temperature on Corrosion Fatigue Crack Propagation in Reactor Pressure Vessel Steels (1993), 6th NACE/TMS Conference, Env. Degradation Water Reactors.

17 Angelova D & Akid R. "A Normalisation of Corrosion Fatigue Behaviour : an example using an offshore structural steel in chloride environments" (1999), Fatigue Fract. Engng. Mater. Struct. Vol 22. 409

18 Murtaza G. and R. Akid: Eng. Fract. Mech., 2000, 67, (5), 461–474.

19 Dmytrakh I. M. and Akid R.: Fatigue damage accumulation: the role of corrosion on the early stages of crack development, Corrosion Engineering, Science and Technology 2006 Vol 41 NO 4.

20 Gunn R. N. (1997). Duplex stainless steels. Abington publishing.

21 Harry Brearley: Stainless Pioneer. Sheffield, U.K.: British Stainless Steel (now Avesta Sheffield), 1989. 105.

22 Lamb S. CASTI Handbook of Stainless Steels & Nickel Alloys. CASTI Publishing Inc. First ed 1999.

23 Hronsky C. W., Duquette, D. J. (1982); Corrosion-Nace, Vol. 38, 63.

24 Sedriks A. J., (1996), Corrosion of Stainless Steels. J.W.

25 Marshall, (1984), "Austenitic Stainless Steels, Microstructure and Mechanical Properties", Elsevier Applied Science Publishers LTD, England.

26 Honeycombe R. W. K., and Bhadeshia H. K. D. H. Steels-microstructure and properties. Elsevier Ltd, third edition (2006).

27 http://www.machinist-materials.com/stainless_table_two.htm.

28 Mansfield F., Tsai R., Shih H., Little B., Ray R. and Wagner P. (1990); " Results of exposure of stainless steels and titanium to natural seawater", Corrosion Nace 90, p190.

29 Bain E.C. and Griffiths W.E.: *Trans. AIME*, 1927, vol. 75, 166–213.

30 German Patent DT 2 225 673, 1972, Sudwestfalen (krupp).

31 Quik JMA, Guedeke M: Conf Corrosion 94, NACE, Baltimore, 1994, 393.

32 Noble DN, Gunn RN: Stainless Steel Europe 4 (19-20), 24-29.

33 Neubert V: Proc conf Duplex Stainless Steels 94 Glasgow, TWI, 1994, Vol. 1.

34 Christianus D: Proc conf Duplex Stainless Steels, 91 Beaune, Les editions de physique, 1991, Vo. 2, 1353-1361.

35 Avesta Sheffield: informations sheets for SAF 2304, 2205, and 2507.

36 Neubert V et al: 'Improvements of high alloy duplex steels for application in desulphurisation plants, acid gas environments and chemical production plants; Final Report COST 504 H, Clausthal, Germany, August 1993.

37 HASHIMOTO K., ASAMI K.and TERAMOTO K., *Corros. Sci.* 19 (1979) 3.

38 Sedriks AJ: Conf proc Stainless Steels, 84 Goteborg, Institute of metals, 1985, 125.

39 Charles J: Proc conf Duplex Stainless Steels, 91, Beaune, Les editions de physique, 1991, Vol. 1, 3-48.

40 POLAk J. and Zezulka P. (2005) Blackwell Publishing Ltd. Fatigue Fract Engng Mater Struct 28, 923–935.

41 Truman JE, Coleman MJ, Pirt KR: British Corrosion journal 12, 1977, 236.

42 Bandy R et al :Electrochemical society, Book, 1984.

43 Newman RC, Shahrabi T: corrosion scince 27 (8), 1987, 827.

44 Osozawa K, Okato N: Corrosion 86 Houston, Nace, 1986.

45 Charles J, Bonnefois B: Sem proc weldability of new ferritic and stainless steels, Cambridge, TWI, 1990.

46 Lizlovs EA: Climax molybdenum report RP-33-08-08, 1981.

47 I-Hsuang Lo, Wen-Ta Tsai: Effect of selective dissolution on fatigue in 2205DSS, Corrosion Science 49 (2007) 1847-1861.

48 Avesta Sheffield: informations sheets for SAF 2304, 2205, and 2507.

49 Weir Materials Ltd: Technical data sheets for zeron 100. wmlpub. 2.950301 Issue B.

50 Gysel W, Dybowski G, Wojtas HJ, Schenk R: conf proc Duplex stainless steels, 86 the hague, Nederland institute voor Lastechniek, 1986, 32, 326-330.

51 Dupoiron F, Verneau M, Audouard J P, Charles J: conf proc duplex stainless steels, 94 Glasgow, TWI, 1994, vol. 3, 92.

52 Haynes AG: Conf proc Application of stainless steels ,92, Stockholm, Jernkontoret, 1992, vol. 1, 415-435.

53 Bock H. E., "On the Stress and Fatigue Corrosion Cracking Behavior of Nitrogen-Alloyed Austenitic and Ferritic-Austenitic Chromium-Nickel-(Molybdenum) Steels" (1978) *Tech Mit Kr. For.,* Vol. 36, No. 2,.

54 Jaske CE, Payer JH, Ballint VS: corrosion fatigue properties of metal in marine environments, Springer-Verlag and Batelle Press, 1981.

55 Asphahani AI, Sridhar N: Corrosion, 38 (11), NACE, 1982, 587-595.

56 Amzallag C, Rabbe P, Desestret A: Corrosion-Fatigue Technology, ASTM STP 642, 1978, 117-132.

57 M. Liljas and R. M. Davison, 1986 "Duplex Stainless Steel Suction Rolls Fabricated from Plate," NACE/Corrosion 86.

58 Wensley A, Reid C: (1992) Stainless Steel Europe 32-38.

59 Kelley, C. E. Vestola, J. and Pelloux, R. M. (1975) *TAPPI,* Vol. 58, 80.

60 Smith RF., Pennington A: (1994) Corrosion , Baltimore, NACE, , 389.

61 Fruytier DJA: Beaune, (1991), vol. 1, 497-509.

62 Wagner GH, Munster R: Beaune, (1992), 2, vol. 1, 541-550.

63 Winnik S, Fitzgerald BJ: Corrosion (1994), Baltimore, Nace, (1994), 390.

64 Albert, W. A. J. (1838) "Über Treibseile am Harz" Archive für Mineralogie Geognosie Bergbau und Hüttenkunde, vol. 10, 215-34.

65 Suresh, S. "Fatigue of Materials" (1998) Cambridge University Press, Cambridge.

66 Wohler, A. (1860) Versuche uber die Festigleist der Eisenbahn-wagen-Achsen. Z. Bauweson 10.

67 Gerber H (1874). Bestimmung der Zulässigen Spannungen in Eisen-konstruktionen. *Z Bayer Arch Ingenieur-Vereins* 6:101–110.

68 Forsyth P. J., "Two stage process of fatigue crack growth", Proc. Crack Propagation Symp., (1961) Cranfield, Vol. 9, 453.

69 Hobson P. D., "The formulation of a Crack Growth Equation for Short Cracks" (1982), Fat. Fract. Engng. Mater. Struct. Vol. 5, No. 4, 323.

70 Navarro A. and de los Rios E. R. ' A Microstructurally Short Fatigue Crack Growth Equation" (1988), Fat. Fract. Engng. Mater. Struct. Vol. 11, No. 5, 383.

71 Wignall C.M., "Torsional Fatigue of three 316L Stainless Steels in Air and Artificial Sea water" (1997), Ph.D. Thesis, The university of Sheffield.

72 Miller K. J. and Akid R. "The Application of Microstructural Fracture Mechanics to various Metal Surface States.", (1996), Proc. R. Soc. Lond. A, 452, 1411.

73 Wang C. H. and Miller K. J. (1993), Fat. Fract. Engng. Mater. Struct. Vol. 16, No. 2, p.181.

74 Miller K. J. " The Behaviour of Short Fatigue Cracks and their Initiation., part II" (1987), Fat. Fract. Engng. Mater. Struct. Vol. 10, No. 2, 93.

75 Cox B. N. , Parde W. J. and Morris, W. L. "A Statistical Model of Intermittent Short Fatigue Crack Growth. Fat. (1986), Fract. Engng. Mater. Struct. Vol. 9, No. 5, 435.

76 Fine M. E., "Fatigue Resistance of Metals", (1980) Metall. Trans. A, 11, 365.

77 Paris P.C. and Erdongan F. A, "Critical Analysis of Crack Propagation laws", (1963) Journal of Basic Engineering Vol. 85, 528.

78 Akid R. "The influence of environment upon the accumulation of damage under corrosion fatigue conditions", (1996), Fat. Fract. Engng. Mater. Struct. Vol. 19, No. 8, 277.

79 Goto M. "Corrosion fatigue behaviour of a heat-treated carbon steel and its statistical characterstics" (1992), Engineering Fracture Mechanics, Vol. 42, No. 6, 893.

80 Boukerrou A. and Cottis R. A. "Crack initiation in the corrosion fatigue of structural steel in salt solution", (1993), Corrosion Science, Vol.35, No.1-4, p.577.

81 Wu X. D. "Experimental and theoretical studies of corrosion fatigue in a high strength steel" (1995) Ph.D. Thesis, University of Sheffield.

82 Stuart Lyon and Bob Akid, 2006, "Cost of Corrosion," (2007).

83 Michiel P.H. Brongers, 2004, "Cost of Corrosion Study," (2007).

84 Gonzales-Sanchez J., "Corrosion fatigue initiation in stainless steels" (2002) Ph.D. Thesis, Sheffield Hallam University.

85 Erwan le Roy, EunAe Cho (2000) Paper No. 140, 7th International Symposium on Electrochemical Methods in Corrosion Science.

86 Szklarska-Smialowska and Janik-Czachor M, (1967), Corrosion science, Vol.7, 65.

87 Komachi U. and Katada Y(2000) Paper No. 106, 7th International Symposium on Electrochemical Methods in Corrosion Science.

88 Okamoto G.and T. Shibata T., *Passivity of Metals,* Corrosion Monograph Series, R. P. Frankenthal, The Electrochemical Society, Pennington, NJ, 646, 1978.

89 Tatner I. "The effect of notches and pits on corrosion fatigue strength" (2004), Ph.D. Thesis, Sheffield Hallam University.

90 Isaacs H. S. "The localised breackdown and repair of passive surfaces during pitting", (1989), Corrosion science. Vol. 29 No. 2-3, 313.

91 Cottis R. A. and Husain Z. "Corrosion-fatigue initiation processes...", (1982) Metals Technology. Vol.9.

92 Burstein G. T. Pistorius P. C. And Mattin S. P. "The nucleation and growth of corrosion pits on stainless steel" (1993). Corrosion Science. Vol.35, 57.

93 Fontana M. G. and Green N. D., "Corrosion Engineering", (1967) McGraw-Hill, New York, 51.

94 Godard H. P., Canadian Journal of Chemical Engineering. (1960), Vol. 38, 167.

95 British Stainless Steels Association. http://www.bssa.org.uk/topics.php?article=111.

96 Gangloff, R. P. (1990), "Environmental Cracking-Corrosion Fatigue" in Corrosion Tests and Standards Manual, 253.

97 Scott P. M. "Chemistry Effects in Corrosion Fatigue", (1983), Corrosion Fatigue: Mechanics, Metallurgy, Electrochemistry and Engineering, ASTM STP 801, 319.

98 Harris J.A. and Fay P.A., "Fatigue life evaluation of structural adhesives for automotive applications", INT.J.Adhesion and Adhesives VOL. 12 (1992), 9-18.

99 Lee H. H. and Uhlig H., (1972), Metallurgical Transactions, Vol.3, 2949.

100 Taylor M. E. and Barsom J. M., , in "Fracture Mechanics (Thirteenth Conference)" (1981), ASTM STP 743, R. Roberts Ed., 599.

101 Rajpathak S. and Hartt W. H., in "Environmentally Assisted Cracking": (1990), Science and Engineering, ASTM STP 1049, W.B. Lisagor, T. Crooker , Eds., 425.

102 Novak S. R., in "Corrosion Fatigue Technology" (1978), ASTM STP 642, Craig H.L., Crooker T.W. and Hoeppner W. Eds., 26.

103 Cowley W.E. and Robinson F., (1968) British Corrosion Journal, Vol. 3, 223.

104 Broek D., "Elementry Engineering Fracture Mechanics" (1991), 4th edition, Kluwer Academic Publishers, Dordrecht, The Netherlands.

105 Laird C. and Duquette D. J. "Mechanisms of Fatigue Crack Nucleation" (1972), Corrosion Fatigue: chemistry, mechanics and microstructure, eds. Devereux O.et al.), 88:, Houston, Tex., NACE.

106 Duquette D. J. and Uhlig H., (1969), Transactions ASM, Vol. 62, 839.

107 Congleton J., Oleih R. A. and Parkins R. N., "Some electrochemical and microstructural aspects of corrosion fatigue", (1983), in Corrosion Fatigue: Mechanics, Metallurgy, Electrochemistry and Engineering, ASTM STP 801, 368.

108 Sudarshan T. S., Srivatsan T. S. and Harveyii D. P., (1990), "Fatigue process in metals - role of aqueous environments", Engng. Fraet. Mech., 36, 6. 827.

109 Duquette D. J., "In Environment Induced Cracking of Metals", (1990), Gangloff R.P and Ives M.B, Eds. NACE, Houston, 45.

110 Gangloff R.P, "in Environment Induced Cracking of Metals", (1990), Gangloff R.P. and Ives M.B, Eds. NACE, Houston, 55.

111 Murakami R. and Ferguson, W.G. "The Effects of Cathodic Potential and Calcareous Deposits on Corrosion Fatigue Crack Growth rate in Seawater for two Offshore Structural Steels." (1987), Fatigue Fract. Engng. Mater. Struct. Vol. 9, 477.

112 Ragab, A. Alawi H. and Sorein K., "Corrosion Fatigue of Steel in various Aqueous Environments", (1989), Fatigue Fract. Engng. Mater. Struct. Vol. 12, 469.

113 Duquette D. J., "A review of aqueous corrosion fatigue", (1972), Corrosion Fatigue: chemistry, mechanics and microstructure, (eds. 0. Devereux et al.), 12, Houston, Tex., NACE.

114 Hu H., "Fatigue and Corrosion Fatigue Crack Growth Resistance of RTQ5OL Steel", (1997), Ph.D. Thesis, The University of Sheffield.

115 Akid R., "The initiation and growth of short fatigue cracks in aqueous saline environment", (1987), Ph.D. Thesis, University of Sheffield.

116 Akid R., "The role of Stress-Assisted Localised Corrosion in the Development of Short Fatigue Cracks" (1997), Effects of the environment on the initiation of crack growth, ASTM STP 1298, 3, Van Der Sluys W. A., Piascik R. S. and Zawierucha R., Eds.

117 Quian Y.R. and Cahoon J.R., "Crack Initiation Mechanisms for Corrosion Fatigue of Austenitic Stainless Steel", (1997), Corrosion-NACE, Vol. 53, No. 2, 129

118 Magnin T., Coudreuse L. and Lardon J., "A quantitative approach to fatigue damage evolution in FCC and BCC stainless steels", (1985), Scripta Metall, Vol. 19, 1486

119 Gangloff R.P., "Crack-size Effects on the Driving Force for Aqueous Corrosion fatigue" (1985), Metallurgical Transactions 16A, 953.

120 Dmytrakh I. M., Akid R. and Miller K., "Electrochemistry of Deformed Smooth Surfaces and Short Corrosion fatigue Crack Growth Behaviour", (1997), British Corrosion Journal, Vol. 32, No. 2, 138

121 Wang Y. and Akid R., "Role of Nonmetallic Inclusions in Fatigue, Pitting and Corrosion Fatigue", (1996), Corrosion-NACE, Vol.52, No. 2, 92

122 Wang Y., Akid R. and Miller K.J., "The Effect of Cathodic Polarisation on Corrosion Fatigue of a High Strength Steel in Salt water", (1995), Fatigue Fract. Engng. Mater. Struct. Vol. 18, No. 3, 293.

123 Hoeppner D.W., "Model for Prediction of Fatigue lives Based upon a Pitting Corrosion Fatigue Process", (1979), Fatigue mechanisms, Proceedings ASTM STP *675*, 841, J.T. Fong, Ed.

124 Kawai S. and Kasai K., "Considerations of Allowable Stress of Corrosion Fatigue (focused on the influence of Pitting)" (1985), Fatigue Fract. Engng. Mater. Struct. Vol. 8, No. 2, 115.

125 Hoeppner D.W., Chandrasekaran V. and Taylor A.M., "Review of Pitting Corrosion Fatigue Models", (2000) The corrosion doctors Journal.

126 Withers PJ, Bhadshia HKDH., Residual Stresses, Patr 1 – Measurement techniques. Material Science and Technology, (2001); vol. 17, 355-65.

127 Prevey PS., "Current Applications of X-Ray Diffraction Residual Stress Measurement", (1996) ASM International, Materials Park, OH, , 103-110.

128 Handbook of Residual Stress and Deformation of Steel, ASM International, ISBN 0-87170-729-2.

129 Khan H., Michal G. M., Ernst F. and Heuer A.H., "Poisson Effects on X-Ray Diffraction..", (2009), Metallurgical and Materials Transactions Vol. 40A, 1799-1804.

130 A National Measurement Good Practice Guide No. 52, Determination of residual stresses by X-ray Diffraction – Issue 2, National Physical Laboratory, (2005); ISSN 1744-3911.

131 Lipson HS., Crystals and X-rays, Wykham publications (London) Ltd, 1970, ISBN – 0 851091504.

132 Gnefid S. A., Akid R. "The Impact of Surface Treatment...", (2010) The 1$^{st}$ symposium for Libyans Engineers .

133 Cullity B D, Stock SR., Elements of x-ray diffraction, Upper Saddle River, NJ: Prentice Hall, (2001), ISBN 0-20161-091-4.

134 Operational manuals, Philips X-pert Stress Analysis Equipment, Sheffield Hallam University, Sheffield.

135 Vignal V., Delrue O. and Peultier J. "Influence of the passive film properties and residual stresses on the micro-electrochemical behavior of duplex stainless steels", Electrochimica Acta Volume 55, 23, (2010), 7118-7125.

136 Dalaeia K., Karlssona B., Svenssona L.-E., "Stability of residual stresses created by shot peening of pearlitic steel and their influence on fatigue behavior", Procedia Engineering 2 (2010) 613–622.

137 John F. Watts, John Wolstenholme, , "An Introduction to Surface Analysis by XPS and AES," (2003) John Wiley & Sons Ltd, The Atrium, Southern Gate, Chichester , West Sussex PO19 8SQ, England , 212.

138 Operating manual/ Instructions, alicona® Infinite focuos microscope.

139 Operating manual, Philips XL40 analytical SEM.

140 BS 4490 "Methods for Micrographic determination of the grain size of steel" (1989).

141 Cogger N D. and Evans N J., "An Introduction to Electrochemical Impedance Measurement," (2007).

142 H. Krawiec, V. Vignal and R. Akid, Electrochimica Acta. Vol 53 (2008). 5252-5259.

143 Akid R., Roffey P., Greenfield D. and Guillen D.. "Local probe techniques". Woodhead Publishing Limited, Cambridge (2007), 23-32.

144 Kirsten Agnes Lill, Achim Walter Hassel Georg Frommeyer and Martin Stratmann. Electrochemica Acta, Vol.51 (2005), 978-983.

145 Achim Walter Hassel and Masahiro Seo. Electrochemica Acta, Vol. 44 (1999), 3769-3777.

146 Zhou, S. and Turnbull, A. "Influence of pitting on the fatigue life of a turbine blade steel". (1999) *Fatigue Fract. Eng.Mater. Struct.*, 22, 1083–1093.

147 Zhou S. and Turnbull A., "Development of a pre-pitting procedure for turbine disc steel". *British Corrosion J.* 35 2 (2000), 120.

148 William Stephen Tait, "An Introduction to Electrochemical Corrosion Testing for Practicing Engineers and Scientists," (1994), Pai Viscor Publications, Raciene, Wisconsin, USA, 79-93.

149 Gamry instruments, "Electrochemical Impedance Spectroscopy Theory" (2007).

150 Vaidya R.U., Rangaswamy P., (2001) Metallurgical and Materials Transactions A, Volume 32, Number 6, 1459-1465.

151 Noyan IC, Cohen JB., "Residual Stress in Materials", (1991) American Scientist, Vol 79-2, 142-53,.

152 Cullity BD, Stock SR., "Elements of X-ray differaction", (2001) Upper Saddle River, NJ: Prentice Hall,; ISBN 0-20161-091-4.

153 Oliver W. C. and Pharr G. M., "An Improved Technique for Determining Hardness and Elastic Modulus", (1992), J. Mater. Res 7 1564.

154 Lohrengel M. M., · Moehring A. and· Pilaski M., "Electrochemical surface analysis with the scanning droplet cell". Fresenius J Anal Chem (2000) 367 :334–339.

155 Fujimoto S., Kawachi S., Nishio T., Shibata T. J.of Electroanalytical Chemistry (1999), Vol. 473, 265-271.

156 http://www.lasurface.com, Accessed (April 2009).

157 Ramasubramanian N., Preocanin N. and Davidson R. D., J. Electrochem. Soc., 132 (1985), 793–798.

158 Souto R. M., Mirza Rosca I. C. and Gonzales S., Corrosion, 57 (2001), 300–306.

159 Filho N., Mansur T. and Rabello E. "Effect of the Environment on Fatigue Strength Limit ..", (2007) *Transactions,* SMiRT 19, Toronto, August.

160 Giordani E.J., Guimarães V.A., Pinto T.B. and Ferreira I., Effect of precipitates on the corrosion-fatigue crack initiation of ISO 5832-9 stainless steel biomaterial, *Int J Fatigue* 26 (2004), p. 1129–1136.

161 Yang Y., Yan Q., Ma R., Zhu F., Zhang L., and Ge C. "Corrosion Behavior of Modified UNS N08367 Austenitic Steel in Supercritical Water" (2010) Corrosion 66,; 3490311.

162 Suter T. and Böhni H., "A new microelectrochemical method to study pit initiation on stainless steels" (1997) Electrochim. Acta 42, p. 3275.

163 Cheng X., L X.i,Dong C. "A Diffusivities of Point Defects Study of Passive State on 316L.." (2010) IEEE 978-1-4244-4813-5.

164 Paijkull M., Kähönen A., Nytomt S. "The use of duplex stainless steel grades.." (2008) Stainless Steel World.

165 Leftheriotis G., Papaefthimiou S., Yianoulis P., "Dependence of the estimated diffusion coefficient of $Li_xWO_3$ films on the scan rate of cyclic voltammetry experiments" (2007) Solid State Ionics 178:259

166 Kocijan A., Donik C. and M. Jenko, "Electrochemical and XPS studies of the passive film formed on stainless steels in borate buffer and chloride solutions", (2007) Corros. Sci. 49, pp. 2083–2098.

167 Ramasubramanian N., Preocanin N. and Davidson R. D., J. Electrochem. Soc., 132 (1985), 793–798.

168 Gojić, M., Marijinn, D. and Kosec, L., Corrosion, 56 (2000) 839.

169 Pallotta, C., De Cristofano, N., Salvarezza, R.C. and Arvia, A.J., Electrochim. Acta, 31 (1986) 1265.

170 Urretabizkaya, M., Pallotta, C., De Cristofano, N., Salvarezza, R.C. and Arvia, A.J., Electrochim. Acta, 33 (1988) 1645.

171 Langevoort, J.C., Sutherland, I., Hanekamp, L.J. and Gellings, P.J., Appl. Surf. Sci., 28 (1987) 167.

172 Pidaparti R., Patel R. "Investigation of a single pit/defect evolution during the corrosion process" Corrosion Science 52 (2010) 3150–3153.

173 Vignal V., Oltra R., and Josse C., (2003) Scripta Materialia, 49, 779-784,.

174 Vignal V., Mary N., Oltra R., and Peultier J., (2006) Journal of the Electrochemical Society, 153 (9), B352-B357,.

175 Vignal V., Mary N., C. Valot, R. Oltra, and L. Coudreuse, Electrochemical and Solid-State Letters, 7(4), 39-42, 2004.

176 Sri Hastuty, Atsushi Nishikata, Tooru Tsuru. "Pitting corrosion of Type 430 stainless steel under chloride solution droplet". (2010) Corrosion Science 52 2035–2043.

177 Brown B.E., Lu H.H., and Duquette D. J., (1992) Corrosion 48, P.970.

178 Krawiec Halina, Vignal Vincent and Akid Robert. "Numericalmodelling of the electrochemical behaviour of 316 stainless steel based upon static and dynamic experimental microcapillary-based techniques: effect of electrolyte flow and capillary size", (2008) *Surf. Interface Anal.*; 40: 315–319.

179 Matsudaria M., Suzuki M. and Sato Y., (1981), MP 21 P.55.

180 Mansfeld F., J.V. Kenkel, Corrosion 35 (1979), P. 43.
181 Vrsalovic L., Klis Kic M., Rados Evic J. and Gudic S. "The effect of electrolyte flow rate and temperature on corrosion" (2005) Journal of Applied Electrochemistry 35:1059–1065.

182 Lohrengel M.M. and Rosenkranz Chr., (2005), Corrosion Science, Vol. 47, 785-794.

183 Hong T., Nagumo M. "Effects of surface roughness on early stages of pitting corrosion of type 301 stainless steel" (1997) Corrosion Science, Vol. 39, No. 9, 1665-1672.

184 Pujar M.G., Parvathavarthini N., Dayal R.K. "Influence of solution-annealing and stress-relieving on the pitting corrosion resistance of modified 316N SS weld metals: A study using EN technique" (2010) Materials Chemistry and Physics, Volume 123, Issues 2-3. 407-416.

185 Sieradzki K. and Newman R.C., "Brittle behaviour of ductile metals during stress corrosion cracking", (1985) Philos Mag A 51, 95–132.

186 Vignal V., Olive J.M., Desjardins D.Effect of molybdenum on passivity of stainlesssteelsin chloride media using ex situ near fieldmicroscopyobservations Corrosion Science, Volume 41, Issue 5, (1999), Pages 869-884.

187 Vignal V., Kempf D. "Influnce of heterogeneous Plastic Strain Fields on the Corrosion Susceptibility of Duplex Stainless Steels at the Microscale", (2007) Advances in Materials Science, Vol. 7, No. 1 11, 77-82.

188 Isaacs H.S. and Kissel G., *J. Electrochem.* "surface preparation and pit propagation in stainless steels" (1972), *Soc.* 119 1628.

189 Szklarska-Smialowska, Pitting corrosion of metals, (1971), 114.

190 Ebara R. "Corrosion fatigue crack initiation behavior of stainless steels", (2010) Procedia Engineering 2 1297–1306.

191 Akid R., Dmytrakh I. M., and Gonzalez-Sanchez J. "Fatigue Damage Accumulation: Aspects of Enviroments" (2006) Materials Science, Vol. 42, No. 1.

192 Li Y.-F., Farrington G. C. and Laird C. "Cyclic Response-Electrochemical Interaction in Mono-and Polycrystalline AISI 316L The Influence of Mechanical Strain

on The Transient Dissolution Behaviour During Corrosion Fatigue" (1993) Acta metall, mater. Vol. 41, No. 3, pp. 693-708.

193 Hu H. and Akid R., "A comparison of short fatigue crack growth (SFCG) rates in a medium strength steel under in-air and corrosion fatigue loading conditions," (2002) in: Corrosion-Deformation Interactions Conf., September 22–26, 2002, TMS, Wyoming, USA.


194 Masaki K., Ochi Y. and Matsumura T. "Small crack property of austenitic stainless steel with artificial corrosion▸ pit in long life regime of fatigue" (2006) International Journal of Fatigue 28 1603–1610.

# INITIATION & GROWTH OF CORROSION FATIGUE CRACK FOR AVPP TREATED STAINLESS STEEL

## SALAH A. GNEFID

### Ph.D.

### SHEFFIELD HALLAM UNIVERSITY

### 2011